Cooling & Sensing using Whispering Gallery Mode Resonators

Ying Lia Li

A thesis submitted to University College London
in partial fulfilment of the requirements for the
degree of Doctor of Philosophy

Department of Physics and Astronomy
University College London
August 2016

I, Ying Lia Li, confirm that the work presented in this thesis is my own. Where information has been derived from other sources, I confirm that this has been indicated in the thesis.

Signed .... Date ....

Abstract

This thesis reports on a detailed exploration of the optomechanical interaction between a tapered optical fibre and a silica microsphere mounted on a cantilever. The amount of light evanescently coupled from the fibre into the optical whispering gallery mode of the sphere is exquisitely sensitive to their separation allowing fast measurement of picometer displacements of both the microsphere-cantilever and the fibre. By exploiting this enhanced transduction, strong active feedback damping/cooling of the thermal motion of both the fibre and microsphere-cantilever have been demonstrated to the noise limit of the system.

The cavity enhanced optical dipole force between the fibre and the sphere was used to damp multiple mechanical modes of the tapered fibre, while a piezo-stack at the clamped end of the microsphere-cantilever allowed for cooling of its centre-of-mass motion and the second mechanical eigenmode. The effect of noise within the feedback loop was shown to invert the measured mechanical mode spectrum at high feedback gain as the noise itself is fed into the resonator. A rich variety of feedback induced spring stiffening and softening of the mode is measured when time delays are introduced. Cooling of the mechanical modes of the taper, which are ubiquitous to many WGM experiments and are considered as unwanted noise, has not been achieved previously. Simultaneous operation of both feedback schemes was demonstrated for the first time, providing stabilization of the system.

By using the microsphere-cantilever as an inertial test mass, measurement of its displacement induced by acceleration can resolve micro-g accelerations at high bandwidth.

Contents

List of Abbreviations

Abbreviation	Definition
AFM	Atomic force microscopy
AOM	Acousto-optic modulator
BW	Bandwidth
CCW/CW	Counterclockwise/clockwise
CEODF	Cavity enhanced optical dipole force
CSL	Continuous spontaneous localisation
ECDL	External cavity diode laser
EM	Electromagnetic
EOM	Electro-optic modulator
FEM	Finite Element Modelling
FFT	Fast Fourier transform
F-P	Fabry-Perot
FPGA	Field programmable gate array
FSR	Free spectral range
FWHM	Full width half maximum
HWHM	Half width half maximum
IMU	Inertial measurement unit
LO	Local oscillator
MEMS	Micro-electro-mechanical systems
PDH	Pound Drever Hall
PI/PID	Proportional integral differential
PSD	Power spectral density
PZT	Piezo-stack (Lead zirconate titanate)
QND	Quantum non-demolition
RF	Radio frequency
RMS	Root mean square
S/N	Signal to noise
SQL	Standard quantum limit
TE	Transverse electric
TIR	Total internal reflection
TM	Transverse magnetic
VRE	Vibration rectification error
WGM	Whispering gallery mode
ZPF	Zero point fluctuation

To my father, who continues to inspire me.

Acknowledgments

When I decided to apply for this Ph.D., I knew it would alter the course of my life. Embarking on a new project, in an area with no legacy of experience within the group, certainly puts one through a trial by fire. I could have easily burnt out without the support and guidance of my supervisor Prof. Peter Barker. He has provided me with the type of training that brings out a level of tenacity, forward-thinking, and courage I once thought was beyond my reach. Along the way, I have grown to love my experiment, and I now find myself in a wonderful mix of specialisms, filled with amazing scientists conducting experiments that will herald innovative technologies.

My experiences could not have been the same without the past and present members of the Barker group, as well as John and Rafid in the workshop. I cannot sum up in words how thankful I am to Dr. James Millen, a true friend and mentor, who I have looked up to since we were at Imperial College. I extend my thanks to Dr. Pete Edmunds, Ilhan, Dr. Alexandros Gerackis, Giacomo, Manish, Dr. Anis Rahman, Dan, Joel, and Anas, for many great conversations about work, life, and advanced dinosaur top trumps. I thank my friends around the world, who continue to keep me grounded and make me laugh.

One completely unpredictable outcome of my Ph.D. is that I would meet the love of my life; Joe King Burgess, my Joe-beans. On our first date he traversed the snow to meet me at UCL (I was working over the weekend), and unlike any other sane human being, decided he could tolerate being second place to my work. He continues to push me intellectually and creatively, and I would be broken without his love and support.

I am forever grateful for my father, the son of a farmer, who took the greatest risk by moving to the UK to pursue an engineering Ph.D. with nothing but £20. The sacrifices he made, and the chain of events that led him to meet his dear friend and greatest mentor, the late Prof. David Smith, has shaped the person I am today. Of course, 'behind every successful man is a great woman', and my fiercely devoted mother (also a doctor of engineering), has held our family of 3 together for the past 25 years as we continue to be separated by land and water from our extended family. Behind every great woman is a majestic cat, so it is only right I thank Marty Mc Fly (a.k.a. Swish King), my favourite feline companion.

Without being cliché, the words of Frost sum up my Ph.D. experience best:

Somewhere ages and ages hence:
Two roads diverged in a wood, and I-
I took the one less travelled by,
And that has made all the difference.

Robert Frost (1874-1963), 'The Road Not Taken'.

Publications

1. Ying Lia Li, *Don't hesitate, innovate*, Nature Nanotechnology **11** (652), (2016)
2. Ying Lia Li, James Millen and P. F. Barker, *Simultaneous cooling of coupled mechanical oscillators using whispering gallery mode resonances*, Optics Express **24** (2), (2016)
3. Ying Lia Li, James Millen and P. F. Barker, *Cooling the centre-of-mass motion of a silica microsphere*, Proc. SPIE 9164, Optical Trapping and Optical Micromanipulation XI **916404**, (2014)
4. P. F. Barker, James Millen, Ying Lia Li, Manish Trivedi and T. S. Monteiro, *Cooling optically trapped particles*, Proc. SPIE 8458, Optical Trapping and Optical Micromanipulation IX **845808** , (2012)

Chapter 1

Introduction

The field of cavity optomechanics, which studies the interplay between mechanical motion and an optical field, has undergone rapid progress in the last decade. Experiments within this area exploit an optical coupling between a mechanical oscillator and the cavity field; the most prevalent being dispersive coupling, where motion shifts the cavity resonance frequency. This imprinting of information onto the light field, termed ‘transduction’, allows for exquisitely sensitive measurements of displacements below the femtometre scale [1–4], enhanced by the ability to fabricate high optical quality factor cavities, for example, high reflectivity Fabry-Perot (F-P) cavities [5–8], photonic crystals [9–12], and whispering gallery mode (WGM) resonators [4, 13–15]. Such displacement sensitivity allows for many promising near-term real-life applications such as force sensing [16–19], and accelerometry [12, 20–24].

One fundamental aim of cavity optomechanics is to study the quantum behaviour of mechanical oscillators when the motion is cooled towards its quantum ground state, defined by an average phonon occupancy of $\bar{n} < 1$. Following inspiration from the atomic-physics community, who employ sideband cooling of trapped atoms by pumping the red-detuned mechanically induced sideband, such a feat has been achieved using macroscopic mechanical oscillators [25–27]. Here, the mechanical motion is optomechanically coupled to a cavity pumped with red-detuned light, such that viscous damping is obtained using dynamical backaction from cavity enhanced optical forces e.g. radiation pressure[1]. Alternatively, many groups are advancing towards ground state cooling by utilising optomechanical transduction in an active feedback scheme, created by electronically processing

---

[1] In contrast to atomic cooling, the internal degrees of freedom are decoupled to the macroscopic motion e.g. the centre of mass motion of a levitated sphere, and forms the basis for many experiments being conducted in the field of optomechanics.

the detected output light of the cavity into a signal proportional to the velocity of the mechanical oscillator. This feedback signal is used to drive a damping force provided by, but not limited to, a piezo-stack [28–31], or an optical gradient force [3, 7, 15, 32].

Although the prospect of conducting fundamental quantum experiments using macroscopic objects has never been so tangible [33, 34], the most successfully cooled devices consist of a clamped or tethered mechanical oscillator, such that performing Young's double slit experiment is not feasible, and environmental coupling prevents the creation of a macroscopic superposition. Nonetheless, on the path towards achieving these goals, the cooling of mechanical motion can enhance the sensing limits [17, 24, 35, 36]. The ability to damp thermal motion, which is considered detrimental to the sensitivity, is an important prerequisite for resolving displacements with a minimum measurement imprecision (i.e. noise) without the use of squeezed light, known as the standard quantum limit. This heralded the ground-breaking discovery of gravitational waves in late 2015 using a F-P interferometer cavity and a damped mirror [37]. Suppressing thermal motion also increases the sensing bandwidth, and combined with the use of shot-noise limited light, has successfully detected the quantum fluctuations of radiation pressure [38, 39], as well as the zero point fluctuations of a mechanical oscillator [40].

In this thesis, the optomechanical coupling between mechanical motion and an optical WGM is investigated. The transduction of thermal motion and optical cooling using WGM transduction of thermal motion, and WGM enhanced optical cooling is realised. WGMs are morphology dependent resonances which circulate around an equatorial path, tightly confined to the surface [13]. The ray-optics description of a WGM is shown in fig. 1.1 for a silica microsphere with refractive index n_2 surrounded by air (or vacuum) with $n_1 < n_2$. Total internal reflection (TIR) occurs at the sphere-air interface when light approaches at an incidence angle θ_i larger than the critical angle $\theta_\mathrm{c} = \arcsin\left(\frac{n_1}{n_2}\right)$, creating a WGM that undergoes an integral number of reflections. Dependent on the surface quality, WGM resonators can possess extremely high optical quality factors close to $\mathrm{Q}_\mathrm{opt} = 10^{10}$ [41], since very little light is lost at each 'bounce'. However, Maxwell's equations impose boundary conditions that require the continuity of the electromagnetic (EM) field across the dielectric boundary[2], which gives rise to the evanescent field (i.e. a transmitted wave that extends into air), allowing the WGM to interact and be perturbed

---

[2] The ray-optics picture fails to describe this evanescent field since Snell's law dictates there is no transmitted light across the interface beyond this critical angle. A thorough description of WGMs using electromagnetic (EM) theory is presented in this chapter.

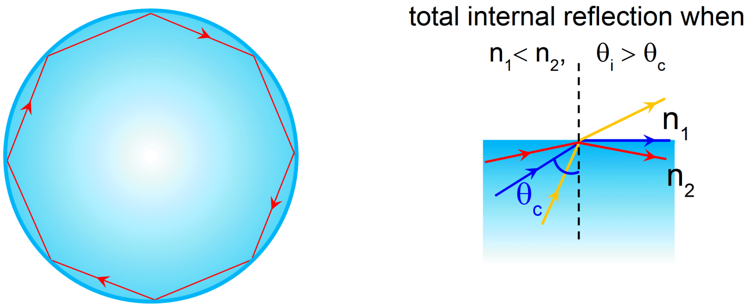

Figure 1.1: A basic ray diagram to show TIR within a sphere of refractive index n_2 in an environment such as air with a refractive index n_1. The beam undergoes an integral number of reflections, returning to its starting position and forms the WGM. It requires that the incident light approaches the sphere/air boundary at an angle larger than the critical angle $\theta_i > \theta_c$, as shown in the inset figure.

by outside influences. This makes WGM devices attractive for enhanced near-field sensing and amplified optical forces.

Until the last five years, the vast majority of cavity optomechanics relied on F-P resonators, where one mirror, or an intracavity object is cooled [5–8]. In 2006 an alternative type of cavity, a WGM resonator in the form of a toroid (disk with a curved edge analogous to a doughnut, anchored by a pillar) was introduced, and the internal radial breathing modes of this structure were sideband cooled close to the ground state, aided by the localisation of the mode with the WGM optical field [4]. An unexplored area is cooling of the *external* motion of the WGM resonator (i.e. the cavity). This is advantageous for making a compact sensor whilst minimising the number of movable components. For this reason, the optomechanics of a WGM resonator formed by a silica microsphere attached to a cantilever (a 'microsphere-cantilever') is described in this thesis, where the microsphere is the WGM resonator, and its vibrational motion is cooled.

Unlike a microdisk or toroid, the centre-of-mass (c.o.m.) of the microsphere-cantilever is explored here, which can be used for inertial sensing. It is also less complicated to fabricate and model compared to other optomechanics sensors which involve micro-electro-mechanical system (MEMS) machining [12, 19, 22], complex tailored optical fields [12, 19], or levitation [18]. In order to excite a WGM in the microsphere, a tapered fibre is used which acts as both a waveguide and an output channel [42–47]. Overlapping the evanescent field of both objects allows for efficient light coupling, which is highly sensitive to the thermal displacement of the microsphere-cantilever (and the tapered fibre) [45]. This allows for active feedback cooling of the c.o.m. motion of the cavity itself, demonstrated in this thesis for the first time.

The mass of the microsphere-cantilever, on the order of micrograms, is larger than typical optomechanical devices, which makes it an extremely susceptible accelerometer. Despite one study conducted 15 years ago using a tethered WGM resonator to sense acceleration [20], little to no information exists that truly characterises the acceleration sensing range, drift, and non-linear behaviour. Therefore, the microsphere-cantilever studied in this Ph.D. is experimentally tested as an accelerometer, providing new specifications essential for further development of a micro-g ($g=9.81\,\mathrm{ms}^{-2}$) accelerometer. A common issue that degrades the sensitivity of high bandwidth sensors (e.g. accelerometers) is noise in the form of technical noise from apparatus or nearby mechanical modes [12, 48]. In the classical regime, these extraneous thermal noise peaks pose a fundamental limit for mechanics-based measurements such as gravitational wave detection [49, 50], atomic force microscopy [51], and inertial sensing [12, 52]. This is true for the system studied here, where mechanical modes of the tapered fibre degrade both the sensing capability, and the cooling of the microsphere-cantilever. Apart from the combined efforts of LIGO, only one optomechanics system has implemented direct damping of external modes [48][3]. In this thesis, cooling of the thermal noise from mechanical taper modes is demonstrated for the first time by utilising the WGM cavity enhanced optical dipole force (CEODF).

The structure of this introductory chapter is arranged as follows:

- The motivation for carrying out this work is discussed, including relevant literature.
- The theoretical description of WGMs (i.e. expressions to describe the EM field), and coupling of light to WGMs is presented.
- The thesis outline.

1.1 Motivation

In terms of originality, the work presented in this thesis is the first optomechanics set-up using optical WGMs in Prof. Barker's research group, requiring the design and build of the experimental set-ups from scratch. It also comprises the first study of the interaction between WGMs and mechanical motion at UCL, and to the best of our knowledge, is the only WGM cooling experiment in the UK[4].

---

[3] The extraneous modes of [48] are from supporting mounts.

[4] There are many great labs in the UK currently studying optical WGMs for, but not limited to, biosensing, environmental sensing (i.e. temperature), optomagnonics, and creation of optical devices (i.e. frequency comb generation).

The range of WGM resonators used in sensing and cooling experiments is shown in fig. 1.2. The WGM resonator of interest in this thesis is that of fig. 1.2 d) where a microsphere remains tethered to a stem, and is called a 'microsphere-cantilever'.

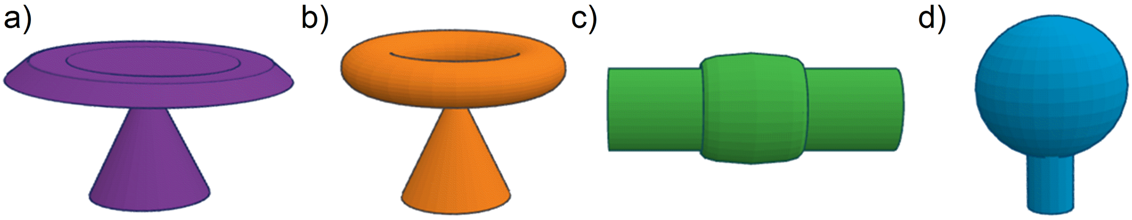

Figure 1.2: A variety of WGM resonators commonly used in experiments comprising of a) disks with polished sidewalls [15, 32], b) toroids where the edge of a disk is reflowed [46, 53], c) bottle resonators [54] which can be hollow inside, and d) microspheres that are attached or unattached to a cantilever/pendulum [13, 20, 45, 55]. The WGM resonator studied in this thesis is that of d) which is named a microsphere-cantilever.

The microsphere-cantilever is chosen for the ease of fabrication, since toroids and microdisks require micro-electro-mechanical (MEMS) processes. It should be noted that a silica microsphere tethered to a stem was one of the first studied WGM resonators in the 80's [13]. However, cooling of the c.o.m. motion of the microsphere itself has only recently been achieved and described in this thesis. The cooling of the mechanical modes of the tapered fibre with the CEODF is also described for the first time.

1.1.1 Whispering Gallery Mode Sensors

The role of the optical whispering gallery mode for sensing purposes is well established, and spans across a variety of resonator shapes, such as those in fig. 1.2. The resonance can respond to perturbations through a change in frequency, linewidth (Q-factor), and amplitude (via loss or scattering). This has been harnessed within this thesis to measure changes in temperature (chapter 2), displacement (chapter 3), and acceleration (chapter 6). Other sensing mechanisms that have been explored elsewhere are measurements of rotation (using the Sagnac effect) [56, 57], pressure [58], water content [59, 60], and electric fields [61]. More elaborate schemes employ the whispering gallery mode for single molecule detection and bio-sensing [62–65].

The use of WGMs for measuring displacement has emerged within the optomechanics community over the past 10 years, spurred on by the successful detection and cooling of radial breathing modes (these are radial expansions and contractions) of a toroid close to the ground state [4]. A dispersive coupling between the WGM and the breathing modes exists, such that the motion shifts the WGM resonance frequency, enhanced due to the high optical quality factor of the WGM (i.e. narrow linewidth). This cavity enhanced transduction has also been used to detect near-field coupled mechanical motion where the motion affects the evanescent field of the WGM resonator [1, 3, 9, 10, 15, 25, 40, 66–70]. One of the first demonstrations of measuring displacement to the standard quantum limit, which is the optimum detection sensitivity using non-squeezed light, utilises near-field coupling to a toroid [71].

Despite the success of WGM transduction for detecting motion of near-field coupled oscillators, the detection of the thermal motion of the WGM resonator itself has only been studied by two groups [20, 45]. Unlike a simple dielectric structure placed in the WGM evanescent field, the waveguide mediates the coupling of light, requiring a different theory to describe how changes to the coupling distance are transduced. Here, the thermal motion of the waveguide (and/or WGM resonator) changes the coupling rate as well as dispersively shifting the resonance. The theory quantifying this transduction was derived in 2015 [45]. Not only does the work in this thesis verify the experimental results of [45], but extends the field of WGM cooling by implementing active feedback cooling of the WGM resonator itself, and the mechanical modes of the tapered fibre.

1.1.2 Cooling of Macroscopic Objects using Whispering Gallery Modes

Ashkin first demonstrated that the optical gradient force from a focused laser beam can trap and levitate micro and nano particles [72]. Such an 'optical tweezer' is now a common tool for the manipulation of biological samples within liquids [73–75], and optical trapping of particles at low gas pressure [8, 76–79]. Waveguides can also strongly confine the optical field to create a gradient force capable of actuating nanoscale devices [80].

Such forces from light are often weak (i.e. the scattering force is $< 10^{-12}$N for 1 mW monochromatic light reflecting from an object with near-perfect reflectivity) unless losses are reduced (i.e. use high reflectivity), or the laser power is increased to over 100 mW. The use of an optical cavity can relax this limitation as it resonantly enhances the intracavity light intensity. Enhancement of the optical force was first demonstrated in the microwave regime by Braginsky using a F-P cavity [81]. The advent of MEMS techniques allows tailoring of these forces by fabrication of exotic cavities such as photonic crystal nanobeams in a 'zipper cavity' scheme [9]. With regards to WGM resonators, it was Ashkin again who demonstrated cavity enhanced radiation pressure by tuning the wavelength of an optical tweezer onto the WGMs of a dielectric silica sphere [82]. This resonance dependent propulsion has been used to investigate size-sorting of spheres [83].

When light is coupled into a WGM, the high intracavity intensity, and the low optical losses associated with total internal reflection, allows for WGMs to be long lived within the WGM resonator, confined within a small volume. This enhances optical forces, in particular, internal radiation pressure (which has been used to cool radial breathing modes), and the optical dipole force associated with the evanescent field gradient. Near-field cooling of mechanical objects placed in the WGM evanescent field utilise this CEODF [1, 15, 84]. However, rather than cooling the WGM resonator c.o.m. motion itself, the flapping motion between two stacked WGM disks [15], and the mechanical modes of a nanostring in the near-field of a microdisk have been demonstrated [1]. Therefore the combination of using WGMs to transduce motion (chapter 3), and then applying active feedback using transduction to cool the thermal motion of the WGM resonator itself and modes of the coupling waveguide (chapter 4) is a novel goal. Using the CEODF to damp the mechanical modes of the taper waveguide has not been previously reported, despite mention of these noise peaks as detrimental for sensing [12].

Performing Quantum Experiments

Based on the rapid progress obtaining ground state cooled mechanical oscillators, it would seem that quantum mechanics does not explicitly prohibit a macroscopic system from being in a superposition of two states. Currently, no optomechanics device has truly shown a superposition of mechanical states. Until this feat is met, many quantum theories that attempt to correlate mass and size with collapse models remain unproven [34, 85–87]. Ghirardi, Rimini, and Weber [88] have proposed a mechanism that prohibits macroscopic superposition states, which they term spontaneous localization theory. This includes a modification to the evolution of quantum states (described by the Schrodinger equation) with the addition of a randomly occurring interaction (i.e. stochastic noise) called 'Gaussian hits' that localise the object. Gravitational induced decoherence has also been proposed by Penrose [89], and Diosi [34]. The decoherence rate for gravitational induced collapse is determined by the gravitational self-energy of a system, and is predicted to be dominant for superpositions of objects 100 nm in size with a mass equal to the 'Planck mass' (approximately 0.02 mg). Experimentally, one could verify decoherence concepts, ideally using a levitated ground state cooled microsphere. Stochastic noise that leads to spontaneous localisation may be detected, requiring ultralow vacuum pressures $< 10^{-9}$ mbar to decouple from the environment. If the trap is switched off such that the microsphere undergoes free-fall, a modification to gravitational collapse theory may be made if the wavefunction expands to create a superposition state.

Lastly, quantum mechanical oscillators can be used as quantum networking devices, since the motion can also couple to spins [90], superconducting qubits [27], microwave resonators [91], and quantum dots [92]. A quantum optomechanical system could offer an effective way to convert quantum information from different frequency regimes, for example, from GHz (superconducting qubits) to optical frequencies (photons). Lehnert demonstrated coupling between microwaves and an optomechanical vibrating drum (15 μm diameter) that could store quantum information for 25 μs [91].

1.2 Whispering Gallery Mode Theory

Morphology dependent resonances were first observed by John William Strutt (Lord Rayleigh), who analysed the propagation of whispers within the dome of St. Paul's cathedral in the late 1800's [93]. He found that the acoustic waves were confined around the curved structure by undergoing total internal reflection at the surface boundary. This long lived acoustic wave allows whispers to be heard by a listener at any point around the dome. Such waves constructively interfere to form standing waves and were termed 'whispering gallery modes' (WGMs).

Optical WGMs can also be excited when light waves are confined within spherical structures such as those in fig. 1.2, as well as within liquid droplets [94, 95]. An evanescent waveguide (i.e. a tapered optical fibre with sub-micron waist [42–47]) is most commonly used for coupling light into the WGM, although prisms [41], side polished fibres [96–98], and free-space coupling [99, 100] have been achieved.

The following sections will briefly cover the theoretical framework of WGMs, allowing computation of the approximate resonance locations, the decay of the evanescent field, and the optical properties of the WGM, such as mode volume.

The existence of optical WGM resonances can be seen in the spectrum of light scattered from small spherical particles, as described in investigations by Gustav Mie in 1908 [101]. The sharp features that occur across specific laser frequencies correspond to resonant circulation of optical energy within the sphere, which enhance the scattering co-efficient. Analytical expressions following the work of Mie and Debye that describes scattering of a plane wave by a dielectric sphere [102–104] provide a means to calculate the locations of WGM resonances, dependent only on the dimensions and material properties of the sphere. The first step is to start with Maxwell's equations for the electric (E) and magnetic (B) fields, which can be used to derive the Helmholtz equation for EM radiation in a homogenous non-conductive dielectric with refractive index n, and wave number k (where $\mathrm{k} = n\frac{\omega}{c}$ inside the sphere):

$$\begin{aligned} \nabla^2 \mathrm{E} + \mathrm{k}^2\, \mathrm{E} &= 0, \\ \nabla^2 \mathrm{B} + \mathrm{k}^2\, \mathrm{B} &= 0. \end{aligned} \tag{1.1}$$

A solution φ that satisfies the scalar Helmholtz equation is:

$$\nabla^2 \varphi + \mathrm{k}^2 \varphi = 0, \tag{1.2}$$

which can be solved by separating φ into three differential equations. These lead to three mode numbers (s, l, m) which can describe the EM field and its distribution without requiring further manipulation to derive the full solution for the E (B) field. Such rigorous studies can be found in [104, 105].

Equation 1.2 can be written in spherical coordinates, depicted in fig. 1.3, where r is the radial distance between the origin, set at the microsphere centre (position O), to a position of interest on the sphere at P.

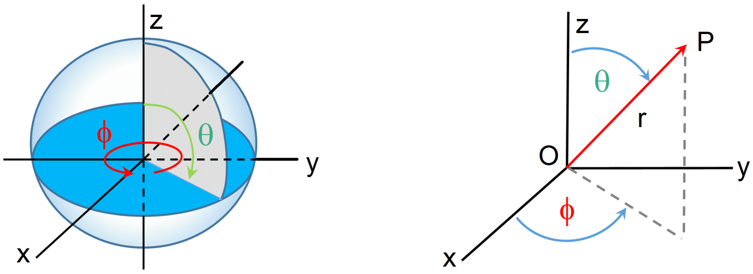

Figure 1.3: Spherical co-ordinate representation of the microsphere, where the polar angle is θ, and the azimuth angle is ϕ.

The inclination between the zenith direction and the position vector OP is denoted as the polar angle θ, measured between 0 and π radians, and the azimuth angle ϕ (measured between 0 and 2π radians) describe the angular distribution. Solutions to eq. 1.2 fall under two classes known as transverse magnetic TM (E= $\nabla \times (r\varphi)$) or transverse electric TE (E= $\nabla \times \nabla(r\varphi)$) modes. Due to spherical symmetry, TE and TM modes are decoupled and have zero radial electric and magnetic fields respectively. For TE modes, the electric field points in the polar direction and the magnetic field in the radial direction (vice versa for TM modes). In spherical co-ordinates, eq. 1.2 is written as:

$$\frac{1}{r^2}\frac{\partial}{\partial r}\left(r^2\frac{\partial \varphi}{\partial r}\right)+\frac{1}{r^2\sin(\theta)}\frac{\partial}{\partial \theta}\left(\sin(\theta)\frac{\partial \varphi}{\partial \theta}\right)+\frac{1}{r^2\sin^2(\theta)}\frac{\partial^2\varphi}{\partial \phi^2}+\mathrm{k}^2\varphi=0, \tag{1.3}$$

which can be separated into three differential equations to provide eigenfunctions for the radial, azimuthal and polar fields:

$$\varphi(r,\theta,\phi)=\varphi_r(r)\,\varphi_\theta(\theta)\varphi_\phi(\phi), \tag{1.4}$$

which satisfy the conditions:

$$r^2\frac{\mathrm{d}^2\varphi_r(r)}{\mathrm{d}r^2}+2r\frac{\mathrm{d}\varphi_r(r)}{\mathrm{d}r}+\left(\mathrm{k}^2r^2-p^2\right)\varphi(r)=0, \tag{1.5}$$

$$\frac{1}{\sin(\theta)}\frac{\mathrm{d}}{\mathrm{d}\theta}\left(\sin(\theta)\frac{\mathrm{d}\varphi_\theta(\theta)}{\mathrm{d}\theta}\right)+\left(p^2-\frac{q^2}{\sin^2(\theta)}\right)\varphi_\theta(\theta)=0, \tag{1.6}$$

$$\frac{\mathrm{d}^2\varphi_\phi(\phi)}{\mathrm{d}\phi^2}+q^2\,\varphi_\phi(\phi)=0, \tag{1.7}$$

where the real parameters p and q are separation constants.

The azimuthal eigenfunctions of eq. 1.7, which are periodic, are given by:

$$\varphi_\phi(\phi)=C_1e^{im\phi}+C_2e^{-im\phi}, \tag{1.8}$$

where C_1, C_2 denote complex constants and the separation constant q is replaced by the azimuthal mode number m.

Solving the polar equation, eq. 1.6, requires a change in variable $\upsilon=\cos(\theta)$:

$$\left(1-\upsilon^2\right)\frac{\mathrm{d}^2g_\theta(\upsilon)}{\mathrm{d}\upsilon^2}-2\upsilon\frac{\mathrm{d}g_\theta(\upsilon)}{\mathrm{d}\upsilon}+\left(p^2-\frac{m^2}{1-\upsilon^2}\right)g_\theta(\upsilon)=0, \tag{1.9}$$

where $\varphi_\theta(\theta)=g_\theta(\cos(\theta))$. The solutions to this linear second order differential equation are known as the hypergeometric functions [106], and have non-zero solutions if $p^2 = l(l+1)$, where $l \leq |m|$. The parameter l is known as the polar mode number and for each

l, the allowed azimuthal mode numbers are in the range $-l < m < l$, leading to a $2l+1$ degeneracy in m. The complete solutions to eq. 1.9 are the associated Legendre functions $P_l^m(\cos(\theta)) = P_l^m(\upsilon)$. Physically, l is the number of wavelengths in one round trip of the light within the microsphere (l is therefore an integer). For the case $m \geq 0$, $g_\theta(\upsilon)$ is given by [104]:

$$g_\theta(\upsilon) = P_l^m(\upsilon) = (-1)^m (1-\upsilon^2)^{m/2} \frac{\mathrm{d}^m}{\mathrm{d}\upsilon^m} P_l(\upsilon), \tag{1.10}$$

where $P_l(\upsilon) = \frac{1}{2^l l!} \frac{\mathrm{d}}{\mathrm{d}\upsilon^l} (\upsilon^2 - 1)^l$ is the Legendre polynomial of degree l. For $m \leq 0$, corresponding to modes propagating in the opposite direction, $P_l^{-m}(\upsilon) = (-1)^m \frac{(l-m)!}{(l+m)!} P_l^m(\upsilon)$.

Bringing together the product of $\varphi_\phi(\phi)$ and $\varphi_\theta(\theta)$ gives:

$$Y_l^m(\theta, \phi) = C_{l,m} \, P_l^m(\cos(\theta)) \, e^{im\phi} \qquad -l \leq m \leq l, \tag{1.11}$$

where $Y_l^m(\theta, \phi)$ are known as the spherical surface harmonics[5] of degree l and order m and the normalisation constant is $C_{l,m} = \sqrt{\frac{(2l+1)}{4\pi} \frac{(l-m)!}{(l+m)!}}$.

Lastly, the radial dependency of eq. 1.5 can be written as:

$$x^2 \frac{\mathrm{d}^2 g_r(x)}{\mathrm{d}x^2} + 2x \frac{\mathrm{d}g_r(x)}{\mathrm{d}x} + [x^2 - l(l+1)] \, g_r(x) = 0, \tag{1.12}$$

where $p^2 = l(l+1)$ is used, alongside the substitution $g_r = \varphi_r(x/\mathrm{k})$ where $x = \mathrm{k}r$. There are two linearly independent solutions to eq. 1.12 for a sphere, known as the spherical Bessel functions of the first and second kinds, denoted by $j_l(x)$ and $y_l(x)$ respectively [106]. The radial function $\varphi_r(r)$ can therefore be expressed as a linear combination of these spherical Bessel functions such that:

$$\varphi_r(r) = \alpha_l \, j_l(\mathrm{k}r) + \beta_l \, y_l(\mathrm{k}r), \tag{1.13}$$

where α_l, β_l are complex constants. One should note that the role of each Bessel function is dependent on the problem to be solved.

- Bessel functions of the second kind have a singularity at the origin (centre of sphere) and are unsuitable for describing the EM field within the microsphere. Therefore TM and TE modes inside the sphere are described by $j_l(x)$.
- Near the sphere boundary and beyond, modes are expressed as a linear combination

---

[5] The complex conjugate is given as $(Y_l^m)^*(\theta, \phi) = (-1)^m Y_l^{-m}(\theta, \phi)$

of the first and second Bessel functions (eq. 1.13), known as the Hankel function, where the constants are determined by the interface at the sphere boundary.

The radial EM field distribution gives rise to peaks (regions of high intensity), where the number of peaks equals the quantum number s. The lowest lying state $s = 1$ is confined as close as possible to the surface of the sphere and occurs for $l \approx n\, x_{\mathrm{wgm}}$, where n is an integer number, and x_{wgm} is known as the size parameter relating the wavevector k with the sphere radius, a, and the WGM wavelength λ:

$$x_{\mathrm{wgm}} = \mathrm{k}\, a = \frac{2\pi a}{\lambda}. \tag{1.14}$$

Combining eqs. 1.11 & 1.13, the general solution of the scalar wave equation is therefore:

$$\varphi(r, \theta, \phi) = \sum_{l=0}^{\infty} \sum_{m=l}^{m=-l} \left[\alpha_l j_l(\mathrm{k}r) + \beta_l y_l(\mathrm{k}r)\right] Y_m^l(\theta, \phi). \tag{1.15}$$

The field distribution and resonance locations are computed by matching the solutions interior and exterior to the microsphere at the dielectric-air boundary [102] using the vector Helmholtz equation. A characteristic equation is formed which has many roots (the root number denoted by mode number s) that determine an infinite set of eigenfrequencies (WGMs) for a given radius.

1.2.1 Mode Numbers & Eccentricity

The mode numbers *s,m,l* have a physical interpretation, whereby:

- s is the number of peaks in the radial intensity distribution,
- *2m* describes the number of maxima in the azimuthal spatial distribution
- modes with $m < 0$ propagate in the opposite direction to $m > 0$
- l is the number of waves resonant along the circumference with the polar intensity distribution containing $(l - |m| + 1)$ lobes.

Shown in fig. 1.4 are a variety of polar plots (i.e. $\phi = 0$ and θ is varied) that illustrate the electric field distribution of a WGM in a microsphere, simulated using a Matlab code by Balac and Feron [104]. The first column shows varying mode number $s = 1, 2, 3$ with fixed $m = l$, where the number of field maxima is equal to s. In the second column $s = 1$, with varying l, m, where the number of lobes is equal to $(l - |m| + 1)$.

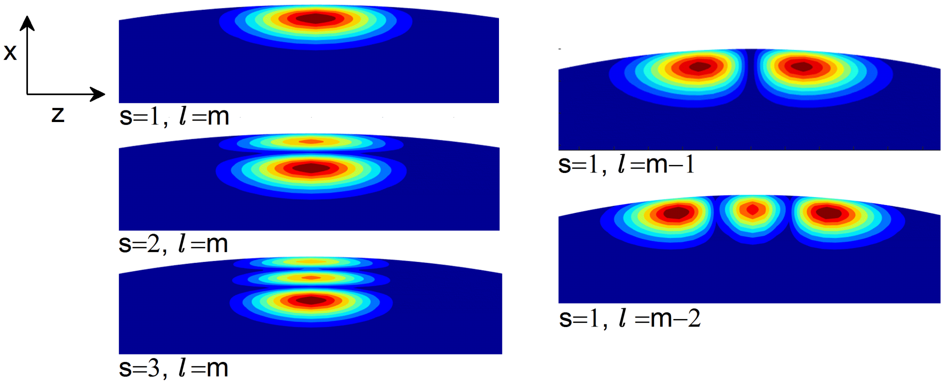

Figure 1.4: A variety of polar plots (i.e. $\phi = 0$ and θ is varied) showing the electric field distribution of a WGMs with varying mode numbers s, l, and m in a silica microsphere, simulated using a Matlab code by Balac and Feron [104].

The WGMs typically excited are those with the lowest s, high l, and $|m \approx l|$. Modes with large s tend to have lower optical quality factors due to greater leakage out of the sphere, and the intensity peaks in the radial distribution are less confined to the surface. When $m = l$, a fundamental WGM mode is created such that if $s = 1$, from a geometric point of view, the modes correspond to near-glancing rays incident upon the interior surface. If a light ray has a smaller angle of incidence on the sphere surface, then two round trips may be necessary for phase matching meaning the mode deeply penetrates inside the sphere e.g. $s = 2$, to create a different set of resonances with different wavelength but the same l number (i.e. same number of reflections).

In reality, spheres will have deformations and eccentricity which removes the $2l + 1$ degeneracy in m, creating new resonances that must be calculated using perturbation theory, discussed elsewhere [102]. The degeneracy of the counterpropagating WGMs (i.e.$\pm m$) can be broken when the sphere has surface defects or dust (acting as a scatterer), and a portion of the mode in one direction can propagate in the opposite direction. The two modes behave as coupled oscillators which split the WGM resonance into a doublet. Such an effect has been beneficial for sensing applications, where the split mode can be used to detect the presence of a surface scatterer, such as a virus [107]. However, the use of split WGMs is actively avoided within this thesis to minimise cross-coupling of counterpropagating signals.

1.3 Properties of Whispering Gallery Mode Resonators

Following the work of Lam [108] and Schiller [109], who utilise an analytic approximation of the Bessel functions, a closed-form expression describing the position of WGMs at frequency ω_0, in a sphere, is given by:

$$\omega_0 = \frac{c\, n_a}{n\, a}\left(l + 1/2 + \nu_1 \left[\frac{l + 1/2}{2}\right]^{1/3} + ...\right), \tag{1.16}$$

where $-\nu_1$ is the first zero of the Airy function ($\nu_1 \approx 2.34$), n is the refractive index of the sphere, a is sphere radius, and n_a is the refractive index of the surrounding medium, i.e. air or vacuum. This equation shows the dependence on refractive index of both resonator and surrounding medium, as well as the resonator size. To first order, when $n_a = 1$, eq. 1.16 is approximately $2\pi n a = l\lambda$, which is easily recognised as the condition for constructive interference of a wave after undergoing a round trip of the resonator circumference. This approximation is most accurate for WGMs with low l mode numbers but is often useful for estimating the free spectra range (FSR) (ω_{FSR}, in radians) and the cavity finesse F:

$$\omega_{\mathrm{FSR}} = |\omega_{s,m,l} - \omega_{s,m,l+1}| \approx \frac{c}{n\, a}, \tag{1.17}$$

$$F = \mathrm{Q}_{\mathrm{opt}} \frac{\omega_{\mathrm{FSR}}}{\omega_{s,m,l}} = \frac{\mathrm{Q}_{\mathrm{opt}}\, c}{\omega_0\, n\, a}, \tag{1.18}$$

where $\mathrm{Q}_{\mathrm{opt}}$ is known as the optical quality factor, discussed shortly. The finesse (typically 75,000 for WGM resonators in this thesis) relates the cavity losses $\mathrm{Q}_{\mathrm{opt}}$ and the round trip time τ_{rt}, such that $\tau_{\mathrm{rt}} = \frac{2\pi n a}{c} \approx 3\,\mathrm{ps}$ for a 177 μm diameter sphere such as the one studied in chapter 4.

1.3.1 Optical Quality Factor

The amount of energy dissipation in an oscillating system is defined by the quality factor of the mode, which is the energy storage time normalised with respect to the period of oscillation:

$$\mathrm{Q}_{\mathrm{opt}} = \omega_0\, \tau, \tag{1.19}$$

where $\mathrm{Q}_{\mathrm{opt}}$ is the optical quality factor for a WGM resonance at frequency ω_0, τ is the decay time governing loss (the inverse of the total WGM decay rate κ). For a lossless cavity the storage time would be infinite such that no energy is radiated or absorbed.

For real systems, loss mechanisms can be split into two categories; intrinsic and extrinsic, where those belonging to the cavity itself are intrinsic (coupled at a rate γ_i), whereas those related to external perturbations, such as a waveguide, are extrinsic (at rate γ_e). Each loss mechanism sets a limit to the quality factor such that $\mathrm{Q}_{\mathrm{opt}}^{-1} = \mathrm{Q_i}^{-1} + \mathrm{Q_e}^{-1}$, where $\mathrm{Q_i}$ and $\mathrm{Q_e}$ is the quality factor limited by intrinsic and extrinsic losses respectively.

In the absence of coupling waveguides, the optical energy in the WGM resonator decays exponentially with time constant $\tau_0 = \frac{1}{\gamma_i}$, such that the quality factor is limited to $\mathrm{Q_i}$. The sum of intrinsic losses due to material absorption (including surface contaminants), scattering losses (intrinsic bulk and surface inhomogeneities) and radiative/tunnel losses defines τ_i. Tunnelling losses occur due to incomplete TIR at the curved interface and produces a small amount of transmittance due to photons tunnelling out of their bound states (i.e. into free-space), but is typically negligible [41]. Bulk absorption in the material limits the quality factor to $\mathrm{Q}_{\mathrm{mat}} = \frac{2\pi n}{\alpha\lambda} \approx 10^{11}$, where α is the material absorption coefficient. No WGM system has achieved the bulk absorption limited quality factor yet. Similarly, scattering at the surface, which scales with surface roughness, should not be of great concern since reflowing the WGM resonator with a high power laser provides smooth surfaces due to surface tension, although it has been shown that redeposition of evaporated silica can lead to sub-wavelength defects and the presence of surface waves can deform the surface [102]. However, large dust particles (μm's in diameter) adhering to the surface are the dominant scattering source, causing a decrease in $\mathrm{Q}_{\mathrm{opt}}$ (as well as a WGM doublet due to the broken degeneracy of $\pm m$ modes) [110]. Another surface loss is water chemically adsorbed onto the highly hygroscopic silica which has been measured to cause $\mathrm{Q}_{\mathrm{opt}}$ to drop by 20% in the first five minutes after fabrication [41], although partial recovery of $\mathrm{Q}_{\mathrm{opt}}$ can be achieved using a 400^o C bakeout [111].

The extrinsic losses are dominated by the intentional coupling to a waveguide that allows light in and out of the WGM resonator. Such a propagating mode further reduces the storage time by introducing an extrinsic decay rate $\gamma_e = \frac{1}{\tau_e}$ so that the total decay rate becomes $\kappa = \gamma_e + \gamma_i$, and the so-called 'loaded' quality factor is:

$$\mathrm{Q}_{\mathrm{opt}} = \frac{\omega_0}{\kappa} = \frac{\omega_0}{\gamma_e + \gamma_i} = \omega_0\,(\tau_e + \tau_0). \tag{1.20}$$

Typical $\mathrm{Q}_{\mathrm{opt}}$ obtained in experiments using WGM in silica microspheres are of the order $10^7 - 10^8$, and the highest obtained is 0.8×10^{10} [41]. Those for microdisks are considerably lower ($\approx 10^6$) due to etching imperfections in the MEMS fabrication method, but can be improved by reflowing with a CO_2 laser to form a toroid. A high Q_{opt} ensures a long photon lifetime, which is the time required for the light energy in the resonator to decay to $1/e$ of its original value. A $Q_{\text{opt}} = 0.5 \times 10^8$ at 1064 nm gives a lifetime of around 28 ns, which corresponds to $\approx 20,000$ cycles (i.e. round trips) for a 177 μm diameter sphere.

1.3.2 Evanescent Field

Light trapped inside a WGM resonator undergoing TIR at the curved boundary will have an associated evanescent field extending beyond the resonator edge into the surrounding medium (i.e. air), shown in fig. 1.5 which plots the radial field distribution for a fundamental WGM with $m = l$, $s = 1$.

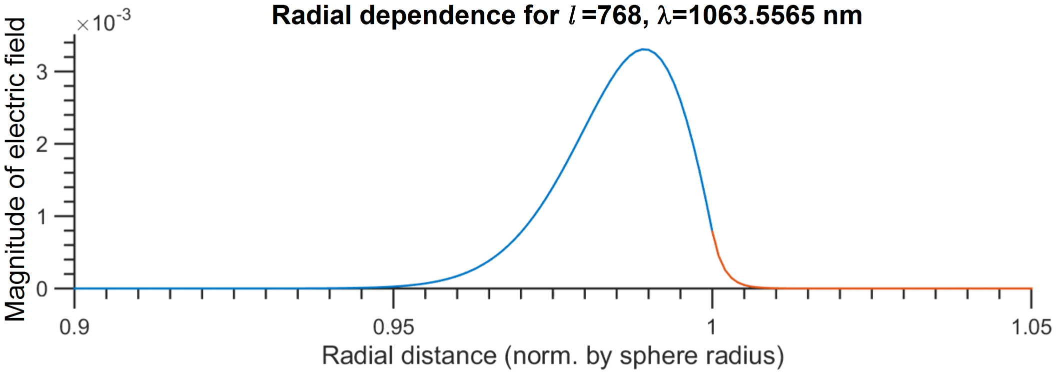

Figure 1.5: The radial dependence of the EM field of a 177 μm diameter silica microsphere with mode numbers $s = 1$, $l = m = 768$. The electric field distribution is plotted against the radial distance, normalised by the sphere radius, so that 1 indicates the sphere boundary. The evanescent field is coloured in orange.

The evanescent field decays as $\propto e^{-\alpha_s r}$, and the decay constant α_s is given by [112]:

$$\alpha_s = \sqrt{\beta_s^2 - \mathrm{k}^2 n_a^2}, \tag{1.21}$$

where $\beta_s = \frac{\sqrt{l(l+1)}}{a}$ is known as the propagation constant. For large spheres the approximations $\beta_s \approx \frac{l}{a}$, and $l = \mathrm{k}na$ can be used to give the evanescent field decay length (for a sphere surrounded by air $n_a = 1$) as [112]:

$$\alpha_s^{-1} \approx \frac{c}{\omega_0 \sqrt{n^2 - 1}}, \tag{1.22}$$

which is ≈ 150 nm for 1064 nm light. The evanescent field allows for near-field evanescent coupling to a waveguide to excite the WGMs (detailed later), as well as sensing changes to its surroundings such as pressure [58], water content [59], and mechanical motion [1, 3, 9, 10, 15, 25, 40, 66–70].

1.3.3 Mode Volume

One unique feature of WGMs is the confinement of the field within a small mode volume V_{m}, which plays an important role for a variety of applications that require a high optical energy density, such as enhancing the optical dipole force ('cavity enhanced optical dipole force' [32] used in chapter 3 & 4) or non-linear Kerr effects [41]. The expression for the mode volume is given by [113]:

$$V_{\mathrm{m}} = \frac{\int \epsilon(r)\,|\mathrm{E}|^2}{\max\left(\epsilon(\mathrm{r})\,|\mathrm{E}|^2\right)}\,\mathrm{d}V, \tag{1.23}$$

where $\epsilon = n^2(r)$ is the dielectric constant of the material at position r. Equation 1.23 can be analytically solved using a Matlab simulation by Balac and Feron [104], giving $V_{\mathrm{eff}} = 4.35 \times 10^{-15}\,\mathrm{m}^3$ for the mode shown in fig. 1.5. The electric field distribution of this mode is shown in fig. 1.6 in both the a) polar and b) azimuthal planes, where the WGM is confined, and circulates around the equator.

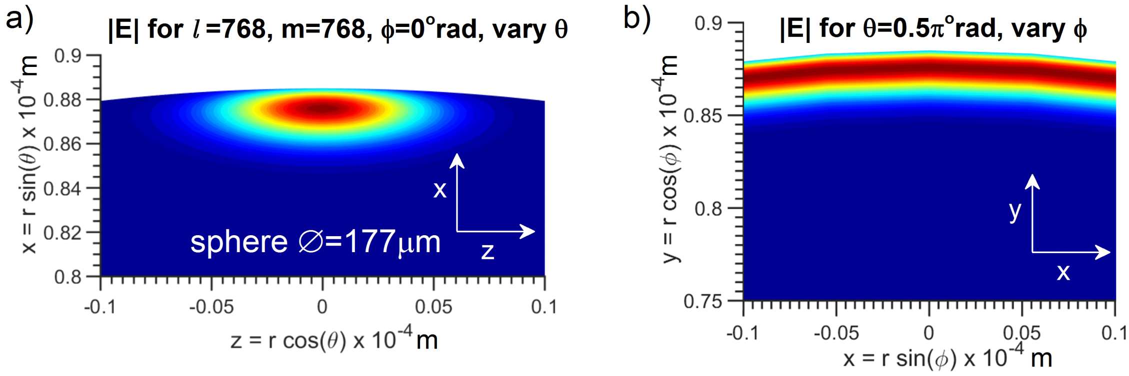

Figure 1.6: The electric field distribution for the $s = 1$, $l = m = 768$ fundamental WGM mode in a $\oslash = 177\,\mu$m silica microsphere, excited with 1064 nm light (1063.5565 nm) shown in a) the polar plane ($\phi = 0^o$ rad with varying $0 < \theta < \pi$), which is zoomed-in. Displayed in b) is the distribution along the azimuthal plane when $\theta = \frac{\pi}{2}$ and $-0.11^o < \phi < 0.11^o$ rad. Note that b) is a zoomed in view of the mode which circulates all around the circumference i.e. $0 < \phi < 2\pi$.

Braginsky provides an approximate solution to eq. 1.23 for $s = 1$ modes [13]:

$$V_{\mathrm{eff}} \approx 3.4\pi^{3/2}\left(\frac{\lambda}{2\pi n}\right)^3 l^{11/6}\sqrt{l - m + 1}, \tag{1.24}$$

which gives $V_{\text{eff}} = 5.30 \times 10^{-15}\,\text{m}^3$ for the mode in fig. 1.6, around 20% larger than that found by modelling.

1.3.4 Comparison with Theory using White Light Excitation

A Matlab code written by Christian Matzler [103] can be used to predict the WGM resonance locations by numerically solving the scattering theory in section 1.2. The output of this code is the reduced scattering coefficient (reduced refers to the incorporation of the anisotropy coefficient) as a function of excitation wavelength. Such a spectrum was used in the early experiments of this Ph.D. to validate the excitation of WGMs in a levitated $10\,\mu$m diameter silica sphere, trapped in a quadrupole trap. Here, broadband white light was successfully used to excite a spectrum of WGMs, and the scattered light collected from a $\oslash \approx 10\,\mu$m silica sphere is plotted in fig. 1.7 (bottom blue trace). The periodic peaks correspond to WGMs of varying linewidth from ≈ 100 GHz to THz. The details of this set-up is outlined in the appendix, section 8.1. The top black trace is the simulated resonance locations for a sphere of refractive index 1.45 and diameter $\oslash = 9\,\mu$m, where the difference in diameter is related to the variance of the microsphere sizes (colloidally produced spheres often have standard deviation of 10-20 % in size), as well as the difference in refractive index which has not been measured[6].

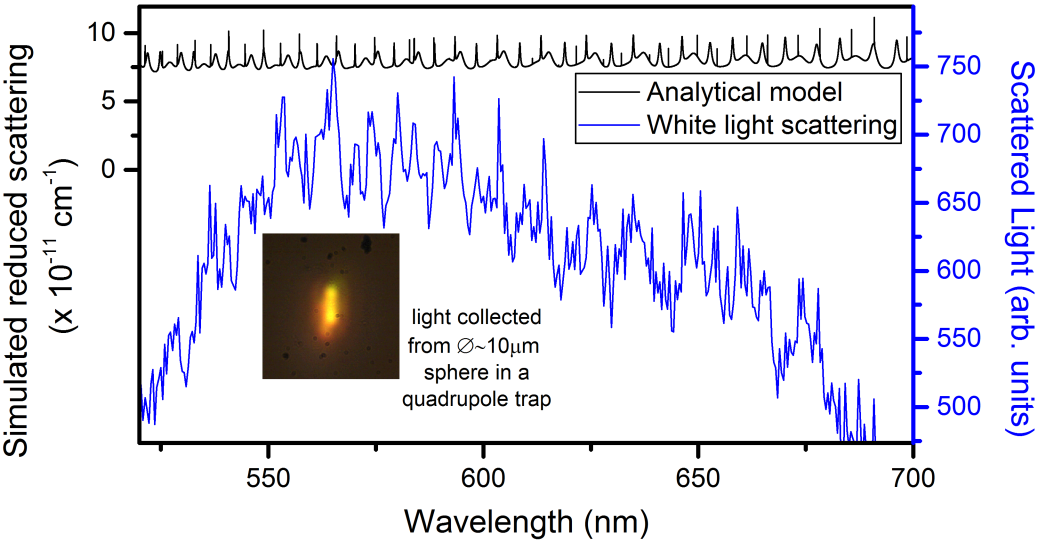

Figure 1.7: Blue data: Experimentally measured WGM resonances of an ≈ $10\,\mu$m diameter silica microsphere, levitated in an quadrupole trap at trap frequency 20 Hz, and illuminated with focused white light. The scattered light collected is collected using a spectrometer. Black data: The predicted locations of the WGMs of a $9\,\mu$m diameter silica microsphere.

---

[6] The refractive index is quoted between 1.43-1.46 from Bangs Laboratory who supplied the silica microspheres.

Similar broadband excitation has been achieved elsewhere, using levitated aerosol droplets [95]. The narrowest predicted WGMs cannot be measured due to the poor surface quality of the colloidally produced spheres, but is also limited by the resolution of the spectrometer[7], and the low excitation and collection efficiency via free space coupling. Despite the benefits of an environmentally decoupled WGM resonator, the low ion trap frequency of 20 Hz, and its lack of spatial confinement (which gives the elongated appearance in the microscope image, inset of fig. 1.7) as well as the poor surface quality of the spheres resulted in unsuccessful monochromatic coupling. This is the primary reason for developing the clamped microsphere-cantilever instead of pursuing a levitated set-up. One benefit with using spheres with diameters above 100μm, is that there are more WGM modes within a given wavelength range due to a smaller free spectral range.

1.4 Theory of Optical Coupling to Whispering Gallery Modes

The excitation of WGMs is highly dependent on phase matching to minimize scattering loss, making free space coupling inefficient due to the different phase velocity of the propagating light in air and silica. Although recent advances have shown low efficiency (10-20%) monochromatic coupling to deformed (high eccentricity) spheres using free space coupling [99, 100][8], it is accepted that evanescent coupling techniques are far superior. The majority of experiments conducted since the 1950s use waveguide coupling methods which rely on bringing the evanescent field regions of a waveguide and sphere in close proximity ($< 1\,\mu$m). The first techniques involved prism coupling [41], and later moved onto polished fibres [96–98], and tapers [42–47]. Recently, planar waveguides formed using MEMS techniques have emerged as promising coupling elements, especially for chip-based systems [20]. The highest coupling efficiencies of over 95% have been achieved with tapered fibres [42, 47] due to the taper surface quality, and the ability to tailor the tapering angle and diameter for a specific sized WGM resonator. The tapered fibre operates by having a region where the fibre waist is on the order of the laser wavelength so that a large portion of the fundamental fibre mode protrudes as an evanescent wave beyond the boundary. The elegance of using a tapered fibre is that it allows for near-complete extraction of light

---

[7] Ocean-optics 2000+, resolution 0.1 nm FWHM

[8] One group have successfully used free-space coupling of a laser to the WGM of a deformed sphere to cool radial breathing modes [99] using resolved sideband cooling.

from the cavity, removing the need to detect and resolve information from scattered fields which are usually low in power and noisy. For this reason, tapered fibres are employed in this work.

1.4.1 Tapered Optical Fibres

Tapered fibres are typically produced by pulling single mode fibre whilst heating a central portion with either hydrogen [45] or butane [114] flames, a ceramic heating cube [115], or a CO_2 laser [116]. For small diameters, a dielectric cylindrical waveguide only supports a single propagating mode. The required waist size of the tapered fibre for confining only the fundamental mode of the taper, the HE_{11} mode, is often quoted with respect to the normalized frequency V-parameter [117]:

$$\mathrm{V} = \frac{2\pi a_{\mathrm{w}}}{\lambda}\mathrm{N.A.} = \frac{2\pi a_{\mathrm{w}}}{\lambda}\sqrt{n_{\mathrm{core}}^2 - n_{\mathrm{cladding}}^2}\,, \tag{1.25}$$

where N.A. is the numerical aperature and a_{w} is the radius of the taper waist. A single mode waveguide requires V to be smaller than 2.405 [118]. This means for $\lambda = 1064\,\mathrm{nm}$, $n_{\mathrm{core}} \approx 1.45$ (i.e. n_{core} is now the refractive index of the cladding for a tapered fibre), $n_{\mathrm{cladding}} = 1$ (i.e. air), a taper waist of $2a_{\mathrm{w}} = 0.78\,\mu\mathrm{m}$ is required.

The radial direction of the field (transverse to the fibre length) decays exponentially as an evanescent field. Overlapping this field with the evanescent field of a WGM allows for exchange of light. One condition for efficient coupling is the matching of the propagation constant β_t of the fundamental mode in the taper, to that of the WGM resonance (β_s, defined in the text before eq. 1.22 pg. 18). The evanescent decay length of the microsphere and taper are $\alpha_s^{-1}, \alpha_t^{-1}$ respectively, leading to a total coupling length of $\eta^{-1} \approx (\alpha_t^{-1} + \alpha_s^{-1}) \approx 2\left(\sqrt{\beta_s^2 - k^2 n_a^2}\right)^{-1}$ due to phase matching [112]. This can be approximated as $\eta^{-1} = \frac{2}{k\sqrt{n^2-1}}$, assuming $n_a = 1$. Phase matching with the WGM can be tuned because β_t varies with the taper radius. By approaching the WGM resonator tangentially to the taper, both fields remain in phase over the extended interaction length, known as the coupling junction, which allows for efficient coupling.

The following section details the theoretical description of this coupling, including the perturbative effect on the WGM due to the presence of the taper.

1.4.2 Evanescent Coupling Theory

When the tapered fibre, with a higher refractive index than the air surrounding the microsphere, is positioned within a few wavelengths from the WGM resonator boundary, the WGM evanescent field will feel its presence as it changes the effective refractive index within the coupling junction. EM energy can be transferred from the optical mode in the waveguide to the WGM in a process called frustrated total internal reflection. The exchange of light into and out of the WGM resonator can be mathematically described using the coupled mode equations [119] in the slowly varying amplitude approximation for weak coupling. The rates of energy transfer are shown in fig. 1.8 for a microsphere coupled to a tapered fibre, but are applicable for other types of waveguides.

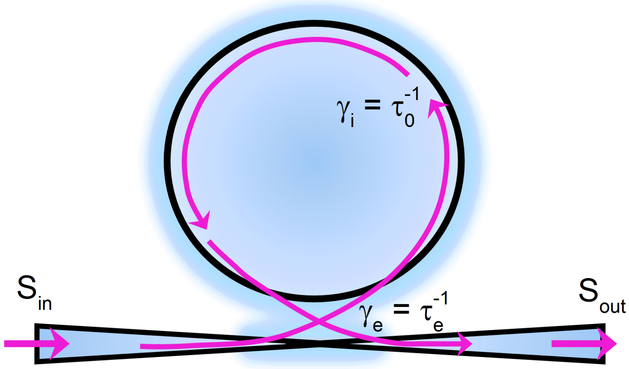

Figure 1.8: Coupling light into a WGM resonator with a tapered fibre, where the overlap of the evanescent fields forms the coupling junction. Here, light propagating into the taper with amplitude S_{in} enters the WGM resonator at the extrinsic coupling rate γ_e, where it remains confined inside the sphere, decaying at the intrinsic rate of γ_i through absorption and radiative processes, as well as coupling back into the taper at the rate γ_e. The transmission past this coupling junction is S_{out} and contains information relating to the WGM as well as any residual uncoupled light from S_{in}.

The complex scalar mode amplitude $\tilde{a}(t)$ is introduced, normalised such that $|\tilde{a}(t)|^2$ is the energy. In the quantum picture, $|\tilde{a}(t)|^2$ is the number of photons, rescaled by $\hbar\omega_0$. Three parameters describe the evolution of $\tilde{a}$; the resonant WGM frequency ω_0, the decay rate of the mode due to internal cavity losses $\gamma_i = \frac{1}{\tau_i}$ (referred to as the intrinsic loss), and the cavity decay rate due to coupling to the waveguide mode $\gamma_e = \frac{1}{\tau_e}$ (referred to as the extrinsic loss). The mode amplitude therefore follows a time evolution according to:

$$\dot{\tilde{a}}(t) = \left(-i\omega_0 - \frac{\kappa}{2}\right)\tilde{a}(t) + \frac{S_{\text{in}}(t)}{\sqrt{\tau_e}}, \tag{1.26}$$

where S_{in} is the amplitude of the mode in the fibre taper, coupled into the WGM with a time constant τ_e, normalised so that $|S_{\text{in}}(t)|^2$ is the power (or photon flux) impinging on the coupling region, and $\kappa = \gamma_e + \gamma_i$ is the total cavity loss rate which broadens the WGM linewidth. Since the driving field oscillates harmonically at an angular frequency of ω_l such that $\tilde{S}_{\text{in}}(t) = S_{\text{in}}(t)e^{-i\omega_l t}$, working in a rotating frame at this frequency is convenient to simplify the analysis [119]. Therefore, eq. 1.26 can be written as:

$$\dot{a}(t) = \left(i\Delta - \frac{\kappa}{2}\right) a(t) + \frac{S_{\text{in}}(t)}{\sqrt{\tau_e}}, \tag{1.27}$$

where $\Delta = \omega_l - \omega_0$ is the detuning with respect to the WGM resonance. In order to calculate the power circulating in the cavity $\left(\left|\bar{S}\right|^2 = \frac{|\bar{a}|^2}{\tau_{\text{rt}}} = \frac{1}{\tau_{\text{rt}}}\right)$, the steady state of eq. 1.27, $\bar{a}$ is required. Using a continuous driving amplitude of $S_{\text{in}}(t) = \bar{S}_{\text{in}}$ and setting the time derivative to zero, $\bar{a}$ is:

$$\bar{a} = \frac{1}{-i\Delta + \kappa/2} \frac{\bar{S}_{\text{in}}}{\sqrt{\tau_e}}. \tag{1.28}$$

The power circulating in the cavity is therefore:

$$\begin{aligned} \left|\bar{S}\right|^2 = \frac{|\bar{a}|^2}{\tau_{\text{rt}}} &= \frac{1}{\tau_{\text{rt}}} \frac{1}{\Delta^2 + (\kappa/2)^2} \frac{\left|\bar{S}_{\text{in}}\right|^2}{\tau_e} \\ &= 2\eta_c \frac{F}{\pi} \frac{1}{1 + 4\Delta^2/\kappa^2} \left|\bar{S}_{\text{in}}\right|^2, \end{aligned} \tag{1.29}$$

where τ_{rt} is the round trip time, F is the finesse, and η_c is the coupling parameter defined as $\eta_c = \frac{\tau_0}{\tau_0 + \tau_e}$. For a cavity where $\eta_c = 0.5$, the enhancement of intracavity power compared to launched power is $\left|\bar{S}/\bar{S}_{\text{in}}\right|^2 = F/\pi$ (on-resonance), showing how high finesse cavities can build up power and consequently enhance detection of perturbations.

Next, the transmission of the tapered fibre is derived, which contains information about perturbations detected by the WGM. This is what a photodetector measures (i.e. energy of the field). The transmitted light amplitude emerging past the coupling region is:

$$S_{\text{out}}(t) = S_{\text{in}}(t) - \frac{a(t)}{\sqrt{\tau_e}}, \tag{1.30}$$

which in the steady state gives:

$$\begin{aligned} \bar{S}_{\text{out}} &= \frac{\tau_e - \tau_0 - 2i\tau_e\tau_0\Delta}{\tau_e + \tau_0 - 2i\tau_e\tau_0\Delta} \bar{S}_{\text{in}} \\ &= \frac{(1 - 2\eta_c)\,\kappa/2 - i\Delta}{\kappa/2 - i\Delta} \bar{S}_{\text{in}}. \end{aligned} \tag{1.31}$$

The transmitted power, denoted by $\mathcal{T}$ is therefore:

$$\begin{aligned}\mathcal{T} = \left|\bar{S}_{\text{out}}\right|^2 &= \frac{(\tau_e - \tau_0)^2 + (2\tau_e\,\tau_0\,\Delta)^2}{(\tau_e + \tau_0)^2 + (2\tau_e\,\tau_0\,\Delta)^2}\left|\bar{S}_{\text{in}}\right|^2 \\ &= \left(1 - \frac{\eta_c(1-\eta_c)\,\kappa^2}{(\kappa/2)^2 + \Delta^2}\right)\left|\bar{S}_{\text{in}}\right|^2\end{aligned} \tag{1.32}$$

which is a Lorentzian dip of FWHM linewidth κ. This equation can be expressed in terms of the intrinsic coupling rate γ_i, and the extrinsic coupling rate γ_e: $\mathcal{T} = \left(1 - \frac{\gamma_e\gamma_i}{(\kappa/2)^2+\Delta^2}\right)\left|\bar{S}_{\text{in}}\right|^2$, such that on-resonance, the transmission is:

$$\mathcal{T}_{\text{on}} = \frac{(1-\gamma_e/\gamma_i)^2}{(1+\gamma_e/\gamma_i)^2}\left|\bar{S}_{\text{in}}\right|^2, \tag{1.33}$$

which is related to the on-resonance power coupled to the WGM $\mathrm{P_c}$, by $\mathrm{P_c} = (1 - \mathcal{T}_{\text{on}})\left|\bar{S}_{\text{in}}\right|^2$. Note that $\mathrm{P_c}$ is not the intracavity circulating power, derived in eq. 1.29.

1.4.3 Coupling Regime

It can be seen in eq. 1.33 that on-resonance, the amount of coupling depends on the ratio between the extrinsic and intrinsic coupling rates, which creates 3 coupling regimes:

- Undercoupling: $\gamma_i > \gamma_e$. The amplitude of the cavity leakage field coupled back from the resonator into the taper with phase shift between 0 and π (π for on-resonance) is much smaller than the amplitude of the transmitted uncoupled fibre field. Both fields interfere destructively causing a decrease in transmission.
- Overcoupling: $\gamma_e > \gamma_i$. The accumulated circulating cavity power is much higher than the remaining pump field within the taper therefore the amplitude of the cavity field coupled back into the taper maintains a high transmission.
- Critical coupling: $\gamma_e = \gamma_i$, for $\eta_c = 0.5$. The transmission past the resonator vanishes due to complete power transfer between the waveguide to the cavity mode. The leakage field and the propagating field within the taper have equal magnitude but phase shifted by π causing complete destructive interference.

The overlap between the evanescent field of the taper and that of the WGM sets the coupling strength of γ_e, such that γ_e increases exponentially as $\sqrt{\gamma_e} \propto e^{-i\alpha_s d}$, where d is the coupling distance, and α_s is the decay length defined in eq. 1.22. Note that γ_i remains constant. Therefore the coupling regime can be easily tuned by changing d, as explored experimentally in chapter 3[9]. Critical coupling to WGMs using tapers can produce coupling efficiencies as high as 99.97% [120], where the taper diameter is optimised so that the WGM is not coupled to higher order fibre modes. Coupling to these modes leads to loss as these modes die off when the taper diameter transitions to single mode operation. Other non-resonant losses can occur due to the presence of the taper itself, which may scatter part of the light into free-space modes.

In the case of on-resonance coupling $\Delta = 0$, at critical coupling $\gamma_i = \gamma_e$, the intracavity circulating power $\left|\bar{S}\right|^2$ of eq. 1.29, labelled as $\mathrm{P_{circ}}$ becomes:

$$\mathrm{P_{circ}} = \frac{\left|\bar{S}_{\mathrm{in}}\right|^2}{\tau_{\mathrm{rt}}\,\gamma_i} = \frac{\lambda_0\,\mathrm{Q_{opt}}}{2\pi^2\,n\,a}\,\mathrm{P_i}, \tag{1.34}$$

where λ_0 is the WGM wavelength, a is the microsphere radius, n is the refractive index of the microsphere, and $\mathrm{P_i}$ is the power coupled into the taper. The light intensity inside the cavity is:

$$\mathrm{I} = \frac{\mathrm{P_{circ}}}{A} = \frac{\lambda_0\,\mathrm{Q_{opt}}}{\pi\,n\,2\pi\,a\,A}\,\mathrm{P_i} \approx \frac{\lambda_0\,\mathrm{Q_{opt}}}{\pi\,n\,V_{\mathrm{m}}}\,\mathrm{P_i} \tag{1.35}$$

where A is the mode area, and $V_{\mathrm{m}} \approx A\,2\pi a$ is the mode volume. For example, a silica microsphere $\oslash = 177\,\mu\mathrm{m}$, with $n \approx 1.5$, and $\mathrm{Q_{opt}} = 10^8$ with input power $\mathrm{P_i} = 1\,\mathrm{mW}$, has $\mathrm{P_{circ}}$ of 40 W which is concentrated into a mode volume of $4.35 \times 10^{-15}\,\mathrm{m}^3$ (for $n = 1$, $l = m = 768$), giving a large intracavity intensity of $5.2\,\mathrm{MW\,mm^{-2}}$. Such a build up of optical power can be beneficial for miniature lasers, and optical parametric oscillators. However, it leads to bulk heating due to the absorption of light into the cavity medium, and unwanted non-linear thermal effects due to the Kerr non-linearity [121].

1.5 Thesis Outline

The preceding sections outlined the theory behind WGMs and coupling light into WGMs using a tapered fibre. Here, the layout of the thesis is described according to the main achievements within each chapter:

- Chapter 2: The experimental apparatus for fabricating microsphere-cantilevers and tapered fibres is described. A homebuilt tunable laser for excitating WGMs is characterised, and the set-up for coupling light into the microsphere-cantilever is presented,

---

[9] In a Fabry-Perot cavity the three coupling regimes are accessed by changing the transmittivity of the mirrors, where critical coupling has equal transmittivity for the two end mirrors.

including active and passive laser stabilisation methods. The results of this section provide the foundation for all other chapters.

- Chapter 3: The WGM enhanced transduction mechanism for detecting thermal motion is discussed, and the optimum experimental settings are verified against theory. The transmission can be processed into a power spectral density (PSD) in units of energy such that the mechanical properties of the transduced thermal motion can be extracted. The WGM transduction forms the basis of a feedback signal, which is used in chapter 4. The feedback forces are identified by actuating the microsphere-cantilever and the tapered fibre using a piezo-stack and the CEODF respectively.
- Chapter 4: Using the transduction mechanism in chapter 3, the WGM signal is processed into a feedback signal using differentiation and amplification. This drives the actuating forces to cool the c.o.m. motion (and second eigenfrequency) of the microsphere-cantilever, and higher order modes of the tapered fibre. Also shown is simultaneous cooling of mechanical modes belonging to both objects.
- Chapter 5: Passive cooling, which does not require electronic signal processing or a feedback loop, is classically modelled for two types of optomechanical coupling between mechanical motion and the WGM light field; dispersive cooling where the motion shifts the WGM resonance, and dissipative cooling where the motion alters the cavity decay rate. The use of classical modelling validates the original quantum noise theory of dissipative cooling, showing cooling when light is blue-detuned to the WGM resonance. The dispersive and dissipative coupling between the tapered fibre and the WGM in the microsphere-cantilever is experimentally measured, and a novel future experiment to obtain dissipative cooling is presented.
- Chapter 6: The WGM transduction of motion is used to measure acceleration, where the displacement of the test-mass (i.e. the microsphere-cantilever), is proportional to acceleration. Experiments that characterise the sensing performance such as range, sensitivity, and drift have never been performed on this type of system. An experimental comparison of performance with a commercial sensor shows great promise for a WGM accelerometer.
- Chapter 7: A range of further experiments are highlighted. Since improvements to the experiment for specific applications are identified within individual chapters,

this concluding section provides an outlook for exploring new areas of research. Two applications are considered; reaching the quantum ground state and inertial sensing. A conclusion summarising the experimental achievements of the entire thesis is presented.

Chapter 2

Excitation of Whispering Gallery Modes

2.1 Introduction

This chapter details the experimental coupling of light into the WGM resonator under study; the microsphere-cantilever. Following from the introduction to WGMs in chapter 1, a tapered fibre is selected as the evanescent coupling waveguide. This method is preferred as it is less alignment dependent, provides a fibre output channel, and obtains higher coupling efficiencies than other waveguides. The theory of tapered fibre coupling can be found in section 1.4.2 (pg. 23) of chapter 1. The large free spectral range of the WGMs, typically over 700 GHz for an 100 μm diameter silica sphere, require a tunable laser source swept in frequency to locate WGMs. In this thesis a homebuilt 1064 nm laser is used, which is able to produce a single mode output that is mode-hop free over a range of 6 GHz[1]. The properties of this laser will be discussed in this chapter.

The use of WGMs in experiments often requires the excitation laser to be fixed on-resonance (or, at a set detuning from resonance) in which case active stabilisation methods such as Pound-Drever-Hall (PDH) locking can be employed. Such locking must be robust to counteract bulk heating effects associated with the large intracavity intensity of the WGM (up to MW/mm^2), which shifts the resonance since the refractive index and/or cavity dimensions change. The characteristics of this thermo-optic effect, including stable self-locking using this phenomena, are explored in this chapter alongside the capabilities

---

[1] This tuning range is over 100 times smaller than the free spectral range of WGMs in 100 μm diameter spheres, but the cost to build the laser is an order of magnitude lower than commercial 1064 nm tunable lasers with over 1 THz tuning range.

of the PDH locking.

The aim of this chapter is to present the primary experimental set-up used for the remainder of this thesis. In this chapter is described:

- Fabrication of the microsphere-cantilever and tapered optical fibre using a CO_2 laser and a tapering rig respectively, both developed during this Ph.D. The modification of a homebuilt 1064 nm laser for a large frequency tuning range is characterised.
- Experimental results showing excitation of WGMs within the microsphere. The relationship between the WGM with respect to the gap between the microsphere and the tapered fibre (the 'coupling distance') is investigated.
- Active PDH stabilisation of the laser to the WGM, which is also used to investigate the thermo-optic effect. The thermo-optic effect is then exploited for implementation of passive thermal locking.

2.2 Fabrication of the Microsphere-cantilever & Tapered Fibre

2.2.1 Microsphere-cantilever

The WGM resonator used throughout this thesis is a microsphere attached to a cantilever, where the microsphere forms the optical cavity. The cantilever allows for clamping and creates the mechanical modes that are transduced by the WGMs as described in chapter 3, and actively cooled as described in chapter 4.

The microsphere-cantilever is fabricated by melting the end of a tapered/untapered optical fibre using a continuously pulsed CO_2 laser, focused with a 20 cm focal length zinc selenide lens. An image of the scattered light from a melting fibre is shown in fig. 2.1 a). The peak laser power is set to 5 W, which at the centre of the focus can reach peak intensities over $1\,\mathrm{kW/mm^2}$. Silica strongly absorbs the emitted light at $10.6\,\mu$m, causing the fibre to soften at approximately $1650\,^o$C, forming a sphere due to surface tension. The high viscosity of silica results in spherical structures with low eccentricities of 1% or less, and low intrinsic roughness (root mean squared roughness of the order of 1 nm) [122]. The size of the sphere and stem can be measured using a microscope and pixel counting, referenced to a stripped single mode optical fibre of diameter $125\,\mu$m, shown in fig. 2.1 c). This method of measurement results in errors due to issues with illuminating the curved object, and is limited by the resolution of the microscope and the pixel size of the camera. For this reason, larger microsphere-cantilevers with microsphere and cantilever diameters over 100 μm are used in experiments to minimise the influence of this error.

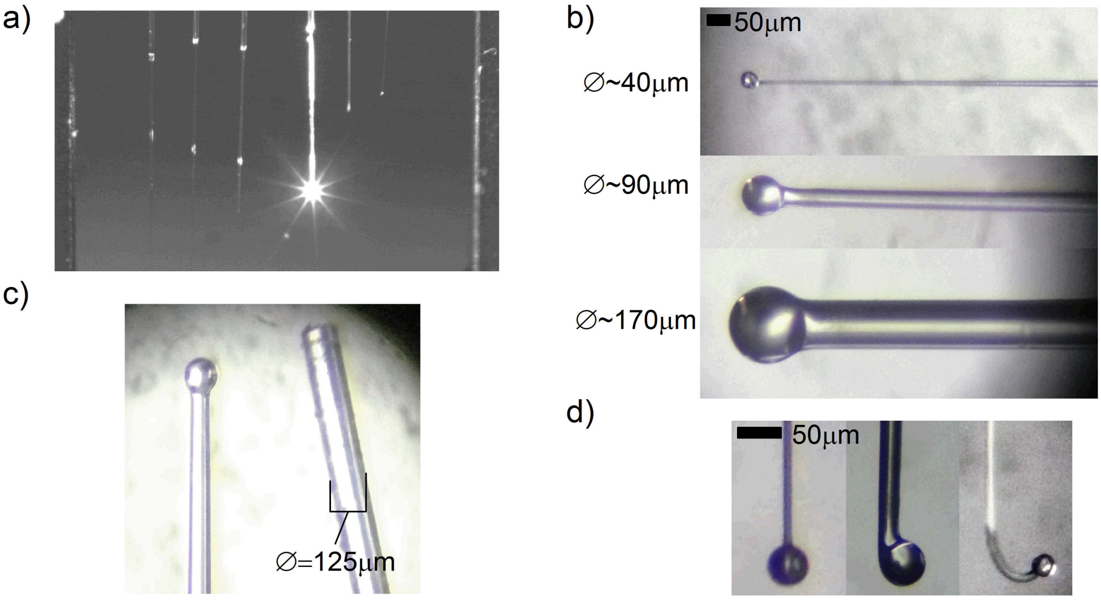

Figure 2.1: a) The ends of fibres are suspended and illuminated with a CO_2 laser which melts the tip to form a microsphere tethered to a stem, where different stem diameters can be used to create varying sized microspheres shown in b). The dimensions can be calibrated using pixel counting with respect to a stripped single mode fibre as in c). The symmetry of the microsphere-cantilever can vary, shown in d), where hooked ends, or asymmetry can exist.

Controlling the diameter of the microsphere with respect to the cantilever stem is achieved by melting optical fibres with different diameters created by the tapering procedure described next. Alternatively, melting a larger length of fibre creates larger spheres. A range of sphere sizes between 40 to 200 μm in diameter can be fabricated, shown in fig. 2.1 b). Although the sphere is attached to the optical fibre from which it was formed, the presence of the stem does not affect WGM propagation because the excited optical modes lie in the equatorial plane and thus have negligible overlap with this perturbation region. Poor alignment of the CO_2 laser can result in spheres that are non-centered on the stem or at the end of hooks, as in the latter two examples of fig. 2.1 d). The hook shape is undesirable as it is difficult to couple light into a clean equatorial path.

2.2.2 Tapered Fibre

The tapering rig used to fabricate tapers from a single mode fibre[2] is shown in fig. 2.2. A butane torch acts as the heat source, reaching temperatures of over 1300^o C. The flame size can be manually adjusted from diameters of 1 mm to 4 mm. Two piezo linear actuators with 25.4 mm travel range[3], used with translation stages, pull the taper in opposite directions, controlled using an open-loop driver.

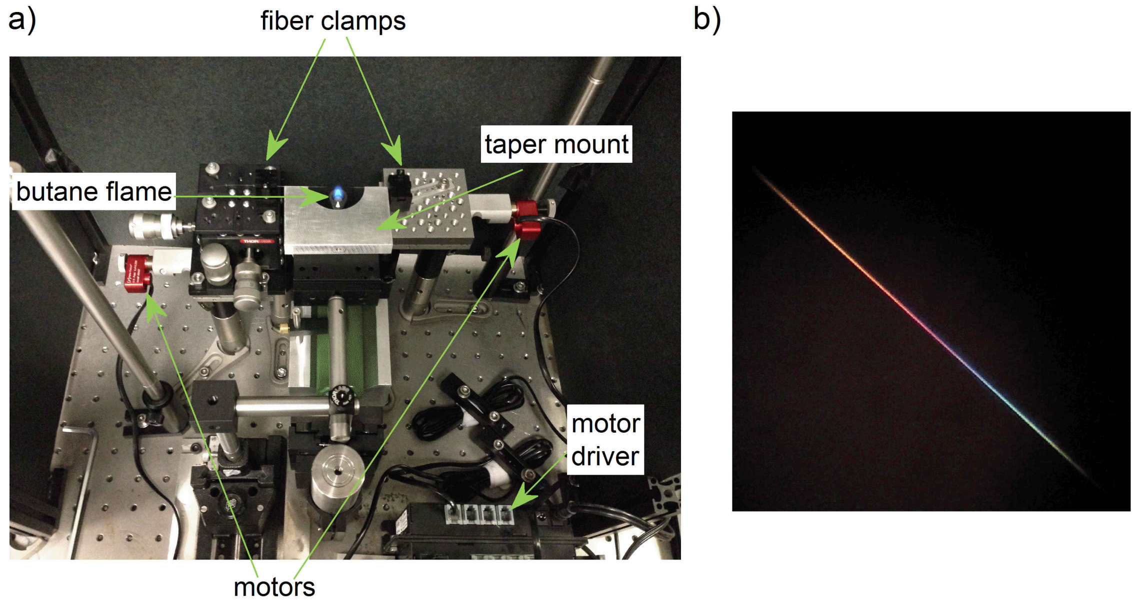

Figure 2.2: a) The tapering rig built during this thesis consists of two motors, and a butane flame. Two fibre clamps are used to secure the stripped section of fibre. After tapering, the taper is mounted and an image of the taper waist, illuminated with white light is shown in b). The appearance of interference colours is related to the thinness of the taper, comparable to the visible light wavelengths.

Prior to pulling, the acrylate coating of the fibre is stripped (approximately 2 cm length is stripped) and cleaned thoroughly with isopropyl alcohol until 'squeaking' is heard, which ensures there is no oil contaminating the surface i.e. from handling the optical fibre. This exposed segment is clamped on both sides with V-grooved fibre clamps. One clamp sits upon a 3-axis flexure stage to align the fibre centrally through the flame, with extreme care taken to ensure both clamps are parallel and all parts of the fibre are co-linear to avoid bends and kinks forming during tapering. Various flame widths were tested as these offer different rates of heating. It was found that a pulling speed of approximately 40 μm/s worked well with a medium sized flame approximately 2 mm diameter, where the taper is placed just above the central blue flame (the hottest part).

---

[2] Thorlabs 1060XP.

[3] Picomotor model 8302.

Tapering Transmission

One method to identify when the taper fulfils the criteria of eq. 1.25 (pg. 22), such that only the fundamental HE_{11} mode is supported, is to continuously monitor the transmission of 1064 nm light whilst pulling. A typical trace recorded on a photodetector, is shown in fig. 2.3 where after a few seconds of pulling the transmission oscillates in time due to interference between modes. This indicates that higher order modes can propagate as the cladding melts with the core, forming beat patterns. When the taper only supports the fundamental single mode HE_{11} the beat patterns disappear.

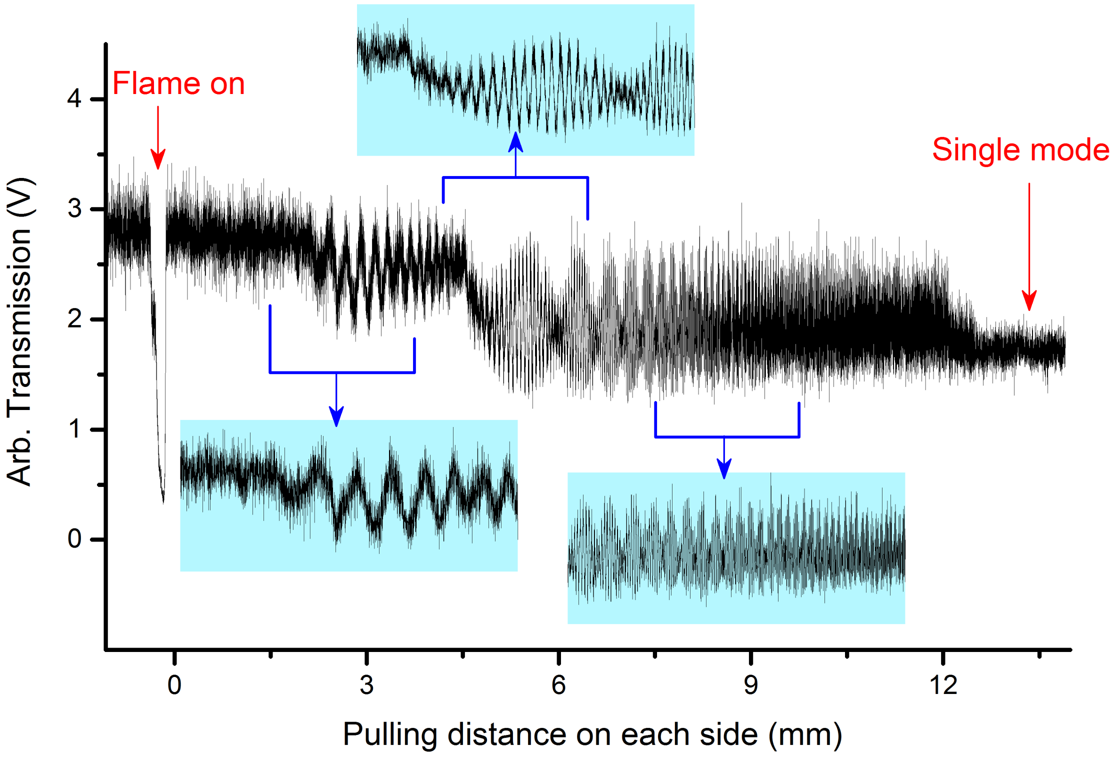

Figure 2.3: A typical tapering transmission where light propagates through a single mode fibre as it is heated and pulled by over 12 mm on either side. The transmission is comprised of various beat patterns associated with the interference of higher order modes with the fundamental mode of the fibre (HE_{11}), the amount of interference dependent on the pulled waist diameter. When the taper waist reaches the criteria set by eq. 1.25 (pg. 22), single mode transmission dominates, the waist is comparable to the wavelength of light (1064 nm here), and no higher modes can propagate within the core.

Typical pulling lengths of around 12-14 mm on each side (i.e. total length of 24-28 mm) coincide with single mode transmission. The transmission loss during tapering (typically between 23% to 70%) is due to non-adiabatic tapering transitions, as indicated by the beat patterns. As the taper waist changes, the fundamental mode becomes guided by the cladding, and light from this mode can be transferred into higher order modes i.e. HE_{12} unless the taper profile transitions slowly (adiabatically)[123]. The adiabatic condition can be defined by the local tapering angle $\Omega_t(z)$, where z donates the position along the taper where the taper radius is $r(z)$, and Ω_t must be shallow enough such that the mode essentially sees a straight fibre [124]. This means that the local taper length $z_a = \frac{r(z)}{\tan \Omega_t} \approx \frac{r(z)}{\Omega_t}$ is larger than the coupling length between the HE_{11} and HE_{12} modes, defined by the beat length $z_b = \frac{2\pi}{\beta_1(r) - \beta_2(r)}$, where β_1 ,β_2 define the propagation constant of the HE_{11} and HE_{12} modes[4] at each r. If $z_a > z_b$ the fundamental mode propagates through the taper with no loss, allowing groups to fabricate adiabatic tapers using clean heating elements such as hydrogen flames or ceramic heaters[5], such that the transmission post-tapering reaches above 95 % [115].

The typical taper profile can be approximately measured using a microscope and pixel counting, as shown in fig. 2.4, where the minimum diameter is $1.1 \pm 0.6\,\mu$m. Such a large error is related to the resolution of the microscope, and poor illumination of the cylindrical sides. The taper in fig. 2.4 represents typical taper dimensions fabricated in this thesis as the same pulling speed, number of pulling steps, and approximately the same flame heights are used each time. The adiabatic condition is not satisfied until the taper is less than $30\,\mu$m diameter (corresponding to ± 8 mm distance from the centre of the taper in fig. 2.4, and after 8 mm pulling distance in fig. 2.3), which explains why there is a DC loss in transmission in fig. 2.3 due to light exchanged from the fundamental mode to a higher order mode which is not transmitted. The loss can be decreased by tapering at a slower rate, which will produce a larger length taper. However, since large coupling powers are not stringently required, the confirmation of a $<$ 1064 nm waist using the transmission graph fig. 2.3 is adequate for the experiments in this thesis.

The taper profile shows some asymmetry about '0' mm pulling distance in fig. 2.4 which is related to the motors being switched on one after the other.

Immediately after tapering the fibre must be tightened using the flexure stage as a small vertical bend usually ensues. Straightening the taper increases the transmittance by less than 10% but can benefit stability and alignment. The taper is permanently mounted on a bracket-like-mount made from steel with a 30 mm wide notch. Since it is mounted in a clamped-clamped string configuration, where the taper portion is left free-hanging, there are mechanical modes associated with the taper, experimentally measured in chapter 3,

---

[4] The values of β can be found by solving the appropriate boundary value problem at varying fibre waist size using the scalar wave equation.

[5] The use of a butane flame is often considered 'dirty' due to the presence of carbon deposits.

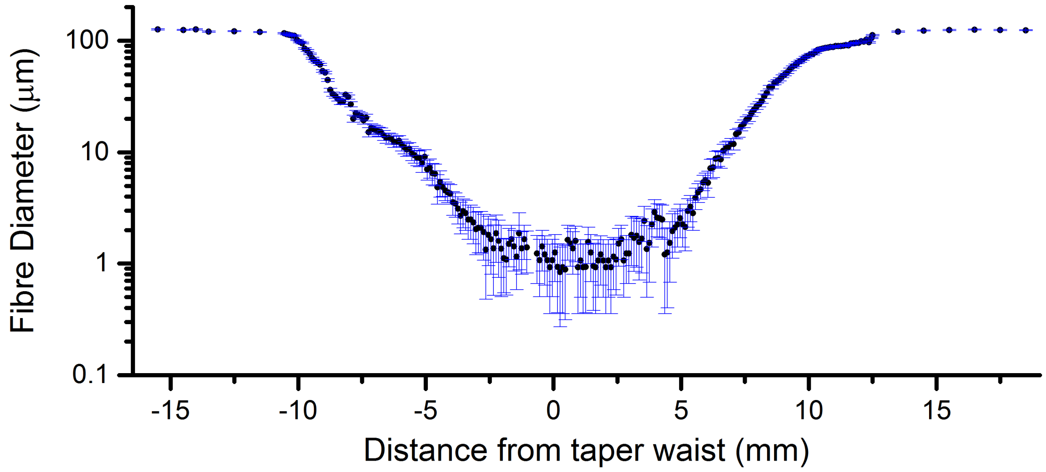

Figure 2.4: A typical tapered fibre profile, measured by imaging sections of the taper with a microscope. The minimum measured diameter is $1.1 \pm 0.6\,\mu$m, limited by poor illumination of the taper and the resolution of the microscope.

and actively cooled in chapter 4. Nail varnish (nitrocellulose plus plasticizers and resins) is used to glue the taper onto the mount, chosen for the relatively fast curing time (around 30 mins), as well as a refractive index well matched to silica.

Lifespan of Tapered Fibres

Tapers must immediately be placed in a sealed chamber, or kept at low pressure to avoid contamination. It has been shown elsewhere [110] that long term degradation of the taper transmission is due to dust adhesion, measured by comparing a dust free environment clean room (cleanliness class 10) with normal laboratory conditions where dust particle sizes of $0.3\,\mu$m, $0.5\,\mu$m, and $1\,\mu$m were detected. Tapers left in the clean room showed 1% degradation of transmission over 48 hours, whereas normal lab conditions resulted in over 50% degradation in 4 hours. Similar effects were seen in the tapers fabricated in this thesis, whose lifespan could be prolonged by carefully cleaning the taper surfaces using methanol. Discrete jumps in transmission are seen when a bubble of methane is created at the end of a syringe and skimmed over the surface. This can increase transmission by a factor of 10 to 100. No matter how much cleaning is conducted the majority of dust remains due to strong electrostatic forces and van der Waals forces, and the resulting transmittance at the end of 3 weeks can be as low as 1% of the initial value. The transmission degradation due to surface scatterers is one driving factor for researchers who have embedded tapered fibres in a low refractive index polymer matrix [125]. However, for the purposes of this thesis, where free-space is required between the taper and the microsphere in order to transduce motion, encapsulation cannot be used.

One final comment on taper lifespan is heating due to the light intensity at the thinnest taper region. For the tapers fabricated in this thesis, intensities exceeding 1 MW/mm^2 for 1 mW input power can cause the taper to melt and break, especially at low pressure where residual gas cannot conduct heat from the material. Any surface contaminants in the taper region create hot spots as they scatter light, which further decreases the maximum coupled power before melting.

2.3 Tunable Laser Source

The main requirement for a laser source to interrogate the spectrum of WGMs is tuneability. Firstly, the laser needs to be tuned in wavelength (frequency) to locate a resonance, and secondly, it must follow frequency shifts due to temperature or size variations that can shift the WGM by hundreds of linewidths. The laser source used in this thesis is a diode pumped solid state neodynium doped yttrium vanadate (Nd:YVO$_4$) microchip laser, pumped with an 808 nm diode, with an intracavity electro-optic modulator (EOM) to tune the output wavelength via path length modulation [126] [6].

2.3.1 Nd:YVO$_4$ Laser

The schematic of the laser operation is shown in fig. 2.5 and photos of the laser are shown in fig. 2.6

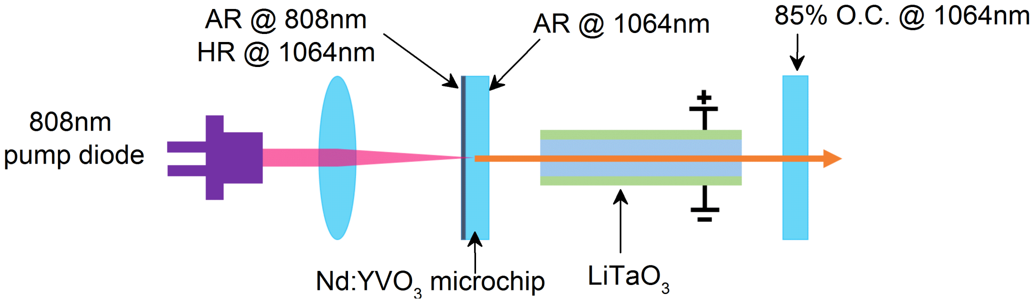

Figure 2.5: The schematic of the tunable 1064 nm output laser. An 808 nm diode provides pumping that causes stimulated emission from a Nd:YVO$_4$ microchip laser which forms a cavity with the output-coupler. An LiTaO$_3$ EOM is placed in the middle of this cavity, connected to electrodes that send a voltage through the EOM to change the cavity path length, thus tuning the output wavelength.

---

[6] The laser was built by a previous student [126], and modifications described in this section were conducted within this Ph.D

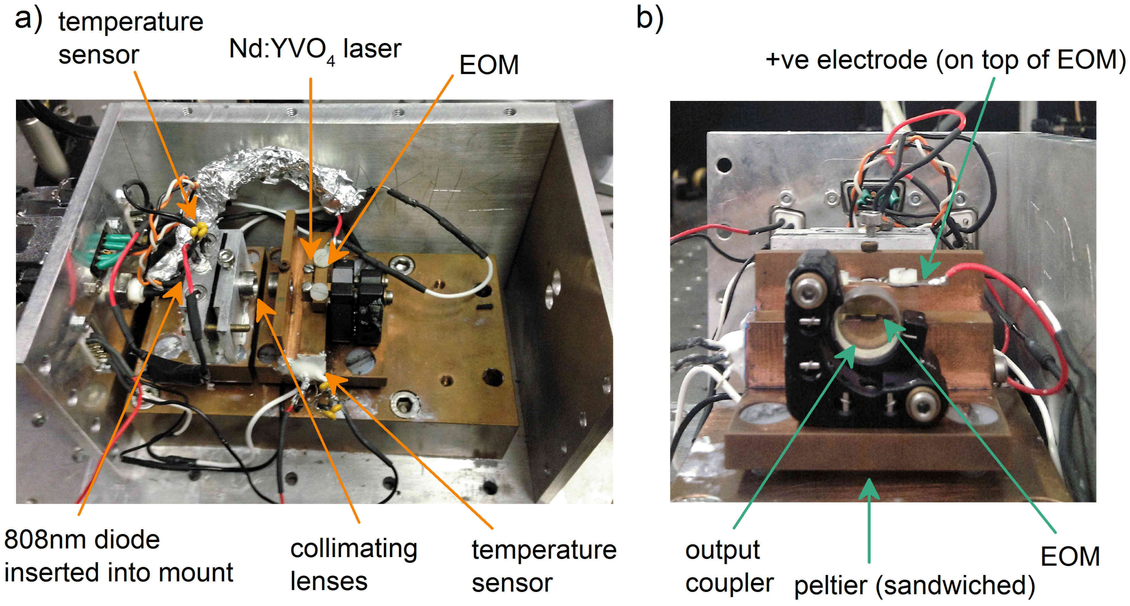

Figure 2.6: a) Side profile of the inside of the laser. All components sit upon a copper block, with two sandwiched Peltier devices that control the temperature of the pump diode and the microchip laser respectively, measured using two separate AD590 temperature sensors that are shielded from RF noise with a ring of capacitors. b) Front facing profile of the laser showing the output coupler and the EOM, centred to coincide with the optical beam path. The positive electrode sits on top of the EOM chip (the ground electrode is the block that the EOM sits upon).

A 1 W diode[7] with centre frequency 808 nm is collimated and then focused onto the Nd:YVO_4 microchip[8] with anti-reflection coating for 808 nm and a highly reflective coating for 1064 nm on the pumping face, and anti-reflection coating for both wavelengths on the other face. The output wavelength is tunable around 1064 nm. The diode and microchip are thermally attached to a copper block that is Peltier controlled and temperature tuned so as to pump the 809 nm absorption band in the neodymium ion. An output coupler is used to create the cavity (the end face of the Nd:YVO_4 forms the other end of the cavity) and allow transmission of the output beam.

An intra cavity EOM with dimensions $(1 \times 3 \times 5)$ mm is inserted between the gain medium and output coupler following the work of Repasky [127][9]. The EOM consists of a crystal whose refractive index changes when an electric field is applied across it, created by placing a parallel plate capacitor across it. During exposure to an electric field the optical path length increases, altering the output frequency of the emerging laser beam.

---

[7] Thorlabs L808P1WJ

[8] CASIX, 500 μm thick

[9] In [127], a frequency chirped external cavity diode laser could be tuned 2.4 GHz with an intracavity EOM

2.3.2 Laser Output Power

With the pumping diode temperature set to 15.6 ^{o}C and the temperature around the Nd:YVO$_4$ microchip and EOM set to 19.77 ^{o}C, the 1064 nm output power versus the current used to pump the 808 nm diode is recorded, and plotted in fig. 2.7. This output power is not optimised since inserting the EOM leads to a small amount of misalignment. The maximum output power is 366 mW with multimode operation, and a maximum of 34 mW power for single mode operation.

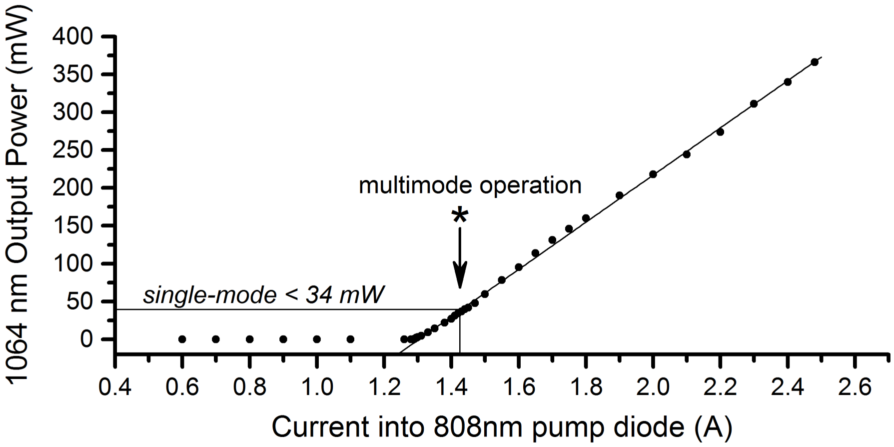

Figure 2.7: The onset of lasing and the output power as a function of the current sent to the pump diode. The start of multimode operation is marked by the arrow, giving an upper power output for single mode operation of 34 mW.

The power stability of the free running laser is measured to have less than a 0.6% drift over 13 mins.

2.3.3 Single Mode, Mode-hop Free Tuning Range

Applying a triangle ramp in voltage to the EOM tunes the laser output frequency. Shown in fig. 2.8 a) is a combination of voltage tuning and DC current tuning. The maximum range of the voltage amplifier ($\approx$ 350 V) can tune the laser over 3.79 GHz, whereas a mode-hop free tuning range of 6.65 GHz can be achieved by increasing the current to the pumping diode. Although current tuning can scan the laser frequency over a greater range, the laser output stability is affected, requiring some time for the temperature to stabilise. A 6.65 GHz mode-hop free tuning range is $\approx$ 2% of the FSR for WGM modes in a $\oslash$ =177 μm sphere. Therefore tuning the sphere size instead (i.e. fabricating 20 or more spheres through trial and error) is the most effective method for locating a resonance. The relation between the applied tuning voltage and laser frequency is found to be 14.70$\pm$0.05 MHz/V.

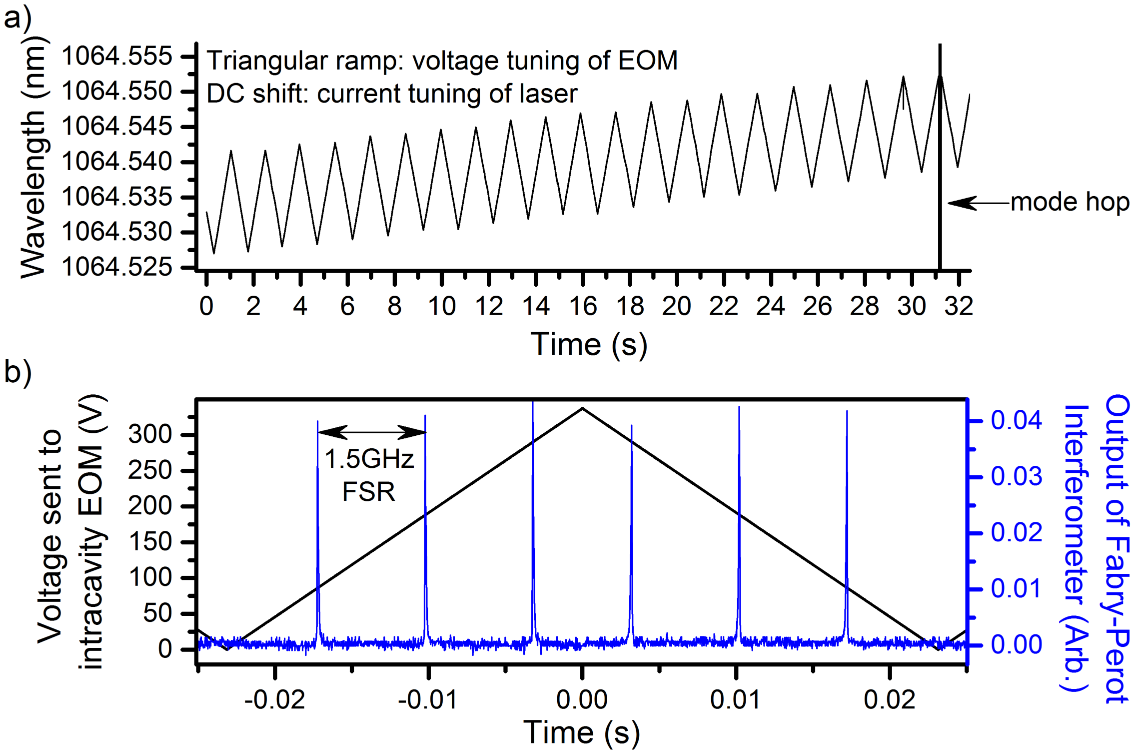

Figure 2.8: a) The single mode, mode-hop free scanning range of the laser is measured by driving the EOM with a ramped triangle voltage, and applying a linear increase to the pump diode current. The voltage ramp fine tunes over 3.79 GHz, whereas current tuning tunes over 6.65 GHz. The mode-hop is marked by an arrow. b) An alternative method that does not require the wavemeter involves sending the light into a Fabry-Perot (F-P) interferometer whose output is recorded whilst the laser is tuned via a voltage ramp to the EOM. The separation between the peaks is equal to the 1.5 GHz FSR of the F-P cavity so that the total scan range can be calibrated by the (non-integer) number of FSRs.

In fig. 2.8 b) shows an alternative method to measure the tuned frequency using a commercial Fabry-Perot (F-P) interferometer[10]. A photodetector records the transmission of the F-P cavity and the (non-integer) number of peaks is counted against the voltage ramp to the EOM. The distance between each peak is equal to the FSR of the F-P cavity, 1.5 GHz.

2.4 Experimental Set-Up for Exciting Whispering Gallery Mode Resonances

A simple experimental set-up for exciting WGMs, used at the start of the Ph.D., is shown in fig. 2.9. An isolator is placed in front of the laser to prevent feedback, with an amplified voltage supply controlling the intracavity EOM to tune the laser frequency. A flip mirror in

---

[10] The compact F-P is dedicated for daily calibration measurements such as the WGM linewidth, whereas the wavemeter is shared amongst the group.

the path of the beam allows for the use of the F-P cavity for calibration. After calibration, the flip mirror is removed from the beam path, and the laser is coupled into the taper where the transmission is measured using a photodetector (PD 1). The output of PD 1 is sent to an oscilloscope with built-in spectrum analyser functionality.

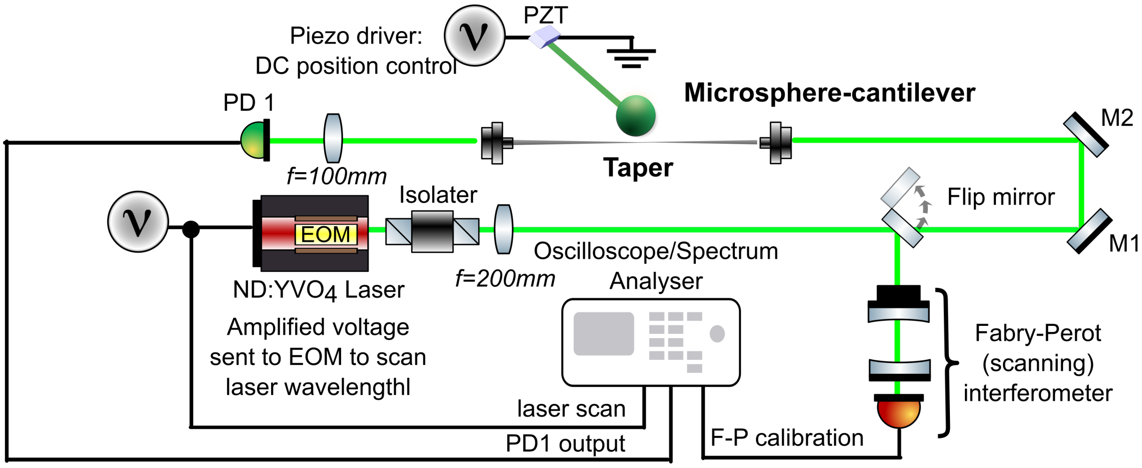

Figure 2.9: A simple set-up for exciting WGM resonances within a microsphere-cantilever.

The microsphere-cantilever is mounted in a fibre clamp that secures it in place. This sits on a homemade 1D translation stage controlled with piezo-stacks (PZT) for fine tuning the vertical displacement i.e. the coupling distance with respect to the taper. This stage is secured onto a 3-axis flexure stage to provide rough manual translation using differential adjusters. The taper, attached to a bracket mount, is clamped below the microsphere-cantilever and placed perpendicular to the cantilever stem. Both ends of the taper are stripped, cleaved, and glued into APC fibre connectors before being polished. All are placed inside a vacuum chamber to shield against air currents and dust[11]. The 3D flexure stage supporting the microsphere-cantilever is used to roughly tune the coupling distance as the laser is scanning. Excitation of WGMs can then be achieved using a mixture of manual alignment and fine tuning with the piezo-stacks to slowly decrease the separation distance[12], and is monitored from above using a microscope. The set-up is shown in fig. 2.10 a), and the microscope view in fig. 2.10 b) where the appearance of a WGM can be deduced visually.

---

[11] The majority of experiments conducted in this thesis operate at atmospheric pressure in air, unless specified.

[12] At separation distances of $d < 50\,\mathrm{nm}$, the cavity enhanced optical dipole force, electrostatic forces, or van der Waals forces attract the sphere towards the taper until they touch. Separation of the two objects requires a large actuation of the piezo-stack supporting the microsphere-cantilever (i.e. displacement of over $1\,\mu\mathrm{m}$) to overcome the van der Waals forces.

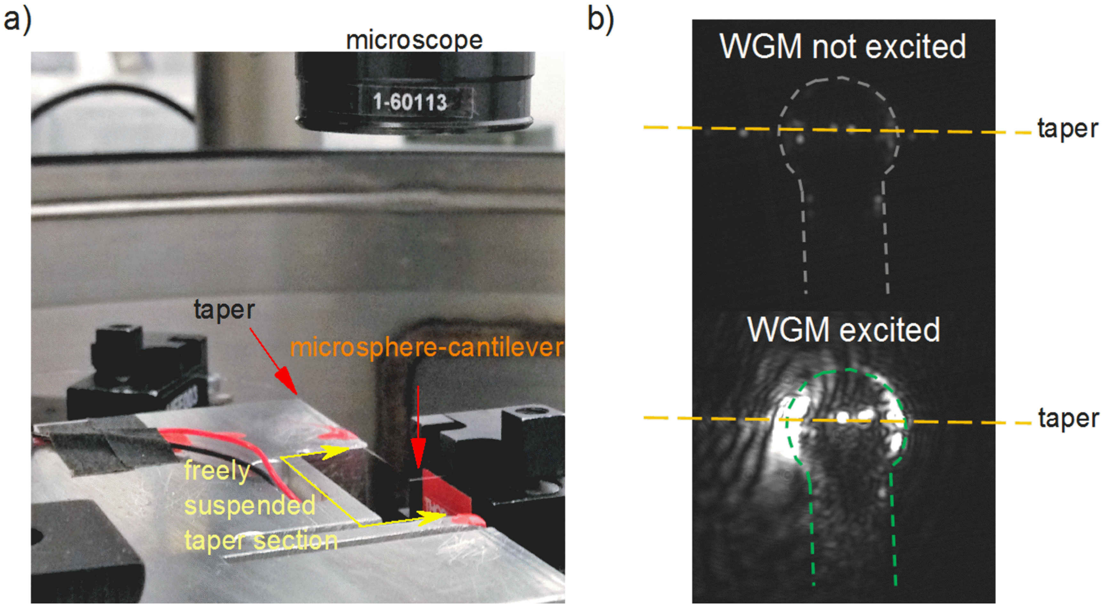

Figure 2.10: a) The layout of the microsphere-cantilever and tapered optical fibre, placed perpendicular to one another. A microscope can view, from above, the coupling junction. When a WGM is excited (bottom panel, b)) non-uniform scattering can be seen, which indicates the WGM propagating around the equator of the sphere (in and out of the page).

2.4.1 Results

Alongside the increased scattering, a dip in the transmission, $\mathcal{T}$, will present itself when coupling occurs, such as that displayed in fig. 2.11.

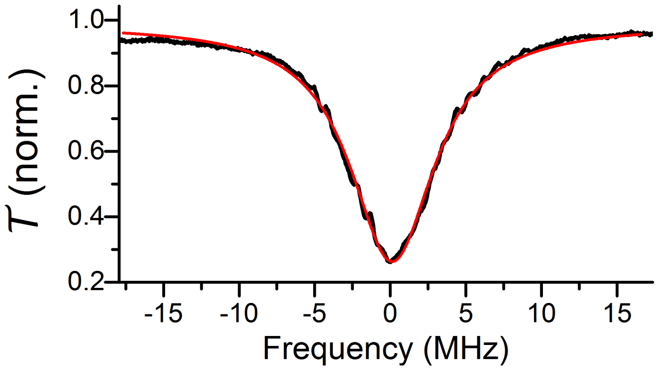

Figure 2.11: A narrow WGM fitted with a Lorentzian of linewidth 5 MHz FWHM, excited with 1064 nm light at low laser powers to avoid thermo-optic effects. It is recorded as a dip in the transmission $\mathcal{T}$ of the tapered fibre waveguide used to couple light in/out of the microsphere-cantilever.

WGMs of varying linewidth have been successfully excited and range from a FWHM linewidth of 5 MHz, to a FWHM of 1 GHz. The narrowest WGM is shown in fig. 2.11 which has a linewidth of 5 MHz FWHM, corresponding to a $\mathrm{Q_{opt}} = 5.6 \times 10^7$, which could be limited due to adhesion of dust, seen as light scatterers in fig. 2.10 b).

The optical properties of the WGM such as linewidth, resonance frequency and power coupled are dependent on the external coupling rate γ_e, as discussed in the introduction. If heating occurs within the WGM bulk material due to the high circulating intensity, or a change in environmental temperature, this adds a thermally induced shift to the resonance location. Both aspects are investigated in this section, namely, the coupling distance dependence of γ_e, and the thermo-optic effect relating bulk heating to shifts of the WGM resonance frequency [13, 41, 128, 129].

Coupling Distance Dependence

Due to the evanescent field overlap between the tapered fibre and the WGM resonator, γ_e is exponentially dependent on the coupling distance, d. Using the experimental set-up detailed above, the piezo-stack supporting the microsphere-cantilever is used to vary d, and the WGM lineshape and position is monitored in the transmitted light $\mathcal{T}$. This is plotted in fig. 2.12.

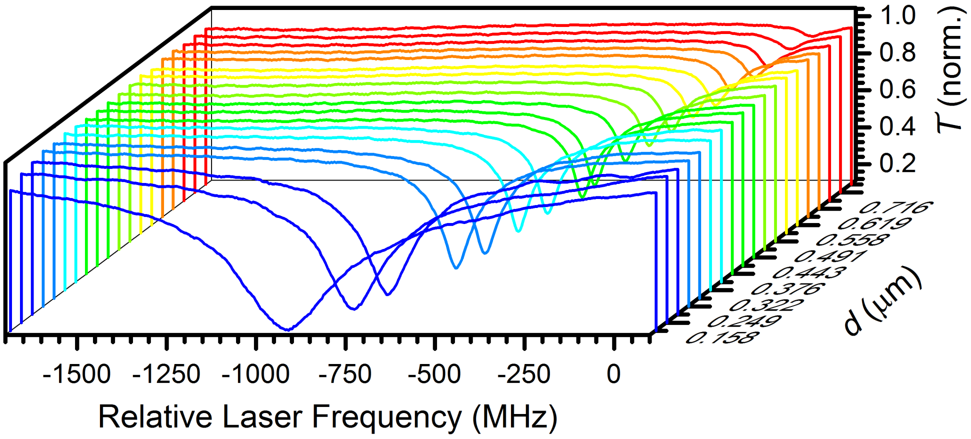

Figure 2.12: The transmission, $\mathcal{T}$, of a WGM excited in a microsphere-cantilever as a function of coupling distance, d, (red to blue traces correspond to separation gaps between 700 nm to 120 nm). The extrinsic coupling rate γ_e varies exponentially with d, causing the WGM to broaden and $\mathcal{T}$ to decrease on-resonance. A red-shift is also observed with decreasing d. Note that when d <120 nm and further decreased (not shown here for clarity), $\mathcal{T}$ increases and is included in the plots of fig. 2.13).

As the extrinsic coupling rate γ_e increases, the WGM resonance widens as the total decay rate κ increases. There is also a red-shift of the WGM resonance due to the change in the effective refractive index surrounding the coupling junction, resulting in a longer path length that decreases the resonance frequency. The shift in frequency is exponentially dependent on d, related to dispersive coupling, discussed further in chapter 3, and chapter 5.

From chapter 1 (pg. 23), the on-resonance transmission is related to the normalised power coupled into the WGM, $\mathrm{P_c}$, by the relationship $1 - \mathcal{T}_{\mathrm{on}} = \mathrm{P_c}$. The measurement of $\mathrm{P_c}$ at varying d (i.e. applied to the data shown in fig. 2.12), is plotted in fig. 2.13 a). The actuation of the piezo-stack (i.e. the voltage sent to the piezo-stack, V_d) is recorded between each measurement, noting that the required actuation for the microsphere to touch the tapered fibre i.e. $V_{d=0}$, corresponds to a coupling distance of $d = 0$. All previous measurements of $\mathcal{T}$ or $\mathrm{P_c}$ can be calibrated from $V_{d=0}$ by using the specifications of the piezo-stack to convert from driving voltage to the actual displacement in meters. The undercoupled, critically coupled ($d \approx$150 nm) and overcoupled regimes are marked. The DC transmission level can therefore be associated with an equilibrium coupling distance. In order to extract the values of γ_e, the intrinsic coupling rate γ_i, and the decay constant η, the data is re-plotted in fig. 2.13 b) using a re-arranged form of eq. 1.33 (pg. 25): $\frac{\gamma_e}{\gamma_i} = \frac{\sqrt{\mathcal{T}_{\mathrm{on}}}-1}{\sqrt{\mathcal{T}_{\mathrm{on}}}+1}$. Fitting b) with an exponential function $\frac{\gamma_e}{\gamma_i} = \gamma_{e,0}e^{-\eta d}$, provides measurements of the WGM parameters that are used to apply the non-linear fit for $\mathrm{P_c}$ versus d, shown in fig. 2.13 a).

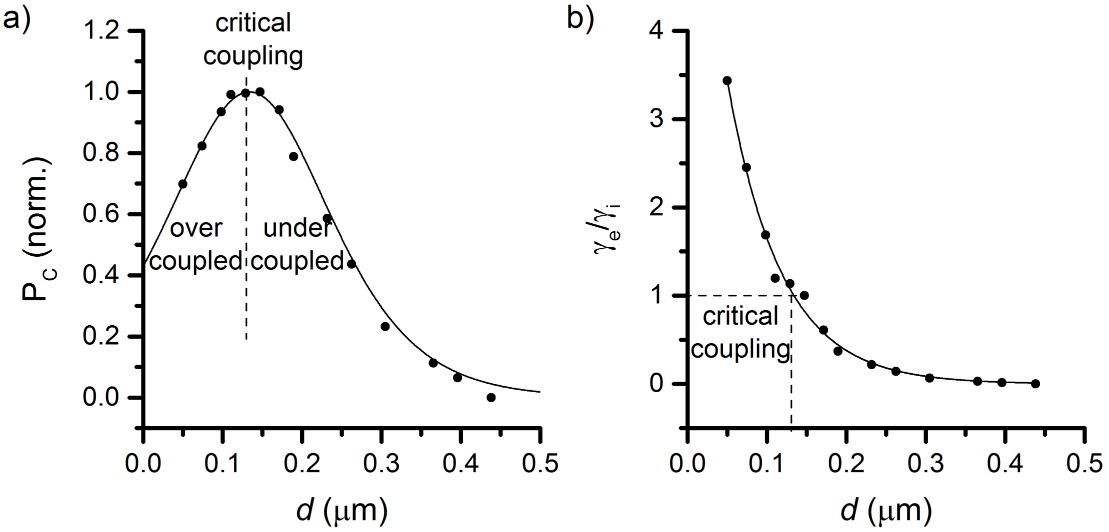

Figure 2.13: a) The power coupled to the WGM as a function of the coupling distance between the tapered fibre and the microsphere-cantilever. The coupling regimes of undercoupled, critically coupled ($d \approx$150 nm) and overcoupled are shown. The plot is fitted with $\mathrm{P_c} = 1 - T_{\mathrm{on}} = 1 - \left(\frac{1-\gamma_e/\gamma_i}{1+\gamma_e/\gamma_i}\right)^2$, where $\frac{\gamma_e}{\gamma_i}$ can be found using plot b), fitted with an exponential function $\frac{\gamma_e}{\gamma_i} \propto e^{-\eta d}$, where η is the decay constant.

The fit to this curve gives $\frac{\gamma_e}{\gamma_i} = 7.16\, e^{-1.47\times10^7 d}$ (note that d is in units of m). The extrinsic coupling is $\propto e^{-\eta d} \approx e^{-2\alpha_s d}$, where η^{-1} is the total decay length and α_s^{-1} is the evanescent decay length of the WGM, see chapter 1 (pg. 22). The experimental data in fig. 2.13 sets $\eta/2 = \alpha_s = 1.36 \times 10^{-7}$ which is $< 10\%$ smaller than the value predicted using eq. 1.22 (pg. 18). Using the experimentally deduced $\frac{\gamma_i}{\gamma_e}$, fig. 2.13 a) can be fitted using $\mathrm{P_c} = 1 - \left(\frac{1-\gamma_e/\gamma_i}{1+\gamma_e/\gamma_i}\right)^2$, which can be used as a guide to indicate d in experiments.

As mentioned earlier, heating of the microsphere will shift the WGM frequency until the bulk temperature is in equilibrium with the surrounding temperature. This poses a technical challenge if the laser is stabilised onto the WGM dip, and must actively 'chase' the mode. This thermal effect is described in the following section.

Thermal Bi-stability

Since the mode volumes are so small within WGM resonators, circulating intensities of 1 MW/mm^2 can be obtained for launch powers below 50 μW which primarily drives thermo-optic effects, and to a lesser extent, high order non-linear optical effects. The isotropic nature of amorphous silica results in the lowest order non-linearities[13] of order χ^3, specifically the Raman and Kerr effects [121][14]. At the low optical powers used in this thesis (100's of μW), the Kerr and Raman non-linearities are negligible [53]. The dominant cause of the WGM frequency shift is known as the thermo-optic effect which changes the refractive index and geometry due to bulk heating via absorption. This effect can arise with coupling powers as low as 2 μW, causing hysteresis when scanning a laser over the resonance. An approximate equation describing thermally induced shifts $\Delta\lambda$ of the WGM resonance at wavelength λ is [130]:

$$\begin{aligned} &\frac{\Delta\lambda}{\lambda} = \frac{\Delta(na)}{na} = \frac{\Delta a}{a} + \frac{\Delta n}{n} = (\zeta + \xi)\Delta T, \quad \text{therefore} \\ &\Delta T = \frac{1}{\zeta + \xi}\frac{\Delta\lambda}{\lambda}, \end{aligned} \tag{2.1}$$

where ζ is the thermal expansion co-efficient that changes the sphere radius a, and ξ governs the refractive index change, known as the temperature co-efficient of the refractive index [130]. This is not the same as n_2, the second-order non-linear refractive index that governs the Kerr effect. For silica ζ, ξ are $5.5 \times 10^{-7}\,\mathrm{K}^{-1}$ and $8.53 \times 10^{-6}\,\mathrm{K}^{-1}$ respectively, showing that the refractive index change is 10 times more dominant. Since the refractive index change of silica (at room temperature) is positive with an increase in temperature, it implies that the WGM is always red-shifted with increased coupling power. Approaching

---

[13] There are no χ^2 non-linearities

[14] The Raman non-linearity involves the inelastic scattering of optical photons onto vibrational phonons in the structure, that can be enhanced with the large intracavity power (known as stimulated Raman scattering). The Kerr non-linearity causes a modification of the refractive index, dependent on the intensity of circulating light as $n(I) = n + n_2 I$, where n_2 is the second order non-linear refractive index. With high intensities the Kerr effect can generate parametric gain and oscillations

the WGM from the red or blue side therefore has hysteresis, with thermal bi-stability [13, 41, 128, 129], shown in fig. 2.14.

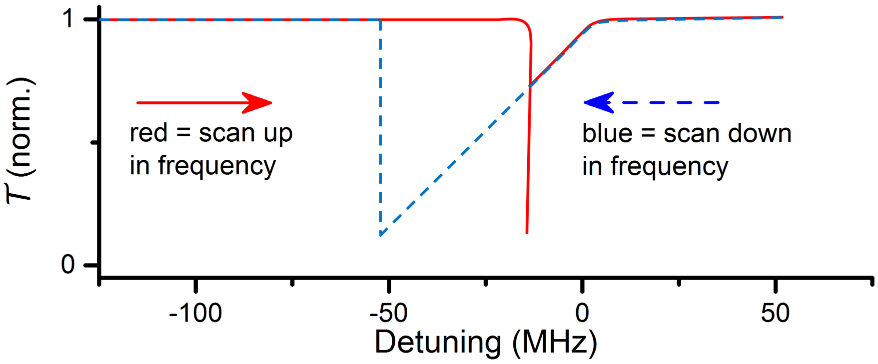

Figure 2.14: The thermo-optic effect, where power coupled to the WGM causes bulk heating and a red-shift of the resonance frequency. This creates a bi-stability seen here as differing WGM linewidth profiles as the laser is scanned from red-detuned to on-resonance (here 0 MHz detuning corresponds to the 'cold' WGM resonance) versus the scan from blue-detuned.

During the down-frequency ramp (fig. 2.14 (blue)) the WGM transmission is broadened in a characteristic 'shark fin' shape as the pump and WGM frequency travel together. The cavity stays resonant for a large range of detunings since thermal shifting is in general, faster than the rate of laser scan. During the up-frequency ramp (red) the WGM resonance is narrowed as the pump and WGM resonance move in opposing directions. This causes the bulk temperature to decrease until the scan wavelength meets the shifted resonance (at a frequency smaller than for the down-scan), where the cavity jumps into resonance [13]. The bi-stability is observed in the microsphere-cantilever when $P_c > 10\,\mu W$ is coupled into a WGM, and the laser frequency is scanned towards and away from the resonance, shown in fig. 2.15 b). In fig. 2.15 a), less laser power is used, and a lower Q_{opt} WGM is excited such that negligible bi-stability is presented.

If the laser is not scanned, but set a fixed detuning with respect to the WGM, the thermo-optic bi-stability determines one side of the cavity resonance (i.e. ± detuning) stable when subjected to a continuous pump laser whereas the other is unstable. At room temperature the unstable side is the red-detuned side, whereas at cryogenic temperatures it is the blue-detuned side, related to the temperature dependence of the refractive index of silica. The stable coupling equilibrium on the blue-detuned side is studied later in this chapter for passive locking. However, if the intracavity power is high, or if P_c has large fluctuations, maintaining continuous coupling on-resonance (or on the red-detuned side) requires active fast feedback systems, described in the next section.

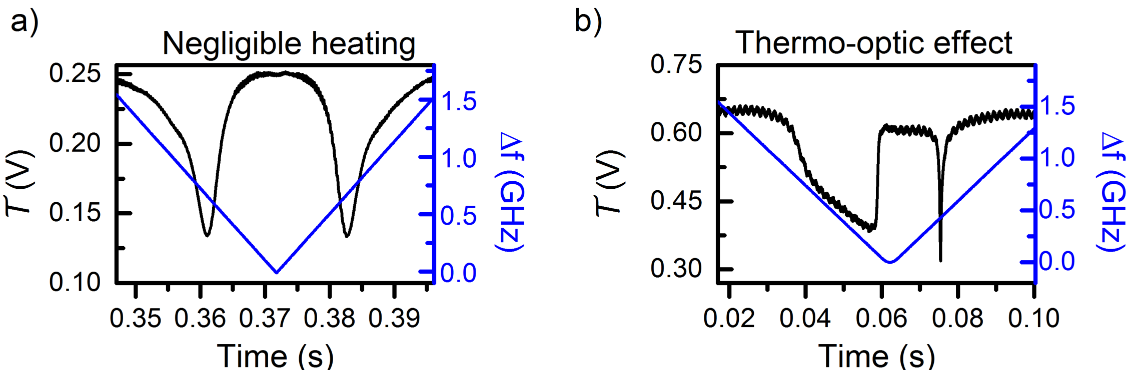

Figure 2.15: WGMs are excited in microsphere-cantilevers by tuning the laser frequency with a triangular ramp, and the transmission $\mathcal{T}$ is recorded. The WGM on the up-scan is the same WGM on the down-scan. With negligible thermal heating present, a) shows no difference in the WGM lineshapes on the up/down scan, due to the low Q_{opt} and lower laser power used. In the presence of bulk heating, thermal bi-stability is clearly seen in b), where the WGM lineshape during the down-scan is significantly different to that obtained in the up-scan.

2.5 Laser Locking to Whispering Gallery Mode Resonances

Maintaining continuous coupling to a WGM requires the laser cavity to remain stable and frequency locked onto the WGM resonance. Thermal fluctuations, air currents, and vibrations can cause frequency drift of the laser, whereas the thermo-optic effect can shift the WGM resonance. Two types of feedback are used to keep the laser frequency stabilised; active Pound-Drever-Hall (PDH) locking, and a passive thermal locking in section 2.5.2 (pg. 50).

2.5.1 Implementation of Pound-Drever-Hall Locking

Many experiments employ PDH locking [131, 132] when working with WGM resonators [45, 54] as it has a large recapture range and is not limited by the resonator bandwidth. PDH locking requires phase modulated light, consisting of a carrier frequency and two sidebands, which is coupled to the WGM of a microsphere. The transmitted light[15] consists of two unaltered sidebands along with a phase shifted carrier component. A photodetector measures the transmission, and the photodetector signal is mixed down with a local oscillator (L.O.), which is in phase with the modulated light. After phase shifting and filtering, the resulting electronic signal, called the error signal, gives a measure of how far

---

[15] In the usual configuration for PDH locking to a Fabry-Perot cavity, the reflected signal is used. However, the transmission from the WGM resonator is equivalent to this reflected signal as it contains light coupled back into the taper from the cavity.

the laser carrier is off resonance with the cavity and is used in a feedback loop for active stabilization. A proportional integral (PI) controller carries out the feedback, taking the PDH error signal and converting it into a voltage that can be fed back to the laser to keep it locked on resonance with the cavity.

The error signal is given by:

$$\epsilon = 2\sqrt{\mathrm{P_c P_s}}\,\mathrm{Im}\left[\mathrm{F}(\omega_0)\mathrm{F}^*(\omega_0+\Omega) - \mathrm{F}^*(\omega)\mathrm{F}(\omega_0-\Omega)\right], \tag{2.2}$$

where $\mathrm{F}(\omega)$ is the transmission coefficient of the WGM cavity at frequency ω, $\mathrm{P_c}$ is the power in the carrier and $\mathrm{P_s}$ is the power in each sideband. Examples of error signals obtained from WGMs are shown in the section that follows.

Experimental Set-up

The experimental set-up for applying PDH locking is shown in fig. 2.16. The intracavity EOM of the laser modulates the phase of the laser by 140 MHz, comparable to the FWHM of typical WGMs used in this work. The RF modulation is set by the L.O., and sent as a voltage to the EOM. Since the EOM is also used for tuning the laser frequency (using a high voltage supply >100 V), a bias-T is required to prevent cross coupling of these signals. The bias-T is formed using a capacitor of 0.6 pF that blocks signals below 80 MHz and an inductor of 5.6 μH that blocks signals above 80 MHz. The RF voltage is therefore sent through the capacitor channel. The phase modulated light is coupled into the WGM resonator. The non-coupled light through the taper beats with the light emitted from the cavity back into the fibre, and is detected by the photodetector PD 1. The mixer multiplies this beat pattern with the reference signal from the L.O. to form the error signal. Typical

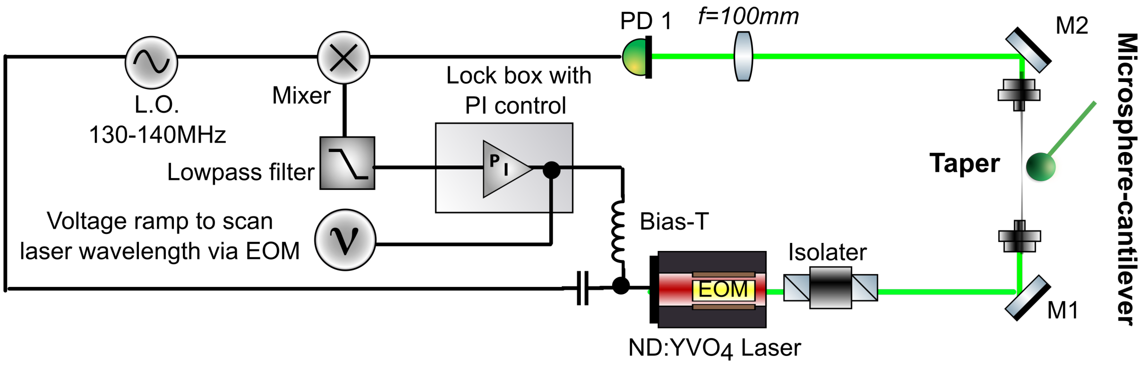

Figure 2.16: The basic set-up for Pound-Drever-Hall locking of the laser to the WGMs of a microsphere-cantilever.

error signals obtained from WGMs with and without the thermo-optic bi-stability are shown in figs. 2.17 a) & b), respectively.

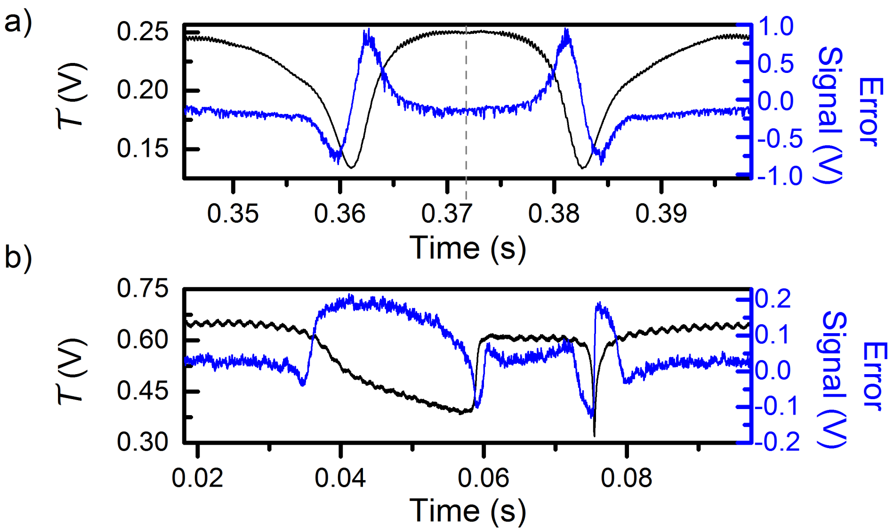

Figure 2.17: Typical error signals obtained from WGMs of microsphere-cantilevers (blue data) when there is negligible thermo-optic effect in a), and with the thermo-optic bi-stability (hysteresis) in b). The corresponding WGMs, recorded in the transmission $\mathcal{T}$ are shown in black.

The error signal in fig. 2.17 b) parallels the thermo-optic behaviour causing uneven spacing of the sidebands. These plots are typical of WGM resonators where pump powers above 2 μW are used [54].

The error signal can be set so that the point where it crosses zero is the lock set-point, in figs. 2.17 a) b) this is set on-resonance with the WGM. Any detected frequency drift will offset this zero crossing point which is countered by a change in the voltage sent to the EOM (via the inductor arm of the bias-T) to tune the laser frequency back onto resonance.

Results

The PDH locking process to stabilise the laser frequency onto the WGM mode is shown in fig. 2.18. At the point of lock engagement (marked with a red arrow in fig. 2.18), power is coupled into the WGM resonance and the lock box latches onto the position in the laser frequency sweep that correlates to the WGM resonance (the lock-point). However, thermal heating due to the influx of power (P_c) causes the WGM to drift, seen in the shaded box in fig. 2.18, as the laser frequency chases the WGM.

Once the microsphere bulk temperature re-thermalises with its surroundings (on a time scale of 0.1 ms for the 85 μm diameter sphere used in this set of data), the WGM is continuously coupled and is in a steady state, with any fluctuations in frequency countered

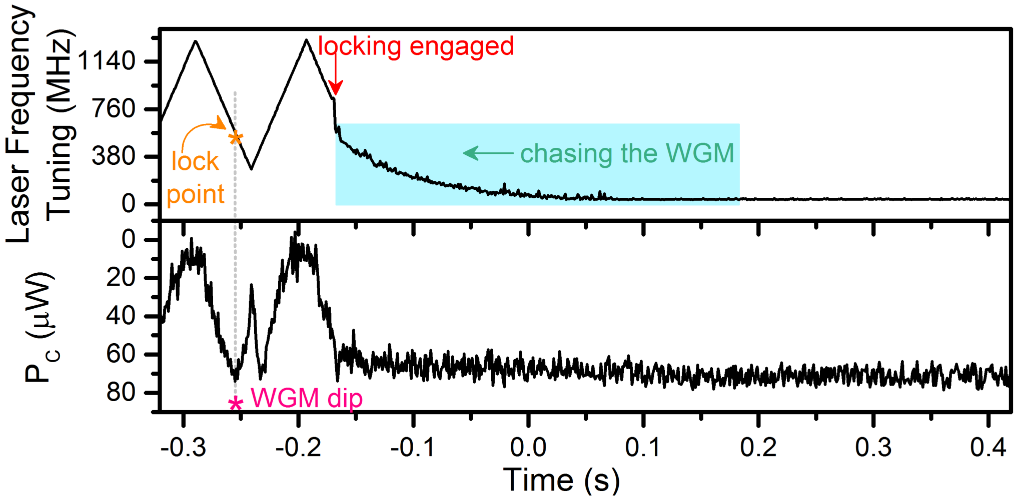

Figure 2.18: Experimental data showing the locking process as a function of time. Prior to the lock engagement, the laser is scanned in frequency to find a WGM in a 85 μm diameter sphere. The lock point marks the laser frequency corresponding to the maximum P_C. After locking, the laser undergoes further tuning (marked in shaded box), related to the bulk heating of the microsphere that shifts the WGM resonance.

by the PDH locking. In frequency space, this reduces the noise in the system, as shown in the fast Fourier transform (FFT) of the transmission, fig. 2.19. Shorter rethermalisation times are expected for smaller microspheres.

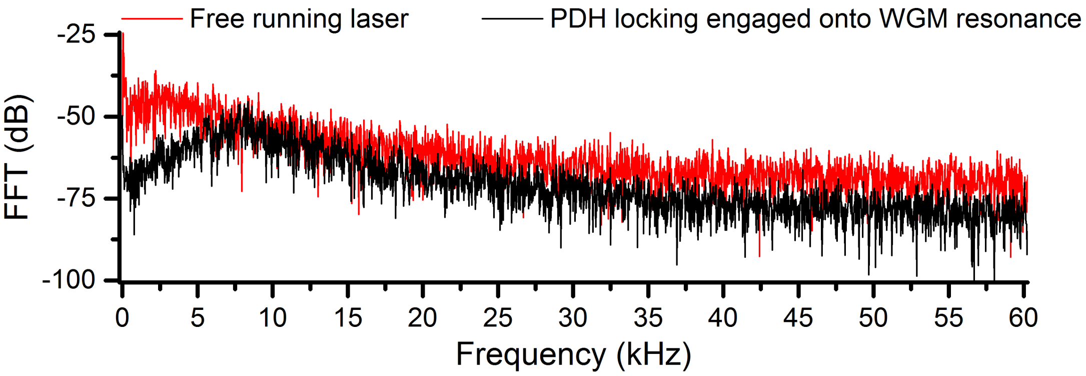

Figure 2.19: The FFT of the transmission from the WGM-taper system when a WGM is excited with 1064 nm light and is running freely (red), versus the lower noise floor obtained when active PDH locking is engaged (black).

When active PDH locking of the laser is employed in fig. 2.19, the noise floor drops by over 20 dB within a bandwidth of 7 kHz, and less than 10 dB for higher frequencies. This noise is attributed to classical fluctuations of the laser, and may be mechanically induced frequency drifts due to the homebuilt design and alignment of the intracavity components of the laser (see fig. 2.6 (pg. 2.6)). The PDH lock is stable against small external perturbations such as normal lab vibrations for long periods of time, but unlocks when large changes in P_c of over 20 % are applied.

The bulk heating of the microsphere can be directly measured during the PDH locking process. Looking at fig. 2.18, the shift in the WGM resonance can be found by measuring the change in laser frequency immediately after engaging the lock. A set of results where this process is repeated with increasing $\mathrm{P_c}$ on-resonance to the 85 μm diameter sphere of used in fig. 2.18 is shown in fig. 2.20.

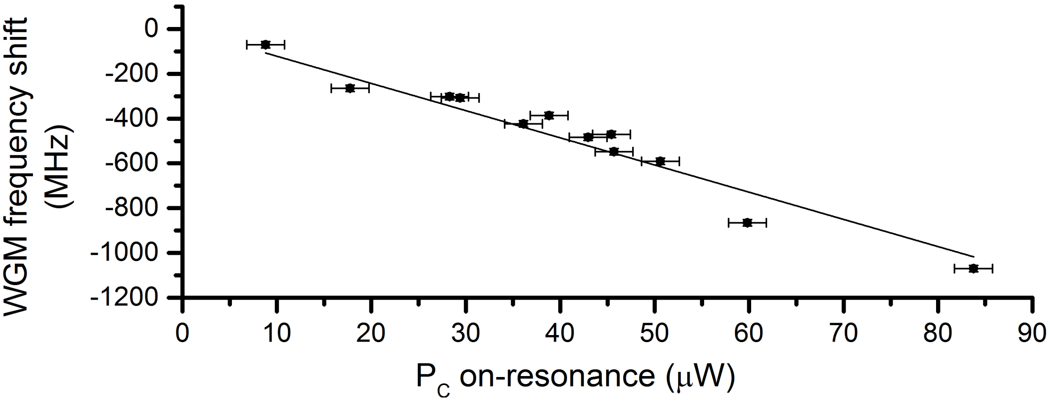

Figure 2.20: Using locking graphs such as that in fig. 2.18, the WGM red-shift versus the power coupled to the WGM can be measured. Note that this set of data is taken with a 85 μm diameter sphere.

The rate of frequency change with P_c is to be $-13 \pm 1\,\mathrm{MHz}/\mu\mathrm{W}$, found by using a linear fit to fig. 2.20, which agrees well with that found elsewhere [133]. Using eq. 2.1, a resonance frequency shift of $-2.56\,\mathrm{GHz/K}$ is expected which correlates to a heating rate of $0.005\,\mathrm{K}/\mu\mathrm{W}$ for a 85 μm diameter microsphere-cantilever.

2.5.2 Implementation of Passive Thermal Locking

There are some situations where the PDH scheme employed in the previous section destabilises. For example, if the coupling distance is quickly modulated with a large sinusoidal amplitude of $\Delta d > 20\,\mathrm{nm}$ (as is the case in chapter 6, when using shaker tests to apply angular accelerations), or, if large modulations in $\mathrm{P_c}$ are required (i.e. over 20 % change in $\mathrm{P_c}$), such as to control the cavity enhanced optical dipole force of the WGM resonator (used to cool mechanical taper modes in chapter 4). An alternative stabilisation method can be implemented, known as passive thermal locking, which exploits the thermo-optic bi-stability.

Passive thermal locking was demonstrated by Carmon et. al in [128], and further studied in [134], showing the ability of the WGM to ‘self-lock’ onto the pump laser. The laser latches onto the blue-detuned side of the WGM through the heating of the resonator by absorption, without an active electronic feedback loop. This can compensate for laser drifts or perturbations such as mechanical motion due to negative thermal feedback, whereas the red detuned side of the WGM is unstable due to positive thermal feedback [129], described in fig 2.21.

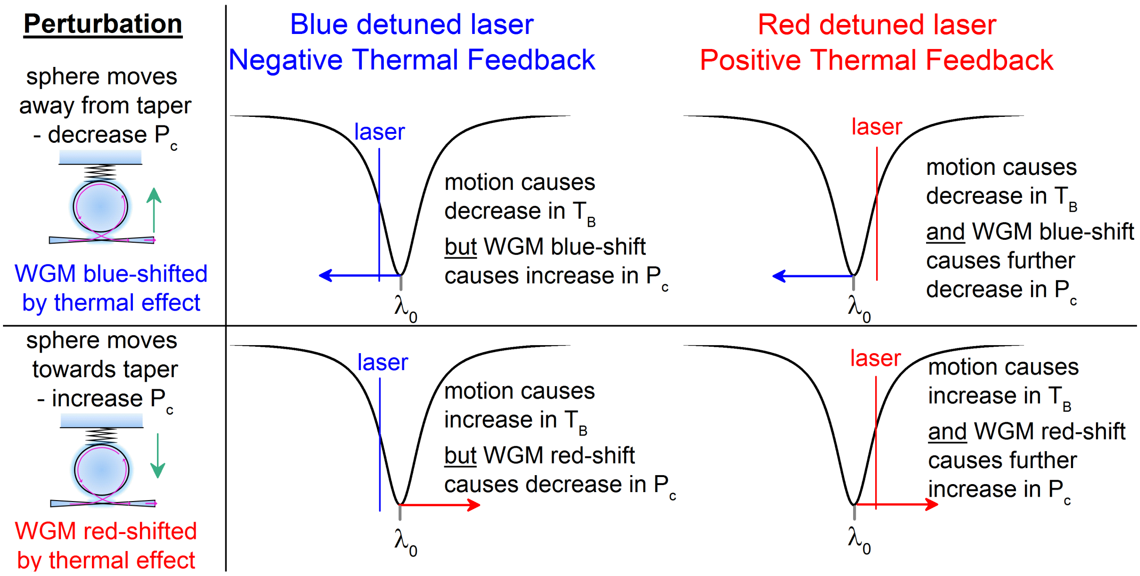

Figure 2.21: A schematic to describe the thermo-optic feedback effect when light is continuously coupled at a laser wavelength detuning of $\pm\Delta = \lambda_l - \lambda_0$, where λ_0 is the WGM resonance wavelength, and λ_l is the wavelength of the laser. The power coupled into the WGM is denoted by $\mathrm{P_c}$, and the bulk temperature is $\mathrm{T_B}$. In the presence of perturbations, the blue-detuned side of the WGM offers a stable self-compensating thermal feedback mechanism.

On the blue detuned side, motion of the sphere away and towards the taper causes a decrease and increase in the power coupled to the WGM respectively (i.e. related to the dependence of $\mathrm{P_c}$ on d in fig. 2.13 pg. 43). This changes the intracavity intensity, and through absorption changes the bulk temperature $\mathrm{T_B}$. The thermo-optic effect causes a subsequent blue and red-shift (equal to an increase and decrease in $\mathrm{P_c}$, respectively) which counteracts the initial mechanical perturbation. Conversely, if the perturbation is from a drift of the ambient temperature that causes $\mathrm{T_B}$ to decrease, the resonance shifts to a higher frequency (lower wavelength), increasing $\mathrm{P_c}$ which in turn raises $\mathrm{T_B}$, red-shifting the WGM. This compensates the initial perturbation in a negative thermal feedback loop. A positive thermal feedback loop exists on the red-detuned side, which only amplifies mechanical perturbations, laser drifts, or changes in the surrounding temperature, making the lock unstable.

The resilience to perturbations is experimentally verified by passively locking the laser to the blue-detuned side of a WGM, as close to resonance as possible. This is indicated in fig. 2.22 a) by the drop in transmission.

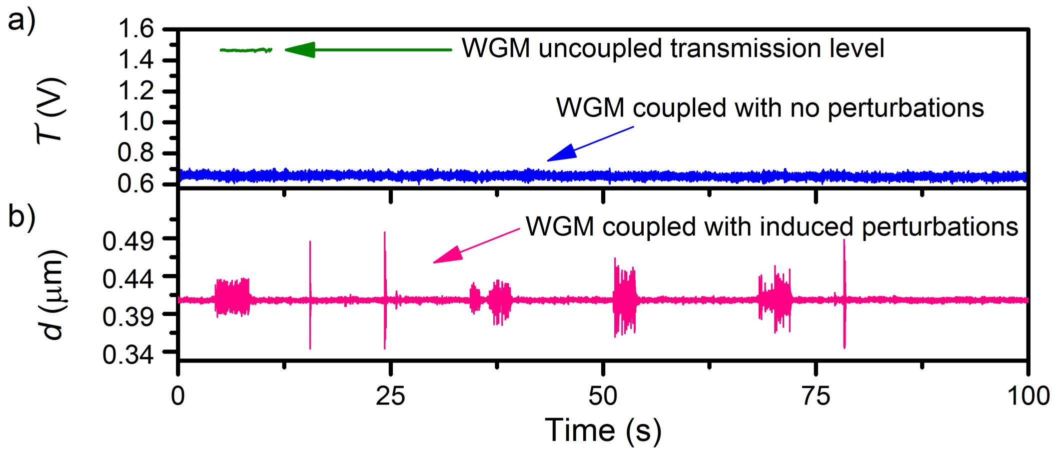

Figure 2.22: Passive thermal locking can be successfully applied close to the WGM resonance but on the blue detuned side, allowing a) continuous coupling to the WGM with no external active electrical feedback components, and b) resilience to external perturbations such as mechanical shocks. In b) the transmission is converted to the coupling distance d using the method in section 2.4.1.

The system is then perturbed by dropping items onto the vacuum chamber and introducing mechanical shocks onto the optical bench. Each event is transduced by the WGM system in the transmission, $\mathcal{T}$. The system immediately relaxes back to a constant coupling distance on a time scale of milliseconds, and maintains coupling throughout, seen in fig. 2.22 b). This reinforces the ability for this system to detect motion, further explored as an accelerometer in chapter 6.

2.6 Counterpropagating Whispering Gallery Modes

One feature of the WGM taper coupled system is the ability to use counterpropagating beams, allowing separation of a transduction beam which can be used to monitor the transmission, and a strong beam that can be used for PDH locking or controlling optical forces. Such a system is employed in active feedback cooling of the thermal motion of the microsphere-cantilever (as well as modes of the tapered fibre) in chapter 4. The elegance of having such counterpropagating beams is that one beam can be detuned from the other, which can be important for sensing applications where the gradient of the WGM Lorenztian lineprofile provides a more sensitive monitoring of frequency/amplitude changes. For this thesis, the role of the strong beam is for PDH locking (or thermal locking) and the role of the transduction beam, which is weaker in intensity, is for monitoring the relative motion of the microsphere-cantilever and tapered fibre. The next chapter details the optimum detuning that should be applied to the transduction beam for a maximum signal to noise measurement of motion.

2.6.1 Utilising a Detuned Transduction Beam

In order to produce a counterpropagating detuned transduction beam, the optical set-up shown in fig. 2.9 is modified by placing a 70/30 beam splitter after the isolator to create the strong beam (denoted in blue) and the transduction beam (in red), shown in fig. 2.23.

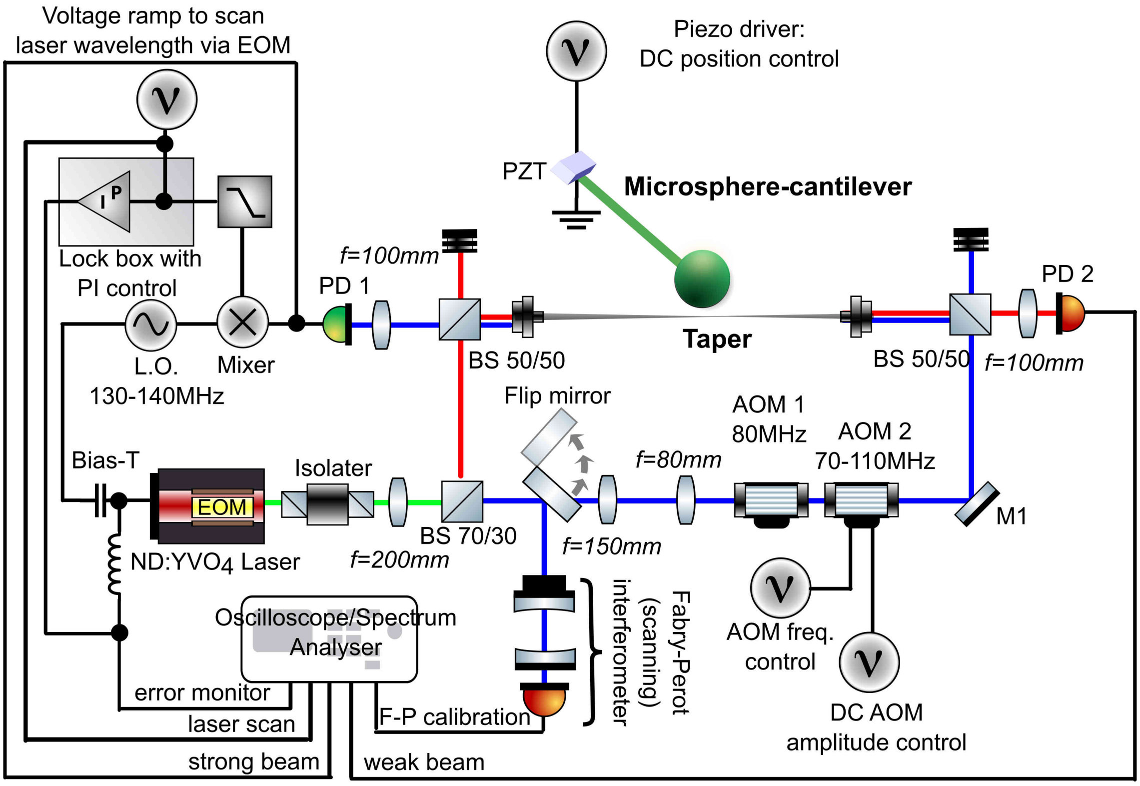

Figure 2.23: Counterpropagating WGM resonances can be excited to provide a strong beam (blue) dedicated for laser stabilisation (i.e. active PDH feedback or thermal locking), or to control actuating forces. The strong beam is detuned using AOM 1 & 2 with respect to a weaker transduction beam (red) that monitors the perturbations of the system as studied in chapter 3. The transduction beam is monitored with PD 2, and the strong beam monitored with PD 1.

In the path of the strong beam are two acoustic-optic modulators (AOMs), the first having a fixed modulation of 80 MHz, and the second AOM tunable between 70-110 MHz, which is calibrated in fig. 2.24 a). The laser power of the output of the second AOM can also be tuned by adjusting the AOM input voltage, fig. 2.24 b).

The transduction beam is fibre coupled from the opposite end of the taper to the strong beam, with 50/50 beam splitters placed prior to each fibre coupling station to allow

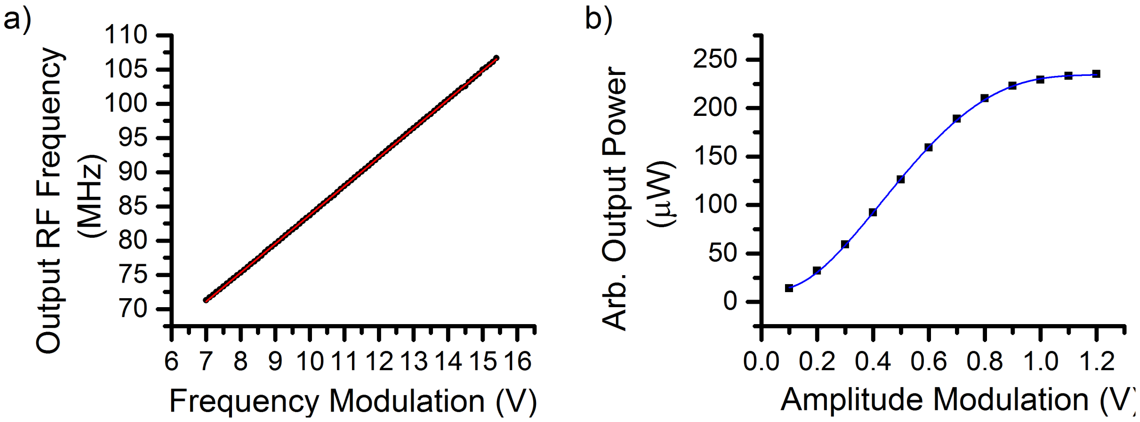

Figure 2.24: The RF frequency tuning range a), and the amplitude output of the acousto-optic modulator (AOM 2) used to detune the transduction beam with respect to the strong beam.

extraction of the respective counterpropagating beams (PD 1 detects the strong beam, PD 2 detects the transduction beam). By choosing the appropriate pair of diffraction orders from AOM 1 and AOM 2, i.e. the ±1 orders, the transduction beam can be detuned with respect to the strong beam over a range of $\pm(-30\,\text{MHz} \rightarrow 10\,\text{MHz})$, $70\,\text{MHz} \rightarrow 110\,\text{MHz}$ and $\pm(150\,\text{MHz} \rightarrow 190\,\text{MHz})$. Therefore to obtain a transduction beam that is red-detuned by $-\Delta$ with respect to the strong beam by detuning the strong beam, the strong beam is tuned by $+\Delta$ using AOM 2, such as the example shown in fig. 2.25. Here, the transduction beam is red-detuned by 20 MHz with respect to the strong beam.

2.7 Conclusion

WGM resonators have a spectrum of resonances, described in the introduction, and experimentally excited in this chapter. The set-ups built during this Ph.D. for fabrication of the microsphere-cantilever and the tapered fibre used to couple light to the microsphere is described. The taper coupled microsphere-cantilever system was experimentally investigated, exciting narrow WGM resonances of 5 MHz FWHM linewidth with $Q_{\text{opt}} > 5 \times 10^7$.

The external coupling rate γ_e that mediates the exchange of photons between taper and microsphere depends exponentially on the coupling distance, d. This was verified in this chapter, and the WGM coupling regime was tuned from undercoupled, to critical coupling ($d \approx 150\,\text{nm}$), to overcoupled.

The high intensity generated within the microsphere leads to bulk heating where the refractive index and sphere dimensions change with increased powers coupled to the WGM. Such an effect presents itself as thermal bi-stability, seen as linewidth broadening and nar-

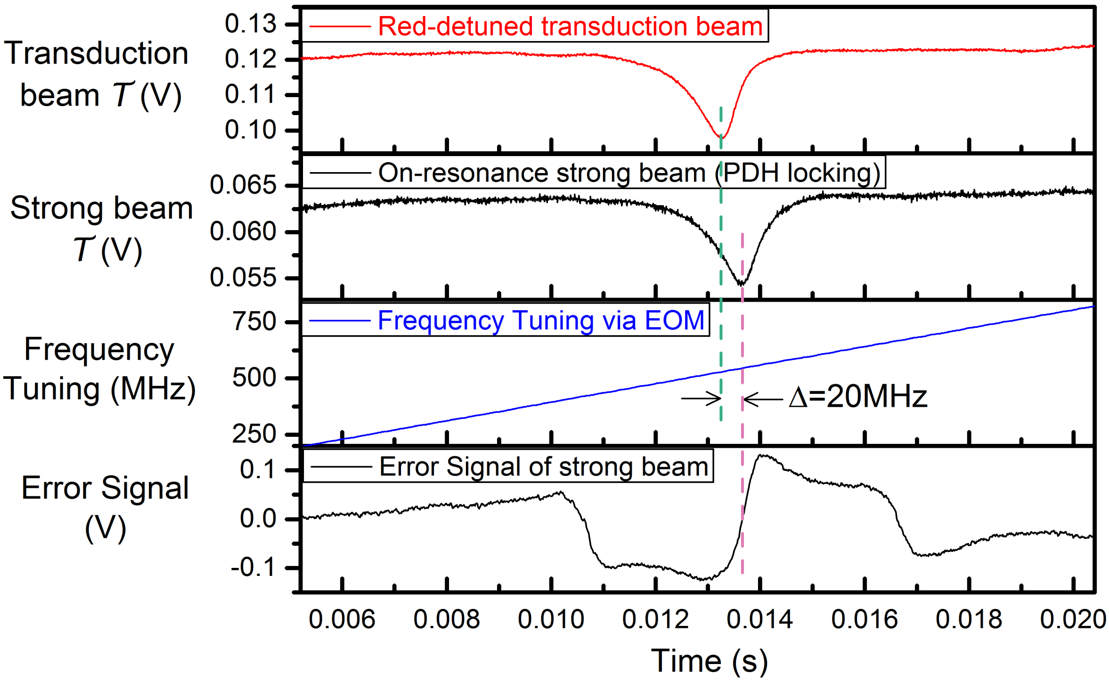

Figure 2.25: Counterpropagating WGMs are excited using the strong beam (black) and a detuned transduction beam (red), detuned by 20 MHz for a 40 MHz FWHM mode. $\mathcal{T}$ denotes the transmission measured by PD 1 (strong beam), and PD 2 (transduction beam). The error signal, formed using the strong beam, is decoupled from the transduction beam so that the zero crossing coincides with the WGM excited by the strong beam.

rowing when the laser is scanned approaching from the blue-detuned side or red-detuned side respectively. Despite this thermal bi-stability, the active PDH locking demonstrated in this chapter can stabilise the laser on-resonance with the WGM. A passive thermal locking equilibrium is successfully applied, where no active feedback electronics are required to keep the WGM excited on the blue-detuned side, useful for cases where a purposely large amplitude modulation of intracavity intensity is required that can break the PDH lock. This is crucial for chapter 4 and chapter 6 where large modulations of the strong beam P_c, and driven displacements are implemented respectively. Lastly, the input-output mechanism of the tapered fibre allows for excitation of the counterpropagating WGM (i.e. the $\pm m$ degenerate modes), for the purposes of the active cooling presented in chapter 4, where one beam is dedicated for transduction and the other for maintaining laser stabilisation to the WGM resonance (or modulating optical forces). The transduction beam is investigated in chapter 3.

Chapter 3

Transduction of Mechanical Motion using Whispering Gallery Modes

3.1 Introduction

This chapter investigates the optomechanical coupling between whispering gallery modes (WGMs) and the thermal motion of the microsphere-cantilever and tapered fibre. The coupling allows for optical transduction of mechanical motion by detecting the fluctuations imprinted onto the WGM field coupled to that motion. Measuring displacements with WGMs is essential for the sensing and cooling of thermal motion explored in this thesis. For example, to use the microsphere-cantilever for accelerometry, as detailed in chapter 6, it is important to characterise the mechanical parameters that predict its response to stimuli, such as mechanical frequency, mechanical quality factor, spring constant and effective mass. These can be deduced by analysing the power spectral density (PSD) of the WGM transmission i.e. from the dedicated transduction beam created in section 2.6.1 of chapter 2. In active feedback cooling, demonstrated in chapter 4, a feedback signal formed from the transduction beam is required to drive actuating forces to apply damping.

Transduction is defined as the process by which a device converts one type of quantity (e.g. energy) into another. The first transducers were materials that could convert electrical and magnetic fields into mechanical motion, such as via Joule magnetostriction which causes the constriction of iron under the influence of a magnetic field. The Curie brothers discovery in the late 18th century that an electric charge is produced by applying an external mechanical force to quartz crystals.

The transduction of mechanical motion using optical fields can be realised when the displacement of a mechanical oscillator causes perturbations in the optical intensity [135], polarisation [136] (i.e. via the strain-optic effect), wavelength [4, 137, 138], and/or phase [31, 139]. Detection schemes can be as simple as measuring the changing shadow cast by a movable object in front of a light source [135], or can be enhanced by adding a resonant cavity structure such as a Fabry-Perot (F-P) cavity [137, 138]. The modulation to the photon density can be measured by monitoring the intensity directly, or through interferometric or homodyne methods to monitor the phase or frequency shifts. When mechanical motion shifts a cavity resonance frequency, it is said to be dispersively coupled to the optical field, governed by a linear scale-factor called the dispersive coupling parameter, g_{om}, in units of $\mathrm{Hz\,m^{-1}}$. Cavities that have high optical quality factors $\mathrm{Q_{opt}}$, such as the WGM employed in this thesis, can enhance g_{om}, and in some cases provide an interferometric calibration between displacement and frequency [21].

Cavity enhanced optomechanical coupling using optical WGMs has been used to transduce and implement cooling of the radial breathing modes of a toroid [4], the flapping motion of two stacked disks [15], and mechanical modes of nanostrings in the near-field [1]. The g_{om} associated with WGMs is often larger than those for F-P cavities, owing to the higher $\mathrm{Q_{opt}}$ and the mode confinement. For the system studied in this thesis, comprising of a microsphere-cantilever coupled to a waveguide, the use of the WGM around the microsphere to detect the motion of its own cavity has been studied by one other group [45]. In 2015 they derived a theoretical framework for this transduction, showing that both dispersive and dissipative (motion is coupled to the loss of the WGM with dissipative coupling parameter γ_{om}) coupling enhances the displacement measurement. The inclusion of γ_{om} differentiates this system from traditional optomechanics experiments which have negligible γ_{om}. This is discussed in chapter 5.

The sensitivity of a measurement is defined by the imprecision noise of the detector (i.e. noise of the light field plus electronic noise and photodetector noise), and depends on the measurement acquisition time since averaging white noise over long timescales decreases the uncertainty [140]. Displacement sensitivity is measured in units of $\mathrm{m\,Hz^{1/2}}$, and defines the linear relationship between the resolution and the measurement time. This is also the square root of the PSD that characterises the power distribution across frequencies [141].

Imprecision noise defines the noise floor of the PSD, and places a cooling and measurement limit. The benefits of using optical fields to detect motion are related to the lower noise levels easily obtainable in often quantum-limited sources, which can also be squeezed in amplitude or phase [53, 142, 143].

As cooling progresses to a point where $k_B T < \hbar\Omega_m$ (Ω_m is the mechanical frequency, T is the effective bath temperature), quantum zero-point fluctuations of the mechanical oscillator (ZPF) will play a dominant role over thermal fluctuations. Conversely, the light field that probes this motion will have quantum noise that defines the precision of measuring the ZPF, as well as heating the motion through radiation pressure backaction[1]. A discussion of the quantum treatment of noise and the ultimate limits for transduction will be presented.

In summary, this chapter will present:

- The theory and experimental demonstration of WGM transduction, showing detection of the thermal motion of the microsphere-cantilever and tapered fibre.
- Analysis of the classical power spectral density (PSD), created from the transduction signal, allowing calculation of the mode temperature, and structural mechanical properties.
- The identification of actuating forces to control the motion of the microsphere-cantilever and tapered fibre.
- The limitations of continuous displacement measurements.

3.2 Optomechanical Transduction

The successes of many optomechanical cooling experiments take advantage of the transduction of mechanical motion through dispersive (and/or dissipative) coupling to an optical resonance. Dispersive coupling is the most prevalent, and is often parametrised by the optomechanical coupling parameter g_{om}, defined as the shift in the resonance frequency

---

[1] There is no limit on resolving the position from an object in an instantaneous measurement i.e. scattering photons off an object allows detection of the position to an accuracy set by the wavelength of the photon. However, the photon will impart a momentum kick that affects the objects future motion. By measuring the whole trajectory one can measure both position and momentum in a weak measurement where Heisenberg's uncertainty principle is obeyed through the existence of backaction [144]. Such weak measurements involve integrating the signal over time, instead of a strong, projective measurement. The large size of the mechanical oscillators in this thesis result in zero point fluctuations comparable to the size of a proton so that an instantaneous measurement using photons of extremely small wavelength will resolve the much larger fluctuations of individual atoms rather than the centre-of-mass co-ordinate.

(ω_0) per meter of displacement, $g_{\mathrm{om}} = \frac{\mathrm{d}\omega_0}{\mathrm{d}x}$. Dissipative coupling results in a change of the optical losses $\frac{\mathrm{d}\kappa}{\mathrm{d}x}$, where κ is the total decay rate.

3.2.1 Cavity Enhanced Transduction

The simplest detection of motion can be achieved by reflecting photons from a mechanical oscillator as in fig. 3.1 a).

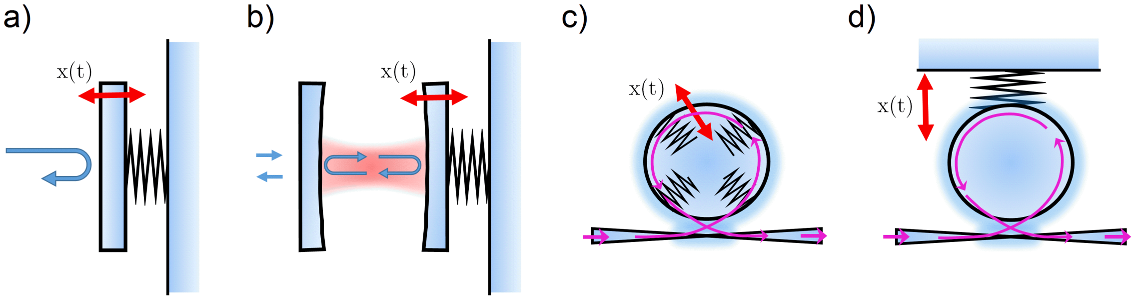

Figure 3.1: Typical transduction schemes to monitor motion: a) Simple reflection from a moving mirror to detect its motion $x(t)$ through a phase change. b) The moving mirror can form a Fabry-Perot cavity, which amplifies the phase change, as well as modulating the intracavity intensity. c) The radial breathing modes of a WGM resonator cause the diameter to change in size by $x(t)$, modulating the path length that is detected in the output transmission of the coupling waveguide. d) The system studied in this thesis, where the WGM resonator is attached to a spring (cantilever) whose c.o.m. motion changes the amount of light coupled into the WGM from the waveguide.

Using the simple case of fig. 3.1 a), where the oscillator is a movable mirror whose motion δx, changes the phase of the reflected beam:

$$\delta\theta = 4\pi\frac{\delta x}{\lambda}, \tag{3.1}$$

where λ is the wavelength of light. Since δx is often smaller than λ, the phase change is very small. If the movable mirror is used to form the end-mirror in a F-P cavity, as in fig. 3.1 b), the phase change is amplified by $\frac{2F}{\pi}$ as the photon makes multiple passes through the cavity [145]:

$$\delta\theta = 8F\frac{\delta x}{\lambda}, \tag{3.2}$$

where F is the cavity finesse, which is the effective resolution of the cavity if used as an interferometer (i.e. roughly the number of different frequencies it can distinguish), and is defined as $F = \frac{\Delta_{\mathrm{FSR}}}{\kappa}$ where $\Delta_{\mathrm{FSR}} = \frac{\pi c}{L}$ is the free spectral range for a cavity with length L and κ is the decay rate. Note for a WGM cavity, $\Delta_{\mathrm{FSR}} \approx \frac{c}{2\pi n a}$, where a is the radius of the microsphere, and n is the refractive index.

3.2.2 The Dispersive Coupling Parameter g_{om}

The lowest resonance frequency of a F-P cavity, which results in a maximum transmission, is:

$$\omega_0 = \frac{c\pi}{L}, \tag{3.3}$$

which will shift to $\omega_0^{'}$ by an amount mediated by the dispersive coupling parameter g_{om} when the cavity length increases and decreases due to $x(t)$:

$$\omega_0^{'}(t) = \omega_0 + g_{\mathrm{om}} x(t) = \frac{\pi c}{L + x} = \frac{\omega_0}{1 + \frac{x}{L}}, \tag{3.4}$$

which can be approximated for small displacements as $\omega_0^{'} \approx \omega_0 \left(1 - \frac{x}{L}\right)$. This means g_{om} for a F-P cavity is equal to:

$$g_{\mathrm{om}} = -\frac{\omega_0}{L}. \tag{3.5}$$

Experiments that use WGM cavities for transduction are usually coupled to radial breathing modes of a toroid (fig. 3.1 c)), or to objects placed in the evanescent field of the WGM resonator. The radial breathing modes alter the cavity diameter so that $g_{\mathrm{om}} = -\frac{\omega_c}{R}$ where R is the sphere radius [14]. However, for a near-field coupled oscillator, such as the dielectric tapered fibre, the calculation of g_{om} is more complex as g_{om} is now related to the evanescent field perturbation from the taper. The frequency shift, derived elsewhere [3] is:

$$\frac{\Delta\omega_0}{\omega_0} = -\frac{1}{2} \frac{\int_{V_t} (\epsilon(r) - 1)) \left|\mathrm{E}(r)\right|^2 \, \mathrm{d}^3 r}{n^2 V_{\mathrm{m}} \left|\mathrm{E}_{\mathrm{max}}(r)\right|^2}, \tag{3.6}$$

where V_{m} is the WGM mode volume, V_t is the taper volume, $\epsilon(r)$ is the relative permittivity, and n is the refractive index. At a distance d (i.e. the coupling distance) from the microsphere surface, the WGM evanescent field is given by $\mathrm{E}(d) \approx \mathrm{E}_{\mathrm{max}}\, e^{-\alpha_s d}$, where the decay constant of the evanescent field is α_s^{-1}. Taking account of this dependence on d, eq. 3.6 becomes [3]:

$$\frac{\Delta\omega_0}{\omega_0} \approx -\frac{1}{2} \frac{A}{V_{\mathrm{m}}} \frac{1 - e^{-2\alpha_s T}}{2\alpha_s} (n^2 - 1)\, e^{-2\alpha_s d}, \tag{3.7}$$

where A is the area of the tapered fibre sampled by the WGM optical field, n is the refractive index of the tapered fibre, and T is the thickness of the taper[2]. Unlike the F-P

---

[2] For tapers of small diameter, i.e. $T << 1/2\alpha_s$, eq. 3.7 can be approximated as $\frac{\Delta\omega_0}{\omega_0} \approx -\frac{1}{2}\frac{V_t}{V_{\mathrm{m}}}(n^2 - 1)\, e^{-2\alpha_s d}$ [3].

cavity, this equation implies that g_{om} will vary exponentially with d, but calculating eq. 3.7 requires precise knowledge of the refractive index and the dimensions of the microsphere and taper which cannot be achieved currently due to technical limitations (discussed in chapter 2, section 2.2). However, one can see that a smaller mode volume, which will scale with the diameter of the sphere allows for larger dispersive coupling. The parameter g_{om} can instead be measured experimentally as in chapter 5 and in the following analysis.

3.2.3 Whispering Gallery Mode Transduction Theory

Although the taper can be considered as a mechanical oscillator in the near-field of the microsphere-cantilever, a dissipative coupling is also present due to the extrinsic coupling rate γ_e introduced in chapter 1 (section 1.4.2). This coupling between the WGM and the taper increases the cavity losses, κ, as the coupling distance d decreases, as shown previously in chapter 2 (fig. 2.4.1, pg. 42). This unique combination of dissipative and dispersive coupling is schematically shown in fig. 3.2, which describe the changes to the WGM resonance and linewidth when coupled with mechanical motion causing d to change by Δd.

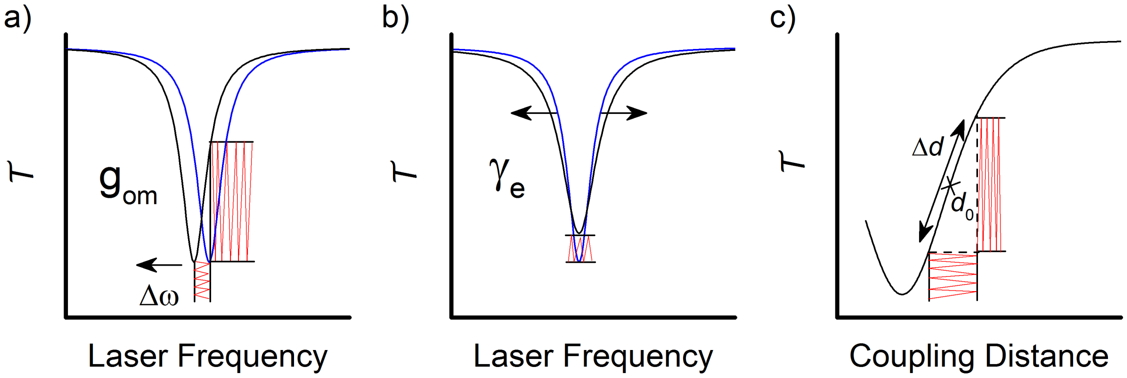

Figure 3.2: The relative motion between a WGM resonator and its coupling waveguide cause modulations to the transmission, $\mathcal{T}$, due to: a) dispersive coupling through g_{om} that shifts the WGM resonance frequency, changing the amount of light coupled to the WGM, b) dissipative coupling that modulates the external coupling rate γ_e (which is linked to the dissipative parameter γ_{om}) by broadening the WGM resonance via extra losses, also causing a change in $\mathcal{T}$. c) If the light is frequency stabilised on the WGM, and the WGM resonator placed at a DC coupling distance d_0, a displacement of $\pm\Delta d$ modulates $\mathcal{T}$, governed by γ_{om} and g_{om}. This figure exaggerates the effect since the thermal motion is over 1000 times smaller than the coupling distance separation.

Dispersion (fig. 3.2 a)), and dissipation (fig. 3.2 b)) is transduced as a shift in the resonance frequency and a broadening of the WGM FWHM respectively. If the driving laser is frequency stabilized near-resonance, the sum of both effects causes a modulation to the transmitted light as in fig. 3.2 c) in response to a displacement of Δd from the DC coupling position d_0. The normalised power coupled to the WGM is equal to $1 - \mathcal{T}$.

The existence of dissipative coupling is intuitive, considering the extrinsic coupling rate $\gamma_e = \gamma_{e,0}\, e^{-\eta d}$ is shown in chapter 2 (fig. 2.12) to broaden the WGM linewidth as d is reduced. The relationship between γ_e and the dissipative coupling parameter g_{om} is $g_{\mathrm{om}} = \gamma_{e,0}\eta\, e^{-\eta d_0}$, where d_0 is the DC coupling position, and g_{om} is valid for small Δd around d_0.

The transduction of the thermal motion of the microsphere-cantilever will be seen in the Fourier transform of the transduction beam as a peak centred at the mechanical frequency Ω_{m}. The magnitude of the transduction can be deduced from the peak amplitude at Ω_{m}. Therefore, a suitable figure of merit to describe the transduction effectiveness is the signal to noise ratio (S/N), and is labelled as S/N. The analytical expression that links the parameters g_{om} and γ_{om} to the S/N for a tapered fibre coupled to a WGM of a microsphere was recently derived and experimentally tested by Madugani et. al [45]. Their proof is summarised below.

The derivation relates mechanical motion with the dispersive shift of the WGM resonance, and the change in the extrinsic coupling rate γ_e that mediates photons exchanged from the WGM to the tapered fibre. The equation governing the rate of change of photons from the cavity ($\frac{\mathrm{d}a}{\mathrm{d}t} = \dot{a}$) is detailed in chapter 1 (section 1.4.2). Since the low kilohertz mechanical frequencies of either the tapered fibre or the microsphere-cantilever are significantly lower than the intrinsic coupling rate γ_i, the steady state condition $\dot{a} = 0$ is valid, and $\bar{a} = \frac{\sqrt{\gamma_e}\bar{S}_{\mathrm{in}}}{i\Delta + \gamma_i/2 + \gamma_e/2}$ (as in eq. 1.28 pg. 24). Therefore the steady state normalised transmission through the tapered fibre, given by $\mathcal{T} = \left|\frac{a_{\mathrm{out}}}{a_{\mathrm{in}}}\right|^2$, can be written as:

$$\mathcal{T} = \left|1 - \frac{2K_e}{1 + K_e + i\Delta'}\right|^2, \tag{3.8}$$

where $K_e = \frac{\gamma_e}{\gamma_i}$, $K_i = 1 = \frac{\gamma_i}{\gamma_i}$ and $\Delta' = \frac{\Delta}{\gamma_i}$, normalised for clarity following [45].

A mechanical motion of the form $\mathcal{D}\cos(\Omega_{\mathrm{m}}\mathrm{t})$ where $\mathcal{D}$ is the peak displacement, will cause both dispersive and dissipative perturbations to the WGM mediated by g_{om} and γ_{om}. Dispersive coupling results in red-shifting the WGM when the microsphere-cantilever moves towards the tapered fibre:

$$\Delta(t) = \Delta_0 - g_{\mathrm{om}}\mathcal{D}\cos(\Omega_{\mathrm{m}}t), \tag{3.9}$$

which is normalised by γ_i to form: $\Delta^{'}(t) = \Delta^{'}_0 - \mathrm{G_{om}}\mathcal{D}\cos(\Omega_\mathrm{m}t)$, where $\mathrm{G_{om}} = \frac{\mathrm{g_{om}}}{\gamma_\mathrm{i}}$. Dissipative coupling causes increased losses as the microsphere-cantilever moves closer to the taper, increasing the WGM linewidth, and modifies the extrinsic coupling rate:

$$\gamma^{'}_e(d_0, t) = \gamma_{e,0}e^{-\eta(d_0 - \mathcal{D}\cos(\Omega_\mathrm{m}t))}, \tag{3.10}$$

valid for motion around a DC coupling distance d_0. The peak amplitude of the motion, $\mathcal{D}$ modifies γ_e via γ_om, which can be found by expanding eq. 3.10:

$$\gamma^{'}_e(d_0, t) = \gamma_{e,0}e^{-\eta d_0}\left(1 + \eta\mathcal{D}\right) = \gamma_e(d_0) + \gamma_\mathrm{om}(d_0)\mathcal{D}, \tag{3.11}$$

where the Taylor expanded form of $e^{\eta\mathcal{D}}$ is used, truncated after the first two terms. This expression is valid at a set d_0 because of the exponential dependence on the coupling distance d, i.e. $\gamma_\mathrm{om}(d) = \eta\gamma_e(d)$.

It is clear that d and Δ_0 will influence the S/N of the transduction signal measuring the motion $\mathcal{D}\cos(\Omega_\mathrm{m}\mathrm{t})$. In order to find γ_om, η, and g_om one must establish an analytical expression linking these parameters with d and Δ_0.

First, eq. 3.10 can be expanded into a series representation defined as the generating function of the modified Bessel function of the first kind $\sum_{n=-\infty}^{\infty} \mathrm{I}_n(z)e^{inq} = e^{z\cos(q)}$:

$$\sum_{n=-\infty}^{\infty} \mathrm{I}_n(\eta\mathcal{D})e^{in\Omega_\mathrm{m}\mathrm{t}} = e^{\eta\mathcal{D}\cos(\Omega_\mathrm{m}t)}. \tag{3.12}$$

The real part of eq. 3.12 results in a series of harmonics $\cos(n\Omega_\mathrm{m}t)$ for $n = 1, 2, 3..$, which can be linearised to its first order term under the assumption the motion of the microsphere-cantilever is small. Therefore $\gamma^{'}_e(d_0, t)$, which is now normalised by γ_i, becomes:

$$K^{'}_e(d_0, t) \approx K_e(d_0)\left(1 + 2\beta\cos(\Omega_\mathrm{m}t)\right), \tag{3.13}$$

where $\beta = I_\mathrm{n}(\eta\mathcal{D})$ is the modified Bessel function of the first kind. Substituting $K_e(t)$ and $\Delta^{'}(t)$ into eq. 3.8, the authors of [45] Fourier transform the modified expression for transmission and approximate the result as:

$$\mathcal{F}[\mathcal{T}] \approx \frac{4K_e(d_0)\left|2\Delta^{'}_0\mathrm{G_{om}}(d_0) - 2\beta\left(K^2_e(d_0) - \Delta'^2_0 - 1\right)\right|}{\left[\left(K_e(d_0) + 1\right)\Delta^{'}_0\right]^2 + \Delta'^4_0 + \left(K_e(d_0) + 1\right)^4}, \tag{3.14}$$

where the S/N at Ω_{m} is the magnitude of the transduction, dependent on d_0 and Δ_0. The optimised settings are measured in the next section, and values for g_{om} and γ_{om} can be estimated from this process using eq. 3.14.

3.3 Experimental Method to Optimise Transduction

The optical set-up shown in fig. 3.3 is used to measure transduction. The laser power is heavily attenuated below $1\,\mu$W to avoid thermal drifts of the WGM mode and the transduction beam can be frequency tuned using the intracavity laser EOM. The transmission of the transduction beam is sent into a spectrum analyser which computes the FFT.

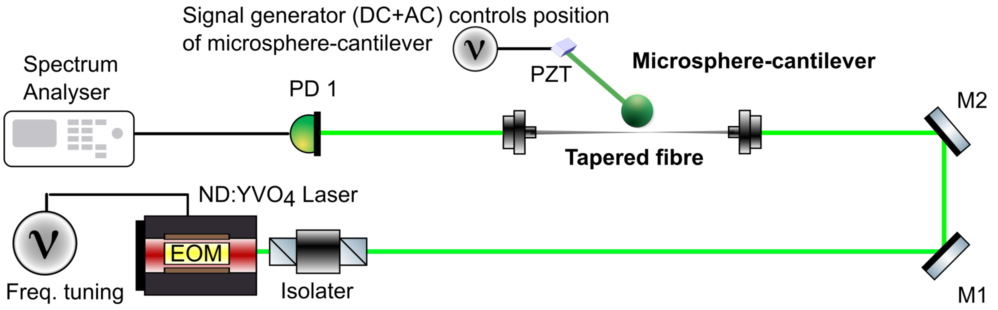

Figure 3.3: A simplified experimental set-up to characterise and optimise WGM transduction of the thermal motion of a microsphere-cantilever, defined as the signal to noise ratio (S/N) of the mechanical peak in the FFT of the transmission. An amplified voltage source is used to tune the laser frequency via the intracavity EOM, and the piezo-stack (PZT) at the clamped end of the cantilever is used to change the DC coupling distance. Offset thermal locking is possible because the input light is heavily attenuated at $\approx 1\,\mu$W.

Two variables will affect the S/N; the coupling distance, d, and the laser detuning with respect to the WGM. The dependence of the S/N on laser frequency is investigated by setting the microsphere-cantilever at an equilibrium DC coupling distance, d_0 to the tapered fibre, and measuring the transmission as the intracavity EOM tunes the laser frequency across the WGM. Next the laser frequency is thermally stabilised whilst d is varied with the piezo-stack (PZT).

3.3.1 Results

Following the experimental procedure detailed above, the S/N can be measured using a single trace FFT as shown in fig. 3.4. Here, the coupling distance d is decreased and the S/N of the FFT of the transduction signal is measured, normalised to the maximum peak amplitude[3].

---

[3] The value of d is calibrated by using the methodology described in section 2.4.1

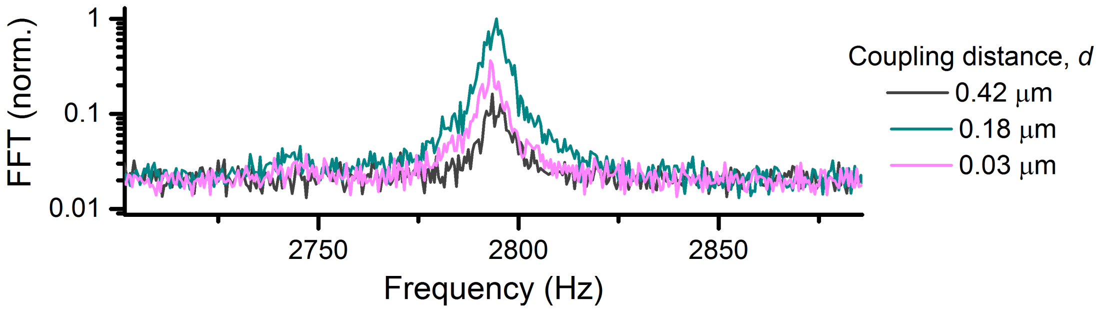

Figure 3.4: The FFT of the transduction beam at various coupling distances d shows a peak at the mechanical frequency of the c.o.m. of a microsphere-cantilever (this mode is cooled in chapter 4). The FFT is normalised to the maximum S/N.

The S/N relationship with d when the laser is thermally locked at a detuning of $\Delta \approx \frac{\gamma_i}{2}$ is shown in fig. 3.5 c). The relationship between S/N and laser detuning is plotted in fig. 3.5 a) at a set coupling distance of $d \approx 180\,\mathrm{nm}$. The graph of fig. 3.5 b) showing the

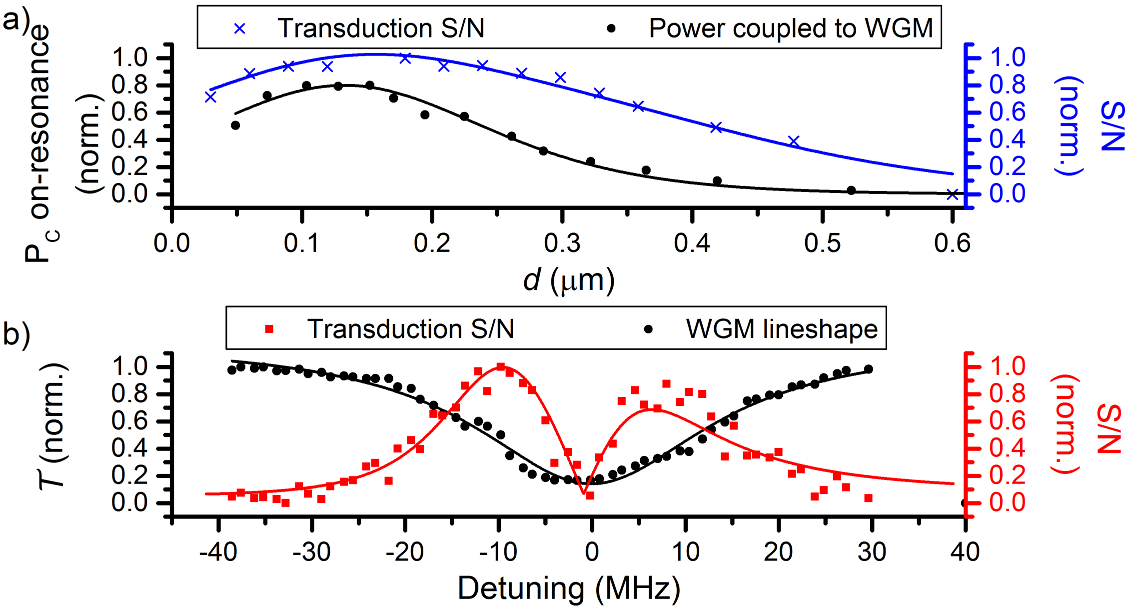

Figure 3.5: Optimising WGM transduction: a) The S/N as a function of coupling distance d (blue data), where the S/N is normalised to the peak maximum amplitude. The data is fitted with eq. 3.14. The power coupled to the WGM on-resonance is also shown in black data, where $\gamma_e/\gamma_i = (4.4 \pm 0.6)e^{-(11.6\pm1.2)d}$. b) The relationship between laser detuning with respect to the WGM resonance and S/N is measured (red data) and fitted using eq. 3.14 (red line). The transmission, $\mathcal{T}$, is simultaneously measured (black data) with a Lorentzian fit over the WGM profile, obtaining (30 ± 1) MHz FWHM.

S/N versus Δ_0 at a fixed coupling distance $d_0 \approx 180\,\mathrm{nm}$, is fitted with eq. 3.14 such that $g_{\mathrm{om}}(d_0) = \gamma_i G_{\mathrm{om}}$, η, and $\gamma_{\mathrm{om}}(d_0) = \eta K_e \gamma_i$ can be found. The same parameters can be deduced using fig. 3.5 a) (S/N versus d), fitted with the d dependent version of eq. 3.14. However, the parameters are now $g_{\mathrm{om}}(d) = \mathrm{G}_{\mathrm{om}}\gamma_i e^{-\eta d}$, and $\gamma_{\mathrm{om}} = K_e\gamma_i\eta e^{-\eta d}$, which can be compared to those obtained from fig. 3.5 b) by setting $d = d_0$. The intrinsic decay rate γ_i

can be found by analysing fig. 3.5 a) (black data) showing the normalised power coupled to the WGM on-resonance, P_c, as a function of d, fitted with eq. 1.33 (pg. 25) from chapter 1, to obtain $\frac{\gamma_e}{\gamma_i}$. This is compared to the WGM lineshape at $d_0 = 180\,\text{nm}$ (fig. 3.5 b) (black)), whose FWHM is equal to $\gamma_e + \gamma_i$ at d_0. A value of $\gamma_i(d_0) = (19.4 \pm 1.9)\,\text{MHz}$ is obtained.

The optimum d is found to be 150 nm, which corresponds to the distance at which the maximum power is coupled into the WGM. Using a red-detuned transduction beam also increases the S/N. These results are in very good agreement with those obtained by the authors in [45]. The S/N dependence on the sign of the detuning indicates that both dispersive and dissipative changes in the coupling are important, unlike conventional optomechanical systems such as F-P cavities where dispersion is dominant. For those systems, $\beta = 0$ and $\mathcal{F}[\mathcal{T}]$ is symmetric around $\Delta_0 = 0$. Asymmetry arises when there is dissipative coupling [45] which has also been found in a split-beam nanocavity [146]. The fitting of figs. 3.5 a) & b) to eq. 3.14 is achieved numerically, providing fitted values of γ_{om}, η, and g_{om}, shown in table 3.1.

Transduction relationship	Fitted $\gamma_{\text{om}}(d{=}180\,\text{nm})$ (MHz/nm)	Fitted η (m^{-1})	Fitted g_{om} ($d{=}180\,\text{nm}$) (MHz/nm)
Laser detuning	1.61 ± 0.05	$14 \times 10^{6*}$	8.25±0.9
Coupling distance	2.78 ± 1	$(8.6 \pm 0.5) \times 10^6$	5.49±1.5
Ref. [45]	0.4	12 to 14	6.7

Table 3.1: The numerically fitted values for the dispersive (g_{om}) and dissipative (γ_{om}) coupling parameters from fitting eq. 3.14 to figs. 3.5 a) & b). The laser detuning and the coupling distance is varied in a) and b) respectively. Also included is the parameter η which is the decay constant that determines the variation of $g_{\text{om}}, \gamma_{\text{om}}$ with d. The superscript * indicates that this parameter is kept fixed during fitting. The bottom panel displays parameters measured in ref. [45].

The corresponding values of g_{om} and γ_e obtained from fitting the coupling distance dependence (fig. 3.5 a)), versus the laser detuning dependence (fig. 3.5 b)) agree relatively well with one another, although values obtained from the coupling distance graph have a larger error. This is related to the tendency of the taper to drift closer to the microsphere at $d < 100\,\text{nm}$, possibly due to electrostatic forces. In comparison to values obtained by the authors of [45], g_{om} agrees within error, but the value of γ_{om} obtained here is between 5 to 7 times larger. This is likely related to the inclusion of a scattering rate γ_s in the analysis of [45], as well as geometric differences between the microsphere and tapered fibre. The ratio $\frac{\gamma_{\text{om}}}{g_{\text{om}}}$ is approximately 0.2 and 0.5 for fig. 3.5 a) and b) respectively. The latter value agrees well with the ratio obtained using an alternative method in chapter 5 (section 5.4)[4]. By decreasing the coupling distance to maximise $g_{\rm om}, \gamma_{\rm om}$, it is possible to obtain higher S/N and coupling parameters comparable to those found for near-field evanescent coupling between a toroid WGM and nanostring i.e. $\gamma_{\rm om}$=13 MHz/nm, $g_{\rm om}$ = 290 MHz/nm is measured in [84].

A clear message is that the transduction should be placed obtained near critical coupling and be red-detuned from the WGM to provide the highest S/N.

3.3.2 Calibration of Units

Although the Fourier transform provides information on the transduction S/N, further information such as mode temperature and the thermal fluctuations of the microsphere-cantilever can be extracted using the power spectral density (PSD), which describes the energy content per unit frequency. The units of the PSD are $\mathrm{m}^2\ \mathrm{Hz}^{-1}$, and the square root of the background noise level in the PSD sets the transduction sensitivity.

The measured transmission of the WGM transduction beam is a voltage from the photodetector which must be converted to meters. This can be achieved by modulating the microsphere-cantilever at a frequency larger than its fundamental mechanical frequency (in fig. 3.6 a sinuisodial modulation of 3.3 kHz is used for a microsphere-cantilever with a 2.8 kHz c.o.m. frequency) so that the displacement of the cantilever follows that of the shaking frame, and not operated as an accelerometer. The peak amplitude of this shaking is defined by the magnitude of the voltage sent to the piezo-stack, which displaces d by 9.1 μm per 150 V.

Using the calibration curve in fig. 3.6, the specific scaling for this sample is $(0.142 \pm 0.023)\,\mu\mathrm{m}\,V^{-1}$. This process is repeated over a range of driving frequencies and averaged each time the experiment is changed. The work conducted in this thesis has resolved displacements as small as 3 pm, verified by driving the piezo-stack with a small sinusoidal voltage.

3.4 Actuating Forces

The optimised transduction demonstrated in the preceding section allows for detection of the c.o.m. thermal motion of the microsphere-cantilever which can be used for sensing

---

[4] An alternative method for measuring $g_{\rm om}$ and $\gamma_{\rm om}$ is presented in chapter 5 (section 5.4) and includes the effects of scattering.

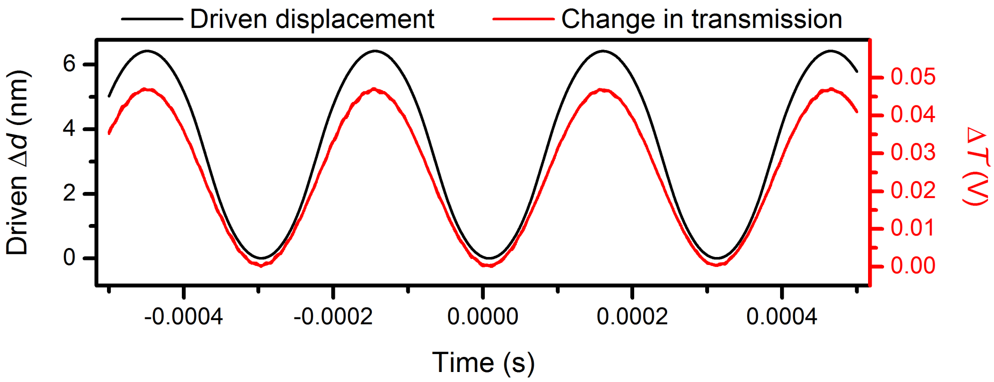

Figure 3.6: Typical calibration graph to find the conversion factor (unit of V/m) between the photodetector output voltage, which measures the transduction beam transmission $\mathcal{T}$, and the *actual* displacement in metres. The piezo-stack that actuates the microsphere-cantilever is driven by a voltage signal to displace the microsphere-cantilever by a set peak displacement (black), in meters. The WGM transduction beam senses this motion as a modulation in $\mathcal{T}$, measured by a photodetector as a voltage (red).

acceleration, as demonstrated in chapter 6. However, the FFT of the WGM transduction beam will contain a spectrum of mechanical peaks alongside the c.o.m. microsphere-cantilever mode, including many mechanical modes of the taper, considered as detrimental noise (as well as low frequency mechanical modes from the supports/seismic vibrations in the lab). In order to control the microsphere-cantilever sensing parameters, or to suppress extraneous thermal motion from the tapered fibre, actuating forces are required.

Two forces are identified and tested in this thesis, capable of actuating the microsphere-cantilever and the tapered fibre. In this chapter they are used to experimentally identify which modes belong to which oscillator by resonantly driving the motion. In chapter 4 these forces are used to apply damping to the c.o.m. motion of the microsphere-cantilever, as well as reduce the thermal noise from the tapered fibre.

In mechanical systems where dissipation channels already exist through clamping, control of motion is often achieved using piezo-stacks, such as in AFM imaging [147]. A piezo-stack is already used to control the position of the microsphere-cantilever which varies the coupling distance (see chapter 2 (section 2.4.1)), as well as calibrate the transduction signal into units of metres (fig. 3.6). It can also provide the appropriate damping force for the active cooling implemented in chapter 4. Here, the piezo supplies mechanical power to the system, which generates a secondary vibrational response that reduces the overall response by destructive interference, cancelling the primary source of vibration [148]. Piezo-stacks can suffer from hysteresis and time delay which must be taken into account, analysed in section 3.4.2 of this chapter.

For those wishing to study quantum effects and cooling to a low phonon occupation, forces from EM fields such as optical gradient forces, radiation pressure and electric gradient forces [149] are preferred. These forces can act across vacuum (i.e. near-field coupling) and can be used in passive cooling methods if the force is optomechanically coupled to the motion. The main two forces that arise from an optical field are radiation pressure (the scattering force) and the optical gradient force (dipole force)[5]. The cavity enhanced optical dipole force (CEODF) associated with the WGM extends beyond the microsphere boundary due to the evanescent field gradient, and can actuate near-field coupled objects [1, 15, 32, 84]. It has been shown elsewhere that a tapered fibre can be actuated by over $1\,\mu$m using the CEODF from a WGM in a microdisk [32]. In the system studied here, despite the ability of the microsphere-cantilever to move (i.e. compared to the fixed microdisk of [32]), the CEODF will actuate the taper towards the microsphere rather than the microsphere-cantilever itself because the taper is much lighter and less stiff (the spring constant and effective masses of both objects are measured in this chapter).

The theory, advantages and disadvantages of these two damping forces are presented below.

3.4.1 Cavity Enhanced Optical Dipole Force

WGM resonators are a type of optical cavity with an associated CEODF related to the stored optical field, which has an evanescent component beyond the dielectric boundary. The CEODF is therefore a gradient force which can polarise a susceptible object in such a way that positively and negatively charged sides of the dipole experience an unequal force. Macroscopic structures such as waveguides or resonators can be considered a collection of individual dipolar subunits [150]. This results in a time averaged net force that can actuate the object, and often provides a larger ‘per-photon force’ than scattering forces when large gradients are used. The magnitude of the force is determined by the mode confinement of the WGM.

An attractive CEODF is obtained when light is resonant with the WGM, and the magnitude is dependent on the optical properties of the WGM and the coupling distance d. This can be theoretically described following the work of [32], where the force can be

---

[5] Another force known as the photothermal force (bolometric force) can occur due to the thermoelastic effect where the strain field (i.e. due to mechanical motion) causes temperature gradients i.e. for a positive thermal expansion material, compression leads to hotter regions. This can be coupled to an optical field whose photons are absorbed to enhance or supress the mechanical motion.

modelled by considering the potential energy of the waveguide ϕ, due to the polarisation induced by the WGM resonator field. Neglecting any contributions that involve cross-overlap of the fields (as these cancel out when the laser is locked on resonance [32]), and assuming linear dielectric susceptibility, the time averaged polarisation energy due to a dipole moment $\mathrm{P}(r)$ (per unit volume) is [32]:

$$\phi = -\frac{1}{2}\int_{V_\mathrm{t}} \mathrm{P}(r)\,\mathrm{E}^*_\mathrm{s}(r)\,\mathrm{d}^3r = -\frac{\epsilon_0\chi_\mathrm{t}}{2}\int_{V_\mathrm{t}} |\mathrm{E}_\mathrm{s}(r)|^2\,\mathrm{d}^3r, \tag{3.15}$$

where V_t is the geometric volume of the taper, χ_t is the electric susceptibility of the taper and $\mathrm{E}_\mathrm{s}(r)$ is the electric field of the microsphere WGM. The average stored energy, U, is related to the effective mode volume of the WGM as $\mathrm{U} = \frac{\epsilon_0 \mathrm{V}_{\mathrm{s}'}\mathrm{n}^2\mathrm{max}\left[|\mathrm{E}_\mathrm{s}(\mathrm{r})|^2\right]}{2}$ where $V_{\mathrm{s}'}$ is the effective mode volume of the sphere and n is the refractive index. This allows one to write eq. 3.15 as:

$$\phi = -\frac{\chi_\mathrm{t}\mathrm{U}}{n^2 V_{\mathrm{s}'}}\int_{V_\mathrm{t}} \left|\widehat{\mathrm{E}_\mathrm{s}}(r)\right|^2\,\mathrm{d}^3r, \tag{3.16}$$

where $\widehat{\mathrm{E}_\mathrm{s}}(r)$ is the unitless electric field eigenfunction of the WGM, normalised such that $\max\left[|\mathrm{E}_\mathrm{s}(r)|^2\right] = 1$. One can relate this to the coupling distance, d, between the microsphere and the tapered fibre, by considering the steady-state internal energy of the WGM:

$$\mathrm{U} = \frac{(1-\mathcal{T})\mathrm{Q}_\mathrm{i}\mathrm{P}_\mathrm{i}}{\omega}, \tag{3.17}$$

where Q_i is the intrinsic optical quality factor, ω is the frequency of light, P_i is the input power through the taper and $\mathcal{T}$ is the transmission which is dependent on the cavity-to-waveguide optical coupling and loss rates. Note that $(1-\mathcal{T})\mathrm{P}_\mathrm{i}$ is equal to the power coupled into the WGM, P_c. On-resonance, $\mathcal{T}(\omega_0) = \mathcal{T}_\mathrm{on}$ where ω_0 is the WGM frequency, and $\mathcal{T}_\mathrm{on}(d) = \left[\frac{\left(1-\frac{\gamma_e(d)}{\gamma_i}\right)}{\left(1+\frac{\gamma_e(d)}{\gamma_i}\right)}\right]^2$, where $\gamma_e(d) = \gamma_{e,0}\,e^{-\eta d}$ is the coupling distance dependent extrinsic coupling rate with decay constant η, and γ_i the intrinsic unloaded decay rate. The intrinsic coupling rate, $\gamma_i = \frac{\omega_0}{\mathrm{Q}_\mathrm{i}}$ remains constant. Substitution of the coupling distance dependence in eq. 3.16 results in [32]:

$$\phi = -\frac{4\chi_\mathrm{t}\gamma_e(0)\mathrm{Q}_\mathrm{i}^2\mathrm{P}_\mathrm{i}}{\omega_0^2 n^2 V_{\mathrm{s}'}}\frac{e^{-\eta d}}{\left(1+\frac{\gamma_e(0)\mathrm{Q}_\mathrm{i}}{\omega_0}e^{-\eta d}\right)^2}\int_{V_t}\left|\widehat{\mathrm{E}_\mathrm{s}}(r)\right|^2\,\mathrm{d}^3r, \tag{3.18}$$

where the integral part can be approximated by $V_{\mathrm{t}'}e^{-\eta d}$ where $V_{\mathrm{t}'}$ is the effective volume of the taper mode. The effective optical force acting on the tapered fibre due to the WGM resonator, which actuates the taper towards the microsphere-cantilever is:

$$\mathrm{F}(d) = -\frac{\partial \phi(d)}{\partial d}. \tag{3.19}$$

The arising CEODF is attractive and given by [32]:

$$\begin{aligned} \mathrm{F}(d) &= -\frac{8\eta\chi_{\mathrm{t}} V_{\mathrm{t}'}\gamma_e(0)\mathrm{Q}_{\mathrm{i}}^2\mathrm{P}_{\mathrm{i}}}{\omega_0^2 n^2 V_{\mathrm{s}'}} \times \frac{e^{\eta d}}{\left(e^{\eta d} + (\gamma_e(0)\mathrm{Q}_{\mathrm{i}}/\omega_0)\right)^3} \\ &= -\frac{2\eta\chi_{\mathrm{t}} V_{\mathrm{t}'}\mathrm{Q}_{\mathrm{i}}}{\omega_0 n^2 V_{\mathrm{s}'}} \times \frac{\mathrm{P}_{\mathrm{c}}}{\left(e^{\eta d} + (\gamma_e(0)\mathrm{Q}_{\mathrm{i}}/\omega_0)\right)}. \end{aligned} \tag{3.20}$$

The variables in eq. 3.20 can be found by scanning over the WGM resonance whilst changing the coupling distance, d. First, the normalised power coupled into the WGM, P_{c} as d is decreased is plotted in fig. 3.7 a) (black data points). Using $\mathcal{T}_{\mathrm{on}} = (1 - \mathrm{P}_{\mathrm{c}})$, a plot of $\frac{1-\sqrt{\mathcal{T}_{\mathrm{on}}}}{1+\sqrt{\mathcal{T}_{\mathrm{on}}}}$ is displayed in fig. 3.7 b) (black data points). The on-resonance transmission $\mathcal{T}_{\mathrm{on}}(d)$ states that the y-axis of eq. 3.7 b) is equivalent to $\frac{\gamma_e(d)}{\gamma_i}$. An exponential fit of fig. 3.7 b) can extract $\gamma_e = \gamma_e(0)e^{-\eta d}$ to find $\gamma_e(0) = (2.5 \pm 0.03) \times 10^9$ rad s^{-1} and $\eta = (20.2 \pm 1) \times 10^6\,\mathrm{m}^{-1}$ for a WGM resonance with a Q-factor of $(9.8 \pm 2) \times 10^6$. The predicted CEODF for varying coupling distance is plotted in fig. 3.7 a) (blue curve) for a $20\,\mu$m diameter microsphere with an effective mode volume $V_{\mathrm{s}'} \approx 70\frac{\lambda}{n}^3 = 2.3 \times 10^{-17}\,\mathrm{m}^3$ and an effective volume of the taper $V_{\mathrm{t}'} \approx 0.35\frac{\lambda}{n}^3 = 1.2 \times 10^{-19}\,\mathrm{m}^3$. A maximum force of approximately 16 nN can be obtained using 1 mW input power, and occurs at a value of d smaller than d^c, the position at which the maximum power is coupled (critical coupling, defined in chapter 1, section 1.4.2). This agrees with the theoretical prediction, where the optimum coupling distance d^* is found by differentiating eq. 3.20 and setting it equal to 0:

$$d^* = \frac{1}{\eta}\ln\left(\frac{\gamma_e(0)\mathrm{Q}_{\mathrm{i}}}{2\omega_0}\right), \tag{3.21}$$

which is smaller than $d^{\mathrm{c}} = \frac{1}{\eta}\ln\left(\frac{\gamma_e(0)\mathrm{Q}_{\mathrm{i}}}{\omega_0}\right)$. The maximum CEODF amplitude at d^*:

$$F(\mathrm{d}^*) = -\frac{32\eta\chi_{\mathrm{t}}}{27\mathrm{n}^2\gamma_{\mathrm{e}}(0)}\frac{V_{\mathrm{t}'}}{V_{\mathrm{s}'}}\mathrm{P}_{\mathrm{i}}. \tag{3.22}$$

This force scales inversely with cavity mode volume, suggesting that as devices approach the nanoscale the force will be larger. The maximum force is also independent of the WGM Q_{i} since increasing Q_{i} pushes the optimum coupling distance further from the edge of the sphere i.e. $d^* \propto \ln(\mathrm{Q}_{\mathrm{i}})$, and cancels the enhancement to the internal field.

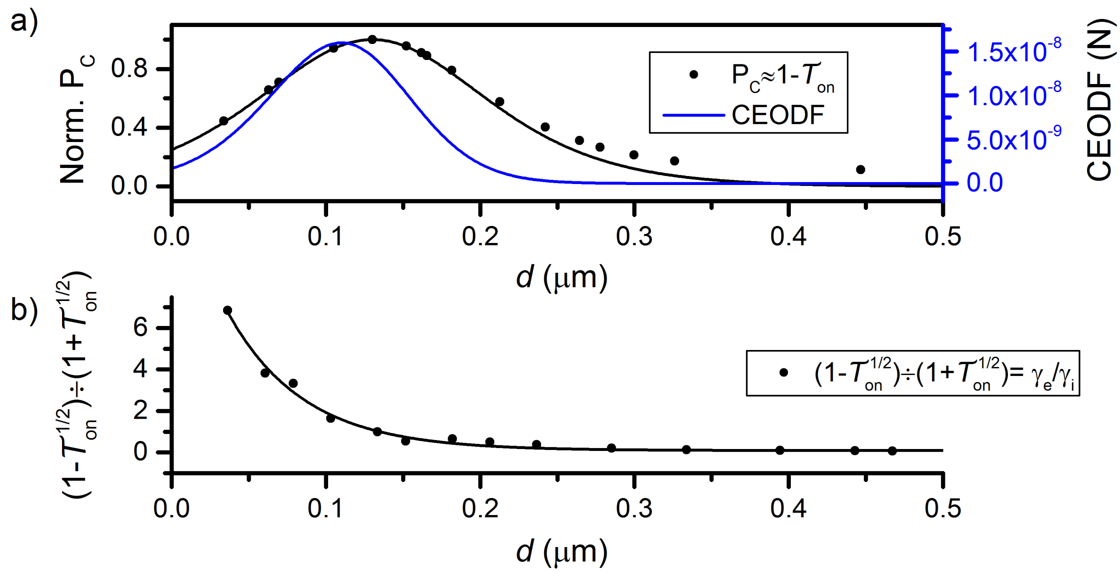

Figure 3.7: a) Shows the normalised power coupled P_c to the WGM (black data), which influences the CEODF (eq. 3.20, blue line) as a function of coupling distance d, measured by scanning over the WGM whilst decreasing d until the microsphere touches the taper. b) A plot of $\frac{1-\mathcal{T}_{\rm on}^{1/2}}{1+\mathcal{T}_{\rm on}^{1/2}}$ against d, by using the data of a) and the expression $P_c = (1 - \mathcal{T}_{\rm on})$. The y axis of b) is therefore a plot of $\frac{\gamma_e(d)}{\gamma_i}$ which can be used to extract $\gamma_e(0)e^{-\eta d}$. The blue curve in a) is the predicted CEODF for a 20 μm microsphere with 1 mW input power, modelled using eq. 3.20 with the extracted values for $\eta, \gamma_e(0)$.

Experimental Test of the Cavity Enhanced Optical Dipole Force

The actuation of the position of the tapered fibre using the CEODF is tested using the set-up of fig. 2.23 (pg. 53) in chapter 2. Counterpropagating beams are employed such that a transduction beam is dedicated for measuring changes in the coupling distance d, and the power in the strong beam can be adjusted using AOM 2 to vary the power coupled to the WGM P_c to modulate the CEODF (as in eq. 3.20). The result of this actuation is shown in fig. 3.8.

The results of fig. 3.8 are performed in the undercoupled regime, away from d^c to avoid the likelihood of the taper touching the microsphere-cantilever. Since the transduction beam is decoupled from the strong beam (less than 5% cross coupling), and both beams counterpropagate from one another, the transduction beam transmission only changes in response to the motion of the taper. Verification that the CEODF cannot actuate the microsphere-cantilever is shown later in this chapter.

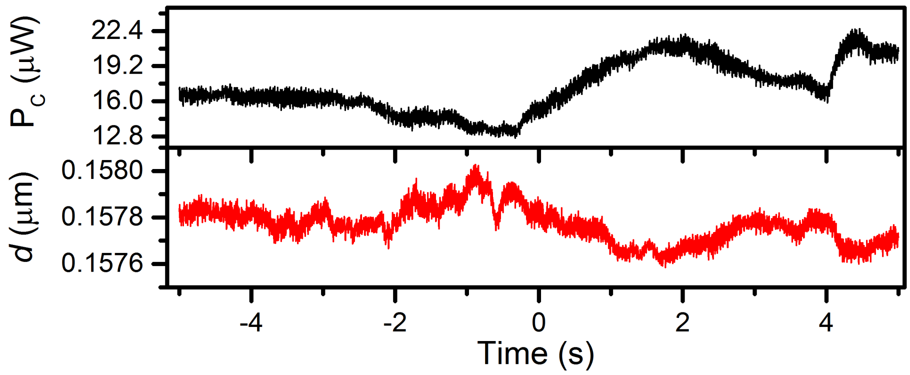

Figure 3.8: The top panel shows a slow modulation of the power coupled to the WGM $\mathrm{P_c}$, through manually adjusting the strong beam output power emerging from AOM 2 (the set-up is shown in fig. 2.23 of chapter 2). A change in $\mathrm{P_c}$, according to eq. 3.20, modulates the CEODF. The bottom panel displays the transmission from the transduction beam, converted into a change in the coupling distance d due to the actuated motion of the tapered fibre due to the CEODF. The approximate anti-phase response of the transduction beam to $\mathrm{P_c}(t)$ is expected for a system in the undercoupled regime.

3.4.2 Piezoelectric Stack

Actuation of the microsphere-cantilever using a piezo-stack[6] is implemented for fine tuning the coupling distance with respect to the tapered fibre in chapter 2, as well as providing calibration of the transduction signal into displacement units, shown in fig. 3.6. Such actuators have been used for feedback cooling by many groups [28–31] and are found in AFM experiments to control the properties of the tip [29, 147]. Here, the piezo-stack is checked to meet the requirements for driving the microsphere-cantilever for the purposes of resonantly identifying the modes in this chapter, and for feedback damping in chapter 4.

Lead-zirconate-titanate (PZT) is the ceramic material that forms the piezo-stack, which undergoes a physical displacement as a result of an applied electric field. The limit of actuation is defined by the noise of the voltage supply or piezo driver, characterised in section 4.5 of chapter 4. The piezo-stack can be driven by frequencies lower than its resonance frequency, f_{PZT}, in this case $f_{\mathrm{PZT}} = 138\,\mathrm{kHz}$ (assuming no mechanical load), which is over 10× larger than the c.o.m. frequency of typical microsphere-cantilevers fabricated in this thesis.

The output current of the voltage source used to drive the piezo-stack can further limit the driving frequency, related to the maximum rate of piezo actuation. This restricts the

---

[6] Thorlabs AE0203D08F

driving frequency sent to the piezo-stack to:

$$f_{\mathrm{max}} = \frac{\mathrm{I}_{\mathrm{max}}}{\pi \mathrm{C} V_{pp}}, \tag{3.23}$$

where $\mathrm{I}_{\mathrm{max}}$ is the maximum current that can be supplied by the driver (60 mA), C is sum total capacitance of the piezo-stack (0.18 μF) plus the driver (1 nF), and V_{pp} is the peak-to-peak voltage change required. A peak-to-peak displacement of 50 pm requires $V_{pp} = 0.8 \times 10^{-3}\,\mathrm{V}$ and sets the maximum driving frequency to 132 MHz, over 25,000 times larger than the mechanical frequencies studied in this thesis. Note that larger modulation amplitudes will reduce this value.

A second consideration when using piezo-stacks is the low-pass filter effect that can introduce a non-linear response with driving frequency. The piezo-stack can be modelled as a capacitor such that it creates a low-pass filter with the output impedance of the driver[7]. The linear response region is defined by the bandwidth, BW:

$$\mathrm{BW} = \frac{1}{2\pi \mathrm{RC}}, \tag{3.24}$$

where R is the resistance of the driver (150 Ω). The bandwidth is given by BW $\approx$ 6 kHz, which means that modulating the piezo-stack at the second eigenfrequency of typical microsphere-cantilevers (around 20 kHz) will provide a smaller peak-to-peak displacement than for frequencies lower than 6 kHz.

Lastly, the slew rate defines the change in charge $\frac{\mathrm{d}V}{\mathrm{d}t} = \frac{\mathrm{I}}{\mathrm{C}}$ and can be used to check the time duration for the piezo-stack to elongate after a voltage is applied. For this system, $\frac{\mathrm{d}V}{\mathrm{d}t} = 330\,\mathrm{kV/s}$ such that a change of 50 pm (by applying 0.8 mV) takes 2 ns, negligible compared to the time period of kHz mechanical oscillations.

The combination of the piezo-driver and the piezo-stack therefore meets the requirements for damping the kilohertz motion of the microsphere-cantilever. Although piezo-actuators have hysteresis when operated in an open-loop voltage-controlled system [151] (i.e. actuating an object vertically by a distance $+y$ and then $-y$ does not return the object to its starting position), this is typically $< 15\%$ when using the total displacement range (maximum driving voltage). Since the piezo-stack is used as an actuator in a closed-loop feedback scheme, the hysteresis is reduced as the position servo-control can eliminate

---

[7] Thorlabs MDT693B

non-linear behaviour.

3.5 The Power Spectral Density

The experimental transduction of thermal motion is best analysed in the form of a power spectral density (PSD), which plots the energy content per unit frequency. The advantage of using PSDs is that mechanical properties including the mode temperature, can be directly determined since the thermal motion of the microsphere-cantilever gives rise to a peak at Ω_{m} in the PSD (derived next). The amplitude, linewidth, and area of the peak can deduce the effective mass m_{eff}, the spring constant k, and the mechanical quality factor $\mathrm{Q_m}$ of the mode (analysed in section 3.6 of this chapter). Crucial to the feedback cooling in chapter 4 is the ability to measure and damp this thermal motion, allowing read out of the reduced mode temperature by using the PSD.

The thermal Brownian motion of a mechanical oscillator is a fluctuating quantity $x(t)$ that is stochastic in nature (random). It is not possible to predict the value of x at any instant since the properties of $x(t)$ are described by a probability distribution $\mathcal{P}(t)$, however, one can make precise statements about the average value. For example, the expected value of the function $f(x)$ is defined as either the integral over time or the integral over the normalised distribution, $\mathcal{P}(x)$, i.e. $\bar{f}(x) = \langle f(x) \rangle = \lim\limits_{T\to\infty} \frac{1}{T} \int_{-T/2}^{T/2} f(x(t))\,\mathrm{d}t = \int f(x)\mathcal{P}(x)\,\mathrm{d}x$. However, to gather information about the temporal properties of the observed quantity, a useful probe is the autocorrelation function[8] which defines how much x at t is correlated with x at t':

$$\big\langle x(t)x(t-t') \big\rangle = \lim_{T\to\infty} \frac{1}{T} \int_{-T/2}^{T/2} x(t)x(t-t')\,\mathrm{d}t. \tag{3.25}$$

One can also define a cross-correlation function $\langle y(t)x(t-t') \rangle$.

The linear response of x when subjected to a force F is expected to contain a delay t', so that the average value of x at time t is:

$$\langle x(t) \rangle_{\mathrm{F}} = \int_{-\infty}^{\infty} \chi(t-t')\mathrm{F}(t')\,\mathrm{d}t', \tag{3.26}$$

where $\chi(t-t')$ is the response function which relates the value of $x(t)$ to a sum over values of the force $\mathrm{F}(t')$ for the timespan $t-t'$. The eq. 3.26 is a convolution of two functions

---

[8] The autocorrelation function is the normalised autocovariance function (normalised by the variance).

which can be written alternatively in the Fourier transform as:

$$\langle x(\omega)\rangle_{\mathrm{F}} = \chi(\omega)\mathrm{F}(\omega). \tag{3.27}$$

Here, the response function is also known as the susceptibility, $\chi(\omega)$, and can be complex in nature, where the real part determines the displacement in phase with the force, whereas the imaginary part gives a displacement that is $\pi/2$ out of phase. The latter corresponds to dissipation as the external force does work on the system, proportional to the velocity. The Langevin force of the air molecules responsible for Brownian motion provides both excitation and damping.

The Fourier transform of a signal $\left(x(\omega) = \lim\limits_{T\to\infty} \int_{-T/2}^{T/2} e^{i\omega t} x(t)\,\mathrm{d}t\right)$ describes how the signal is distributed amongst different frequency components. The PSD ($S_{xx}(\omega)$) is the square of the modulus of the FFT and shows how much power is associated with different frequencies:

$$\begin{aligned} S_{xx}(\omega) &= \langle |x(\omega)| \rangle^2 = \langle x(\omega)x^*(\omega)\rangle \\ &= \lim_{T\to\infty} \frac{1}{T} \int_{-T/2}^{T/2} e^{i\omega t} x(t) dt \int_{-T/2}^{T/2} e^{-i\omega t} x(t')\,\mathrm{d}t'. \end{aligned} \tag{3.28}$$

Since this is a measure of energy, it will produce a single-sided PSD found by adding the square magnitudes of the negative and positive frequency components. For a real signal these are identical so that the single sided density differs by a factor of 2 to the two-sided density[9]. Single sided PSDs will be used throughout this thesis unless stated. The PSD is related to the autocorrelation function by the Wiener-Khinchin theorem by taking the inverse transform of the PSD (eq. 3.28):

$$\int_{-\infty}^{\infty} S_{xx}(\omega) e^{-i\omega\tau} d\omega = \int_{-\infty}^{\infty} \langle x(\omega)x^*(\omega)\rangle\, e^{-i\omega\tau}\,\mathrm{d}\omega \tag{3.29}$$

such that

$$\begin{aligned} \int_{-\infty}^{\infty} S_{xx}(\omega) e^{-i\omega\tau} d\omega &= \lim_{T\to\infty} \frac{1}{T} \int_{-T/2}^{T/2} \int_{-T/2}^{T/2} \delta(t - t' - \tau) x(t) x(t')\,\mathrm{d}t\,\mathrm{d}t' \\ &= \lim_{T\to\infty} \frac{1}{T} \int_{-T/2}^{T/2} x(t) x(t-\tau)\,\mathrm{d}t \\ &= \langle x(t) x(t-\tau)\rangle \end{aligned} \tag{3.30}$$

---

[9] As will be shown later, this breaks down for quantum noise analysis.

Taking $\tau = 0$, eq. 3.30 leads to Parseval's theorem:

$$\left\langle |x(\tau = 0)|^2 \right\rangle = \int_{-\infty}^{\infty} \left\langle |x(\omega)|^2 \right\rangle \mathrm{d}\omega, \tag{3.31}$$

that states the average value of the square of the signal is equal to the variance (when the signal has zero mean), which is also equal to the integral of the PSD.

3.5.1 Brownian Motion

The force responsible for Brownian motion is a stochastic Langevin force $\mathrm{F}^{\mathrm{th}}(t)$. For a harmonic oscillator, it acts to define the equation of motion as:

$$\frac{m\,\mathrm{d}^2 x(t)}{\mathrm{d}t^2} + m\Gamma_0 \frac{\mathrm{d}x(t)}{\mathrm{d}t} + m\Omega_{\mathrm{m}}^2 x(t) = \mathrm{F}^{\mathrm{th}}(t), \tag{3.32}$$

where Γ_0 is the viscous damping factor from air molecules, Ω_{m} is the mechanical resonance frequency and $\mathrm{F}^{\mathrm{th}}(t) = \alpha\sqrt{\frac{2k_B \mathrm{T}\Gamma_0}{m}}$, where $\alpha(t)$ is the normalised white-noise process (for all t and t', $\langle \alpha(t) \rangle = 0$ and $\langle \alpha(t)\alpha'(t) \rangle = \delta(t - t')$ [77]. This thermal force acts as a bath with temperature $\mathrm{T}_0 = 300\,\mathrm{K}$, and is an infinite sum of harmonic oscillators exerting equal amplitude forces. Assuming eq. 3.32 is periodic, it can be solved in the Fourier domain[10] with a general solution analogous to eq. 3.27, of:

$$\delta x(\omega) = \chi_{\mathrm{m}}(\omega)\mathcal{F}^{\mathrm{th}}(\omega), \tag{3.33}$$

where $\delta x(\omega)$ is the motion of the oscillator, $\chi_{\mathrm{m}}(\omega)$ is the mechanical susceptibility and $\mathcal{F}^{\mathrm{th}}(\omega)$ is the thermal Brownian force in frequency space. The mechanical susceptibility is found by taking the Fourier transform of eq. 3.32 and utilising $\mathcal{F}\left[\frac{\mathrm{d}^n}{\mathrm{d}t^n} x(t)\right] = (i\omega)^n \delta x(\omega)$. This gives the following expression:

$$\mathcal{F}^{\mathrm{th}}(\omega) = m\left(-\omega^2 + i\omega\Gamma_0 + \Omega_{\mathrm{m}}^2\right)\delta x(\omega), \tag{3.34}$$

which can be used with eq. 3.33 to obtain the mechanical susceptibility:

$$\chi_{\mathrm{m}} = \frac{1}{m\left(\Omega_{\mathrm{m}}^2 - \omega^2 + i\Gamma_0\omega\right)}. \tag{3.35}$$

---

[10] This assumption is valid as the aim is to obtain a steady state solution that is stable. In order to characterize the full response of the system, including instability and transient responses, one should use the Laplace transform.

At low frequencies, where $\omega << \Omega_{\mathrm{m}}$, the linear response to a sinusoidal force is given by the spring constant $k = m\Omega_{\mathrm{m}}^2$.

The mechanical susceptibility of the oscillator given by eq. 3.35 is Lorentzian-shaped (assuming the mechanical response is harmonic), and relates the PSD of the thermal force $S_{\mathrm{F}}^{\mathrm{th}}(\omega)$ to the PSD of the position of the mechanical oscillator acted upon by that force ($S_{xx,F}(\omega)$). The expression for $S_{xx,F}(\omega)$ is found by using the PSD of eq. 3.33:

$$S_{xx,F}(\omega) = |\chi_{\mathrm{m}}(\omega)|^2 S_{\mathrm{F}}^{\mathrm{th}}(\omega). \tag{3.36}$$

This shows that the Brownian force couples to the displacement spectral density through the mechanical susceptibility. The PSD of the stochastic force $\mathrm{F}^{\mathrm{th}}(t)$ is a constant, which can be derived by considering a random force $\langle \mathrm{F}(t)\mathrm{F}(t')\rangle = A\delta(t-t')$, where $\delta(t-t')$ is the Dirac delta function. The autocorrelation function of this random force is given by the Wiener-Khinchin theorem as $S_{\mathrm{F}}(\omega) = \left\langle |\mathrm{F}(\omega)|^2 \right\rangle = A$. Therefore $S_{\mathrm{F}}^{\mathrm{th}}(\omega) = A$. The fluctuation dissipation theorem, derived elsewhere [144] can be used to derive A. This states that a system in thermal equilibrium [152] can be represented by:

$$\begin{aligned}\int e^{-i\omega t} \langle x(0)x(t)\rangle_{\mathrm{th}} \mathrm{d}t &= \frac{2\mathrm{k_B T_0}}{\omega}\mathrm{Im}\left[\chi_{\mathrm{m}}(\omega)\right] \\ &= S_{xx,\mathrm{F}}(\omega) = S_{\mathrm{F}}^{\mathrm{th}}(\omega)\left|\chi_{\mathrm{m}}(\omega)\right|^2,\end{aligned} \tag{3.37}$$

where $\mathrm{k_B}$ is Boltzmann's constant, and eq. 3.37 connects the mechanical motion to the temperature of the bath at $\mathrm{T_0}$. It also shows the link between the autocorrelation function of the fluctuations with the imaginary part of χ_{m} associated with dissipation. The imaginary part of $\chi_{\mathrm{m}}(\omega)$ is $\frac{1}{m}\frac{\Gamma_0\omega}{(\Omega_m^2-\omega^2)^2+\omega^2\Gamma_0^2}$ which makes $S_{\mathrm{F}}^{\mathrm{th}}(\omega) = 2\mathrm{k_B T_0}\Gamma_0 m$. The complete PSD of a mechanical oscillator in equilibrium with a thermal bath at temperature $\mathrm{T_0}$, driven by Brownian motion and damped by air collisions is:

$$S_{xx,F}(\omega) = \frac{2\mathrm{k_B T_0}}{m}\frac{\Gamma_0}{(\Omega_m^2-\omega^2)^2+\omega^2\Gamma_0^2}, \tag{3.38}$$

which has a Lorenztian-like lineshape centered at frequency Ω_{m} with a mechanical quality factor of $\mathrm{Q_m} = \frac{\Omega_{\mathrm{m}}}{\Gamma_0}$.

The link between the root mean square (RMS) thermal motion $\sqrt{\langle x^2\rangle}$ and the PSD of eq. 3.38 can be derived using the equipartition theorem. The total average energy for a 1-D oscillator in thermal equilibrium is equally distributed between the kinetic energy

$\langle \mathrm{E_k} \rangle$ and the potential energy $\langle \mathrm{E_p} \rangle$ so that $\langle \mathrm{E_{total}} \rangle = \langle \mathrm{E_k} \rangle + \langle \mathrm{E_p} \rangle = \mathrm{k_B T_0}$. Assuming the motion is periodic of the form $x \sin(\Omega_{\mathrm{m}} t + \phi)$, $\mathrm{E_k}$ and $\mathrm{E_p}$ are given by:

$$\mathrm{E_k}(t) = \frac{1}{2} m \left(\frac{\mathrm{d}x}{\mathrm{d}t} \right)^2 = \frac{m\Omega_{\mathrm{m}}^2}{2} x^2 \cos^2(\Omega_{\mathrm{m}} t + \phi), \tag{3.39}$$

$$\mathrm{E_p}(t) = \frac{1}{2} m x^2 = \frac{m\Omega_{\mathrm{m}}^2}{2} x^2 \sin^2(\Omega_{\mathrm{m}} t + \phi), \tag{3.40}$$

which leads to a total time averaged energy of:

$$\langle \mathrm{E_{total}} \rangle = \frac{m}{2} \Omega_m^2 \left\langle x^2 \right\rangle, \tag{3.41}$$

where the relationship between the peak displacement x, and the RMS displacement $\sqrt{\langle x^2 \rangle}$ is given as $x = \sqrt{\frac{\langle x^2 \rangle}{2}}$. Now, taking the integrated area under the PSD of eq. 3.38, and using the relation of eq. 3.31 with eq. 3.37:

$$\int_0^\infty S_{xx,F}(\omega)\, d\omega = \left\langle x(t)^2 \right\rangle = \lim_{t_T \to \infty} \frac{1}{t_T} \int_{-\infty}^{\infty} \left| x(\omega)^2 \right| \mathrm{d}\omega, \tag{3.42}$$

such that:

$$\begin{aligned} \left\langle x(t)^2 \right\rangle &= \frac{\mathrm{k_B T_0 \Gamma_0}}{m} \int_0^\infty \frac{1}{(\Omega_{\mathrm{m}}^2 - \omega^2)^2 + \Gamma_0^2 \omega^2} \mathrm{d}\omega \\ &= \frac{\mathrm{k_B T_0 \Gamma_0}}{m} . \frac{1}{\Gamma_0 \Omega_{\mathrm{m}}^2} = \frac{\mathrm{k_B T_0}}{k}. \end{aligned} \tag{3.43}$$

Therefore the area under the peak in the PSD, equal to $\left\langle x^2 \right\rangle$ is also equal to $\frac{\mathrm{k_B T_0}}{m\Omega_{\mathrm{m}}^2}$.

3.6 Analysis of the Thermal Motion Power Spectral Density

The optimised transduction settings found in section 3.3 are utilised to experimentally obtain a high S/N PSD using the set-up of fig. 2.23 (pg. 53) that can be analysed to find the effective mass m_{eff}, spring constant k, mechanical frequency Ω_{m}, and RMS thermal displacement $\sqrt{x^2}$. The piezo-stack is used to set the microsphere-cantilever at a coupling distance d close to the optimum $d = 150\,\mathrm{nm}$, and AOM 2 is used to red detune the transduction beam with respect to a WGM circulating in the microsphere. The transmission of the transduction beam is measured on PD 2, which is converted to displacement units using the calibration method of section 3.3.2.

3.6.1 Computing the Power Spectra Density from Data

In order to compute the PSD, a total of 30 traces of position as a function of time are sampled from the photodetector measuring the WGM transduction beam (sampling rate of 250×10^5 samples/s, 2 s length). To convert the transduction signal into the PSD the modified periodogram function in Matlab [141, 153] is used. This applies the Wiener-Khinchin relation for the sampled autocorrelation function (as opposed to the integral version). Periodogram refers to the discrete Fourier transform (DFT) performed on one segment of the time series, while modified refers to the application of a time-domain window function. The product of the chosen rectangular window and the sample autocorrelation function undergoes the FFT that results in the one-sided PSD. Averaging over all 30 traces reduces the variance of the spectral estimates.

A typical PSD is shown in fig. 3.9 where the fundamental c.o.m. mode of the microsphere-cantilever is at approximately 2.8 kHz, while a number of taper modes are observed between 0.3 kHz - 15 kHz[11].

The modes are experimentally distinguished by resonantly driving either the taper or the microsphere-cantilever (discussed later in fig. 3.10), with further evidence provided by modelling the system using the finite element modelling (FEM) package COMSOL, as discussed shortly. The spectrum of taper modes is in good agreement with those measured by [12]. Torsional modes of the tapered fibre have been studied elsewhere [136] in the 100's of kHz region. These modes are often unwanted noise peaks that are detrimental for sensing applications [12]. Cantilevers will exhibit eigenmodes with a c.o.m. mode as the fundamental bending mode, and higher order bending eigenmodes (motion transverse to the plane of the cantilever), as well as torsion modes that contain vibration along the axis of the cantilever at much higher frequency [136][12]. The primary focus in this thesis are transverse modes since the c.o.m. motion of the microsphere-cantilever can be used to characterise acceleration, as demonstrated in chapter 6.

The modes belonging to a single oscillator are usually isolated from one another in frequency space, but spectral overlap can occur between modes of 2 separate oscillators

---

[11] Taper modes above 10 kHz not shown here and those above 20 kHz are not detected due to the limited bandwidth of the photodetector. Microsphere-cantilever[$\mathcal{A}$], and taper[$\mathcal{A}$] are used in this set of data. A full list of the microsphere-cantilever dimensions are listed in section 8.4 of the appendix.

[12] Here, the torsional modes change the polarisation of the light propagating through the taper due to the strain-optic effect where the motion creates periodic refractive index variations.

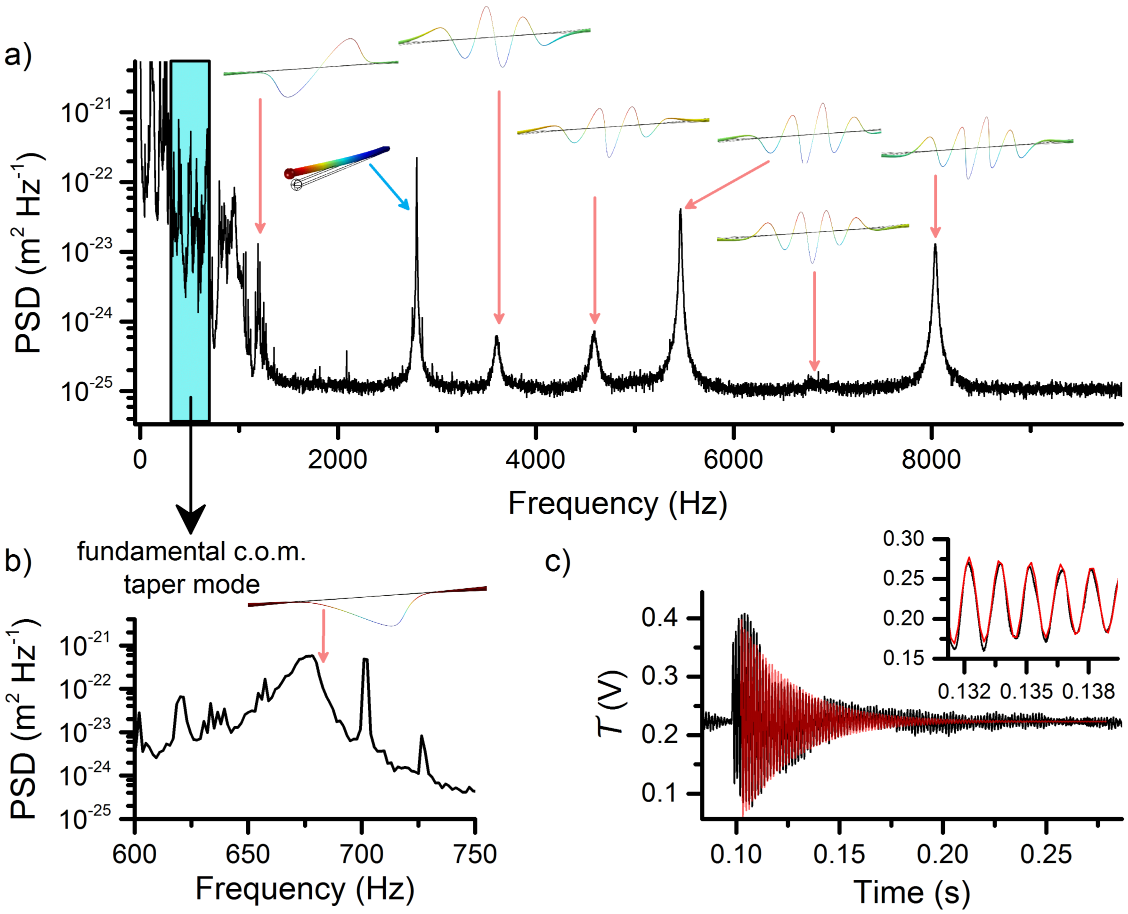

Figure 3.9: a) The full PSD from the transduction signal shows multiple mechanical modes belonging to the microsphere-cantilever or the tapered fibre, with inset images depicting the simulated mode shapes from COMSOL. b) The c.o.m. taper mode is often not probed due to excess low frequency noise, although ringdown measurments c) can identify such a mode from this noise.

when they are coupled by a light field that transduces the relative motion between them. This happens when a mode belonging to the tapered fibre and a mode of the microsphere-cantilever are close together in frequency, as is the case shown in fig. 3.10 a)[13].

The modes in fig. 3.10 can be distinguished by resonantly driving either oscillator with the actuating forces discussed in section 3.4. The microsphere-cantilever is sinusoidally shaken using the piezo-stack attached to the clamped end (fig. 3.10 b) black data), whereas the lighter thinner taper is actuated by sinusoidally modulating the CEODF (fig. 3.10 b) blue data).

The microsphere-cantilever and the tapered fibre are in theory, circular in cross-section and should possess orthogonal modes of vibration with identical resonances. Due to fabrication errors such as unequal heating in the taper pulling rig, or lopsided melting of the microsphere on the cantilever, mode splitting can sometimes be seen in the PSD as a

---

[13] Microsphere-cantilever[$\mathcal{C}$] and taper[$\mathcal{C}$], see section 8.4 in the appendix for dimensions.

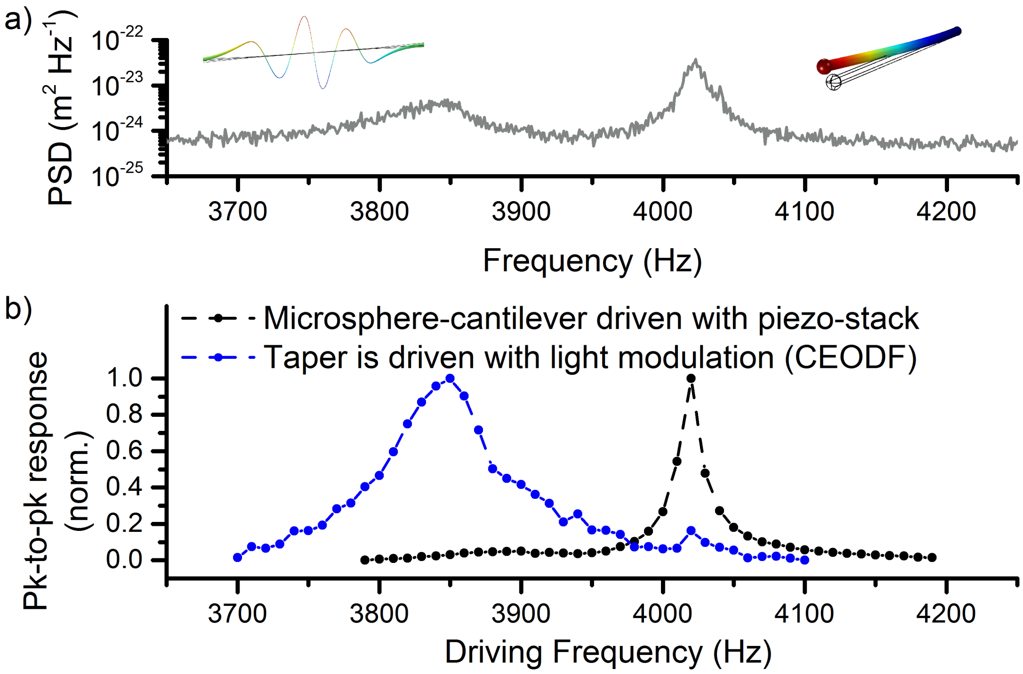

Figure 3.10: a) Since the WGM is sensitive to the relative motion between microsphere-cantilever[$\mathcal{C}$] and tapered fibre[$\mathcal{C}$], mechanical modes belonging to both will be present in the PSD. b) Identification of two spectrally overlapped modes is achieved by resonantly driving either oscillator.

sideband, although often only at low pressures. Such mode splitting is seen in asymmetric cross-sectional geometry cantilevers when the dimensional variance is as low as 2% [154], such as irregular hexagonal nanowires. Mode splitting of mechanical taper modes are seen in [155] and a clamped-clamped SiN string [84] and may have benefits for 2-D inertial sensing, due to cross axis coupling.

3.6.2 Signal-to-noise Ratio & Derived Mechanical Properties

The figure of merit for transduction (S/N) is defined for the PSD as:

$$\mathrm{S/N} = 10\log_{10}\frac{S_{\mathrm{det},xx}(\Omega_{\mathrm{m}})}{S^{\mathrm{imp}}_{\mathrm{det},xx}(\omega)}, \tag{3.44}$$

where $S_{\mathrm{det},xx}(\Omega_{\mathrm{m}})$ is the peak of the detected PSD at the mechanical frequency, Ω_{m}, and $S^{\mathrm{imp}}_{\mathrm{det},xx}(\omega)$ is the measurement imprecision which is the background noise level. The S/N for the mechanical modes that are feedback cooled in chapter 4 are shown in fig. 3.11 for zero feedback, with a S/N of 25.2 ± 0.7 dB for the c.o.m. microsphere-cantilever mode (at atmospheric pressure) and 27.5 ± 1.6 dB for the higher order taper mode (at 0.5 mbar).

The S/N compare well to other transduction set-ups such as WGM coupling to the

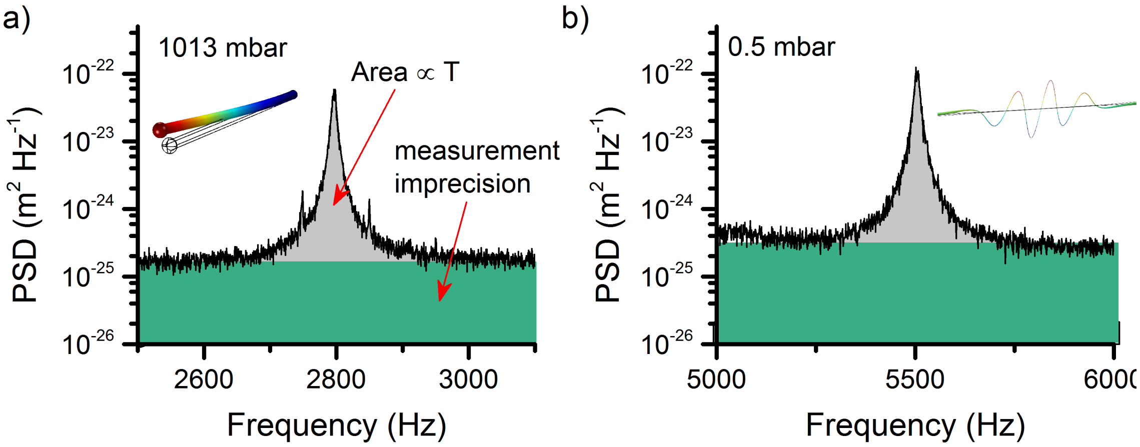

Figure 3.11: At the optimised transduction settings, the PSD is computed for the two primary modes cooled in chapter 4 belonging to a) microsphere-cantilever[$\mathcal{A}$] and b) tapered fibre[$\mathcal{B}$]. The S/N is the ratio of the peak height at Ω_{m} to the measurement imprecision.

radial breathing modes of a toroid which achieved S/N$\approx$ 20 dB [149]. The S/N could be improved to 60 dB using shot-noise limited light to lower $S^{\mathrm{imp}}_{\mathrm{det},xx}(\omega)$ as in [46], where the sensitivity reaches 10^{-18} m Hz$^{1/2}$, which would be sufficient to detect fluctuations near the ground state.

The mechanical frequency, effective mass, RMS thermal fluctuation, spring constant and mechanical quality factor can be extracted from the PSDs of fig. 3.11 by measuring the integrated area under the curve, the peak height at $\omega = \Omega_{\mathrm{m}}$, and the FWHM. Determining the mechanical properties of mechanical oscillators is crucial for characterising their behaviour as an inertial sensing test-mass (chapter 6), calculating the lowest possible feedback cooled temperature (chapter 4), as well as assessing the feasibility for ground state cooling (chapter 5 and chapter 7).

Mechanical Frequencies

It can be seen in a typical PSD such as fig. 3.9 that multiple mechanical peaks are detected. Aside from the experimental identification of the modes through resonant driving, as conducted earlier in this chapter, each mechanical peak can be identified by calculating the expected eigenfrequencies. For the microsphere-cantilever this can be achieved using a simple analytical model, whereas for complex geometries like the tapered fibre, finite element modelling (FEM)[14] is required.

Since the total mass of the cantilever is 1.39×10^{-7} kg and the microsphere is 6.39×10^{-9} kg, both loads must be analysed to find the c.o.m. mechanical resonance frequency.

---

[14] COMSOL is used in this thesis.

The following analysis to predict the eigenfrequencies of the microsphere-cantilever uses the method of superposition that states the total deflection (eigenfrequency) is the sum of the deflections caused by individual loads. The microsphere-cantilever is therefore split into two sub-units. The microsphere is modelled as a point mass equal to $m_s = \frac{4}{3}\pi a^3 \rho$, where a is the radius and ρ is the density of silica ($\rho = 2200\,\mathrm{kg\,m^{-3}}$), which is attached to a massless clamped rod of length L. The cantilever is modelled as a symmetrical beam with uniform cross section, of length L, and uniform distributed mass, defined by $m_c = AL\rho$, where A is the cross-sectional area. The superscript * denotes parameters calculated for the individual sub-units.

The deflection of the massless rod when the microsphere is subjected to a load is fully derived in chapter 6 section 6.3. The deflection at the free-end is given as:

$$y^*(L) = \frac{m_s \mathrm{g} L^3}{3\mathrm{EI}}, \tag{3.45}$$

where g is the acceleration from gravity, $\mathrm{E} = 73.1\,\mathrm{GPa}$ is the elastic modulus (Young's modulus) of silica, and $\mathrm{I} = \frac{\pi \oslash_c^4}{64}$ is the second moment of area for a uniform circular cross-section beam, where $\oslash_c$ is the diameter of the cantilever. Using Hooke's law for a linear spring, $\mathrm{F} = ky(L)$, where F is also equal to $m\mathrm{g}$, and eq. 3.45, the spring constant, k is:

$$k^* = \frac{3\mathrm{EI}}{L^3}, \tag{3.46}$$

which can be used in the relation $\Omega_\mathrm{m} = \sqrt{\frac{k}{m}}$, to derive the eigenfrequency:

$$\Omega^*_\mathrm{m} = \sqrt{\frac{3\mathrm{EI}}{m_s L^3}}. \tag{3.47}$$

The cantilever sub-unit is modelled using the dynamic beam equation (Euler-Lagrange equation) to find the transverse eigenfrequencies [156]. Cantilevers have a restoring force due to the bending rigidity and the equation of motion can be calculated using Euler-Bernoulli theory of beams[15] [140]. This states the Euler-Lagrange equation as:

$$-\mathrm{EI}\frac{\partial^4 y}{\partial x^4} = \rho A \frac{\partial^2 y}{\partial t^2}. \tag{3.48}$$

The left hand term represents the potential energy due to internal forces and the right

---

[15] This theory is a simplification of the linear theory of elasticity which can calculate the load-carrying and deflection of beams subjected to lateral loads. For more information see chapter 6.

hand term is the kinetic energy.

The solution for eq. 3.48 can be found in textbooks [156] and solves the eigenvalue problem using a change in parameter $\kappa^4 = \frac{A\omega_n^2\rho}{\mathrm{EI}}$ (where ω_n are the mechanical eigenfrequencies):

$$\frac{\mathrm{d}^4X}{\mathrm{d}x^4} = \kappa^4X. \tag{3.49}$$

The solution is of the form:

$$\begin{aligned} X =& E(\cos(\kappa x) + \cosh(\kappa x)) + B(\cos(\kappa x) - \cosh(\kappa x)) + \\ & + C(\sin(\kappa x) + \sinh(\kappa x)) + D(\sin(\kappa x) - \sinh(\kappa x)). \end{aligned} \tag{3.50}$$

The constants E, B, C, D are found using boundary conditions for a clamped-free cantilever of length L, which are:

- Deflection is 0 at the clamped end $X = 0$
- Slope is 0 at the clamped end $\frac{\mathrm{d}X}{\mathrm{d}x} = 0$
- Moment is zero at the free end $\frac{\mathrm{d}^2X}{\mathrm{d}x^2} = 0$
- Shear is zero at the free end $\frac{\mathrm{d}^3X}{\mathrm{d}x^3} = 0$

This results in the relation:

$$\frac{D}{B} = -\frac{\cos(\kappa L) + \cosh(\kappa L)}{\sin(\kappa L) + \sinh(\kappa L)} = \frac{(\sin\kappa L) - \sinh(\kappa L)}{\cos(\kappa L) + \cosh(\kappa L)}, \tag{3.51}$$

so that $\cos(\kappa L) \times \cosh(\kappa L) = -1$. The values of κL that satisfy this are found using tables of hyperbolic and trigonometric functions. The first two are $\kappa_1 L = 1.875$ and $\kappa_2 L = 4.694$. Since $\kappa^4 = \frac{A\omega_n^2\rho}{EI}$, the mechanical frequencies of the cantilever beam are thus:

$$\omega_n^* = (\kappa_n L)^2\sqrt{\frac{\mathrm{EI}}{\rho A L^4}}, \tag{3.52}$$

where A is the cross-sectional area of the cantilever. The c.o.m. frequency is:

$$\Omega_{\mathrm{m}}^* = (1.875)^2\sqrt{\frac{\mathrm{EI}}{\rho A L^4}}. \tag{3.53}$$

Combining the sub-unit eigenfrequencies given by eqs. 3.47 & 3.53 gives the c.o.m.

eigenfrequency of the total microsphere-cantilever system:

$$\Omega_{\mathrm{m}} = \sqrt{\frac{3\mathrm{EI}}{(0.2235\rho AL + m_{\mathrm{s}})L^3}}. \tag{3.54}$$

The first two mechanical frequencies calculated using eq. 3.54 for microsphere-cantilever[$\mathcal{A}$] used in chapter 4 (these modes will be cooled) are presented in table 3.2 alongside the experimentally measured values, and those obtained through FEM. The error between the measured frequencies and the predicted frequencies is low due to the large size of the microsphere-cantilever, whose dimensions can be easily measured. Uncertainty regarding the symmetry of the microsphere-cantilever and the refractive index is the main source of error.

Method	Fundamental mode (Hz)	Second eigenmode (Hz)	% Error with Measured Mode 1, Mode 2
Using eq. 3.54	2899	18,174	3.7, 2.5
FEM	2885	18,142	3.2, 2.3
Measured	2795 ± 0.06	$17,732 \pm 2$	-

Table 3.2: Comparison of the resonance frequency of the first two mechanical modes of microsphere-cantilever[$\mathcal{A}$] studied in chapter 4, obtained through eq. 3.54, FEM and experimentally measured.

FEM solves eq. 3.48 for any geometry by splitting the structure into elements called a mesh. The equations are solved for each mesh dependent on the surrounding elements and takes into account the boundary conditions defined by geometry and clamping. The smaller the mesh element the more accurate the results but at a cost of longer processing time. FEM eigenfrequency analysis can output the eigenmode shapes (defection via the strain field, shown as inset pictures in fig. 3.11) by finding the mechanical eigenvectors.

The changing cross section of the tapered fibre causes a non-uniform distribution of mass that cannot be easily incorporated into an expression like eq. 3.1. FEM must be used to indicate the mechanical eigenfrequencies, and those obtained for tapered fibre[$\mathcal{B}$] studied in chapter 4 are shown in table 3.3. The FEM predicted values for the mechanical taper frequencies can deviate by over 10% in table 3.3, due to errors associated with measuring the taper dimensions, non-inclusion of tension, and the approximation of the taper profile as symmetrical. As shown in chapter 2 fig. 2.4, tapers are usually not symmetrical, and tension is often utilised to eliminate bends that form during tapering.

Mode No.:	1	2	3	4	5	6	7	8	9
Measured	514	937	1201	2162	2654	3419	3878	5504	6877
FEM	426	864	1535	2268	2918	3428	4160	5256	6549
Error %	17	8	28	5	10	0.3	7	5	5

Table 3.3: Comparison of the measured and FEM modelled resonance frequencies of the first 9 transverse mechanical modes of tapered optical fibre[$\mathcal{B}$].

Thermal Motion, Spring Constant & Effective Mass

In fig. 3.9 the PSD revealed a spectrum of mechanical modes. The figure of merit that determines the importance of each mode on the total response of the oscillator is known as the modal effective mass m_{eff}[16]. Only a fraction of the total oscillator mass is involved in its motion per mode so a high m_{eff} implies a high reaction force when the structure is excited, useful for acceleration sensing as in chapter 6. The modes with the largest m_{eff} in each axis determine the overall response of the system along that axis, therefore the sum of all m_{eff} (per axis) equals the total mass [157].

The relationship between m_{eff}, the spring constant k, and the thermal motion $\langle x^2 \rangle$, can be derived considering equipartition theory and the PSD. The low frequency (D.C.) response of the microsphere-cantilever is governed by the mechanical susceptibility at $\omega = 0$: $\chi_{\text{m}}(0) = (m_{\text{eff}}\Omega_m^2)^{-1} = 1/k$ where k is the spring constant and can be re-arranged such that the effective mass is:

$$m_{\text{eff}} = \frac{k}{\Omega_{\text{m}}^2}. \tag{3.55}$$

This can be used in the equipartition theorem of eq. 3.41 to form:

$$k \left\langle x^2 \right\rangle = \text{k}_{\text{B}}\text{T}_0, \tag{3.56}$$

where k_{B} is Boltzmann's constant, and T_0 is the temperature of the surroundings. Therefore the RMS thermal motion and spring constant are related by:

$$\sqrt{\langle x^2 \rangle} = \sqrt{\frac{k_{\text{B}} T_0}{k}}. \tag{3.57}$$

The area under the PSD is equal to $\left\langle x^2 \right\rangle$ from eq. 3.43 derived previously. Therefore one can find the thermal motion $\left\langle x^2 \right\rangle$, k, and m_{eff}. The calculated values are shown in table. 3.4 for the first 2 microsphere-cantilever modes, and the 2 higher order taper modes

---

[16] All references to m prior to this section, unless identified as the total mass refer to this effective mass, which will now be used for the duration of the thesis.

that are cooled in chapter 4.

Mode	$\sqrt{\langle x^2 \rangle}$ (m) $\times 10^{-11}$	k (N/m)	m_{eff} (kg) $\times 10^{-9}$
Microsphere-cantilever mode 1	2.57 ± 0.43	6.26 ± 2.1	20.2 ± 0.7
Microsphere-cantilever mode 2	0.71 ± 0.12	82.8 ± 28.0	6.67 ± 2.26
Taper mode 8 (0.5 mbar)	4.90 ± 0.83	1.73 ± 0.58	1.44 ± 0.49
Taper mode 9 (0.5 mbar)	2.59 ± 0.44	6.15 ± 2.07	3.30 ± 1.11

Table 3.4: The experimentally calculated RMS thermal motion $\sqrt{\langle x^2 \rangle}$, spring constant k and effective mass m_{eff} of the four modes cooled in chapter 4 belonging to microsphere-cantilever[$\mathcal{A}$] and taper[$\mathcal{B}$].

Mechanical Quality Factor

The mechanical quality factor describes the dissipation of energy within a resonant element, defined as $\mathrm{Q_m} = \frac{\Omega_\mathrm{m}}{\Gamma_0}$, and has a inverse relationship with bandwidth. The $\mathrm{Q_m}$ for the four modes in table. 3.4 are calculated and shown in table 3.5, measured at atmospheric pressure unless stated, and with no active damping. The $\mathrm{Q_m}$ of the taper modes are measured at 0.5 mbar since cooling of these modes in chapter 4 is not efficient until the pressure is lowered, increasing $\mathrm{Q_m}$. The relationship between $\mathrm{Q_m}$ and pressure is experimentally measured in the next section. Values of $\mathrm{Q_m}$ in the 100's are low compared to those obtained in optical traps [158], SiN beams [84] or microlevers [137]. A high $\mathrm{Q_m}$ results in a larger transduced S/N. If the mechanical oscillator is used as a sensor to detect forces that shift the mechanical frequency, a low $\mathrm{Q_m}$ limits the sensitivity by broadening the linewidth [157]. However, for sensing inertial forces such as acceleration, a high $\mathrm{Q_m}$ results in a longer ring down time and may be detrimental for systems experiencing shocks or transient excitations. This is one motivation for implementing the active feedback shown in chapter 4.

Mode	$\mathrm{Q_m}$
Microsphere-cantilever mode 1	370 ± 3
Microsphere-cantilever mode 2	642 ± 16
Taper mode 8 (0.5 mbar)	381 ± 4
Taper mode 9 (0.5 mbar)	509 ± 5

Table 3.5: The mechanical quality factor $\mathrm{Q_m}$ of the four modes to be cooled in chapter 4 belonging to microsphere-cantilever[$\mathcal{A}$] and taper[$\mathcal{B}$]. The measurement of $\mathrm{Q_m}$ is taken when no active feedback is applied.

The importance of $\mathrm{Q_m}$ for cooling to the mechanical ground state is discussed in chapter 5 and chapter 7, however, two points are briefly covered here. Firstly, the cooled mode temperature $\mathrm{T_{eff}}$, is defined by the initial $\mathrm{Q_m}$ via $\mathrm{T_{eff}} = \mathrm{T_0}\frac{\mathrm{Q_m}}{\mathrm{Q_{eff}}}$, where $0 < Q_{\mathrm{eff}} < \mathrm{Q_m}$ is the damped mode quality factor [159]. Secondly, $\mathrm{Q_m}$ is related to the rate that a ground state cooled oscillator heats up since the average phonon number evolves as $\frac{\mathrm{d}\langle n\rangle}{\mathrm{d}t} = -\Gamma_0[\langle n\rangle - n_{th}]$, where $\langle n\rangle$ is the average phonon occupancy, n_{th} is the initial thermal phonon occupancy, and Γ_0 is the thermal damping rate. An oscillator in the ground state $\langle n\rangle = 0$ at $t = 0$ heats up with a time dependence of $\langle n\rangle(t) = n_{th}(1 - e^{-t/\Gamma_0})$. Therefore the rate that the mechanical oscillator leaves the ground state is given by $\frac{d\langle n(t=0)\rangle}{\mathrm{d}t} = n_{th}\Gamma_0 \approx \frac{\mathrm{k_B T_0}}{\hbar\Omega_\mathrm{m}}\Gamma_0 = \frac{\mathrm{k_B T_0}}{\hbar \mathrm{Q_m}}$ [14], which sets a timescale for performing quantum experiments.

There are two types of damping that limit $\mathrm{Q_m}$: intrinsic and extrinsic. Each dissipation process contributes independently to the overall mechanical losses as $\frac{1}{\mathrm{Q_m}} = \sum_i \frac{1}{\mathrm{Q_i}}$. Extrinsic damping occurs primarily due to losses from air collisions (discussed later) as well as clamping losses via acoustic coupling to the supports [157], and phonon tunnelling [160].

Intrinsic damping can be divided into the dissipation in a perfect crystal lattice and that in a real, imperfect crystal with bulk and surface defects. The upper limit to $\mathrm{Q_m}$ is set by the fundamental losses in a perfect crystal which include thermoelastic damping from anharmonic coupling between mechanical modes and the phonon reservoir, and losses due to electron-phonon and phonon-phonon interactions [157]. The latter effect is caused by the interaction between oscillatory sound waves and thermal phonons. The thermoelastic effect arises from thermal currents generated by vibratory volume changes in an elastic media with a non-zero thermal expansion coefficient [161]. Additional imperfections introduce further losses such as surface defects due to adsorbates which decrease $\mathrm{Q_m}$. However, these are only important when surface losses are dominant, which is not the case for the system in this thesis, as seen in the next section.

3.7 Influence of Air Damping on the Mechanical Quality Factor

The most dominant source of damping comes from the surrounding environment in the form of air molecules colliding with the surface of the mechanical oscillator. There are 3 regions of different damping behaviour when the pressure is decreased from atmospheric pressure, named after the dominant damping mechanism in each region:

- $<$ 0.01 mbar (Intrinsic region): damping due to air is negligible compared to the intrinsic damping of the structure itself. Q_m becomes independent on pressure but other sources of damping such as anchor loss (waves that travel to the clamping/substrate via a tether are considered lost energy), and surface damping (caused by defects or surface stress i.e. due to coatings) will dominate.
- 0.01 mbar → 10 mbar (Molecular, or Knudsen region): Damping is caused by independent collisions of non-interacting air molecules with the surface of the microsphere-cantilever. The mean free path of gas molecules is larger than the device dimensions.
- $>$ 10 mbar (Viscous region): The air acts as a viscous liquid with a drag force calculated using fluid mechanics. Q_m changes very slowly when the pressure is changed.

When no external forces are applied (i.e. no active damping), the microsphere-cantilever (and tapered fibre) is in thermal equilibrium with the surrounding gas. The drag force exerted by the gas contains a velocity proportional term that causes dissipation, which depends on pressure. Lowering the pressure decreases the number of collisions, increasing Q_m, and decouples the oscillator from its thermal bath environment. To understand the influence of pressure on Q_m, the system is pumped down incrementally whilst the PSD of the transduction beam transmission is recorded. The mechanical frequency Ω_m, and the damping rate Γ_0 of the c.o.m. mode of microsphere-cantilever[$\mathcal{A}$] (Ω_m=2.8 kHz) and the 8th eigenmode of taper[$\mathcal{A}$] (Ω_m=5.5 kHz) (both studied in chapter 4), obtained from the PSDs, is measured to infer Q_m, plotted in fig. 3.12.

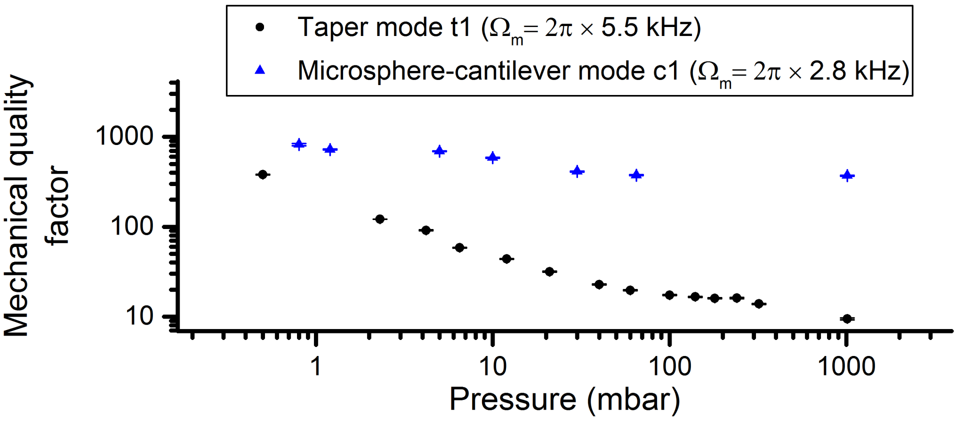

Figure 3.12: The influence of the surrounding pressure on the mechanical quality factor of the c.o.m. of the microsphere-cantilever[$\mathcal{A}$] (blue) and the 8th mode of the tapered fibre[$\mathcal{B}$] (black), both are studied in chapter 4.

Both sets of data in fig. 3.12 show a distinct change in shape around 10 mbar, in good agreement with literature [162], and indicates the system leaving the viscous regime (little change in $\mathrm{Q_m}$ with pressure), and entering the molecular regime. The change in $\mathrm{Q_m}$ for the microsphere-cantilever mode is less than a factor of 2 whereas the taper mode experiences a 40 times increase in $\mathrm{Q_m}$ at low pressure. Such a difference is attributed to the different size and clamping geometries.

It should be noted that if a different background gas is used with a lower molar mass, and the experiment is conducted at a pressure between atmospheric pressure and 0.1 mbar, the $\mathrm{Q_m}$ could be more than doubled when compared to $\mathrm{Q_m}$ at the same pressure in air, as demonstrated in [163]. This is because gas damping is dependent on the RMS speed of the gas molecules which is proportional to $M^{-1/2}$, where M is the molar mass. The damping is also dependent on the density of the gas which varies with M, therefore $\mathrm{Q_m}$ scales with $1/\sqrt{M}$, and will be larger in an environment of helium than in air[17].

The intrinsic region is not reached for either oscillator because the vacuum pressure could not be lowered beyond 0.5 mbar due to vibrations from the vacuum pumps that excite the mechanical modes and distort the PSD lineshape. This often causes the tapered fibre to touch the microsphere-cantilever. The roughing pump, which lowers the pressure to 0.5 mbar, also produces low frequency noise that excite nearly all the low frequency mechanical modes, shown in fig. 3.13 a).

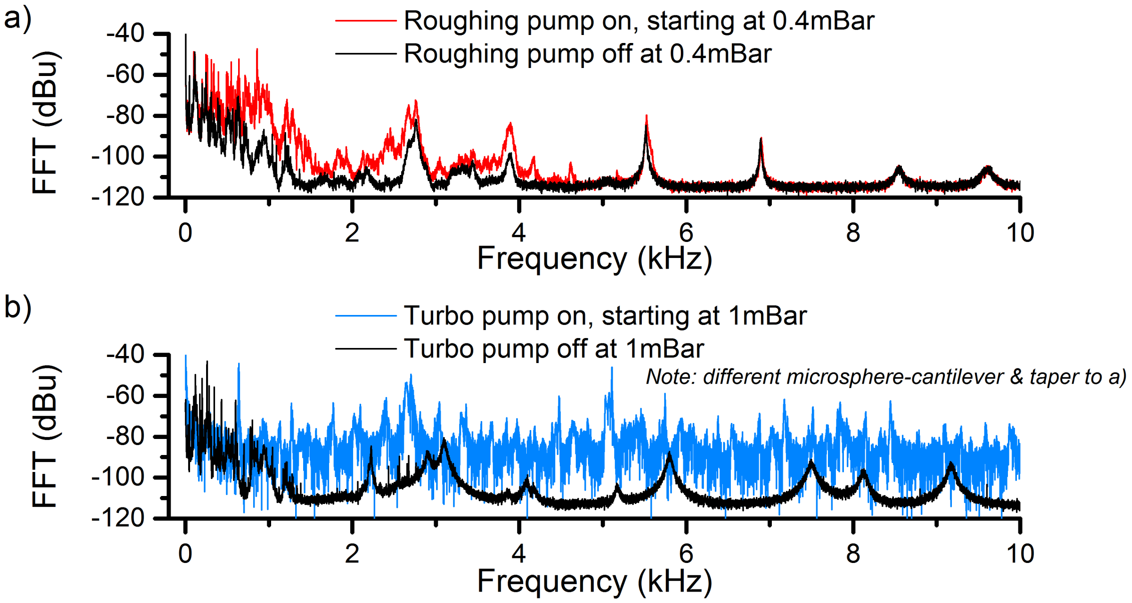

Figure 3.13: The effect of continuous pumping on the PSD from a) the roughing pump using microsphere-cantilever[$\mathcal{B}$] and taper[$\mathcal{B}$]. b) shwows the effect of switching on the the turbo pump using microsphere-cantilever[$\mathcal{D}$]. Both pumps induce extraneous vibrations that are transduced.

---

[17] The molar mass of helium is approximately 7 times smaller than that of air.

To prevent this excitation from influencing the results of this thesis, the pump is always switched off momentarily to capture data, before being switched back on to counteract leakages. Switching on the turbo pump to further lower the pressure resulted in significantly more noise, exciting many mechanical modes across a wide bandwidth of frequencies, fig. 3.13 b). The taper used in fig. 3.13 b) melted soon after the turbo pump is switched on due to less air collisions to conduct heat away. This issue could not be resolved within the experimental time frame and the turbo pump is not used in the later chapters, such that 0.5 mbar is the minimum obtainable pressure.

The sensitivity to environmental vibrations i.e. from the pumps, reiterates the suitability of the system as an accelerometer, the subject of chapter 6.

3.8 Quantum Measurement of Motion

This last section pivots the discussion towards the absolute limit of transducing motion using optical fields. As shown in fig. 3.11, the imprecision noise defines the displacement sensitivity, which can be improved by lowering the noise floor. In chapter 4 it is shown the imprecision noise is classical electronic noise, and limits the cooled mode temperature.

If all classical noise is removed, the ultimate limit in detecting displacement is governed by quantum theory. Here, the fluctuations of both the mechanical oscillator, and the optical field coupled to its mechanical motion, must be reduced to their respective quantum fluctuations[18]. The laws of quantum mechanics dictates that there is still random motion, known as the zero point fluctuations (ZPF) that persist due to Heisenberg's uncertainty relation governing the limit of simultaneously measuring position and momentum. Since the preceding PSDs (e.g. fig. 3.9) have background noise levels around $\sqrt{10^{-25}}\,\mathrm{m\,Hz^{-1/2}}$, the noise of the WGM transduction signal is over 1000 times above sensitivities required to measure ZPF, rendering the system incapable of resolving this quantum effect. To lower the imprecision, electronic noise must be reduced using low noise amplifiers and photodetectors, and excess fluctuations of the light itself can be noise cancelled to reach the vacuum fluctuations (i.e. shot-noise limited light) of the electromagnetic field [165].

In this regime the classical PSD cannot be used for analysis since it implies no noise or fluctuations at $T_{\mathrm{eff}} = 0$, which is infeasible, and reveals nothing about the influence of

---

[18] As shown in chapter 4, the classical thermal noise of the mechanical oscillator can also be reduced, with active feedback methods theoretically predicted to cool to the quantum ground state when stringent detection criteria are met [164].

measuring motion with light. In order to find the ultimate displacement sensitivity, the quantum noise spectra is required instead.

3.8.1 Zero Point Fluctuations

Heisenberg's uncertainty principle determines the existence of motional fluctuations, known as zero point fluctuations (ZPF), even at the zero point energy of a mechanical oscillator. The ZPF in units of displacement is:

$$x_{\mathrm{zpf}} = \sqrt{\frac{\hbar}{2m_{\mathrm{eff}}\Omega_{\mathrm{m}}}}, \tag{3.58}$$

which is derived in section 8.2 of the appendix. Any (non-perturbing) measurement that simultaneously measures both position and momentum with equal precision is limited to the ZPF.

The PSD of ZPF is intrinsically quantum. Quantum noise is special because:

- Classically a system at zero-temperature has no noise, but quantum mechanics predicts fluctuations (ZPF).
- Since $\hat{x}(t)$ and $\hat{x}(t')$ do not need to commute, the autocorrelation function can be complex and $S^*_{xx}(-\omega) \neq S^*_{xx}(\omega)$ (The superscript * denotes the double sided spectrum) whereas classical noise spectral densities are always real and symmetrical.
- Heisenberg constraints are imposed with no classical counterpart.

To derive the PSD of the ZPF, the relation between the PSD $S^*_{xx}(\omega)$ and the autocorrelation function $G_x(t)$, $S^*_{xx}(\omega) = \int_{-\infty}^{\infty} G_x(t)e^{-i\omega t}\,\mathrm{d}t$, is applied. $G_x(t)$ is derived in section 8.2 of the appendix, such that the double sided spectral density is:

$$S^*_{xx}(\omega) = 2\pi x^2_{\mathrm{zpf}} \left\{ \bar{n}\delta(\omega + \Omega_{\mathrm{m}}) + (\bar{n}+1)\delta(\omega - \Omega_{\mathrm{m}}) \right\}, \tag{3.59}$$

where $\bar{n}$ is the average phonon occupancy of the mechanical oscillator, and δ is the Dirac delta function. This PSD is clearly asymmetrical around $\omega = 0$. In the high temperature limit $\mathrm{k_B T_0} >> \hbar\Omega_{\mathrm{m}}$, where $\bar{n} \approx \bar{n} + 1 \approx \frac{\mathrm{k_B T_0}}{\hbar\Omega_{\mathrm{m}}}$, a symmetric PSD is created: $S^*_{xx}(\omega) = \frac{\pi k_{\mathrm{B}}T}{m_{\mathrm{eff}}\Omega^2_{\mathrm{m}}} \left\{ \delta(\omega + \Omega_{\mathrm{m}}) + \delta(\omega - \Omega_{\mathrm{m}}) \right\}$ (derived in section 8.2 of the appendix), which is equivalent to the classical PSD. The positive frequency part of eq. 3.59 is related to the absorption of energy into the oscillator and the negative frequency part is the emission of energy by the oscillator. At the ground state the oscillator can only absorb energy.

For weak damping Γ_0, eq. 3.59 can be written with the delta function replaced by a Lorentzian (assuming the oscillator frequency is still sharply defined) [144], and the equivalent one-sided PSD (which is what a detector measures) is given by:

$$S_{n,xx}(\omega) = x_{\mathrm{zpf}}^2(2\bar{n}+1)\frac{\Gamma_0/2}{(|\omega|-\Omega_m)^2+(\Gamma_0/2)^2}, \tag{3.60}$$

using the definition of the one-sided PSD $S_{xx}(\omega) = \frac{1}{2}[S_{xx}^*(\omega) + S_{xx}^*(-\omega)]$.

When $\bar{n} = 0$ the PSD of the ZPF at the mechanical frequency is:

$$S_{n=0,xx}(\Omega_\mathrm{m}) = x_{\mathrm{zpf}}^2\frac{2}{\Gamma_0} = \frac{\hbar}{m_{\mathrm{eff}}\Gamma_0\Omega_\mathrm{m}}. \tag{3.61}$$

However, when light is used to measure the motion of a highly damped oscillator with $\bar{n}$ phonons, the output PSD of the light will contain the Lorentzian of eq. 3.60 but with additional imprecision and backaction noise due to quantum fluctuations of the light itself. Backaction noise heats the oscillator, and can prevent reaching $\bar{n} = 0$. The next section derives these additional noise contributions.[19]

3.8.2 Detection at the Standard Quantum Limit

Light as a detector can be represented as a black box with an input port that couples to the signal source (the mechanical oscillator), and the output port used to access the transduced signal. The total noise of this detection system will have noise added to the output from the light itself, as well as backaction noise feeding back to the mechanical oscillator that affects its motion. The quantum noise of coherent light is described in section 8.2 of the appendix, but can be summarised as phase noise (referred to as shot noise here), S_{SN}, and radiation pressure backaction noise, S_{RP}, which scale with $1/\sqrt{n_p}$ and $\sqrt{n_p}$, respectively.

If quantum limited light is used to measure displacement, the equivalent background noise floor (imprecision) in units of $\mathrm{m}^2\,\mathrm{Hz}^{-1}$ is given by $S_{\mathrm{imp,xx}}$ (equivalent to S_{SN}). The radiation backaction noise $S_{\mathrm{BA,xx}}$ (equivalent to S_{RP}), simultaneously heats the mechanical oscillator. Heisenberg's uncertainty relation bounds $\sqrt{S_{\mathrm{BA,xx}}S_{\mathrm{imp,xx}}} \geq \frac{\hbar}{2}$. Therefore, a

---

[19] It should be noted that the quantum PSD for the quantised mechanical oscillator is related to its classical counterpart through the relation $\bar{n} = \left(e^{\frac{\hbar\omega}{\mathrm{k_B T_0}}} - 1\right)$. For high bath temperature $\mathrm{T_0}$, $\bar{n} \approx \frac{\mathrm{k_B T_0}}{\hbar\omega} - 1/2$, the PSD of the thermal force is equal to $\frac{S_{n,xx}}{|\chi(\omega)|^2}$. At the mechanical resonance this equals $2\mathrm{k_B T_0} m_{\mathrm{eff}}\Gamma_0$ which agrees with that derived classically [2].

measurement may have an imprecision below the ZPF of the mechanical oscillator, but Heisenberg's uncertainty principle dictates that there is an associated radiation pressure noise that imparts a momentum kick, and will limit detection of the ZPF as it heats the mechanical oscillator[20].

The combination of a cooled oscillator ($\bar{n} = 0$), plus a quantum limited light source provides the ideal measurement sensitivity. The backaction noise can be represented by a force F_{BA}, which limits the response of the oscillator by causing an additional displacement of $x_{\mathrm{BA}}(\omega) = \chi_{\mathrm{m}}\mathrm{F}_{\mathrm{BA}}(\omega)$, where the mechanical susceptibility is $\chi_{\mathrm{m}} = \frac{1}{m_{\mathrm{eff}}}\frac{1}{\Omega_{\mathrm{m}}^2-\omega^2-i\Gamma_0\omega}$ as before. The total noise PSD is given by:

$$\begin{aligned} S_{\mathrm{det},xx}(\omega) =& S_{n=0,xx}(\omega) + \frac{|\chi_{\mathrm{m}}(\omega)|^2}{2}(S^{*}_{\mathrm{BA},xx}(+\omega) + S^{*}_{\mathrm{BA},xx}(-\omega)) \\ &+ \frac{1}{2}(S^{*}_{\mathrm{imp},xx}(+\omega) + S^{*}_{\mathrm{imp},xx}(-\omega)), \end{aligned} \tag{3.62}$$

where the first term is the ZPF of the oscillator, the second term is the backaction noise and the third term the measurement imprecision of the quantum light source. Since $S_{\mathrm{imp},xx}S_{\mathrm{BA},xx}$ is bounded by $\hbar^2/4$ [144], the latter two terms of eq. 3.62, i.e. the total minimum added noise, is:

$$S_{\mathrm{min},xx}(\omega) = |\chi_{\mathrm{m}}(\omega)|^2 S_{\mathrm{BA},xx}(\omega) + \frac{\hbar^2}{4S_{\mathrm{BA},xx}(\omega)}, \tag{3.63}$$

which for a quantum limited light source corresponds to the standard quantum limit (SQL). It should be noted that eq. 3.63 is a function of frequency, which is why imprecision can be obtained below the SQL at frequencies far from the mechanical resonance [166]. However, one is usually concerned with minimising this noise on-resonance ($\omega = \Omega_{\mathrm{m}}$). This occurs when $S_{\mathrm{BA},xx}(\Omega_{\mathrm{m}}) = \frac{\hbar}{2|\chi_{\mathrm{m}}(\Omega_{\mathrm{m}})|} = \frac{\hbar}{2}m_{\mathrm{eff}}\Omega_{\mathrm{m}}\Gamma_0$. Inserting the expressions for $S_{n=0,xx}$, $S_{\mathrm{imp},xx}$, and $S_{\mathrm{BA},xx}$ into the total detector PSD (eq. 3.62) forms:

$$S_{\mathrm{det},xx}(\omega) = x_{\mathrm{zpf}}^2\frac{\Gamma_0/2}{(|\omega|-\Omega_m)^2+(\Gamma_0/2)^2} + \frac{\hbar}{2}\left(\frac{|\chi_{\mathrm{m}}(\omega)|^2}{|\chi_{\mathrm{m}}(\Omega_m)|} + |\chi_{\mathrm{m}}(\Omega_m)|\right), \tag{3.64}$$

---

[20] When the light is detuned, this backaction can present itself as dynamical backaction, described in this thesis as passive cooling which is discussed in chapter 5. The role of radiation pressure backaction was studied in the taper coupled microsphere-cantilever system by increasing the laser power from 10 μW to approximately 800 μW, with no measurable change in the linewidth or peak amplitude in the PSD. Therefore the assumption of using classical PSDs in chapter 4 is valid.

where the last two terms equal the SQL, optimised for minimum noise at Ω_m:

$$S_{\mathrm{SQL},xx}(\omega) = \frac{\hbar}{m_{\mathrm{eff}}\sqrt{(\Omega_\mathrm{m}^2-\omega^2)^2+\Gamma_0^2\omega^2}} = \hbar\,|\chi_\mathrm{m}|\,. \tag{3.65}$$

Using the approximation $S_{n=0,xx}(\Omega_\mathrm{m}) = \frac{2x_\mathrm{ZPF}^2}{\Gamma_0} = \hbar\,|\chi_\mathrm{m}(\Omega_\mathrm{m})|$, eq. 3.64 can be defined as:

$$S_{\mathrm{det},xx}(\omega) \approx \frac{x_\mathrm{zpf}^2}{\Gamma_0}\left(1+3\frac{(\Gamma_0/2)^2}{(|\omega|-\Omega_m)^2+(\Gamma_0/2)^2}\right), \tag{3.66}$$

which is plotted in fig. 3.14 showing the summation of each noise term, so that the optimum measurement of the ZPF on-resonance is limited to a precision equal to $2 \times S_{n=0,xx}(\Omega_\mathrm{m})$, and implies resolving displacements $2 \times x_\mathrm{ZPF}$ [144, 166, 167].

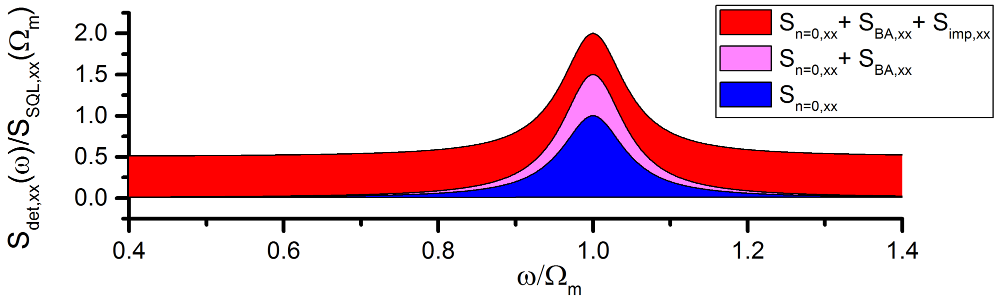

Figure 3.14: The ideal PSD output from quantum limited light probing the ZPF of a ground-state cooled mechanical oscillator $S_{n=0,xx}$ (blue). The radiation backaction of the random fluctuations of photons $S_{\mathrm{BA},xx}$ causes the oscillator to heat up (pink), whereas the shot noise (phase fluctuations) add imprecision noise $S_{\mathrm{imp},xx}$ (red). The y-axis is the ratio of the detected PSD with respect to the PSD at the SQL. Both sources of noise are minimised on-resonance (i.e. $S_{\mathrm{det},xx}(\omega) - S_{n=0,xx}(\omega) = S_{\mathrm{SQL},xx}(\Omega_\mathrm{m})$), bounded by Heisenberg's uncertainity principle.

Such an ideal case requires a quantum limited detector with high detection efficiency ϵ, and strong coupling (i.e. to avoid using high laser powers, discussed in section 8.2 of the appendix). The more stringent requirement is cooling the oscillator to its ground state. No such experiment has achieved reaching the SQL with a mechanical oscillator cooled to $\bar{n} = 0$. Typical issues encountered in experiments are related to optical absorption which increases backaction noise, and thermorefractive noise which degrades measurement imprecision [67]. However, even with $\bar{n} > 0$, and non-ideal detection efficiency (section 8.2 of the appendix derives the inclusion of $\bar{n} > 0$ and $\epsilon < 1$), interesting quantum phenomena has been studied. Many systems have obtained imprecision noise below the SQL at frequencies away from Ω_m [1–3], and quantum backaction limited measurements have been achieved to measure the motion of a SiN membrane [39] and other devices [168, 169][21]. Detection of ZPF has been achieved in [40] with $\bar{n} = 2.6$, and direct observation of backaction noise imprinted onto the mechanical oscillator has been observed in a photonic crystal [38][22]. In order to surpass the barrier of cooling to the ground state whilst evading unwanted backaction heating, new methods involving squeezed light have been proposed.

Squeezed light decreases S_{SN} at the expense of increasing S_{BA} (or vice versa), and can lower the laser power required to reach the SQL [170]. Such a scheme has been used with a WGM resonator toroid to detect the radial breathing modes with a sensitivity (imprecision noise) -0.72 dB below the shot-noise level [143]. However, any losses in the system i.e. propagation losses within the taper, or losses associated with coupling squeezed light can degrade the squeezing by up to 30% [143].

Another method to surpass backaction is to use measurements of observables where no perturbing measurement backaction occurs. These are known as quantum non-demolition (QND) observables. One such pair are energy and phase. Energy can be measured when the light couples quadratically to displacement, which can be backaction evading [140].

3.9 Conclusion

In this chapter it was demonstrated that the WGM is able to measure the thermal motion of the microsphere-cantilever that supports it, as well as the tapered fibre used to couple light to the WGM. The motion is detected by the transduction beam set up in chapter 2, and optimised here. The maximum S/N is obtained when the transduction beam is red-detuned with respect to the WGM, and at a set DC coupling distance between sphere and taper, close to critical coupling. This transduction mechanism is found to contain both dispersive and dissipative coupling with motion that change the WGM resonance frequency and the WGM linewidth respectively [45]. Cavity enhanced transduction using the WGM is important for resolving the sub-nanometer thermal motion of the micron-sized microsphere-cantilever and tapered fibre.

The transduction beam was further analysed by transforming it into a PSD in units of $\mathrm{m}^2\ \mathrm{Hz}^{-1}$, which defines the total power content within a given bandwidth. Such a spectrum reveals multiple mechanical modes of both the tapered optical fibre and the microsphere-

---

[21] Note that [169] measures the backaction force as it starts to heat the c.o.m. of a cloud of ultracold atoms

[22] Active feedback cooling can in theory damp backaction noise to cool mechanical oscillations to the ZPF [164] as feedback treats radiation backaction the same as Brownian noise.

cantilever, and is used to extract the effective mass and the spring constant for each mode. FEM is used to simulate the mode shapes, and provides verification of the experimentally measured mechanical eigenfrequencies. Identification of taper and microsphere-cantilever modes can also be experimentally achieved through resonantly driving one or the other using actuating forces. The microsphere-cantilever is driven with a piezo-stack, whereas the CEODF can actuate the tapered fibre. At atmospheric pressure, the taper modes are present but damped by the surrounding gas. When the pressure is decreased to 0.5 mbar, the mechanical quality factor $\mathrm{Q_m}$ of the taper modes increases by a factor of 40 whereas the $\mathrm{Q_m}$ of the c.o.m. mode of the microsphere-cantilever only doubles. When the PSD is dominated by the spectrum of tapered fibre modes in this way, the detection of sinusoidal forces, vibrations, or accelerations using the microsphere-cantilever is masked, and may resonantly drive the taper motion. However, avoiding the use of low pressures is not appropriate for many applications. For example, quantum limited sensing requires the microsphere-cantilever requires is de-coupled from its environment by lowering the pressure. The extraneous thermal noise of the tapered fibre must then be suppressed, which motivates the importance of the active feedback damping successfully used in the next chapter to cool these modes.

Lastly the difference between classical and quantum noise was discussed in order to determine the ultimate limits of displacement measurement. The ideal detector consists of quantum-limited light to measure the motion of a cooled mechanical oscillator. This ideal detection is still plagued by noise from the light field that adds imprecision (shot noise), and can heat up the cooled oscillator (radiation pressure backaction). These noise sources obey Heisenberg's uncertainty principle so that the minimum added noise for displacement detection at the mechanical frequency is equivalent to the PSD of the ZPF, known as the SQL. The smallest displacement that can be measured is therefore $2 \times x_{\mathrm{ZPF}}$. In reality, detection efficiencies, losses and thermal motion will result in a sensitivity incapable of reaching the SQL.

Chapter 4

Active Feedback Cooling

4.1 Introduction

The preceding chapter describes the use of the optical whispering gallery mode (WGM) to enhance the transduction of thermal motion of both the microsphere-cantilever, and the tapered optical fibre that acts as the evanescent coupler. The continuous measurement of displacement over time can be differentiated into a velocity proportional feedback signal. This is used to drive a force capable of actuating the mechanical oscillator such that it cools the motional temperature by reducing thermal fluctuations. Section 3.4 of chapter 3 identified the cavity enhanced optical dipole force (CEODF) and the force from the piezo-stack as suitable damping forces to cool the motion of the taper and the microsphere-cantilever respectively. In this chapter, electronic signal processing is used to differentiate the transduction signal which is then amplified to drive the actuating force which reduces the measured motion, creating a closed feedback loop. The combination of ultrasensitive transduction and active feedback has been used to cool mechanical oscillators close to their zero point motion [1, 171], and has enabled cooling of a kilogram-scale oscillator to 1.4 μK [172]. This 'active' feedback is different to 'passive' cooling where the latter involves the actuating force storing and dissipating energy.

Active feedback on vibration is used for many applications, ranging from the suppression of vibration in large structures such as helicopter fuselages [173], to the control of space structures [174], and control of micro-electro-mechanical systems (MEMS) for sensing and atomic-force microscopy (AFM) imaging [147, 175, 176]. Feedback control can greatly improve the sensing range and bandwidth of sensors. It is also used to suppress transient responses to shock [177] and for reducing non-linear behaviour in sensors [178].

Precision measurements, such as the detection of gravitational waves using the LIGO observatory [37], also rely on feedback damping methods to reduce noise, and decouple environmental vibrations [50].

In order to use active feedback to cool thermal mechanical motion, the precision with which one can measure such motion is the limit to cooling, and ideally, requires low noise electronics, minimal delays in the feedback loop, and quantum limited detection. An optimum feedback system should therefore be dominated by the shot-noise of the laser such that one can reach an imprecision (sensitivity) at the standard quantum limit [1, 31, 39], discussed in chapter 3. Optomechanical devices using shot-noise limited light have achieved impressive transduction sensitivities on the order of $10^{-19}\,\mathrm{m\,Hz^{-1/2}}$ (10^{-19} m can be measured over an integration time of 1 s) [179], which rivals values obtained in kilometre long interferometers [37, 172, 180], at a fraction of the size.

For typical feedback cooling experiments the actuating force is commonly from a piezo-electric stack [28–31], or an optical force such as the scattering force (radiation pressure) [1, 19, 77, 145, 172, 179, 181, 182], or the optical dipole force [78, 149], ([149] use a cavity enhanced optical dipole force)[1]. Cavity enhanced optical dipole forces (CEODFs), discussed in chapter 3 (section 3.4.1), are associated with WGMs due to the small mode volume confinement of the high Q optical field, which has an evanescent portion that extends beyond the dielectric boundary, free to interact with near-field objects such as the tapered fibre.

In fig. 4.1 is shown the active feedback cooling implemented on the taper coupled, microsphere-cantilever system described in this chapter.

The CEODF, $\mathrm{F_{CEODF}}$, acts as an attractive force between the tapered fibre and the microsphere-cantilever and is used to provide feedback damping $\propto -\frac{\mathrm{d}y_c}{\mathrm{d}t}$ on the motion of the micron-diameter taper, $y_t(t)$. A piezo-electric stack is used to damp the motion of the much larger (177 μm in diameter), heavier (20×10^{-9} kg), and stiffer microsphere-cantilever whose motion is described by $y_c(t)$. The transmission through the taper continuously monitors the relative displacement between the two oscillators as this changes the coupling distance, d, and alters the WGM.

Active cooling of the taper modes, which has not been achieved until now, demonstrates the feasibility of optically cooling a waveguide with the CEODF, and shows stabilization

---

[1] Other types of less commonly used cooling forces have been demonstrated, such as the photothermal force [137] and bolometric force [17], the electric gradient force [53, 149], and magnetic damping [176]

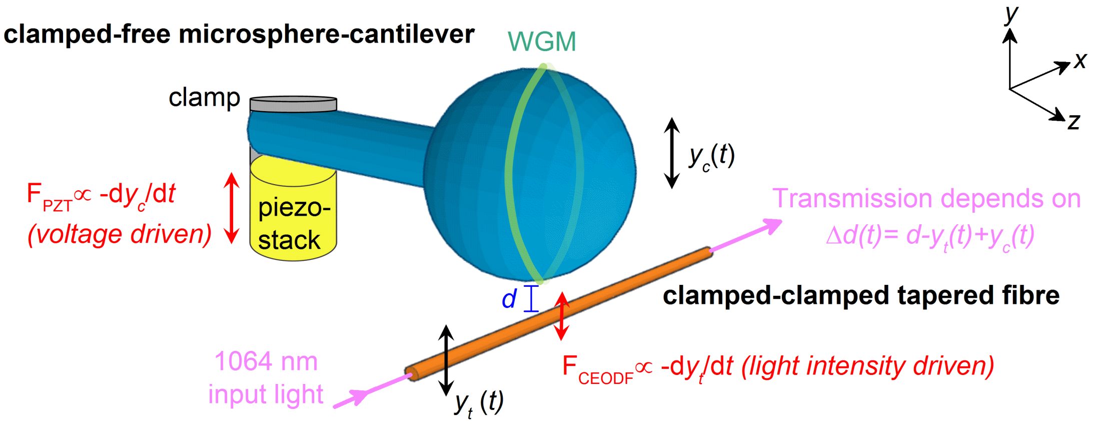

Figure 4.1: The microsphere-cantilever, evanescently coupled to the tapered fibre to excite a WGM, is used in an active feedback cooling scheme where the WGM transduction (chapter 3) measures the motion of the taper, $y_t(t)$, and microsphere-cantilever, $y_c(t)$, which is imprinted onto the transmission due to the change in the coupling distance, Δd. The transmission is differentiated to produce a velocity proportional feedback signal which drives the piezo-stack, $\mathrm{F}_{\mathrm{PZT}}$, and the CEODF, $\mathrm{F}_{\mathrm{CEODF}}$, to cool mechanical modes of the microsphere-cantilever the tapered optical fibre respectively.

of the coupling junction through reducing the mechanical motion of the taper itself. The spectrum of mechanical modes of tapered fibres is often seen as unwanted noise that can mask measurements by introducing noise peaks across an otherwise flat noise floor [12], and causes a fluctuating coupling to the WGM [136]. The cooling of taper modes is a type of stabilization that differs from that reported in [183], where only low frequency drifts ($< 20\,\mathrm{Hz}$) in coupling distance are counteracted. Cooling of the microsphere-cantilever is also a novel demonstration of using the WGM to transduce and aid damping of the motion belonging to the cavity that supports the resonance itself. In the feedback schemes used in this chapter, multiple mechanical modes of each oscillator can be cooled, and mode temperatures below 10 K are reached for the dominant mode. This temperature is consistent with limits determined by the measurement noise of the system. Both feedback schemes are operated simultaneously to provide stabilisation and damping of the coupled oscillators. Such a system could be used as a high range accelerometer that can counteract shock events by reducing the transient response of the system [177], and eliminate drift [19].

This chapter will present:

- The theoretical framework for active feedback cooling, and its effect on the power spectral density (PSD) is used to measure the damping rate and temperature.
- The experimental method employed in this thesis to create the feedback loop that

processes the WGM transduction described in chapter 3. A velocity proportional feedback signal is created.

- The results of active cooling of multiple mechanical modes of the microsphere-cantilever using a piezo-stack, and the use of the CEODF to cool multiple modes of the tapered optical fibre. The actuating forces are driven by the feedback signal.
- Simultaneous cooling of mechanical modes of the coupled oscillator system.
- The performance of active feedback cooling in the presence of time delays, imprecisions in measurement, and noise.

4.2 Active Feedback Cooling Theory

The transduction of the thermal motion of the tapered fibre and the microsphere-cantilever using WGMs, investigated in chapter 3, provides the foundation for implementing active feedback cooling. This measurement of displacement over time, $x(t)$, is differentiated into a velocity proportional signal, $\frac{\mathrm{d}x}{\mathrm{d}t}$, that can be used in a feedback loop. The loop drives actuating forces that damp the mechanical mode towards the quantum zero point motion if the measurement imprecision and additional noise sources are minimised. The reduction of thermal motion through cooling is seen in the PSD, which now differs from eq. 3.38 (pg. 78) in chapter 3, and requires a new PSD, derived as follows.

4.2.1 Power Spectral Density of Feedback Damped Oscillators

The 1-D PSD for a thermally damped, driven harmonic oscillator, derived in chapter 3 (eq. 3.38), is used to describe the motion and temperature of mechanical modes in equilibrium with the environment at T_0. Active feedback reduces this thermal motion by introducing a damping force, $\mathrm{F}^{\mathrm{fb}}(t)$. A new form of the PSD can be derived, allowing deduction of the *cooled* mode temperature. Starting with the equation of motion[2]:

$$\frac{\mathrm{d}^2x(t)}{\mathrm{d}t^2} + \Gamma_0\frac{\mathrm{d}x(t)}{\mathrm{d}t} + \omega_0^2x(t) = \frac{\mathrm{F}^{\mathrm{th}}(t)}{m_{\mathrm{eff}}} + \frac{\mathrm{F}^{\mathrm{fb}}(t)}{m_{\mathrm{eff}}}, \tag{4.1}$$

where $\mathrm{F}^{\mathrm{th}}(t) = \eta_B(t)\sqrt{2\mathrm{k_B}\mathrm{T}_0\Gamma_0}$ is the Brownian stochastic force defined by $\eta_B(t)$, the normalised white-noise process. If the feedback force is proportional to velocity, $\mathrm{F}^{\mathrm{fb}} =$

---

[2] The parameter x is equivalent to y_c or y_t in fig. 4.1.

$-\Gamma_{\mathrm{fb}}\frac{\mathrm{d}x}{\mathrm{d}t}$, where Γ_{fb} is the feedback damping rate, eq. 4.1 can be written as:

$$\frac{\mathrm{d}^2x(t)}{\mathrm{d}t^2} + (\Gamma_0 + \Gamma_{\mathrm{fb}})\frac{\mathrm{d}x(t)}{\mathrm{d}t} + \Omega_{\mathrm{m}}^2 x(t) = \eta_B(t)\sqrt{\frac{2\mathrm{k_B}\mathrm{T}_0\Gamma_0}{m_{\mathrm{eff}}^2}}. \tag{4.2}$$

In contrast to damping due to the background gas, damping from feedback does not appear in the driving term (right hand side of eq. 4.2), which is why this type of cooling is often referred to as ‘cold damping’. Working in frequency space reveals how feedback affects the mode temperature and lineshape in the PSD. Following the derivation of the PSD in chapter 3 (section 3.5.1), the motion of the oscillator in frequency space is:

$$\delta x(\omega) = \chi_{\mathrm{m}}(\omega)(\mathcal{F}^{\mathrm{th}}(\omega) + \mathcal{F}^{\mathrm{fb}}(\omega)), \tag{4.3}$$

where $\chi_{\mathrm{m}}(\omega)$ is the bare mechanical susceptibility derived in eq. 3.35, and $\mathcal{F}^{\mathrm{fb}}(\omega)$, $\mathcal{F}^{\mathrm{th}}(\omega)$ is the feedback force and the thermal force in frequency space, respectively. The feedback force can be represented by $m_{\mathrm{eff}}g\mathrm{H}^{\mathrm{fb}}(\omega)\delta x(\omega)$, where g is a dimensionless gain and $\mathrm{H}^{\mathrm{fb}}(\omega)$ represents the feedback force transfer function.

The mechanical susceptibility is modified due to this additional feedback force. Substituting $g\mathrm{H}^{\mathrm{fb}}(\omega)$ into eq. 4.3 and re-arranging in terms of $\delta x(\omega)$ gives:

$$\delta x(\omega) = \frac{\chi_{\mathrm{m}}(\omega)}{1 - g\mathrm{H}^{\mathrm{fb}}(\omega)\chi_{\mathrm{m}}(\omega)}\mathcal{F}^{\mathrm{th}}(\omega), \tag{4.4}$$

which shows a modification to $\chi_{\mathrm{m}}(\omega)$ such that a new effective susceptibility can be derived using $\delta x(\omega) = \chi_{\mathrm{eff}}(\omega)\mathcal{F}^{\mathrm{th}}(\omega)$:

$$\chi_{\mathrm{eff}}(\omega) = \frac{\chi_{\mathrm{m}}(\omega)}{1 - g\mathrm{H}^{\mathrm{fb}}(\omega)\chi_{\mathrm{m}}(\omega)} = \frac{1}{m_{\mathrm{eff}}(\Omega_{\mathrm{m}}^2 - \omega^2 + i\omega\Gamma_0 - g\mathrm{H}^{\mathrm{fb}}(\omega))}. \tag{4.5}$$

If the feedback force is chosen to be proportional to the velocity $\frac{\mathrm{d}x}{\mathrm{d}t}$, the feedback transfer function is of the form:

$$\mathrm{H}^{\mathrm{fb}}(\omega) = \Omega_{\mathrm{m}}\Gamma_0\frac{\mathcal{F}[\frac{\mathrm{d}x}{\mathrm{d}t}]}{\delta x(\omega)} = -i\omega\Omega_{\mathrm{m}}\Gamma_0, \tag{4.6}$$

where the Fourier transform identity $\mathcal{F}\left[\frac{\mathrm{d}x}{\mathrm{d}t}\right] = i\omega\mathcal{F}[x] = i\omega\delta x(\omega)$ is used. The expression for the effective mechanical susceptibility, eq. 4.5, and the transfer function for damping, eq. 4.6, can be used to derive the (one-sided) PSD describing feedback damped thermal motion:

$$S_{xx}^{\mathrm{fb}}(\omega) = |\chi_{\mathrm{eff}}(\omega)|^2 \, S_{\mathrm{F}}^{\mathrm{th}}(\omega), \tag{4.7}$$

where $S_{\mathrm{F}}^{\mathrm{th}}(\omega) = 2\mathrm{k_B T_0}\Gamma_0 m_{\mathrm{eff}}$ is the PSD of the thermal force. Therefore, the PSD for a feedback cooled, thermally driven mechanical oscillator is:

$$S_{xx}^{\mathrm{fb}}(\omega) = \frac{2\mathrm{k_B T_0}}{m_{\mathrm{eff}}} \frac{\Gamma_0}{(\Omega_{\mathrm{m}}^2 - \omega^2)^2 + (1+g)^2\omega^2\Gamma_0^2}. \tag{4.8}$$

Or, alternatively:

$$S_{xx}^{\mathrm{fb}}(\omega) = \frac{2\mathrm{k_B T_{eff}}}{m_{\mathrm{eff}}} \frac{\Gamma_{\mathrm{eff}}}{(\Omega_{\mathrm{m}}^2 - \omega^2)^2 + \omega^2\Gamma_{\mathrm{eff}}^2}, \tag{4.9}$$

where $\mathrm{T_{eff}} = \frac{\mathrm{T_0}}{(1+g)}$ and $\Gamma_{\mathrm{eff}} = \Gamma_0(1+g)$. The use of a differential feedback force results in two changes to the mechanical motion, seen in the PSD:

- A decrease in the temperature from $\mathrm{T_0} \to \mathrm{T_0}/(1+\mathrm{g})$, corresponding to the reduction of the r.m.s. position fluctuations, and seen as a decreasing PSD peak height.
- An increase in the damping rate from $\Gamma_0 \to \Gamma_0(1+g)$, which will broaden the PSD peak.

One may wonder what other types of feedback transfer functions are used for motion control. In general, an imaginary transfer function results in damping (energy dissipation), whereas stabilisation is achieved using a real transfer function, as is the case for displacement proportional feedback, $\mathrm{F}^{\mathrm{prop}}(t) \propto x(t)$. A common effect in feedback cooling experiments is to unintentionally obtain a mixture of differential and proportional feedback due to delays in the feedback loop, (experimentally studied in section 4.4.3 of this chapter). In comparison to eqs. 4.1 & 4.8, the equation of motion, and the PSD of a mechanical oscillator stabilised using displacement proportional feedback are:

$$\frac{\mathrm{d}^2 x(t)}{\mathrm{d}t^2} + \Gamma_0 \frac{\mathrm{d}x(t)}{\mathrm{d}t} + \Omega_{\mathrm{m}}^2 x(t) = \frac{\mathrm{F^{th}}(t)}{m_{\mathrm{eff}}} - \frac{g x(t)\Gamma_0\Omega_{\mathrm{m}} m_{\mathrm{eff}}}{m_{\mathrm{eff}}}, \tag{4.10}$$

$$S_{xx}^{\mathrm{prop}}(\omega) = \frac{2\mathrm{k_B T_0}}{m_{\mathrm{eff}}} \frac{\Gamma_0}{(\Omega_{\mathrm{m}}^2\left(1+\frac{g}{\mathrm{Q_m}}\right) - \omega^2)^2 + \omega^2\Gamma_0^2}, \tag{4.11}$$

which causes a shift in the mechanical oscillator frequency.

Systems with Noise

For real systems, the detection of motion cannot be perfectly precise due to Heisenberg's uncertainty relations (see chapter 3), such that every detector has an associated measurement imprecision[3]. The detector actually detects $x_{\mathrm{det}}(t) = x(t) + u(t)$, where $u(t)$ is the imprecision noise. The PSDs derived in chapter 3 and in the previous section of this chapter describe the *actual* mechanical oscillator motion $x(t)$. This is an accurate approximation of the *detected* PSD when the S/N is high i.e. the PSD peak is approximately a factor of 2 above the noise floor. This assumption is valid when no feedback is applied or for weak damping where the PSD peak has not reached the background noise floor (the imprecision noise). In the case of feedback cooling using high gain, the PSD peak can become comparable to the imprecision noise, such that this noise is fed *back into* the feedback loop, and heats the oscillator motion. In this latter case, the feedback force is described by $\mathrm{F}^{\mathrm{fb}}(t) = -\Gamma_{\mathrm{fb}} \frac{\mathrm{d}x_{\mathrm{det}}}{\mathrm{d}t}$ and the imprecision $u(t)$ in frequency space is represented by $U(\omega)$, with its own associated PSD, $S_{\mathrm{imp},xx}(\omega)$. This modifies the *actual* oscillator motion in frequency space originally defined by eq. 4.3, such that the imprecision noise is included in the driving term:

$$\delta x(\omega) = \chi_{\mathrm{m}}(\omega) \Big(\mathcal{F}^{\mathrm{th}}(\omega) + g\mathrm{H}^{\mathrm{fb}}(\omega)\left[U(\omega) + \delta x(\omega)\right]\Big), \tag{4.12}$$

where $\chi_{\mathrm{m}}(\omega)$ is the unmodified mechanical susceptibility, g is the gain and $\mathrm{H}^{\mathrm{fb}}(\omega)$ represents the feedback force transfer function. Note that the *detected* PSD of the light field, $S^{\mathrm{fb,imp}}_{\mathrm{det},xx}(\omega)$, that transduces the motion given by eq. 4.12 is different, and is studied in detail in section 4.4.3. Rearranging eq. 4.12 in terms of $\delta x(\omega)$:

$$\delta x(\omega) = \frac{\chi_{\mathrm{m}}(\omega)}{1 - g\mathrm{H}^{\mathrm{fb}}(\omega)\chi_{\mathrm{m}}(\omega)} \Big[\mathcal{F}^{\mathrm{th}}(\omega) + g\mathrm{H}^{\mathrm{fb}}(\omega)U(\omega)\Big], \tag{4.13}$$

$$\delta x(\omega) = \chi_{\mathrm{eff}}(\omega) \Big[\mathcal{F}^{\mathrm{th}}(\omega) + g\mathrm{H}^{\mathrm{fb}}(\omega)U(\omega)\Big], \tag{4.14}$$

where the effective mechanical susceptibility, $\chi_{\mathrm{eff}}(\omega)$, is as previously defined in eq. 4.5. Using the relation $S_{xx}(\omega) = \left\langle \delta x(\omega)^2 \right\rangle$, the PSD of the oscillator motion, measured with

---

[3] For monochromatic light, the lowest imprecision noise corresponds to the shot-noise limit and requires suppression of classical intensity and frequency fluctuations.

an imprecise detector which drives a feedback damping force is [53, 149]:

$$S_{xx}^{\mathrm{fb,imp}}(\omega) = |\chi_{\mathrm{eff}}(\omega)|^2 \left[S_{xx}^{\mathrm{th}}(\omega) + \left| g\mathrm{H}^{\mathrm{fb}}(\omega) \right|^2 S_{\mathrm{imp},xx}(\omega) \right], \tag{4.15}$$

$$S_{xx}^{\mathrm{fb,imp}}(\omega) = \frac{S_{xx}^{\mathrm{th}}(\omega) + g^2 \left| \mathrm{H}^{\mathrm{fb}}(\omega) \right|^2 S_{\mathrm{imp},xx}(\omega)}{\left| m_{\mathrm{eff}}(\Omega_{\mathrm{m}}^2 - \omega^2 + i\omega\Gamma_0 - g\mathrm{H}^{\mathrm{fb}}(\omega)) \right|^2}, \tag{4.16}$$

where $S_{\mathrm{imp},xx}(\omega)$ is the imprecision noise of the feedback measurement. If this noise is well below the PSD of the oscillator motion, $S_{xx}^{\mathrm{fb,imp}}(\omega)$, the heating effect of measurement noise can be ignored. However, with increased damping, the measurement imprecision will become comparable or larger than the decreasing $S_{xx}^{\mathrm{fb,imp}}(\omega)$, and will cause heating.

The theoretical PSD of the mechanical motion with active feedback cooling using negative velocity feedback, ($\mathrm{F_{FB}} = -g\frac{\mathrm{d}x}{\mathrm{d}t}$), and negative displacement feedback, ($\mathrm{F_{prop}} = -gx(t)$), inclusive of imprecision noise, are plotted in fig. 4.2, scaled by $S_{xx}^{\mathrm{th}}/(m_{\mathrm{eff}}\Omega_{\mathrm{m}}^2)^2$, with $\mathrm{Q_m} = 500$, $S_{\mathrm{imp,xx}}(\omega) = 10^2$, and applied feedback gains between $0 \leq g \leq 0.4$.

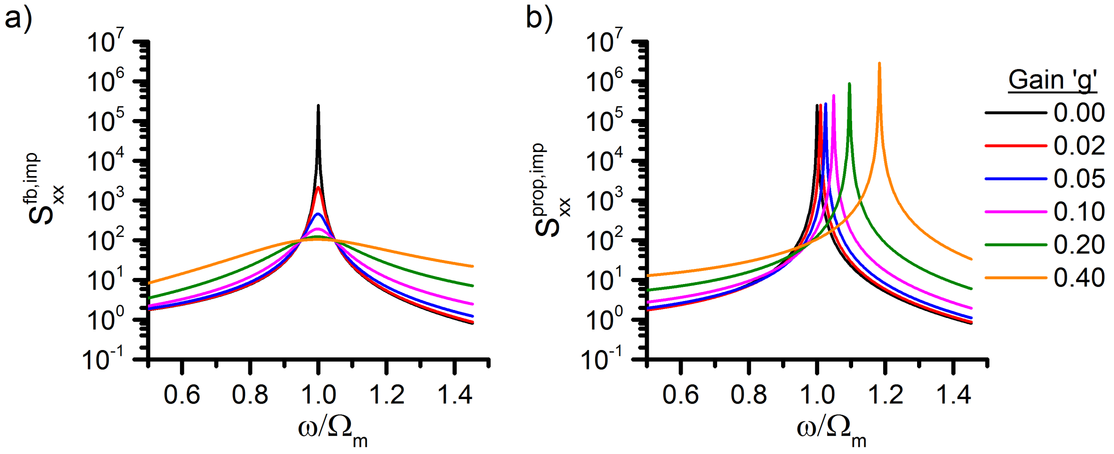

Figure 4.2: Simulated PSD for the *actual* motion of an oscillator with, a) applied derivative feedback, and b), proportional feedback, at varying gain, g, with $\mathrm{Q_m} = 500$, $S_{\mathrm{imp},xx} = 10^2$, and scaled by $S_{xx}^{\mathrm{th}}/(m\Omega_{\mathrm{m}}^2)^2$

Two different responses are shown in fig. 4.2:

- Differential (velocity) cooling, fig. 4.2 a): the transfer function is imaginary which increases the damping rate and decreases the area under the peak. Above a certain gain that reduces the mode temperature $\mathrm{T_{eff}}$ to the minimum cooled temperature, $\mathrm{T_{min}}$ (limited by the imprecision noise), a high level of detector noise is fed back to the resonator which drives the actuating force, increasing $\mathrm{T_{eff}}$, see fig. 4.2 a) when $g > 0.1$. $\mathrm{T_{eff}}$ can be inferred by comparing the r.m.s. thermal fluctuations at the mechanical frequency, which is proportional to $\sqrt{S_{xx}^{\mathrm{fb,imp}}(\Omega_{\mathrm{m}})}$, with and without

($g = 0$) feedback:

$$\frac{\mathrm{T_{eff}}}{\mathrm{T_0}} = \sqrt{\frac{S_{xx}^{\mathrm{fb,imp}}(\Omega_\mathrm{m})}{S_{xx}(\Omega_\mathrm{m})|_{g=0}}}, \tag{4.17}$$

which can be used with eq. 4.15 to find:

$$\frac{\mathrm{T_{eff}}}{\mathrm{T_0}} = \sqrt{1 + \frac{g^2}{\mathrm{S/N}}} \times \frac{1}{1+g}, \tag{4.18}$$

where the signal to noise ratio, (S/N), is the ratio of the PSD of thermal motion with no applied feedback, compared to the imprecision noise, $\mathrm{S/N} = \frac{S_{xx}^{\mathrm{fb,imp}}(\Omega_\mathrm{m})|_{g=0}}{S_{\mathrm{imp},xx}(\omega)}$.

- Displacement proportional feedback, fig. 4.2 b), results in a real transfer function which shifts the mechanical resonance frequency. High feedback gains result in heating for the parameters used in fig. 4.2 b), ($\mathrm{Q_m} = 500$, $\frac{S_{\mathrm{imp},xx}}{S_{xx}^{\mathrm{th}}}/(m_{\mathrm{eff}}\Omega_\mathrm{m}^2)^2 = 10^2$). However, cooling can be achieved but would require gains that are $\mathrm{Q_m}$ times higher to obtain damping of the same factor as derivative feedback [53], where $\mathrm{Q_m}$ is the mechanical quality factor. This will result in more noise entering the system.

For differential feedback cooling, assuming the imprecision noise is smaller than the measured displacement power[4], the following function can be used for fitting the *detected* PSD curve:

$$S_{\mathrm{det},xx}^{\mathrm{fb,imp}}(\omega) = \frac{2\mathrm{k_B T_0}}{m_{\mathrm{eff}}} \frac{\Gamma_0}{(\Omega_\mathrm{m}^2 - \omega^2)^2 + (1+g)^2\omega^2\Gamma_0^2} + S_{\mathrm{imp},xx}(\omega), \tag{4.19}$$

where $S_{\mathrm{imp},xx}(\omega)$ is the background noise floor around Ω_m in the PSD. When the thermal motion is larger than the level of the background noise, eq. 4.18 is approximated as $\frac{\mathrm{T_{eff}}}{\mathrm{T_0}} = \frac{1}{1+g}$, and the minimum cooled temperature $\mathrm{T_{min}}$, can be calculated [31, 53] using:

$$\mathrm{T_{min}} = \sqrt{\frac{m_{\mathrm{eff}}\Omega_\mathrm{m}^3 \mathrm{T_0}}{\mathrm{k_B Q_m}} S_{\mathrm{imp},xx}(\omega)}, \tag{4.20}$$

noting that $S_{\mathrm{imp},xx}(\omega)$ is measured in units of $\mathrm{m^2\,rad^{-1}\,s}$.

In order to infer the cooled temperature $\mathrm{T_{eff}}$, from the PSD, four methods can be used:

1. Direct measurement of the change in damping factor $\Gamma_{\mathrm{eff}}/\Gamma_0$ by fitting the PSD with eq. 4.19 [145, 184]. Qualitatively this equation describes the vibrational mode which

---

[4] Section 4.4.3) in this chapter describes the case when the imprecision noise is higher than the measured thermal motion PSD and eq. 4.19 is not valid for determination of the temperature.

experiences a change from a thermal environment defined by a Langevin force with strength proportional to $\Gamma_0 \mathrm{T}_0$, to an effective environment with a Langevin force of the same strength but now proportional to $\Gamma_{\mathrm{eff}} \mathrm{T}_{\mathrm{eff}}$, such that $\Gamma_0 \mathrm{T}_0 = \Gamma_{\mathrm{eff}} \mathrm{T}_{\mathrm{eff}}$, and thus, $\mathrm{T}_{\mathrm{eff}} = \mathrm{T}_0 \frac{\Gamma_0}{\Gamma_{\mathrm{eff}}}$.

2. Alternatively, measurement of $\frac{2\mathrm{k_B T_0}}{(1+g)m_{\mathrm{eff}}} = \frac{2\mathrm{k_B T_{eff}}}{m_{\mathrm{eff}}}$ can be used, obtained from fitting using eq. 4.19.

3. Measurement of the area under the PSD peak can be used as the energy equipartition theorem relates the thermal displacement fluctuations to the mode temperature, $\langle x^2 \rangle \approx \frac{\mathrm{k_B T_{eff}}}{m_{\mathrm{eff}} \omega_{\mathrm{m}}^2} = \int_{-\infty}^{+\infty} S_{xx}^{\mathrm{fb,imp}}(\omega)\, \mathrm{d}\omega$ [185, 186], valid if operating far from the quantum regime.

4. Measurement of the peak height in the PSD at the resonant frequency Ω_{m}[5], defined as $S_{xx}^{\mathrm{fb,imp}}(\Omega_{\mathrm{m}}) = \frac{2\mathrm{k_B T_0}}{m_{\mathrm{eff}}(1+g)^2 \Omega_{\mathrm{m}}^2 \Gamma_0} = \frac{2\mathrm{k_B T_{eff}}}{m_{\mathrm{eff}} \Omega_{\mathrm{m}}^2 \Gamma_{\mathrm{eff}}}$.

All four methods require precise knowledge about the properties of the mechanical oscillator such as the effective mass, the damping rate from air, and the initial equilibrium temperature. This is not always possible to characterise accurately, therefore, a calibration PSD at zero feedback, ($g = 0$), can be used to set $\Gamma_0, m_{\mathrm{eff}}, \mathrm{T}_0, \Omega_{\mathrm{m}}$, such that all other PSDs can referenced to these initial values. Dependent on the shape of the line profile, it may be easier to measure the area under peak in the PSD rather than fit eq. 4.19, especially if the noise floor is not flat. Peaks which are broadened (e.g. a reduced $\mathrm{Q_m}$ from damping) can have large fitting errors dependent on the standard deviation of the signal (the noise fluctuations). A comparison of the four fitting methods to infer $\mathrm{T}_{\mathrm{eff}}$ for the primary cooled modes in this chapter is shown in the appendix, section 8.3.

4.3 Experimental Method

4.3.1 Optical & Electronic Set-up

Active feedback is performed using the CEODF to damp the motion of the tapered fibre and the piezo-stack is used to cool the motion of the microsphere-cantilever. The experimental set-up from chapter 2 (fig. 2.23, pg. 53) is modified by including components

---

[5] An effective mechanical frequency arises if the feedback transfer function has both real and imaginary components (i.e. mixture of derivative and proportional feedback), discussed in section 4.4.3 of this chapter.

required for the feedback loop. The complete optical and electronic layout is shown in fig. 4.3.

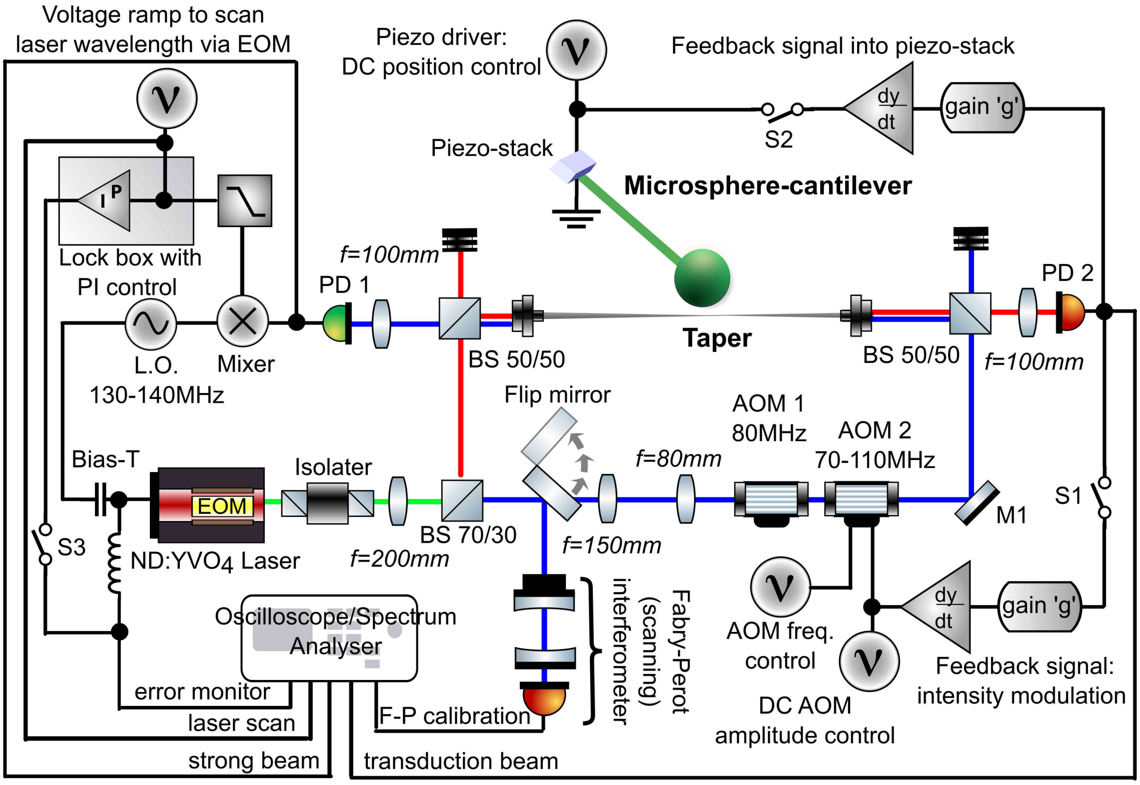

Figure 4.3: The experimental set up of fig. 2.23 in chapter 2 is modified to include a feedback system. The strong beam (blue) is used for PDH locking (controlled with switch S 3) (or thermal locking), and controls the magnitude of the CEODF. The red-detuned transduction beam (red) counterpropagates through the taper and is monitored with an amplified photodetector (PD 2). The output of PD 2 is split and sent to two servo loops, each with a proportional amplifier and a differentiator. The differentiated transduction signal is used to modulate the CEODF by changing strong beam power using AOM 2, and/or sent to modulate the piezo-stack at the clamped end of the microsphere-cantilever. Switches S 1 & S 2 can be used to activate both feedback loops simultaneously.

As before, the tapered optical fibre is placed directly below the microsphere-cantilever and the system is housed within a vacuum chamber. The transduction beam is shown in red and typically 70 μW of this beam is coupled into the tapered fibre. The strong beam shown in blue, counterpropagates through the same tapered fibre, and approximately $300 - 500\,\mu$W is coupled and transmitted into the taper. The flip mirror can be used to steer the strong beam into the scanning F-P interferometer for calibration of the laser tuning and the WGM linewidth, described in chapter 2, section 2.3.3. The strong beam is locked to the centre of the WGM using Pound-Drever-Hall (PDH) locking by closing the switch S 3, or, stabilised close to resonance, on the blue-detuned side, via thermal self-locking [128]. The latter method is employed when a large modulation of the strong beam light intensity is required to control the CEODF which destabilizes the PDH. Both locking schemes are discussed in detail in chapter 2, section 2.5. The frequency (i.e. detuning) of the transduction beam can be tuned with respect to the strong beam using acousto-optic modulators (AOM 1 & AOM 2), as previously in chapter 2 (section 2.6.1). The transmitted light of the transduction beam is detected on an amplified InGaAs variable gain photodetector[6] (PD 2), whose output is monitored on the PC oscilloscope. Real-time monitoring is achieved using the FFT function of the oscilloscope, and the data is processed to create the PSD (see chapter 3 (section 3.6.1)) which contains information about the mechanical motion of both the microsphere-cantilever and the tapered fibre.

To implement active feedback cooling, a differentiator and an amplifier is required to create the feedback signal and tune the feedback gain respectively, which is then used to drive the actuating forces studied in chapter 3. First, the output from PD 2 is sent to a servo controller[7] which is set to proportional gain, with zero integral gain, and simply functions as an amplifier controlled by a potentiometer to adjust the feedback gain, g. The output of the servo is then sent to a home made differentiator[8] formed by an op-amp circuit which measures the rate of change in the voltage output of PD 2. The output from the differentiator (the feedback signal) drives either the piezo-stack (via a piezo driver[9]) or to vary the output amplitude of AOM 2 which in turn, varies the laser power of the strong beam. Each actuating force has its own dedicated servo and differentiator so that the feedback gain of each cooling scheme can be controlled separately, but share the same photodiode signal. Switches S 1 and S 2 control whether one or both feedback loops are operating simultaneously.

4.3.2 Lifetime of Microsphere-cantilever & Tapered Fibre

The usable lifetime of both the microsphere-cantilever and the tapered fibre is limited, and over time periods of a few weeks contaminants adhere to the surface which lowers the quality factor, Q_{opt}, and decreases the transmission of the taper due to scattering. A catastrophic melting of the tapered fibre can occur when too much power is coupled, especially at low vacuum pressures where fewer air molecules can dissipate this heat.

---

[6] Thorlabs PDA20CS

[7] Newport LB1005.

[8] There are 2 differentiators used in this experiment; an older, more complicated one built by a previous Ph.D. student that contains additional filters, used in earlier experiments but was not optimised for kilohertz frequencies, causing time delays. A new differentiator was used in later experiments comprising of a more simple op-amp design.

[9] Thorlabs MDT694B

Therefore, some data sets in this chapter involve a change of either the tapered fibre or the microsphere-cantilever. Care is taken to use microsphere-cantilevers of similar dimension, and tapers are fabricated with the same number of pulling steps, applied with approximately equal tension. Any change of either oscillator will be identified in the text. See section 8.4.

4.3.3 Power Spectral Density Fitting Function

All data presented in this chapter, unless specified, are collected using a PC oscilloscope[10], where 30 traces, each 2 s in length, with a sampling rate of 250×10^3 samples/s, are recorded. These are converted into a one sided PSD, in units of $\mathrm{V}^2\,\mathrm{Hz}^{-1}$ using the periodogram function in Matlab. An averaging of the 30 PSDs is conducted in order to improve the noise. The procedure used in chapter 3 (section 3.3.2) to convert to displacement units ($\mathrm{m}^2\,\mathrm{Hz}^{-1}$) is verified for each change of microsphere-cantilever and WGM, but is found to not vary considerably, since similar DC coupling distances are used.

The PSD of a feedback cooled harmonic oscillator is given by eq. 4.19 and this can be fitted using OriginLab's non-linear fitting tool, which uses a Levenberg Marquardt algorithm for least squares curve fitting. The equation used for fitting is defined as:

$$y = \frac{A_{\mathrm{fb}}\Gamma_{\mathrm{eff}}}{((\Omega_{\mathrm{m}}/2\pi)^2 - (\omega/2\pi)^2)^2 + \Gamma_{\mathrm{eff}}^2(\omega/2\pi)^2} + b, \tag{4.21}$$

where y is the PSD, in $\mathrm{m}^2\,\mathrm{Hz}^{-1}$, A_{fb} is a variable equal to $\frac{2\mathrm{k_B T_0}}{(1+g)m_{\mathrm{eff}}}$, Γ_{eff} is the effective damping rate given by $\Gamma_{\mathrm{eff}} = \Gamma_0(1+g)$, ω is the observed frequency, and b is the background noise level in $\mathrm{m}^2\,\mathrm{Hz}^{-1}$. The lowered mode temperature is $\mathrm{T_{eff}} = \frac{A_{\mathrm{fb}}}{A_0/\mathrm{T_0}}$, where A_0 is the parameter A_{fb} when no feedback is applied ($g = 0$), and $\mathrm{T_0}$ is the equilibrium mode temperature (environment temperature) at zero feedback, chosen for convenience to be 300 K. The value of the feedback gain, g can be calculated from the reduced mode temperature such that $g = \frac{\mathrm{T_0}}{\mathrm{T_{eff}}} - 1$ or $g = \frac{\Gamma_{\mathrm{eff}}}{\Gamma_0} - 1$. Errors quoted for the mode temperatures are derived from the fitting errors.

---

[10] Picoscope 4262

4.4 Experimental Results

4.4.1 Cooling a Microsphere-cantilever with a Piezo-stack

As outlined earlier in chapter 3, the lower spring constant and effective mass of the taper modes, makes this oscillator more susceptible to the CEODF. Therefore the CEODF actuates the taper towards the microsphere rather than the microsphere-cantilever towards the taper. For this reason, a piezo-stack placed at the clamped end of the microsphere-cantilever that actuates the position vertically away and towards the tapered fibre, is used as the damping element.

A microsphere of diameter $\oslash$ =177 μm is selected, which remains attached to the fibre stem of $\oslash$ =120 μm and length 5.6 mm, measured approximately using pixel counting as detailed in chapter 2 (section 2.2.1). A microscope image is shown in fig. 4.4 and this microsphere-cantilever is referred to as 'microsphere-cantilever[$\mathcal{A}$]'. The mechanical properties of the microsphere-cantilever[$\mathcal{A}$] is fully explored in chapter 3 (section 3.6.2) and re-listed in table 4.1. It was also demonstrated in chapter 3, fig. 3.12, that the $\mathrm{Q_m}$ of this micron-size mechanical oscillator is only weakly affected by lowering the pressure, which allows for ambient operation of feedback cooling.

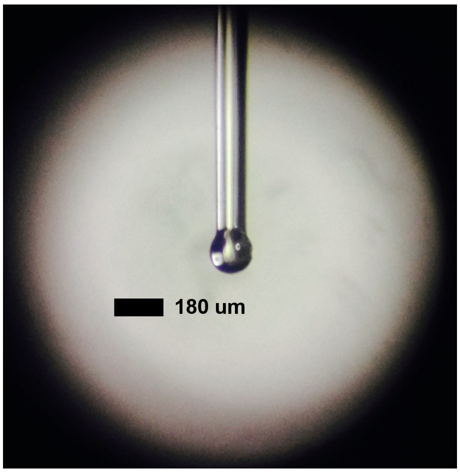

Figure 4.4: Microsphere-cantilever[$\mathcal{A}$], used in the majority of experiments within this thesis, imaged using a 40X microscope. The microsphere has a diameter of 177 μm, which remains attached to a fibre stem 120 μm in diameter and 5.6 mm long.

Microsphere-cantilever[$\mathcal{A}$] is used alongside a taper, labelled as taper[$\mathcal{A}$], in the experimental set-up of fig. 4.3. When differential feedback is applied to the piezo-stack, the motion of the fundamental centre-of-mass (c.o.m.) frequency at 2.80 kHz (mode c1), as well as the second eigenfrequency at 17.73 kHz (mode c2), can be simultaneously cooled,

Property	Fundamental mode (c1)	Second eigenmode (c2)
Frequency (Hz)	2795 ± 0.06	17732 ± 2
$\mathrm{Q_m}$	370 ± 3	642 ± 16
k (N/m)	6.26 ± 2.1	82.8 ± 28.0
m_{eff} $(\times 10^{-9}\,\mathrm{kg})$	20.2 ± 0.7	6.67 ± 2.26

Table 4.1: The mechanical properties of microsphere-cantilever[$\mathcal{A}$], analysed from data in chapter 3 using fig. 3.11 (pg. 83).

shown in fig. 4.5. The gain parameter $g_{\mathrm{c1}}, g_{\mathrm{c2}}$, for each mode is controlled by increasing the *overall* gain of the proportional servo, and $g_{\mathrm{c1}} \neq g_{\mathrm{c2}}$ since the c.o.m. mode and the second eigenmode have different mechanical properties. Cooled mode temperatures of $\mathrm{T_{c1}} = (9 \pm 0.4)\,\mathrm{K}$ and $\mathrm{T_{c2}} = (108 \pm 8)\,\mathrm{K}$ are reached at the maximum gain, at atmospheric pressure.

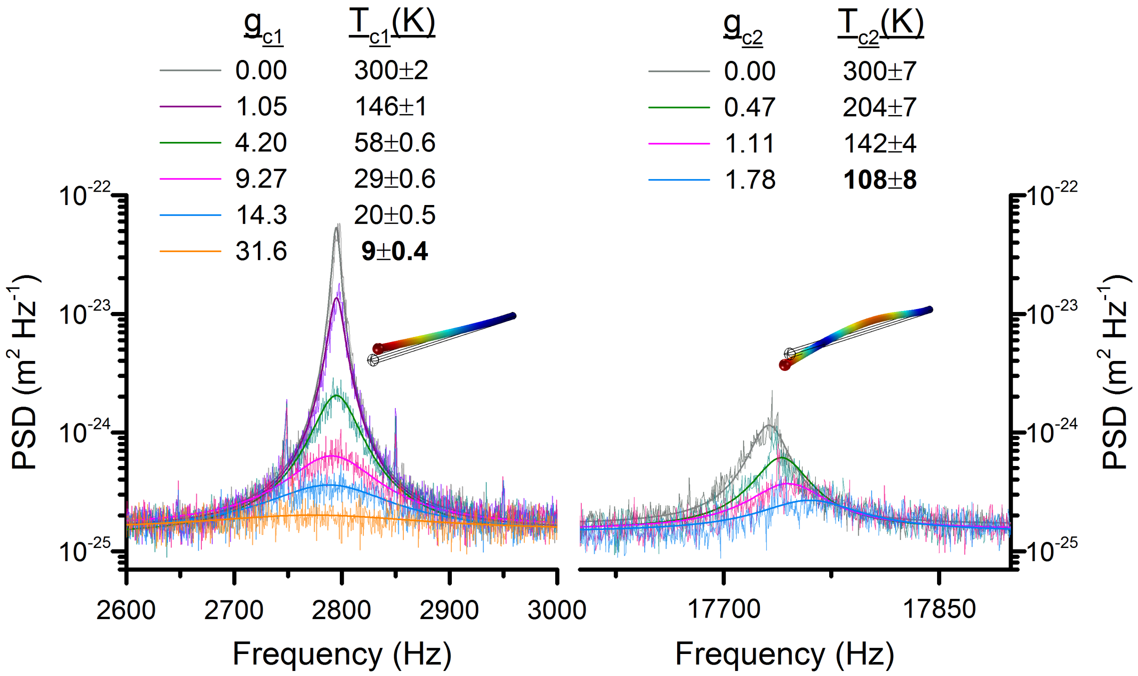

Figure 4.5: Piezo-stack feedback cooling of the fundamental mode (labelled c1) of microsphere-cantilever[$\mathcal{A}$] with $\mathrm{Q_{m1}} = 370$, reaching $\mathrm{T_{c1}}$ at varying feedback gains g_{c1}. The second mechanical eigenfrequency (labelled c2) at 17.73 kHz, with $\mathrm{Q_{m2}} = 640$, is simultaneously cooled to $\mathrm{T_{c2}} = 108\,\mathrm{K}$. Mechanical mode shapes are shown as inset diagrams. Data was taken at atmospheric pressure, with curves fitted using eq. 4.21 to infer the mode temperatures $\mathrm{T_{c1,c2}}$.

The c.o.m. mode is cooled close to the cooling limit, $\mathrm{T_{min,c1}} = 11 \pm 2\,\mathrm{K}$, calculated by using eq. 4.20 and the parameters in table 4.1, with $S_{\mathrm{imp},xx} = (2 \pm 0.4) \times 10^{-26}\,\mathrm{m^2 rad^{-1} s}$, measured from the PSD. The second mechanical eigenfrequency of the cantilever is cooled close to its respective limit of $\mathrm{T_{c2,min}} \approx 80\,\mathrm{K}$, representing effective broadband cooling for this particular oscillator. Multimode cooling of mechanical modes belonging to a single structure has been demonstrated on nanostrings [17], the coupled flapping modes of a double-disk toroidal resonator [15], and modes of the resonant-bar gravitational wave detector AURIGA [180].

In fig. 4.6 the effect of the environmental pressure was found to increase Q_m by only a factor of 1.4 as the pressure is lowered from atmospheric pressure (1013 mbar), to 0.5 mbar pressure. Feedback cooling of the microsphere-cantilever was attempted at 1 mbar, reaching (32 ± 6) K before limited by a parasitic noise peak near 5.5 kHz i.e. a taper mode, that begins to ring with increasing feedback gain. This is shown in the inset graph of fig. 4.6, where feedback gains above $g = 8.4$ drastically increases the noise floor. Such

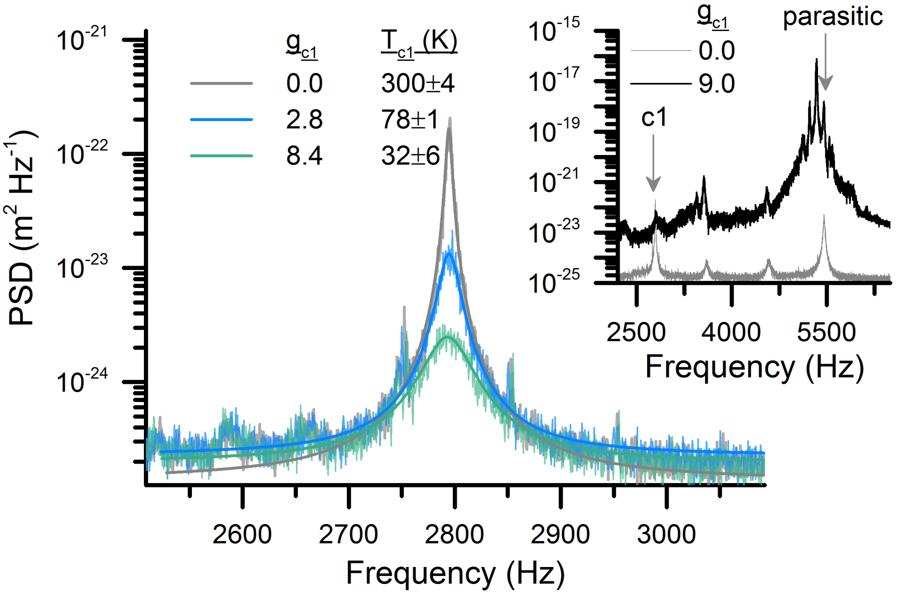

Figure 4.6: Feedback cooling was attempted at a pressure of 1 mbar for microsphere-cantilever[$\mathcal{A}$] where the fundamental c.o.m. mechanical mode at 2.8 kHz is cooled to 32±6 K before a parasitic mode, inset, saturates the feedback loop at gain $g > 9$. The arrow in the inset graph shows the c.o.m. mode and heating of the parasitic mode which increases the noise floor. This extraneous mode belongs to taper[A] (eigenmode 8) at 5.5 kHz, which is also transduced by the WGM. Mode temperatures are found by fitting eq. 4.21.

extraneous modes are often an issue in feedback cooling and can occur when neighbouring mechanical modes are measured and included within the feedback signal. The origin of these modes include cross-axis coupling where the orthogonal degenerate mechanical mode in another axis plane can be detected [154], as well as mechanical modes of the taper (fig. 4.6), and electronic noise. These modes are often not in phase with the mechanical mode to be cooled and can be unintentionally heated leading to saturation of the feedback loop. Frequency filters can be introduced to suppress the parasitic signal but can add phase delays. The effect of delays is experimentally studied in section 4.4.3. Since the mechanical frequencies of both the microsphere-cantilever and tapered fibre are close in frequency, adding narrow band-pass filters can affect the feedback response as the mechanical Q decreases with cooling, which will spread the mode beyond the limits of the filter passband [53].

4.4.2 Cavity Enhanced Optical Dipole Force Cooling of Taper Modes

In order to cool the taper modes with the CEODF arising from the strong beam, thermal locking is used to stabilise the laser close to, but on the blue-detuned side of the WGM, as discussed in chapter 2 (section. 2.5.2). This is because active PDH locking becomes unstable when the power is highly modulated and is therefore switched off using switch S 3 in the set-up of fig. 4.3. A typical strong beam laser power of 300-500 μW is coupled into the tapered fibre with a modulation depth of $\approx 70\,\%$. Microsphere-cantilever[$\mathcal{A}$] shown in fig. 4.4 is used here, but with a different taper (taper[$\mathcal{B}$]) to the one used in figs. 4.5 & 4.6. The mechanical properties of taper[$\mathcal{B}$] are studied in chapter 3 (section 3.6.2). A WGM with a linewidth of 460 MHz is measured using the F-P scanning interferometer such that the variables in eq. 3.20 to predict the CEODF are calculated: $\gamma_e(0) = 1.8 \times 10^{10}\,\mathrm{rad\,s^{-1}}$ and $\eta = 1.4 \times 10^{7}\,\mathrm{m^{-1}}$ for an intrinic quality factor of $\mathrm{Q_i} = 6.1 \times 10^{5}$, following the procedure described in chapter 2 (section 2.4.1) [32]. The force between the taper and the $\oslash = 177\,\mu$m microsphere is predicted to be 80 pN when using 500 μW of input light.

The dependence of $\mathrm{Q_m}$ of eigenmode 8 belonging to taper[$\mathcal{B}$] was experimentally investigated in chapter 3, fig. 3.7 (pg. 89) showing that at atmospheric pressure, the air damping is significant and $\mathrm{Q_m} < 10$. Therefore under these conditions, the damping achieved using the maximum modulation of the CEODF is limited (experimentally verified in section 4.4.2 of this chapter). Cooling is more efficient at low pressures where $\mathrm{Q_m}$ approaches its intrinsic value. In the results presented here, feedback is applied at a pressure no lower than 0.5 mbar since the turbo pump cannot be switched on without adding considerable noise, shown in chapter 3, fig. 3.13 b) (pg. 91). The roughing pump, used to reach 0.5 mbar, also adds noise and excites the mechanical modes, fig. 3.13 a), such that measurements must be taken once the pump is switched off. The chamber slowly begins to let air inside, and measurements must be taken quickly, or at set intervals when the pressure is lowered after a certain amount of time.

A plot of the recorded PSD of two taper[$\mathcal{B}$] modes at 5.50 kHz (mode t1), and 6.88 kHz (mode t2) is displayed in fig. 4.7. These were identified in section 3.6.2 of chapter 3 as eigenmodes 8 and 9, respectively. The data is taken at 0.5 mbar. Both modes are cooled simultaneously to (8 ± 0.5) K, and (85 ± 1) K, respectively, by increasing the feedback gain sent to modulate the CEODF. Taper mode t1 has a different feedback phase relationship and mechanical properties to mode t2, leading to different complex feedback transfer functions where the gains $g_{\mathrm{t1}} \neq g_{\mathrm{t2}}$. Both cannot be simultaneously cooled efficiently with the same signal without optimising the feedback signal further. The properties of these modes at zero gain, $g = 0$, (measured in section 3.6.2 of chapter 3) are displayed in table 4.2:

Property	Eigenmode 8 (t1)	Eigenmode 9 (t2)
Frequency (Hz)	5504 ± 0.01	6877 ± 0.2
$\mathrm{Q_m}$	381 ± 4	509 ± 5
k (N/m)	1.73 ± 0.58	6.15 ± 2.07
m_{eff} ($\times 10^{-9}$ kg)	1.44 ± 0.49	3.30 ± 1.11

Table 4.2: The mechanical properties of eigenmode 8 and 9 of taper[$\mathcal{B}$], analysed from data in section 3.6.2 of chapter 3.

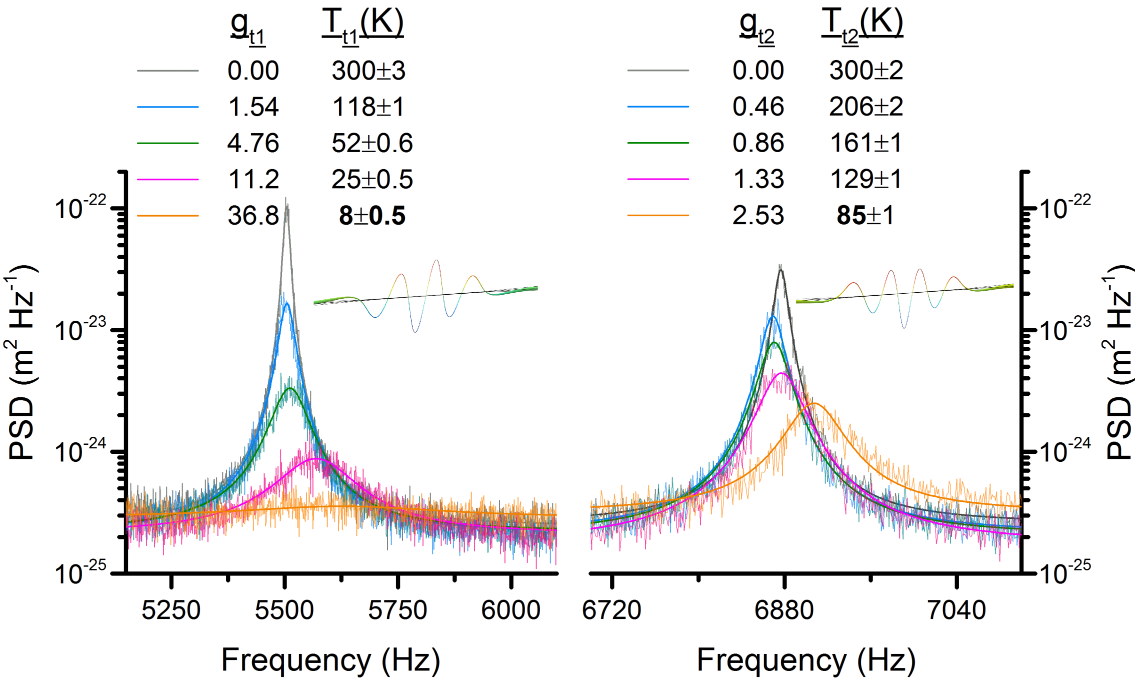

Figure 4.7: Simultaneous CEODF cooling of the 8th and 9th mechanical modes of the tapered optical fibre, obtained at a pressure of 0.5 mbar. Representational mechanical mode shapes are shown. Each mode temperature is defined as $\mathrm{T_{t1}}, \mathrm{T_{t2}}$, at varying gain, $g_{\mathrm{t1}}, g_{\mathrm{t2}}$. Curves are fitted using eq. 4.21 to infer the mode temperatures. The mechanical quality factor of each mode is $\mathrm{Q_{m1}} = 380$, and $\mathrm{Q_{m2}} = 510$.

Mode t1 is cooled close to its predicted minimum temperature given by eq. 4.20, $T_{\mathrm{min,t1}} \approx 8\,\mathrm{K}$. The shift in the mechanical frequency as the feedback gain is increased is related to the use of the older differentiator which adds a phase delay of approximately 24 degrees. The role of this phase (time) delay is studied later in this chapter.

Influence of Pressure on Cooling

Unlike the microsphere-cantilever, the mechanical modes of the tapered fibre are more affected by air damping, and the mechanical quality factor increases by over 40× when the pressure is lowered to 0.5 mbar, as shown in fig. 3.12 (pg. 90) of chapter 3. To explore this effect on feedback cooling, i.e. the minimum experimentally obtainable cooled mode temperature, feedback damping is applied using the CEODF on eigenmode 8 of taper[$\mathcal{B}$] over a range of pressures. The cooled mode temperature is plotted in fig. 4.8 (black data points), alongside the predicted limit of cooling T_{min} (blue data), defined by eq. 4.20 using the reference PSD at $g = 0$.

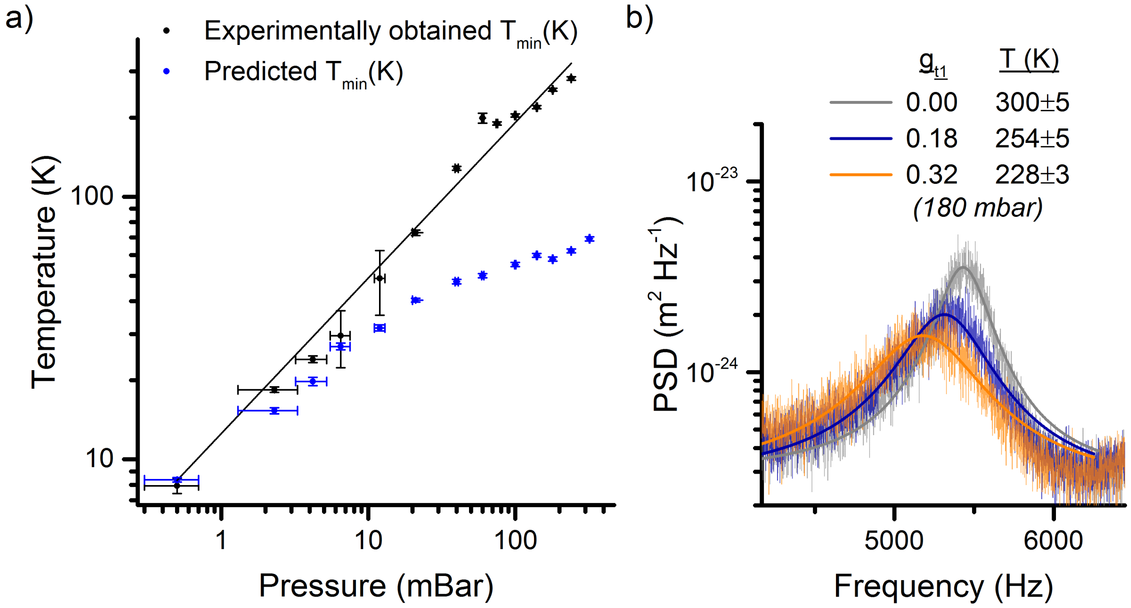

Figure 4.8: a) The minimum experimentally cooled temperature for eigenmode 8 of taper[$\mathcal{B}$], plotted against the background gas pressure (black data points). The predicted minimum temperature (blue points) is calculated using eq. 4.20 and the reference PSD ($g = 0$) at each pressure. Errors are obtained from the fit of eq. 4.19. The experimental values agree with prediction at pressures below 10 mbar only when Q_m is increased. At higher pressures, the balance of thermal excitation and damping from the surrounding gas can be larger than the power limited CEODF. b) Cooling of mode t1 at 180 mbar, where the maximum feedback gain (limited by the servo amplifier and the power coupled to the WGM), does not cool the mode to the noise floor.

It can be seen that at 180 mbar, plotted as an inset in fig. 4.8, the available feedback gain has saturated (i.e. the maximum amplification of the feedback signal to modulate the CEODF prior to causing the feedback to become unstable), but the mechanical mode is far from cooled to the noise floor. This is because the amplitude of the CEODF is too low to continuously damp the remaining thermal excitation provided by the background gas. Increasing the CEODF by using higher laser powers often causes the taper to melt, although this can be prevented when operating in clean room standard conditions. The minimum temperature limit is therefore not met until a pressure below 10 mbar. The non-linear shape of the predicted $\mathrm{T_{min}}$ in fig. 4.8 is related to the changing noise floor which decreases as the pressure is lowered due to less background gas, and the large errors for the experimentally measured $\mathrm{T_{min}}$ data points around 10 mbar is related to changes in the pressure during the measurement time as data is taken whilst the roughing pump is momentarily switched off, as discussed in chapter 3, section 3.7.

4.4.3 Time Delay & Classical Noise in Active Cooling

In this section, modifications to the cooling performance from the feedback loop itself are explored. Two effects are experimentally investigated; time delays that modify the oscillator response, and classical noise from electronics that define the imprecision noise level $S_{\mathrm{imp},xx}(\omega)$. The latter effect is important at high feedback gain when the damped motion, $S_{xx}^{\mathrm{fb,imp}}(\omega)$, becomes comparable to the imprecision noise $S_{\mathrm{imp},xx}(\omega)$.

Delayed Feedback

The effect of time (phase) delays when an older differentiator is used for CEODF cooling of taper modes in fig. 4.7 is seen to shift the mechanical frequency as feedback is applied. Time delays cause unsynchronized application of the feedback force which can degrade the cooling performance as well as induce spring softening or stiffening [53], similar to the optical spring effect [187].

In order to include the effect of a time delay τ, the trial solution for the feedback transfer function is given by:

$$\mathrm{H}^{\mathrm{fb},\tau} = \Gamma_0 \Omega_{\mathrm{m}} \, e^{-i\omega\tau}, \tag{4.22}$$

where Γ_0 is the damping rate, Ω_{m} is the mechanical frequency, and the Fourier transform of a time delayed signal $\mathcal{F}\left[x(t-\tau)\right] = \delta x(\omega) e^{-i\omega\tau}$, is used. Therefore following the procedure used earlier in this chapter to derive the PSD of the mechanical oscillator with instantaneous feedback, the PSD when time delays are present is:

$$S^{\mathrm{fb},\tau}(\omega) = \frac{1}{m_{\mathrm{eff}}} \frac{S_{\mathrm{F}}^{\mathrm{th}}(\omega)}{\left[\Omega_{\mathrm{m}}^{2}\left(1 - \frac{\Gamma_0}{\Omega_{\mathrm{m}}} g \cos\left(\Omega_{\mathrm{m}}\tau\right)\right) - \omega^{2}\right]^{2} + \omega^{2}\Gamma_0^{2}\left(1 + g\sin\left(\Omega_{\mathrm{m}}\tau\right)\right)^{2}}, \tag{4.23}$$

where exponential functions have been replaced with cosine and sine expressions, and the substitution $g^2\Omega_{\mathrm{m}}^2\Gamma_0^2 = g^2\Omega_{\mathrm{m}}^2\Gamma_0^2\left(\sin^2\left(\Omega_{\mathrm{m}}\tau\right) + \cos^2\left(\Omega_{\mathrm{m}}\tau\right)\right)$ is used such that eq. 4.23 is factorised in terms of $(\Omega_{\mathrm{m}}^2 - \omega^2)$, and $\omega^2\Gamma_0^2$.

When $\tau = \frac{\pi}{2\Omega_{\mathrm{m}}}$ (i.e. instantaneous differential feedback) the original feedback PSD of eq. 4.8 is obtained. If $\tau > \frac{\pi}{2\Omega_{\mathrm{m}}}$ a time delayed differential feedback is applied, where a new parameter $\tau_v = \tau - \frac{\pi}{2\Omega_{\mathrm{m}}}$ can be used to define the delay with respect to instantaneous differential feedback. The effective damping factor $\Gamma_{\mathrm{eff}}^{\mathrm{fb},\tau_{\mathrm{v}}}$, and an effective mechanical frequency $\Omega_{\mathrm{eff}}^{\mathrm{fb},\tau_{\mathrm{v}}}$, for a constant time delay τ_{v} is therefore:

$$\Gamma_{\mathrm{eff}}^{\mathrm{fb},\tau_{\mathrm{v}}} = \Gamma_0\left(1 + g\cos\left(\Omega_{\mathrm{m}}\tau_v\right)\right), \tag{4.24}$$

$$\Omega_{\mathrm{eff}}^{\mathrm{fb},\tau_{\mathrm{v}}} = \Omega_{\mathrm{m}}\sqrt{1 + \frac{g}{\mathrm{Q_m}}\sin\left(\Omega_{\mathrm{m}}\tau_v\right)}. \tag{4.25}$$

A plot of these equations is shown in fig. 4.9 for $\Omega_{\mathrm{m}} = 4\,\mathrm{kHz}$:

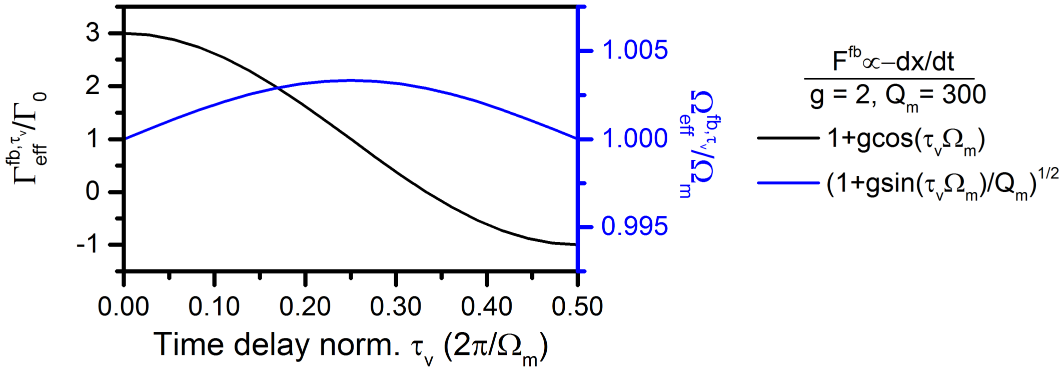

Figure 4.9: The normalised effective damping factor $\frac{\Gamma_{\mathrm{eff}}^{\mathrm{fb},\tau_v}}{\Gamma_0}$ (black), and the normalised effective mechanical frequency $\frac{\Omega_{\mathrm{eff}}}{\Omega_{\mathrm{m},\tau_v}^{\mathrm{fb}}}$ (blue) is modelled against the time delay (normalised to the mechanical oscillation period) for differential active feedback cooling using a feedback gain of $g = 2$.

In order to verify this dependence on time delay, a phase shifter is inserted into the piezo-stack feedback loop and feedback cooling is applied to the microsphere-cantilever labelled microsphere-cantilever[$\mathcal{C}$] with $\Omega_{\mathrm{m}} = 4\,\mathrm{kHz}$. The experiment is conducted at atmospheric pressure. Due to the order of conducting the experiments, the older differentiator with an inherent 24 degree phase delay at 4 kHz is used. This differentiator is responsible for the optical stiffening of the cooled taper[$\mathcal{B}$] modes (i.e. increase in Ω_m) in fig. 4.7. Only additional incremental time delays can be introduced as the 24 degree phase shift associated with the time delay cannot be reduced[11].

The piezo-stack feedback loop is switched on and feedback is applied at a fixed amplification of the servo (note that this proportionally controls the feedback gain, g, which is further modified by the time delay). The time delay is varied by increasing the phase shift[12]. The resulting PSDs are shown in figs. 4.10 a) & b), for negative differential feedback (damping) and positive differential feedback (heating) respectively.

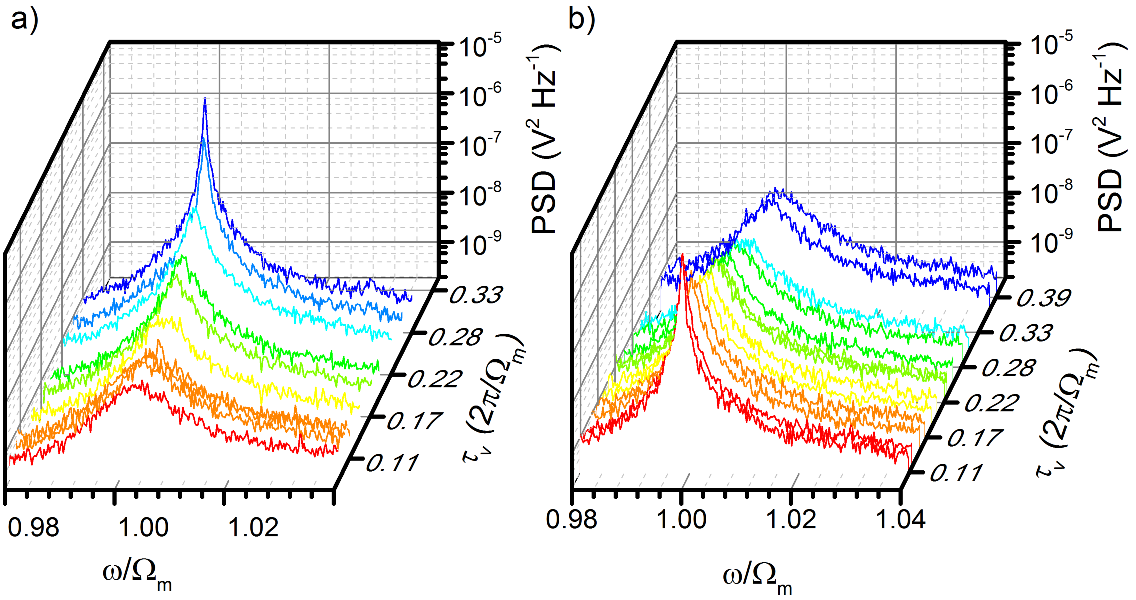

Figure 4.10: Experimental data using microsphere-cantilever[$\mathcal{C}$] showing the effect on the c.o.m. motion when further time delay, τ_v, is introduced for a) negative velocity feedback (i.e. primarily damping) and b) positive negative feedback (i.e. primarily heating). The servo sets a fixed amplifier gain which controls the gain, g. Cooling, heating, spring stiffening and spring softening can be obtained.

Here, it can be seen that the system undergoes spring softening (decrease in Ω_m) and spring stiffening (increase in Ω_m), for both cooling and heating regimes. This could have applications in strategic modification of the spring for sensing, to avoid cross coupling or to aid cooling to lower temperatures in conjunction with passive cooling [188–190]. The increase in mechanical frequency from spring stiffening increases the number of oscillations such that the measurement time window i.e. the period of oscillation, is longer[13]. The

---

[11] In latter experiments, the newer differentiator had a 9 degree phase delay which leads to $< 10\,\mathrm{Hz}$ shifting of the centre frequency in figs. 4.6 & 4.13.

[12] The phase shifter is optimized for the 4 kHz fundamental frequency so that a linear relationship between phase shift and time delay is met.

[13] If the oscillator is cooled to its mechanical quantum ground state, this corresponds to a longer decoherence time [189]

effective damping factor, $\Gamma_{\rm eff}^{{\rm fb},\tau_{\rm v}}$, and effective mechanical frequency, $\Omega_{\rm eff}^{{\rm fb},\tau_{\rm v}}$, are extracted from fig. 4.10 by fitting with eq. 4.21 and plotted in fig. 4.11. Errors are obtained from the fit. The time delay is calibrated by sending a sinusoidal voltage from a function generator (with frequency approximately equal to $\Omega_{\rm m}$) into the differentiator and phase shifter, and measuring the resultant delay.

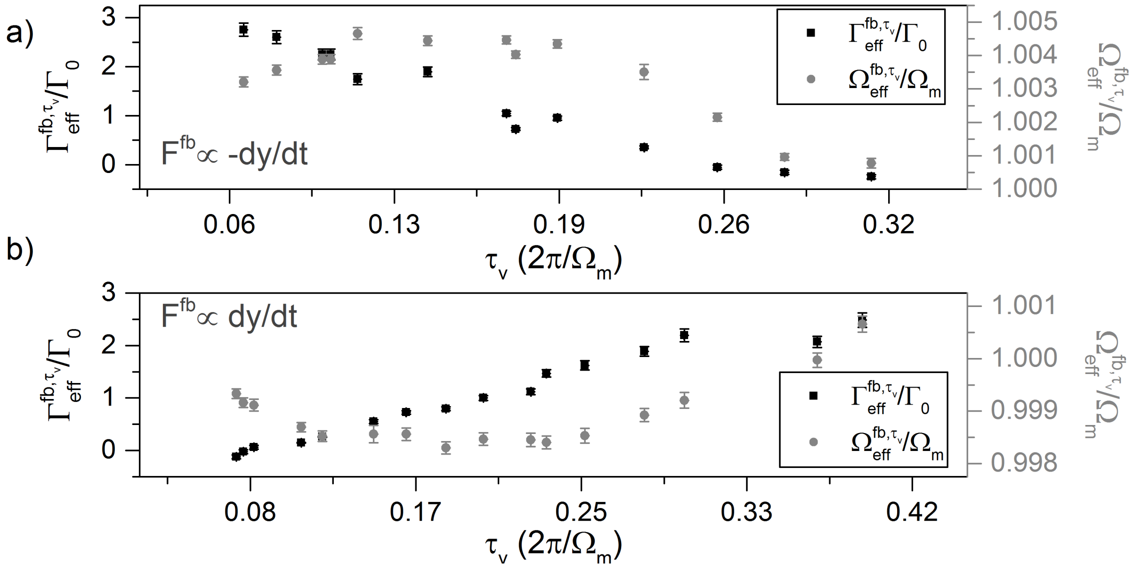

Figure 4.11: The effective damping rate $\Gamma_{\rm eff}$ and mechanical frequency $\Omega_{\rm eff}$ of fig. 4.10 for a) negative velocity feedback and b) positive velocity feedback are found by fitting with eq. 4.21. Errors are obtained from the fit. As the time delay is increased, a) ,b) show a change in damping with a corresponding shift of $\Omega_{\rm eff}$ representing spring stiffening and spring softening such that a) undergoes spring stiffening and transitions from primarily cooling $\frac{\Gamma_{\rm eff}^{{\rm fb},\tau_{\rm v}}}{\Gamma_0} > 0$ to heating $\frac{\Gamma_{\rm eff}^{{\rm fb},\tau_{\rm v}}}{\Gamma_0} < 0$. b) shows the opposite behaviour.

From figs. 4.11 a) & b) it can be seen that an approximate quadratic relationship for $\Omega_{\rm eff}^{{\rm fb},\tau_{\rm v}}$, and a linear relationship for $\Gamma_{\rm eff}^{{\rm fb},\tau_{\rm v}}$ exists, in good agreement with the simulation in fig. 4.9 if one considers these as approximated portions of an overall sinusoidal relationship. However, the turning point of $\frac{\Gamma_{\rm eff}^{{\rm fb},\tau_{\rm v}}}{\Gamma_0}$ in fig. 4.11 a) occurs before the expected time delay of $0.25\times\frac{2\pi}{\Omega_{\rm m}}$, indicating that another source of delay is present in the overall feedback loop. A similar, but much less pronounced effect is also seen in fig. 4.11 b).

For negative differential feedback, time delays reduce $\Gamma_{\rm eff}^{{\rm fb},\tau_{\rm v}}$ because the cooling force is applied when the resonator motion has already advanced, leading to a displacement-proportional component that degrades the cooling performance. Theoretically, a negative velocity feedback loop with a time delay of an entire period, or a positive velocity feedback with a delay of half a period, could be as effective as a instantaneous negative velocity feedback, but requires the oscillator motion to be truly harmonic [53, 191].

Squashing via Feedback

As shown at the beginning of this chapter, the total noise of the feedback loop, known as the imprecision noise $S_{\mathrm{imp},xx}(\omega)$, can modify the mechanical oscillator motion at high feedback gains when the motion $S_{xx}^{\mathrm{fb,imp}}(\omega)$ becomes comparable to $S_{\mathrm{imp},xx}(\omega)$. The influence of noise on the *actual* mechanical motion was simulated in fig. 4.2 by using eq. 4.16. Once thermal fluctuations are cooled to the imprecision noise level, the system starts to send this noise into the feedback loop, which drives the mechanical oscillator to a higher mode temperature. Since this noise driven motion is then detected and fed back into the feedback loop where the noise source originates from, the *detected* PSD, $S_{\mathrm{det},xx}^{\mathrm{fb,imp}}(\omega)$, has a different lineshape to the *actual* oscillator PSD, $S_{xx}^{\mathrm{fb,imp}}(\omega)$. This is because of correlations between the injected feedback noise and the oscillator motion that cause a phenomena known as 'squashing', where the mechanical mode PSD becomes inverted below the noise floor [1, 17, 31, 53]. At this stage, the PSD cannot be fitted with eq. 4.19. The imprinting of noise onto the oscillator motion is an indication that the minimum cooled temperature defined by eq. 4.20, that depends on $S_{\mathrm{imp},xx}(\omega)$, has been surpassed.

Ideally, noise from electronics can be suppressed such that the dominant noise source is from the primary detection system (i.e. the light field), at the quantum shot-noise limit, discussed in chapter 3. When $S_{\mathrm{det},xx}^{\mathrm{fb,imp}}(\omega)$ reaches $S_{\mathrm{imp},xx}(\omega)$, the *detected* motion deviates such that the measured PSD cannot be used to infer the mode temperature of the *actual* motion, i.e. $S_{\mathrm{det},xx}^{\mathrm{fb,imp}} \neq S_{xx}^{\mathrm{fb,imp}}$. A new form of the detected PSD is required which is derived as follows; at high gain the *measurement* of the oscillator motion under feedback (including the backaction heating effect of the imprecision noise, derived in eq. 4.14), is modified by inclusion of the measurement uncertainty:

$$\delta x_{\mathrm{det}}(\omega) = \delta x_{\mathrm{imp}}(\omega) + \chi_{\mathrm{eff}}(\omega)\left[\mathcal{F}^{\mathrm{th}}(\omega) + g\mathrm{H}^{\mathrm{fb}}(\omega)\delta x_{\mathrm{imp}}(\omega)\right], \tag{4.26}$$

$$\delta x_{\mathrm{det}}(\omega) = \delta x_{\mathrm{imp}}(\omega)\left[1 + \chi_{\mathrm{eff}}(\omega)g\mathrm{H}^{\mathrm{fb}}(\omega)\right] + \chi_{\mathrm{eff}}(\omega)\mathcal{F}^{\mathrm{th}}(\omega), \tag{4.27}$$

where $\mathrm{H}^{\mathrm{fb}}(\omega)$ is the feedback transfer function, and $\left[1 + \chi_{\mathrm{eff}}(\omega)g\mathrm{H}^{\mathrm{fb}}(\omega)\right] = \frac{\chi_{\mathrm{eff}}(\omega)}{\chi_{\mathrm{m}}(\omega)}$ using eq. 4.5. The PSD of eq. 4.27 is therefore given by [53, 149]:

$$S_{\mathrm{det},xx}^{\mathrm{fb,imp*}}(\omega) = \frac{\mathcal{F}^{\mathrm{th}}(\omega) + \left|m_{\mathrm{eff}}(\Omega_{\mathrm{m}}^2 - \omega^2 + i\omega\Gamma_0)\right|^2 S_{\mathrm{imp},xx}(\omega)}{\left|m_{\mathrm{eff}}(\Omega_{\mathrm{m}}^2 - \omega^2 + i\omega\Gamma_0 - g\mathrm{H}^{\mathrm{fb}}(\omega))\right|^2}, \tag{4.28}$$

which, for differential feedback cooling, can be written as a PSD fitting function [17, 31]:

$$S^{\text{fb,imp}*}_{\text{det},xx}(\omega) = S^{\text{fb,imp}}_{\text{det},xx}(\omega) + S_{\text{imp},xx}(\omega)\frac{(\Omega_{\text{m}}^2-\omega^2)^2+\Gamma_0^2\omega^2}{(\Omega_{\text{m}}^2-\omega^2)^2+(1+g)^2\Gamma_0^2\omega^2}, \tag{4.29}$$

where $S^{\text{fb,imp}}_{\text{det},xx}(\omega)$ is defined previously for feedback without squashing, in eq. 4.19. The effective mode temperature when squashing is present for high feedback gain is given by [31]:

$$\text{T}^{\text{fb}}_{\text{det}} = \frac{\text{T}_0}{1+g} + \frac{g^2}{1+g}\frac{k\Omega_{\text{m}}S_{\text{imp},xx}(\omega)}{4\text{k}_{\text{B}}\text{Q}_{\text{m}}}. \tag{4.30}$$

A simulation of the *detected* PSD, eq. 4.29, for $\text{Q}_{\text{m}} = 500$, $S_{\text{imp},xx} = 10^2$, and gains between $0 \leq g \leq 0.4$, scaled by $S^{\text{th}}_{xx}(\omega)/(m_{\text{eff}}\Omega_{\text{m}}^2)^2$ is shown in fig. 4.12. The effect of squashing occurs when $g > 0.1$:

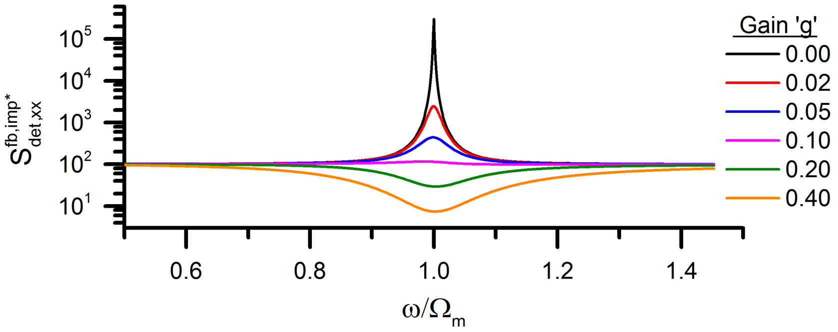

Figure 4.12: Simulated *detected* PSD for negative velocity feedback using eq. 4.29, in constrast with the *actual* PSD in fig. 4.2 a). The same variables are used whereby $\text{Q}_{\text{m}} = 500$, $S_{\text{imp},xx} = 10^2$ and scaled by $S^{\text{th}}/(m_{\text{eff}}\Omega_{\text{m}}^2)^2$. At $g \geq 0.1$ the PSD is inverted below the noise floor, which would suggest an imaginary or negative temperature that is clearly unphysical.

By using a microsphere-cantilever with a lower mechanical Q_{m} of 280 and a higher electronic noise floor due to a noisy differentiator (microsphere-cantilever[$\mathcal{D}$]), the effect of squashing at high feedback gain is experimentally demonstrated in fig. 4.13 a). The noise floor of fig. 4.13 a) is 4 times higher than in fig. 4.5[14]. Increasing the gain beyond the cooling limit pushes the *detected* thermal noise spectra below the measurement noise.

In fig. 4.13 b) the extrapolated cooled temperatures from experiment (fig. 4.13 a) black data points), are plotted alongside the predicted temperature given by eq. 4.30 (black line) at each feedback gain g, which has a turning point at the minimum temperature (22.3 K). Also plotted in blue is the predicted temperature *if* the imprecision noise is zero (in this case, $\text{T}_0(1+g)$ remains valid). The various noise sources of the experiment are

---

[14] Squashing could not be obtained for microspher-cantilever[A] due to a parasitic mode that is amplified prior to reaching this lower noise floor.

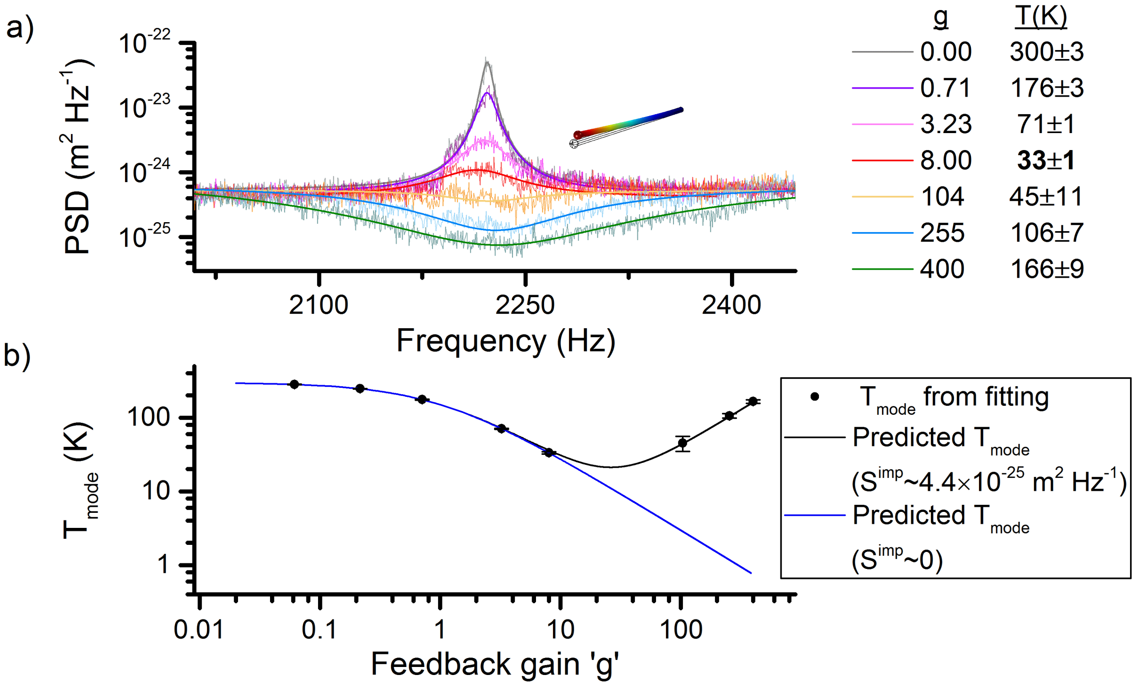

Figure 4.13: a) Piezo-stack cooling of the c.o.m. mode of microsphere-cantilever[$\mathcal{D}$] with a lower $Q_m = 280$ than in fig. 4.5 and 4× higher noise floor, showing squashing with large feedback gain, g. Data was taken at atmospheric pressure, with curves fitted using eq. 4.21 for low gains and eq. 4.29 for squashed data at $g > 8$ (alongside eq. 4.30 to infer the temperature). Errors are from fitting. In b) is shown the experimentally measured mode temperature as a function of the feedback gain g (black data points), the predicted mode temperature using eq. 4.30 (black line), and the equivalent temperature if negligible imprecision noise floor is present i.e. $T_0(1 + g)$ is valid (blue line).

investigated in section 4.5 of this chapter.

4.4.4 Simultaneous Cooling of Two Separate Mechanical Oscillators

Simultaneous operation of both feedback cooling schemes is demonstrated in this section. The performance for simultaneous cooling is not as efficient as the cooling of each mode separately. This is because the bandwidth of the feedback system is not narrow enough to isolate only one mechanical mode. This leads to crosstalk in the feedback signals sent to the piezo-stack and for CEODF modulation. It is possible to remove cross-talk or parasitic noise with filters, but it was found that filters added background noise and extra delays, in agreement with experiments in [53] where the response of the actuation force became modified and distorted with electronic filters.

Instead, simultaneous cooling of microsphere-cantilever[$\mathcal{C}$] and a new taper (taper[$\mathcal{C}$]) is conducted where the mechanical modes belonging to both oscillators are less than 250 Hz apart in frequency, and fewer parasitic modes are present in the PSD. This system is chosen to demonstrate that the same transduction signal can be used to cool two separate mechanical oscillators when the elimination of cross-talk by using filters is not possible. Cooling of this system is presented in the PSDs in figs. 4.14 a) & b) where a phase shifter is used to modify the relative cooling efficiencies. Fitting the PSD can be achieved using the equation:

$$S_{xx}^{\mathrm{fb,sim}}(\omega) = \sum_{n=1}^{n=2} \frac{2\Gamma_{0,n}\mathrm{k_B T_0}}{m_{\mathrm{eff,n}}} \frac{1}{(\Omega_{\mathrm{m,n}}^2 - \omega^2)^2 + (1+g_n)^2\Gamma_{0,n}^2\omega^2} + S_{\mathrm{imp},xx}(\omega), \tag{4.31}$$

which is simply the sum of two feedback cooled modes, and it is assumed the imprecision noise is low.

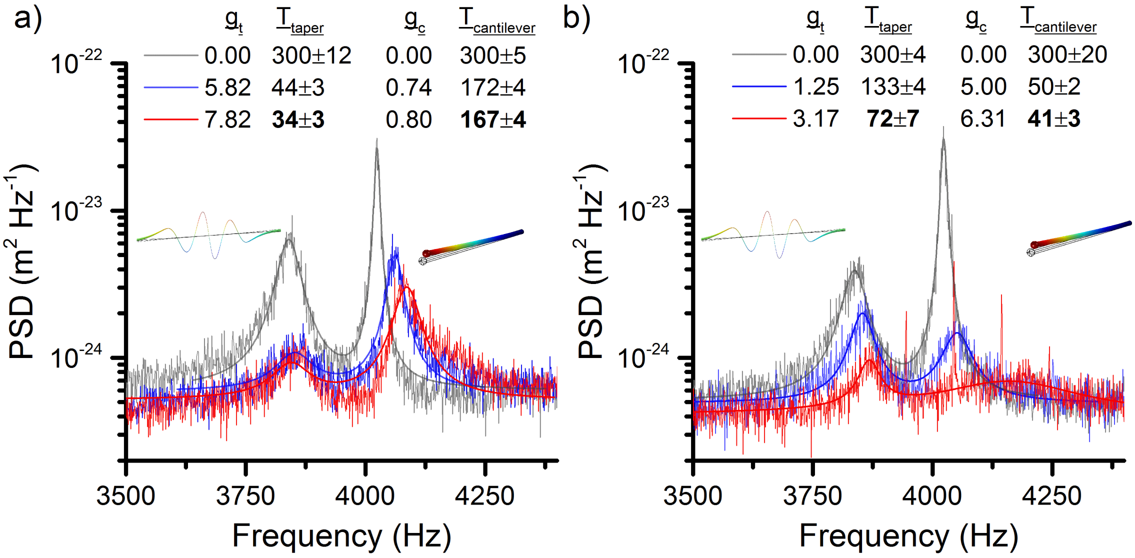

Figure 4.14: Simultaneous feedback cooling of coupled oscillators (microsphere-cantilever[$\mathcal{C}$], taper[$\mathcal{C}$]) at atmospheric pressure. The use of a phase shifter can allow for preferential cooling of either the a) taper mode at 3.8 kHz using the CEODF or b) the c.o.m. motion of microsphere-cantilever at 4 kHz using PZT cooling. Fitting can be achieved using eq. 4.31, however, the damping rate Γ_{eff} of the non-preferentially cooled oscillator does not agree with prediction due to distortion of the mode shape.

In figs. 4.14 a) & b) the simultaneous cooling curves of the same system are presented where time delays are adjusted to optimise cooling of either a) the tapered fibre mode, or, b) the microsphere-cantilever mode. The use of time delays allow for minimisation of cross-talk by shifting the centre frequencies away from one another to avoid distorting the other oscillators' PSD peak. The fitting of eq. 4.31 confirmed this distortion as the damping factor, Γ_{eff}, and effective mode temperature, $\mathrm{T_{eff}}$, did not obey $(g+1) = \frac{\Gamma_{\mathrm{eff}}}{\Gamma_0} = \frac{\mathrm{T_0}}{\mathrm{T_{eff}}}$, which can occur with multimode systems [145]. This is due to the interplay between the feedback schemes which rely on the transduction signal that measures *relative* displacement changes between these two separate oscillators.

In fig. 4.15 a), the same plot of fig. 4.14 b) is shown except the mode temperatures are inferred by integrating the area, which was in good agreement with the fitting of fig. 4.14 b). Such a coupled system requires further investigation, but using experimental data shown in fig. 4.15 b), it is observed that each individual feedback scheme has an effect on the apparent mechanical damping factor and centre frequency of the other oscillator.

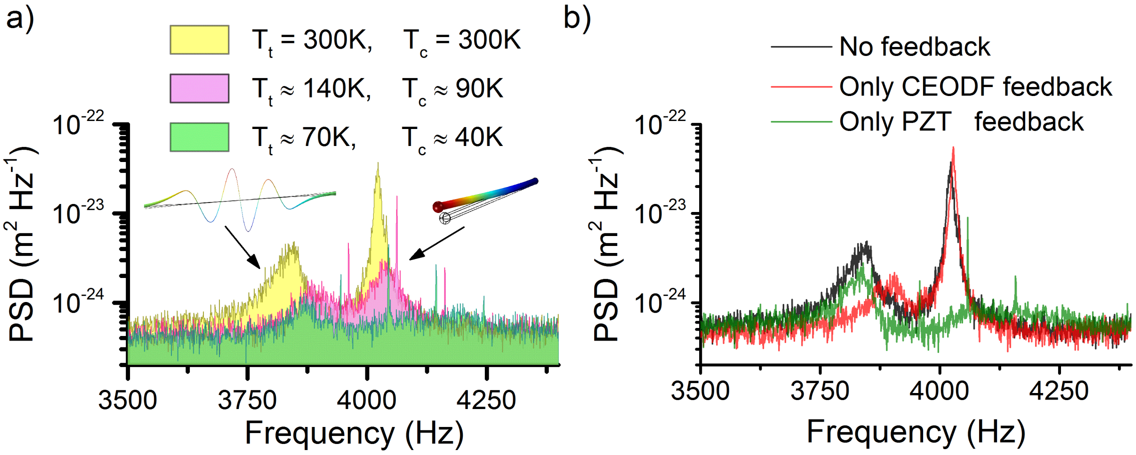

Figure 4.15: a) The inferred mode temperature for the taper mode, T_t, and microsphere-cantilever, T_c, of fig. 4.14 b) by integrating the area under the respective PSD peaks. This is in good agreement with the fitted temperatures of fig. 4.14 b). The influence of each singular feedback loop for such overlapped modes is shown in b) where cooling either oscillator influences the transduced PSD lineshape of the other.

The study of coupled oscillators has importance within optomechanical systems employing waveguide structures or hybrid schemes, where multiple mechanical modes are coupled by light. The cooling of mechanical modes belonging to two different structures has not been demonstrated until now. The tapered optical fibre, for example, is used in nearly all WGM experiments, as well as for coupling to cold atoms [192], or to photonic crystals for sensing [12]. Mechanical noise in the form of the taper modes can be troublesome for sensing applications as highlighted in [12], where the spectrum of modes creates a non-flat background noise floor, and can limit cooling efficiency. Coupled mechanical modes belonging to separate oscillators has been studied elsewhere in [193] where tunable optical coupling can switch between coupled (synchronised), and individual oscillation states. This type of behaviour has not been studied with the microsphere-cantilever system but could be explored in future experiments, and may have applications for timing measurements.

4.5 Noise Sources

Since it has been identified that active feedback is limited by the noise floor of the system, one must consider how to improve the cooling limit by lowering the noise. The absolute noise limit will be the quantum shot-noise of the laser itself, discussed in chapter 3, which limits many optomechanical systems that use passive [46, 194] and feedback cooling [31, 39], but can provide displacement sensitivities on the order of $10^{-19}\,\mathrm{m\,Hz^{-1/2}}$ [179, 195, 196], a factor of 10^7 more sensitive than obtained in this thesis.

It was shown earlier in this chapter that the role of the active feedback loop has a large impact on the cooling dynamics of the system, and components within the loop supply noise that are directly fed into the resonator motion. Sources of noise are contributed by the photodetector, the differentiator, the servo, the piezostack used to modulate the position of the microsphere-cantilever, and the AOM used to modulate the power of the locking beam. Since the Newport LB1005 servo has a low voltage noise density of $10\,\mathrm{nV\,Hz^{-1/2}}$ and the AOM used for modulation of the strong beam is uncoupled from the transduction beam[15], these can be eliminated as dominant noise sources.

The noise output of the other electronic components and the laser itself are experimentally deduced by measurement. The PC oscilloscope is used to record 30 traces of the voltage output of each noise source, which are then converted into an averaged displacement PSD. Those of importance, which are shown in in fig. 4.16 are listed below:

- The PSD of the transduction beam (red), which includes all noise sources as well as the thermal mechanical motion of both the tapered fibre and microsphere-cantilever. This is effectively a sum of all the noise sources present in the system.
- The photodetector noise level at the typical transduction beam laser power ($70\,\mu$W) and photodetector gain setting (40 dB) (orange).
- The output noise of the piezo-driver (purple), driven by the DC voltage output of the servo, and is converted into the resultant piezo-stack displacement noise (i.e. the actuation caused by the piezo-driver noise).
- The output noise of the differentiators used during this project, in particular, the old differentiator ‘differentiator 1’ (cyan) had a much higher noise output than the newer differentiator labelled as ‘differentiator 2’ (green).

---

[15] The strong beam and the transduction beam can be considered de-coupled as they counterpropagate through the tapered fibre and excite degenerate clockwise/anti-clockwise WGMs. Occasionally interference or leakage can occur but often cause less than 5 % signal cross-talk.

- The photodetector at 0 dB gain setting, which has an increased bandwidth from 200 kHz to 10 MHz in order to measure the relaxation oscillation peak of the laser (prior to any optics/coupled into the tapered fibre), shown as an inset graph. This is represented as an equivalent PSD (black data).
- An estimation of the laser shot-noise level (blue line), calculated by fitting the relaxation oscillation peak of the laser (inset). An estimation of the classical laser noise if the laser is pumped with a shot-noise limited source is also shown (red line), found by extrapolating the relaxation peak fit towards lower frequencies. Both estimations of the laser shot-noise and classical noise are converted to the corresponding displacement noise floor level. The procedure for this is detailed below.
- The noise floor of the PC oscilloscope is also shown (grey), which is lower than all noise sources measured.

A rough estimation of the laser shot-noise and classical laser noise is found by fitting the relaxation oscillation peak of the laser output (inset of fig. 4.16) with a fitting function that defines its PSD [197, 198]:

$$S_{\mathrm{ro}}(\omega) = P_0 \frac{A\omega^2 + B}{(\omega_{\mathrm{ro}}^2 + \Gamma^2 - \omega^2)^2 + 4\Gamma^2\omega^2} + c, \tag{4.32}$$

where A, B are fitting constants, ω_{ro} the relaxation oscillation frequency, Γ the damping, and c is the background noise level. The fitted noise floor, c, corresponds to a displacement noise PSD of $2.0 \times 10^{-28}\,\mathrm{m}^2\,\mathrm{Hz}^{-1}$.

From fig. 4.16, the piezo driver and the photodetector are primarily the main sources of noise. In future experiments the photodetector can either be replaced with a temperature controlled photodetector which reduced thermal noise, or, a balanced detector or homodyne detection scheme which eliminates classical frequency noise of the laser from the measurement. However, in order to reach an imprecision defined only by the laser shot-noise, the differentiator noise (cyan and green data in fig. 4.16) as well as the classical laser intensity noise (shown in red, and likely to originate from the pumping source), will also need to be lowered considerably by re-designing the differentiator and using feedback to stabilise the laser output itself [165]. The relaxation oscillation is a noise source that can also be reduced by over 37 dB [199] by feedback methods. At the low frequency range considered here (<10 kHz) there is also noise associated with thermorefractive noise

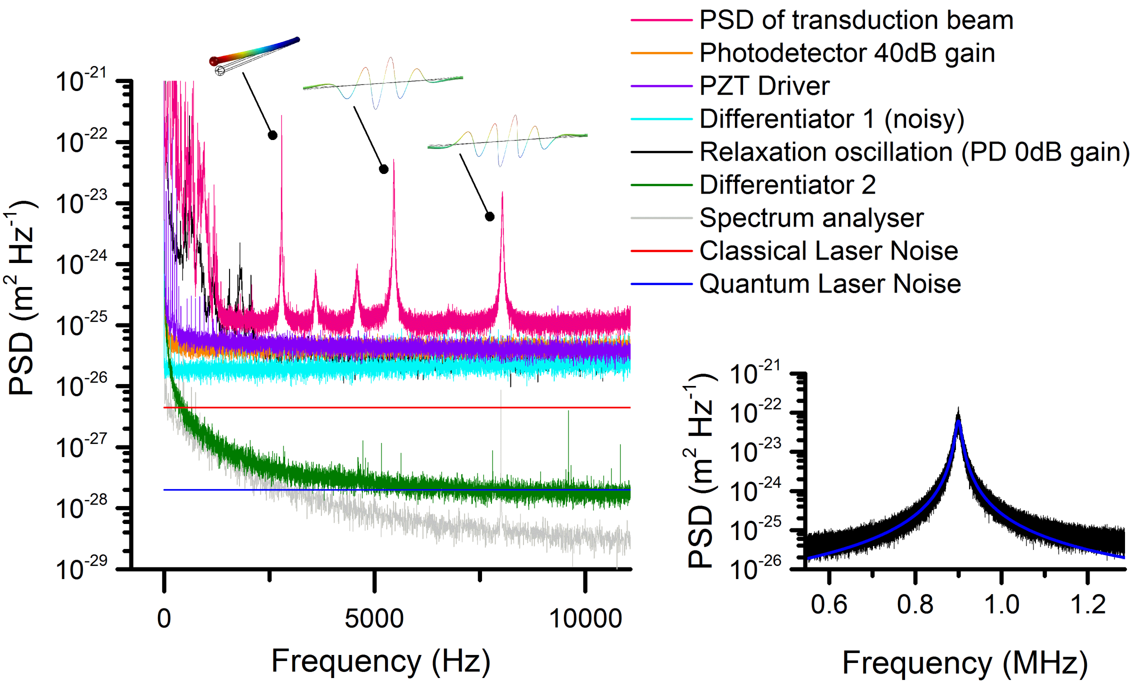

Figure 4.16: The main contributing noise sources are measured and converted to an equivalent PSD. The photodetector and the PZT driver are the main sources of noise, which sets the transduction signal background noise floor 54.9 dB above the extrapolated laser shot-noise, $S_{sn,xx}$. The dB value is found using $10\log_{10}\frac{S^{\text{imp}}_{\text{det},xx}}{S_{sn,xx}}$. Classical sources of noise imprinted onto the laser intensity are 26.9 dB above the laser shot-noise, and represent noise that can be reduced using laser stabilisation methods such as those discussed in chapter 3. The extrapolated laser shot-noise is found by fitting the relaxation oscillation (inset). The relaxation oscillation also sets the classical background laser noise level.

and 1/f noise. Thermorefractive noise[16] occurs due to temperature variations that induce fluctuations in the cavity refractive index and size (i.e. the thermo-optic effect)[200], as well as negligible variations in the resonance linewidth [63, 134]. Such an issue does not add noise if the mechanical frequencies are in the 100's kHz to MHz range. Phase noise due to temperature fluctuations within the tapered fibre from weakening of the fibre after heating and pulling should be investigated in the future, as it can present itself as intensity noise [201].

As well as reducing classical noise, the displacement sensitivity can be further increased by tuning the transduction efficiency, which is proportional to the optical Q of the WGM. Since WGMs with linewidths of between 80-500 MHz are usually employed here, the transduction scaling (i.e. Watts per m, measured by the photodetector) can be improved by up to a factor of 100, if using the narrowest WGM that has been previously excited (5MHz FWHM). Using an improved PDH locking method that is not sensitive to

---

[16] There is also thermoeleastic noise which is negligible relative to thermorefractive noise [128]

amplitude fluctuations will aid such a scheme. If the background noise level is reduced to $1 \times 10^{-30}\,\mathrm{m}^2\,\mathrm{Hz}^{-1}$, the minimum temperature for eigenmode 8 (5.5 kHz) of taper[$\mathcal{B}$], and the c.o.m. mode (2.8 kHz) of microsphere-cantilever[$\mathcal{A}$], is 20 mK and 30 mK respectively, which is still a factor of 10^5 away from being cooled to the zero point motion at $\mathrm{T}_{\mathrm{zpf}} \approx \frac{\hbar\Omega_{\mathrm{m}}}{\mathrm{k}_{\mathrm{B}}}$, and requires cryogenic operation or tailoring of the mechanical oscillator (i.e. Ω_{m}) for further cooling.

4.6 Conclusion

In conclusion, feedback cooling of two micron-scale, microgram, coupled mechanical oscillators using a WGM resonance is experimentally implemented. Mechanical modes belonging to the microsphere-cantilever and the tapered optical fibre can be individually cooled to below 10K, representing position stabilization on the picometer scale, comparable to the diameter of a single atom. The mechanical taper modes can be troublesome for any hybrid WGM system using tapered fibre coupling where the taper mode spectrum is present [12, 136], and direct cooling of these modes has not previously been demonstrated. The minimum phonon occupancy n_{min} can be derived from the predicted minimum cooled temperature (eq. 4.20) as $n_{\mathrm{min}} = \frac{1}{\hbar}\sqrt{\frac{k\mathrm{k}_{\mathrm{B}}\mathrm{T}_0 S^{\mathrm{imp}}}{\Omega_{\mathrm{m}} Q_{\mathrm{m}}}}$ [31], which implies a minimum phonon occupancy for the microsphere-cantilever mode at 2.8 kHz (fig. 4.5) of 8.5×10^7, and $\bar{n}_{\mathrm{min}} = 3.1 \times 10^7$ for the taper mode at 5.5 kHz. Both values are far from obtaining a quantum state, but demonstrate the feasibility of using WGM enhanced transduction and WGM enhanced optical dipole forces for cooling.

The role of the feedback loop is explored by introducing time delays that apply cooling whilst also causing spring softening of stiffening, in good agreement with theoretical predictions. It was shown that time delays reduce the effective feedback damping rate therefore future experiments require further optimisation of the differentiator such that instantaneous differentiation can be obtained, especially important when using higher frequency mechanical oscillators. The onset of squashing, where the detected PSD becomes inverted below the imprecision noise level, is experimentally demonstrated when noise within the system is fed into the mechanical oscillator, and defines reaching the cooling limit. Both oscillators can be cooled simultaneously, stabilizing the coupling distance, which enhances the potential to use the cooled system for ultraprecise closed-loop force sensing. Although there is no improvement in acceleration sensing (discussed in chapter 6), the increased damping rate and the broadening of the mode increases the sensing bandwidth and allows for periodic measurements (where cooling is switched on and off) since the cooling is faster than the heating from air [181][17], and the system responds faster to external forces allowing shorter integration times [19]. The modification of Q_m through damping has applications for AFM probing of soft biological samples like DNA which can be prone to deformation from the tip-sample force if the thermal motion of the AFM tip is large [147].

Currently, the cooling presented in this thesis is limited by detection noise and the low Q_m of the oscillators. However, the ability to cool the c.o.m. motion of objects within this intermediate size and mass scale has not been fully investigated, and is attractive for creating macroscopic quantum objects at the Planck mass to test gravitationally induced collapse [202]. The steps that can be taken to cool oscillators of this size more effectively are to increase Ω_m and Q_m of the oscillators (described in chapter 7), reduce the noise within the system, and increase the transduction sensitivity. Noise reduction strategies are easier in principle to apply, and feedback schemes to lower the classical fluctuations of the laser can be implemented using a noise eater or other servo design [165, 203]. Increasing the transduction sensitivity by choosing higher optical Q WGMs, which in the literature can be as high as 6×10^{10} [204], will improve the ability to resolve smaller fluctuations. However, other enhancements can be made by the inclusion of quantum point contact (QPC) transducers [205], plasmonics [206, 207] or single-electron transistors [208, 209] to improve the transduction mechanism.

---

[17] If the measurement is performed within one oscillation after switching off cooling, the temperature increases by approx $2\pi T_0/Q_m$ at the end of the measurement window

Chapter 5

Passive Cooling

5.1 Introduction

Active cooling using feedback electronics, as demonstrated in chapter 4, is only one method to damp the thermal motion of a mechanical oscillator. Passive cooling, where electronic control is not required to drive the actuating force, can also be implemented. This type of cooling can be preferable to active methods as less components are needed, and may have reduced noise. Instead, an optomechanical coupling between the motion of the oscillator and an optical cavity field mediates damping of the mechanical motion, where displacements alter the optical resonance dispersively or dissipatively. If the oscillator moves faster than the time it takes for photons to decay out of the cavity, a delayed optical response to the motion occurs. This delay creates a dynamical backaction force that can extract motional energy, where cooling is limited by radiation pressure backaction and laser shot-noise[1].

In chapter 3 it was shown that there is a dispersive and dissipative coupling between the WGM of the microsphere-cantilever and the relative motion between the microsphere and the tapered fibre, defined with respect to the coupling distance d between both objects. The dispersive and dissipative coupling rates are defined by $g_{\mathrm{om}}(x) = \frac{\mathrm{d}\omega_0}{\mathrm{d}x}$, and $\gamma_{\mathrm{om}}(x) = \frac{\mathrm{d}\kappa}{\mathrm{d}x}$ such that mechanical motion changes the WGM frequency ω_0, and linewidth κ, respectively. Changes in d due to the thermal motion of either the microsphere-cantilever or the tapered fibre ($x(t)$) can therefore be detected as a fluctuating power coupled to the WGM, $\mathrm{P_c}(t)$. Since the cavity enhanced optical dipole force (CEODF) is dependent on $\mathrm{P_c}$ (see eq. 3.20 in chapter 3), CEODFs can be used for both passive cooling schemes.

---

[1] This is known as the standard quantum limit, which is discussed in section 3.8 of chapter 3.

By utilising dispersive coupling, passive cooling analogous to the Doppler cooling of atoms can be achieved using red-detuned light with respect to the WGM[2]. Dispersive cooling schemes have had success creating nano/micron-scale mechanical oscillators with low phonon occupancies of less than 1 [25–27]. A second method relies on dissipative coupling, where motion changes the decay rate (losses) of the WGM resonance. In the quantum noise picture, interference between the quantum fluctuations of the laser field (white noise), and the dissipative bath of the cavity (which has a resonant lineshape as it is filtered by the cavity susceptibility), can interfere to produce a region in frequency space with no noise, i.e. a 0 K bath [210]. To date, only one system has implemented dissipative cooling [211], although in combination with dispersive cooling.

In this chapter, a simple classical model of the coupled equations of motion describing a mechanical oscillator and an optical cavity field are used to investigate the properties of dispersive and dissipative cooling. Although the dispersive case is well studied [14, 138, 160], the theory of dissipative cooling uses quantum noise analysis [210], valid for low phonon occupancies. Therefore an indication that the predicted dynamics in the quantum model can also be obtained at high phonon occupancies in the classical regime is a useful gauge for future experiments. It should be noted that others have studied dissipative coupling analytically, predicting limits to ground state cooling [212], strong coupling optomechanics [213, 214], chirped pulse cooling [215], and enhancements to sensing [216]. The simple model in this chapter reveals further information on the modification of the damping rate when a combination of g_{om} and γ_{om} coupling is present.

Lastly, g_{om} and γ_{om} are measured for the microsphere-cantilever, taper coupled system studied in this thesis. An alternative experimental and analytical method to that used in chapter 3 is applied, and the values are compared to those obtained in the literature. Dispersive and/or dissipative cooling of a high frequency mechanical mode of a tailored microsphere-cantilever is predicted, or, alternatively, cooling of a high frequency mode of the near-field coupled tapered fibre.

In this chapter is described:

- An introduction to passive cooling and dynamical backaction.
- Modelling of passive cooling (dispersive, dissipative, and a mixture of both) using the classical coupled equations of motion.

---

[2] The decay rate of the cavity is equivalent to the spontaneous emission from atoms.

- Measurement of the dispersive and dissipative rates for the taper coupled, microsphere-cantilever WGM system.
- A proposal for a future experiment to obtain dissipative cooling.

5.2 Passive Cooling Schemes

Optical passive cooling schemes rely on an optomechanical coupling between a cavity light field and a mechanical oscillator. This can be optimised through the detuning incident light with respect to the cavity, such that the thermal motion of the oscillator is damped by an actuating force arising from the optical field. The two most commonly used optical forces are radiation pressure, involving direct momentum transfer (e.g. Fabry-Perot (F-P) cavities with a movable end mirror [145, 217, 218], or the interaction of WGMs and mechanical breathing modes in toroids [46, 196]), and the optical gradient force (e.g. nano-objects in the evanescent field of a waveguide or WGM resonator [3, 15, 55], or, cavity cooling of nanospheres [6–8, 158]).

The two types of optomechanical coupling are dispersive coupling and dissipative coupling, where the mechanical motion modulates the resonant frequency or the damping rate (i.e. losses) of the optical cavity, respectively. The coupling implies that the mechanical oscillator is brought into contact with a colder detector (i.e. the cavity bath), which leads to passive backaction cooling (also referred to as self-cooling via dynamical backaction), similar to a hot object placed in contact with a colder one [140].

WGM resonators can be used for both types of cooling such that the backaction force arises from the CEODF, and acts on an object placed within the WGM evanescent field. This near-field coupling has attracted attention in recent years [1, 3, 9, 10, 15, 25, 40, 66–70], as the enhanced gradient field results in extremely large per-photon forces and the highest dispersive optomechanical coupling rates to date.

The next few sections explain how backaction forces can damp thermal motion. Dispersive cooling is illustrated using the simple F-P cavity as the framework. A qualitative discussion on dissipative cooling is also presented before a model of both types of cooling is demonstrated using classical coupled equations of motion. This can be used as a guide towards future implementation of these types of cooling.

5.2.1 Dispersive Cooling

A F-P cavity with one movable mirror is commonly used to describe the universal phenomena of cavity optomechanics, shown in fig. 5.1.

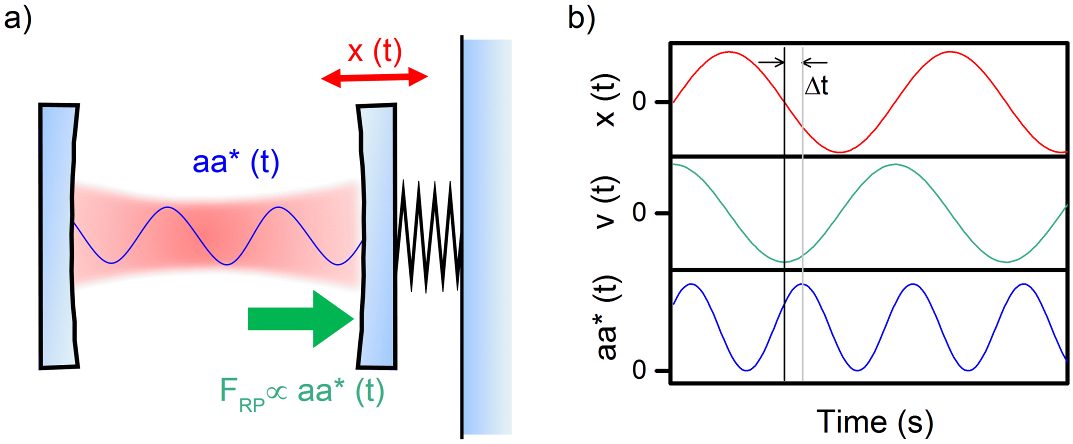

Figure 5.1: a) A Fabry-Perot cavity formed by a fixed mirror, and a movable mirror whose motion is described by $x(t)$. Light is coupled into the F-P such that the intracavity intensity $\propto aa^*(t)$ builds up, and a standing wave forms. The intracavity photon number is $aa^*(t)$. Radiation pressure $\mathrm{F_{RP}}$, proportional to the intensity, is applied by the intracavity field onto the movable mirror. b) The backaction effect can be described by considering the motion of the movable mirror in time, (top panel, red trace), and the velocity, $v(t)$ (middle panel, green) where $x(t)$ changes at a frequency larger than the cavity decay rate. A finite amount of time Δt is required for the cavity resonance condition to stabilise.

The F-P with a movable end-mirror in fig. 5.1 a) experiences a scattering force (radiation pressure) due to the circulating intracavity intensity. The thermal motion of the mirror, $x(t)$, creates a new optical round trip condition by dispersively shifting the cavity resonance relative to the incident field. The optomechanical dispersive coupling rate defines this shift as $g_{\mathrm{om}} = \frac{\mathrm{d}\omega_0}{\mathrm{d}x}$, which for the F-P system is $g_{\mathrm{om}} = \frac{\omega_0}{1+\frac{x}{L}} \approx \frac{-\omega_c}{L}$, where L is the cavity length, and ω_0 is the cavity resonance frequency. The system then evolves to establish a new static equilibrium [219]. A finite time is taken for the cavity response, defined by the linewidth, and known as the cavity decay rate κ. If the mechanical oscillator is tailored to oscillate at a frequency Ω_{m} much faster than κ, by the time the cavity has re-established a maximum intensity (i.e. maximum radiation pressure), the mirror has continued along its motion. This delay, Δt, creates a backaction effect whereby for blue detuning, amplification of the mechanical oscillator motion occurs, and for red-detuning, the motion is cooled. This is due to a net positive or negative transfer of energy from the radiation field to the oscillator, respectively. As with atomic laser cooling, where the spontaneous decay rate is analogous to the cavity linewidth, the maximum cooling or amplification rate occurs when the laser is detuned to the maximum slope of the resonance lineshape. For cavity optomechanics, this corresponds to the half width half maximum (HWHM) of the optical resonance i.e. the WGM [219], although this is no longer valid when $\Omega_\mathrm{m} \gg \kappa$, discussed next.

Sideband-Resolved Cooling

The cooling and amplification process outlined in fig. 5.1, is linked to inelastic scattering due to Stokes and anti-Stokes sidebands on the probe wave. This technique is used to cool molecules beyond the Doppler limit if the spontaneous decay rate κ is smaller than the vibrational frequency, Ω_m, and has achieved ground state cooling of trapped ions [220]. Considering the case of a molecule with a vibrational mode[3] that Doppler shifts incident light to resolve a spectrum of sidebands at frequencies $\omega_0 - j\Omega_\mathrm{m}$, where $j = \pm 1, \pm 2...$, and ω_0 is the unperturbed resonance transition of the molecule. Equal amplitude sidebands at $\pm\Omega_\mathrm{m}$ are created as the vibrational motion Rayleigh scatters the incident light at frequency $\omega_l = \omega_0$. This is an elastic process with no net transfer of energy. Raman scattering is an inelastic process that occurs when the incident light is detuned with respect to ω_0, such that the amplitudes of the sidebands are asymmetrical and photons are preferentially scattered with an increase (anti-Stokes) or decrease (Stokes) in energy. Energy is extracted or added to the vibrational state respectively.

If $\kappa > \Omega_\mathrm{m}$ these sidebands are unresolved fig. 5.2 a) (top panel). Red-detuning ω_l by the HWHM of the resonance (bottom panel) leads to an increase in the anti-Stokes process, such that photons extract energy from the vibrational state, damping the motion. However, since the system is in the unresolved sideband regime, the Stokes process is not heavily suppressed such that cooling is limited to the Doppler limit. When $\kappa \ll \Omega_\mathrm{m}$, the 'resolved-sideband' condition is met and the Stokes $(\omega_l - \Omega_\mathrm{m})$, and Anti-stokes $(\omega_l + \Omega_\mathrm{m})$ sidebands are seen in the cavity transmission, fig. 5.2 b) (top panel). Using red-detuned light at $\omega_l = \omega_0 - \Omega_\mathrm{m}$, shifts the spectrum such that the anti-Stokes process is enhanced, whereas the Stokes process is suppressed (bottom panel). Note that for maximum resolved-sideband cooling or heating, the optimum detuning is $\pm\Omega_\mathrm{m}$ respectively.

In the quantum picture, resolved-sideband cooling can be described by considering the ladder of internal molecular states observed by an incident photon, fig. 5.3. Here, the

---

[3] This is analogous to the microsphere-cantilever such that the vibrational mode of the molecule is equivalent to the c.o.m. motion of the microsphere-cantilever.

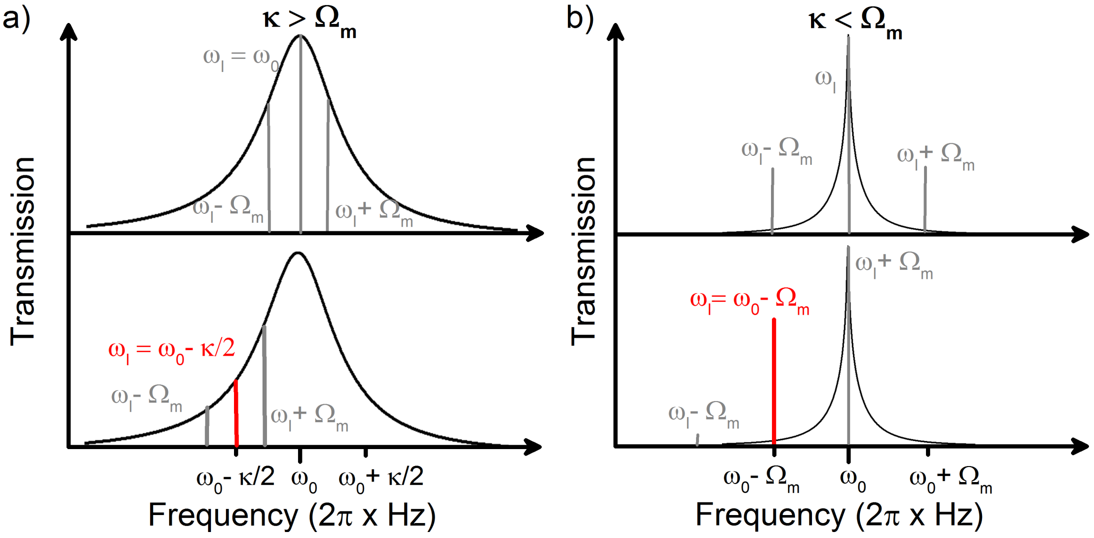

Figure 5.2: The difference between the two regimes of dispersive cooling of an oscillator with motion at frequency Ω_{m}, dispersively coupled to the intracavity field of a cavity with resonance frequency ω_0, and cavity decay rate κ. a) is the non-resolved sideband scheme, when $\kappa > \Omega_{\mathrm{m}}$, and b) is the resolved-sideband scheme when $\kappa \leq \Omega_{\mathrm{m}}$. Damping of the motion is achieved when the incident light at frequency ω_l, is red-detuned to the cavity resonance, such that for a) $\Delta = \omega_l - \omega_0 = -\kappa/2$. In the case of b), $\Delta = -\Omega_{\mathrm{m}}$ such that the light is tuned to the Stokes sideband.

coupling between the light field and the molecule vibrational mode influences the state $|\bar{n}_l, \bar{n}\rangle$ where $\bar{n}_l$ is the average photon occupation and $\bar{n}$ is the average phonon occupation.

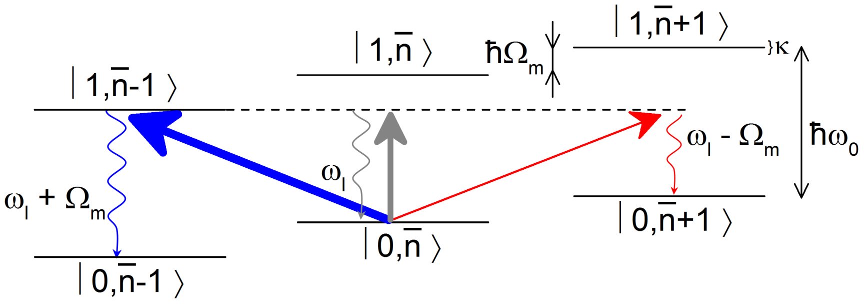

Figure 5.3: The quantum picture of resolved-sideband cooling. The resolved internal states of a molecule (or optomechanical cavity), where the combined state of the average phonon occupancy $\bar{n}$, and photon occupancy $\bar{n}_l$, is represented by $|\bar{n}_l, \bar{n}\rangle$. If the incident laser is red-detuned, with energy $\hbar\omega_l = \hbar(\omega_0 - \Omega_{\mathrm{m}})$, the transition $|0, \bar{n}\rangle \rightarrow |1, \bar{n} - 1\rangle$ (blue arrow) is enhanced, corresponding to anti-Stokes scattering. Rayleigh scattering (grey arrow) and Stokes scattering (red arrow) are suppressed. Re-emission of the photon (wavy lines) occurs with energy $\hbar\omega_0$, where the annihilation of a phonon with energy $\hbar\Omega_{\mathrm{m}}$ makes up for the energy deficit of the incident photon at $\hbar(\omega_0 - \omega_l)$.

When an incident photon of energy $\hbar\omega = \hbar(\omega_0 - \Omega_{\mathrm{m}})$ (i.e. red-detuned to the Stokes sideband), approaches the molecule, the molecule preferentially absorbs the photon through the annihilation of a phonon of energy $\hbar\Omega_{\mathrm{m}}$. This leads to the spontaneous emission of a photon of energy $\hbar\omega_0$. By making the energy scale ($\hbar\kappa$) set by the spontaneous emission very small compared with the spacing between the internal levels ($\hbar\Omega_{\mathrm{m}}$), ground state cooling can be achieved.

The same technique can be applied to the F-P cavity studied in fig. 5.1[4]. Detuning to the Stokes sideband corresponds to transitions where a photon is added to the cavity, whilst simultaneously the occupation of the mechanical oscillator is decreased by one phonon. At the mechanical ground state where the average occupancy is $\bar{n} = 0.5$, both Stokes and anti-Stokes scattering rates are equal, no further cooling is possible, and the mechanical mode is in thermal equilibrium with the optical bath [194].

For both non-resolved and resolved sideband cooling, the in-phase component of the radiation pressure force (real), changes the mechanical oscillator's rigidity, known as the optical spring effect [219], whilst the quadrature component (imaginary) causes damping/heating.

5.2.2 Dissipative Cooling

Optomechanical systems where motion is coupled to the loss (linewidth) of the cavity mode can theoretically cool to the quantum ground state, without being sideband resolved [210]. The authors in [210] derived the noise power spectra (PSD) of the resultant backaction force using the quantum Langevin equations [160, 164]. The backaction noise spectrum mimics a zero-temperature environment due to quantum noise interference between the shot-noise of the incident laser and the intracavity light, outlined in fig. 5.4. This has a Fano lineshape as a consequence of quantum noise interference, where the zero can coincide at the mechanical frequency (i.e. creating a 0 K bath), and suggests no limit to cooling.

Fano lineshapes occur due to interference between a resonant and non-resonant process. For a purely dispersive system noise exists as radiation backaction noise due to the photon number fluctuations of the incident light field. When dissipative coupling exists, the mechanical oscillator mediates the coupling between this backaction noise (which is a non-resonant white noise process), and the cavity's dissipative bath (which is shot-noise limited light filtered by the resonant, frequency dependent cavity susceptibility) [210]. Since this process is independent on the ratio $\frac{\kappa}{\Omega_{\mathrm{m}}}$, cooling can be applied in the non-resolved sideband regime. The detuning of the incident light with respect to the cavity resonance at which

---

[4] Note that in optomechanics, radiation pressure originates from the reflection of photons off the mirror surface and not from absorption and re-emission as is the case in conventional laser cooling. Still, the cooling mechanism of both schemes is completely analogous.

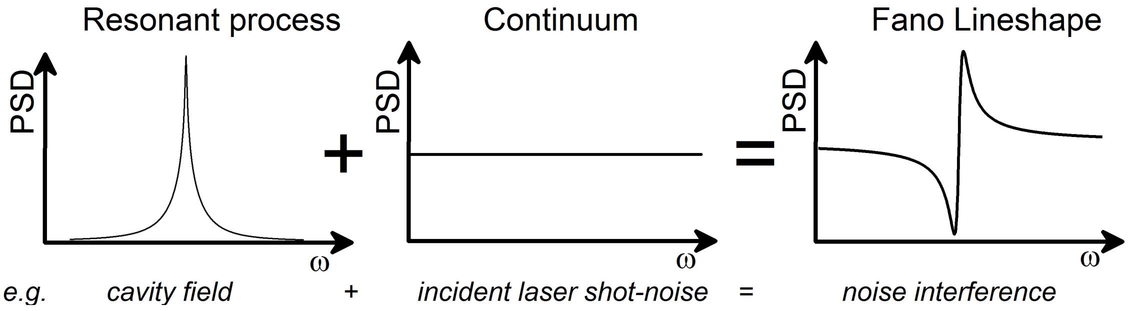

Figure 5.4: The interference between a resonant process and a continuum produces a Fano lineshape with a minimum in the power spectral density (PSD). In the case of WGM experiments using quantum limited light, the WGM cavity acts as a filter (i.e. due to the cavity susceptibility) to create a resonance lineshape that fluctuates due to the coupling to motion, and the continuum corresponds to the incident light which has fluctuations corresponding to a flat noise spectrum. The interference of these noise spectra leads to a Fano lineshape with a 0 K cavity bath temperature at a finite frequency.

maximum cooling occurs is given by:

$$\Delta_{\mathrm{opt}} = \frac{\Omega_{\mathrm{m}}}{2} + \frac{\kappa g_{\mathrm{om}}}{\gamma_{\mathrm{om}}}, \tag{5.1}$$

where $\gamma_{\mathrm{om}} = \frac{\mathrm{d}\kappa}{\mathrm{d}x}$ is the dissipative coupling rate, and $g_{\mathrm{om}} = \frac{\mathrm{d}\omega}{\mathrm{d}x}$ is the dipersive coupling rate. The noise interference outlined in fig. 5.4 creates two cooling and two instability (heating) regions [213], which have been studied using an interferometer set-up [221]. So far, no system has shown purely dissipative coupling to a cavity, although successful combined dissipative and dispersive cooling of a membrane at zero detuning (using light on-resonance with the cavity) has been achieved in a Michelson interferometer [211].

5.3 Modelling of Passive Cooling using Whispering Gallery Modes

The previous sections qualitatively described how dispersive and dissipative coupling can bring about a backaction force to cool mechanical motion optically coupled to a cavity. The dynamics and characteristics of both cooling schemes using a WGM resonator can be modelled by considering the classical coupled equations of motion. This allows for comparison of the damping rates from each scheme, as well as combined cooling using both dispersive and dissipative coupling.

Shown in fig. 5.5 a) & b) are two realisations of near-field coupling between a mechanical oscillator and the evanescent field of a WGM resonator.

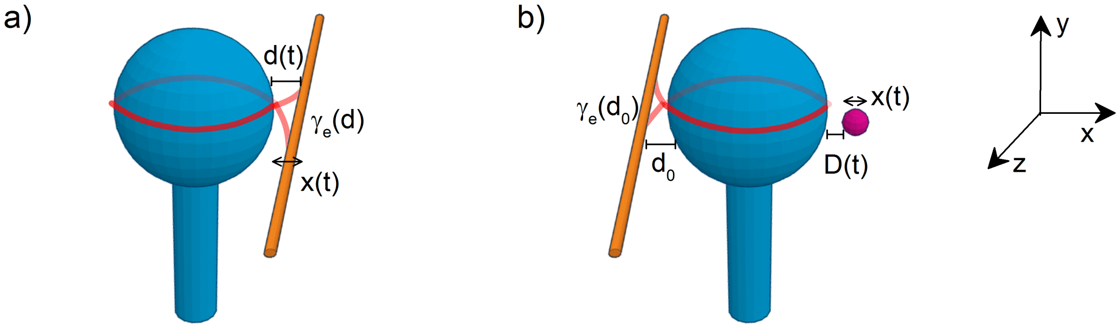

Near-field coupling between
WGM resonator & taper motion x(t)
- coupled by γ_{om}(d), g_{om}(d)
- motion changes d

Near-field coupling between WGM resonator
& levitated sphere motion x(t)
- coupled by g_{om}(D), (γ_{om}(D))
- motion changes D, but d is fixed at d_0

Figure 5.5: a) The taper-microsphere junction, where the tapered fibre (or the microsphere-cantilever) could be cooled passively by using the dynamical backaction force arising from the dispersive g_{om}, and dissipative γ_{om} coupling rates. Both rates depend on the modulation of the coupling distance, $d(t)$, by the motion of the tapered fibre $x(t)$. The value of γ_{om} depends on the extrinsic coupling rate between the WGM and the tapered fibre, $\gamma_e(d)$. b) An alternative near-field coupling scheme where an 'external' oscillator (shown as a levitated sphere) with motion $x(t)$ modulates the distance D to the microsphere surface, whereas d is fixed at d_0, therefore $\gamma_e(d_0)$ is constant.

The system studied throughout this thesis is represented by a), which shows a tapered fibre exchanging light to the WGM belonging to a microsphere-cantilever at the extrinsic rate $\gamma_e(d)$. The DC coupling distance $d(t)$ is modulated by the thermal motion of the tapered fibre $x(t)$[5]. The presence of the taper causes a shift in the WGM centre frequency, which is described by the linearised dispersive coupling rate $g_{\text{om}}(d)$. The dissipative coupling rate, also linearised for small motions around a DC coupling distance d, is equal to the derivative of $\gamma_e(d)$[6]. Shown in fig. 5.5 b) is an alternative version of near-field coupling where the mechanical oscillator coupled to the WGM, displayed as a levitated sphere at distance D(t) from the sphere surface, is not the coupling waveguide. Instead, the WGM is simultaneously coupled to a stiffened waveguide or prism, such that $d = d_0$ and $\gamma_e(d_0)$ are fixed. The motion of the levitated sphere, $x(t)$, alters the effective refractive index around the WGM evanescent field, and shifts the WGM resonance at a rate $g_{\text{om}}(D)$, where g_{om} is exponentially dependent on D. Since this 'external' oscillator typically does not exchange photons with the WGM, there is negligible dissipative coupling. It has been suggested that carbon nanotubes [222], or plasmonic coated spheres [223], where an internal resonance

---

[5] A fixed waveguide such as a prism can be used instead, such that the thermal motion of the microsphere-cantilever is passively cooled.

[6] This linearisation is required because of the exponential dependence of $\gamma_e(d) \propto e^{-\eta d}$ (as well as g_{om}). Note that $\kappa = \gamma_e(d) + \gamma_e$.

provides a loss channel, could be dissipatively coupled to WGMs.

The CEODF of the WGM, used in chapter 4 to cool mechanical modes of the tapered fibre, can be used for passive cooling. In contrast to active feedback damping using the on-resonance DC component of the CEODF (attractive force), the dispersive coupling to a high frequency mechanical mode drives a backaction CEODF defined by:

$$\mathrm{F}_{\mathrm{opt}}^{g_{\mathrm{om}}} = -\frac{1}{\omega_0}\frac{\mathrm{d}\omega_0}{\mathrm{d}x}\bigg|_{\mathrm{k}} \mathrm{U} \propto -g_{\mathrm{om}} \left|a(t)\right|^2 , \tag{5.2}$$

where ω_0 is the cavity resonance frequency, U is the total energy given by $\mathrm{U} = \hbar\omega\left|a\right|^2$, $\left|a\right|^2$ is the intracavity photon number equal to aa^*, where a^* is the complex conjugate of a, and $\frac{\mathrm{d}\omega_0}{\mathrm{d}x} = g_{\mathrm{om}}$ is the dispersive optomechanical coupling rate. The motion of the taper in fig. a) (or the levitated sphere in fig. b)) towards the sphere is defined as a decrease of x (i.e. a decrease of d and D in fig.5.5), leading to an increased red-shift of the WGM such that the force is attractive.

When the CEODF is driven by dissipative coupling, a reactive form of the CEODF arises whose sign (attractive or repulsive) is dependent on the detuning with respect to the WGM (this reactive force is similar to that found in atomic physics [224]):

$$\mathrm{F}_{\mathrm{opt}}^{\gamma_{\mathrm{om}}} = -\frac{\gamma_{\mathrm{om}}\Delta}{\gamma_e}\left|a(t)\right|^2 , \tag{5.3}$$

where $\Delta = \omega_l - \omega_0$ is the detuning. Note that the laser detuning and the sign of γ_{om} determine whether the force is attractive or repulsive.

5.3.1 Coupled Equations of Motion

The classical dynamics are studied for dispersive and dissipative near-field cooling using the WGM and its associated CEODF. It is assumed that the system contains many photons and phonons in order to study the feasibility of cooling from room temperature. Modelling towards ground state cooling requires the quantum Langevin equations, which can predict the minimum average phonon occupancy [160, 164]. This is only necessary for $\bar{n}_{\mathrm{th}} \ll \mathrm{Q}_{\mathrm{m}}$, where $\bar{n}_{\mathrm{th}}$ is the average thermal phonon number, and will not be considered here.

The equations for the WGM cavity field and the motion of the taper were introduced in chapter 2 and chapter 3 respectively. The backaction forces from dispersive and dissipative coupling further modify the equation of motion describing the tapered fibre:

$$\frac{\mathrm{d}^2x(t)}{\mathrm{d}t^2}+\Gamma_0\frac{\mathrm{d}x(t)}{\mathrm{d}t}+\Omega_\mathrm{m}^2x(t)=\frac{1}{m_\mathrm{eff}}\left(-g_\mathrm{om}\left|a(t)\right|^2-\frac{\gamma_\mathrm{om}\Delta}{\gamma_e}\left|a(t)\right|^2+\mathrm{F}^\mathrm{th}(t)+...\right),\quad(5.4)$$

where the forces on the right-hand-side of eq. 5.4 are the dispersive backaction force, the dissipative reactive backaction force, and the thermal force. The first two forces rely on the intracavity intensity $|a(t)|^2=aa^*$, which is the average number of photons. For the case of fig. 5.5 a), where the optomechanical coupling is between the WGM and a movable taper, the coupling distance d is modulated such that the intracavity photon number evolves as:

$$\frac{\mathrm{d}a(t)}{\mathrm{d}t}=\left(i\left[\Delta-g_\mathrm{om}\,d(t)\right]-\frac{\gamma_i}{2}-\frac{\gamma_e(d)}{2}+\frac{\gamma_\mathrm{om}}{2}x(t)\right)a(t)+i\sqrt{\gamma_e(d)-\gamma_\mathrm{om}\,d(t)}\,S_\mathrm{in},\quad(5.5)$$

which describes the cavity field after transformation into the laser frequency rotating frame, as outlined in chapter 1, section. 1.4. As a reminder, the term $S_\mathrm{in}=\sqrt{\frac{\mathrm{P_i}}{\hbar\omega_0}}$ defines the input laser which supplies the cavity with photons at the extrinsic coupling rate $\gamma_e(d)$, using an input power of $\mathrm{P_i}$. Cavity loss of photons back into the waveguide also occurs at the rate $\gamma_e(d)$ that exponentially depends on d. The intrinsic loss, when the cavity is unloaded (i.e. not coupled to the taper), is governed by the fixed rate γ_i. The total loss that defines the loaded WGM linewidth when there is no taper motion is $\kappa=\gamma_i+\gamma_e(d)$. In the presence of taper motion, $\kappa=\gamma_i+\gamma_e(d)-\gamma_\mathrm{om}(d)x(t)$ for small motions around a DC coupling distance d, where $\gamma_\mathrm{om}(d)=-\eta\gamma_e(d)$ is equal to the differential of $\gamma_e=\gamma_{e,0}e^{-\eta d}$, where η is the decay rate. Therefore, the reactive force defined in eq. 5.3 is attractive for red-detuning whereas for blue-detuning it acts as a repulsive force. Note that eq. 5.5 already takes into account the sign of γ_om.

For the case of fig. 5.5 b), d is fixed relative to a stationary taper and the optomechanical coupling exists between an external object with motion $x(t)$, in the near-field of the microsphere-cantilever:

$$\frac{\mathrm{d}a(t)}{\mathrm{d}t}=\left(i\left[\Delta-g_\mathrm{om}\,x(t)\right]-\frac{\gamma_i}{2}-\frac{\gamma_e(d)}{2}+\frac{\gamma_\mathrm{om}}{2}x(t)\right)a(t)+\sqrt{\gamma_e(d)}\,S_\mathrm{in}.\quad(5.6)$$

5.3.2 Approximations

A key difference between the near-field coupling described by eq. 5.5 and eq. 5.6 is the role of $\gamma_e(d)$, which acts as a dissipative channel. In the case of a levitated sphere, $\gamma_e(d)$ is fixed γ_{om} can be found by experimentally monitoring the change in the WGM linewidth as this levitated object is brought closer to the surface of the sphere. One interest of this thesis is to cool the taper motion, where $\gamma_e(d)$ is now modulated by the taper, such that γ_{om} is defined by the linearised form of $\gamma_e(d)$, which is $\gamma_e(d)$ as $\gamma_{e0}e^{-\eta d} - \gamma_{\text{om}} d(t)$ (valid for small modulations around d), where $\gamma_{\text{om}} = \eta\gamma_e(d)$. This means γ_{om} appears twice in eq. 5.5, most notably in the pumping term: $i\sqrt{\gamma_e - \gamma_{\text{om}} d(t)}\, S_{\text{in}}$ [216]. The presence of $d(t)$ in this square root term becomes difficult to factorise when deriving an effective damping rate (studied next). For the preliminary investigation here, it is therefore assumed the pumping term of eq. 5.6 is an adequate approximation for the pumping term of eq. 5.5[7]. The implications of this approximation only influence the ability to dissipatively cool to the quantum ground state, which cannot be predicted using classical modelling and thus will not impact the results here. According to [210], the optimum dissipative system should be dominated by changes in the external coupling to the port used to drive the cavity, i.e. the extrinsic rate γ_e that appears in the pumping term and the loss terms. If the pumping term is not modified, no quantum noise interference is obtained, and the system must be sideband resolved to reach the ground state. However, if a mixture of dispersive and dissipative coupling exists, non-perfect destructive noise interference can arise and a Fano lineshape with a minimum bath temperature ($\neq 0\,\text{K}$) is obtained [212]. Therefore, the assumption that the WGM field can be represented by eq. 5.6, which is coupled to the taper motion described by eq. 5.4 will suffice.

Two further simplifications are imposed for ease of modelling using Mathematica. Firstly, an ideal harmonic motion is assumed by setting $\Gamma_0 = 0$, $\text{F}^{\text{th}} = 0$ in eq. 5.4. Secondly, the equations are normalised into dimensionless units by using the constant $D = \sqrt{m_{\text{eff}}\Omega_{\text{m}}}$. The dimensionless parameters are now $X = Dx$, $\tau = t\,\Omega_{\text{m}}$, $\frac{\text{d}^2X}{\text{d}\tau^2} = \frac{1}{\Omega_{\text{m}}^2}\frac{\text{d}^2X}{\text{d}t^2}$, and $\frac{\text{d}X}{\text{d}\tau} = \frac{1}{\Omega_{\text{m}}}\frac{\text{d}X}{\text{d}t}$. Variables are defined as $\tilde{\Delta} = \frac{\Delta}{\Omega_{\text{m}}}$, $\tilde{\gamma}_i = \frac{\gamma_i}{\Omega_{\text{m}}}$, $\tilde{\gamma}_e = \frac{\gamma_e}{\Omega_{\text{m}}}$ and $\tilde{S}_{\text{in}} = \frac{S_{\text{in}}}{\sqrt{\Omega_{\text{m}}}}$. The dispersive and dissipative rates are now $\tilde{g}_{\text{om}} = \frac{g_{\text{om}}}{\Omega_{\text{m}}D}$ and $\tilde{\gamma}_{\text{om}} = \frac{\gamma_{\text{om}}}{\Omega_{\text{m}}D}$ respectively.

The dimensionless versions of the approximated coupled equations (eq. 5.4 and eq. 5.5), representing the motion of the tapered fibre coupled to the intracavity photon number of the WGM resonator at a set DC coupling distance, are:

$$\frac{\text{d}a(\tau)}{\text{d}t} = \left[i\left(\tilde{\Delta} - \tilde{g}_{\text{om}}X(\tau)\right) - \frac{\tilde{\gamma}_i}{2} - \frac{\tilde{\gamma}_e}{2} + \frac{\tilde{\gamma}_{\text{om}}}{2}X(\tau)\right]a(\tau) + \sqrt{\tilde{\gamma}_e}\tilde{S}_{\text{in}}, \tag{5.7}$$

---

[7] This approximation can be avoided by using the quantum description of the system, derived in [225], but does not give much insight into the cooling dynamics when starting from high phonon occupancy.

$$\frac{\mathrm{d}^2X(\tau)}{\mathrm{d}t^2}+X(\tau)=\left(-\tilde{g}_{\mathrm{om}}+\frac{\tilde{\gamma}_{\mathrm{om}}\tilde{\Delta}}{\tilde{\gamma}_e}\right)|a(\tau)|^2\,. \tag{5.8}$$

Mathematica's inbuilt NDSolve function can iteratively solve these coupled differential equations in the time domain, or, alternatively, the equations can be used to form an effective damping rate, Γ_{opt}, similar to that found for active feedback cooling. The sign of Γ_{opt} determines if the thermal motion is reduced ($+\Gamma_{\mathrm{opt}}$) or increased ($-\Gamma_{\mathrm{opt}}$), using the axis convention of eq. 5.4. The magnitude of Γ_{opt} is proportional to the reduced or increased mode temperature.

The method of deriving an effective damping rate is to consider the backaction force that arises from fluctuations $\partial x(t)$ around the steady state position $\bar{x}$, after linearising eq. 5.8 using $x(t)=\bar{x}+\delta x(t)$. The magnitude of this backaction force depends on the fluctuations of the cavity field $\partial a(t), \partial a^*(t)$ around $\bar{a}, \bar{a}^*$, after linearising eq. 5.7 using $a(t)=\bar{a}+\delta a(t)$, where aa^* is the intracavity photon number. The steady states are obtained by setting $\dot{x}(t)=\dot{a}(t)=\ddot{a}(t)=0$[8], where only the first stable solution is required[9]. The expressions for $\delta x(t)$, $\delta a(t)$ are rewritten in the frequency domain (by using the Fourier transform), and combined with expressions for $\bar{a}, \bar{x}$, to derive the backaction force:

$$\partial\tilde{\mathrm{F}}_{\mathrm{opt}}^{g_{\mathrm{om}},\gamma_{\mathrm{om}}}(\omega)\approx\left(-\tilde{g}_{\mathrm{om}}+\frac{\tilde{\gamma}_{\mathrm{om}}\tilde{\Delta}}{\tilde{\gamma}_e}\right)\left[\bar{a}^*\partial a(\omega)+\bar{a}\partial a^*(\omega)\right], \tag{5.9}$$

which is the dimensionless form of $\partial\mathrm{F}_{\mathrm{opt}}^{g_{\mathrm{om}},\gamma_{\mathrm{om}}}(\omega)$ for combined dispersive and dissipative cooling.

5.3.3 Dispersive Backaction Damping Rate

If only dispersive coupling is considered ($\gamma_{\mathrm{om}}=0$), the backaction force of eq. 5.9 is given by $\partial\mathrm{F}_{\mathrm{opt}}^{\mathrm{g}_{\mathrm{om}}}(\omega)\approx -g_{\mathrm{om}}\left(\bar{a}^*\partial a(\omega)+\bar{a}\partial a^*(\omega)\right)$. The steady state, coupled equations in dimensionless form are:

$$\bar{a}=\frac{\sqrt{\tilde{\gamma}_e}\tilde{S}_{\mathrm{in}}}{-i(\tilde{\Delta}-\tilde{g}_{\mathrm{om}}\bar{X})+\frac{\tilde{\gamma}_i}{2}+\frac{\tilde{\gamma}_e}{2}}, \tag{5.10}$$

$$\bar{X}=-\tilde{g}_{\mathrm{om}}\left|\bar{a}\right|^2. \tag{5.11}$$

---

[8] Derivatives in time, from this point onwards will be denoted by $\dot{a}(t)=\frac{\mathrm{d}a(t)}{\mathrm{d}t}$, $\ddot{a}(t)=\frac{\mathrm{d}^2a(t)}{\mathrm{d}t^2}$

[9] More than one stable solution can be found if the light intensity is large [218], or when floppy mechanical oscillators or high optical quality factor cavities are used.

These equations form an polynomial expression in $\bar{X}$, equal to 0 which can be solved to find the root $\bar{X}$, for a particular combination of $\tilde{S}_{\text{in}}$, $\tilde{\kappa}$, and $\tilde{g}_{\text{om}}$:

$$\tilde{g}_{\text{om}}^2 \bar{X}^3 - 2\tilde{\Delta}\tilde{g}_{\text{om}}\bar{X}^2 + \left(\left(\frac{\tilde{\gamma}_i + \tilde{\gamma}_e}{2} \right)^2 + \tilde{\Delta}^2 \right) \bar{X} + \tilde{g}_{\text{om}}\tilde{\gamma}_e \tilde{S}_{\text{in}}^2 = 0. \tag{5.12}$$

Once $\bar{X}$ is found, it can be used in eq. 5.10 to obtain the corresponding value of $\bar{a}$.

Next, the dynamics of the small modulations $\partial a(\tau)$ and $\partial X(\tau)$ are considered, where second order terms i.e. $\partial a(\tau)\partial X(\tau)$ or $\partial a^*(\tau)\partial a(\tau)$ are neglected:

$$\partial \dot{a}(\tau) = \left(i\tilde{\Delta} - i\tilde{g}_{\text{om}}\bar{X} - \frac{\tilde{\gamma}_i}{2} - \frac{\tilde{\gamma}_e}{2} \right) \partial a(\tau) - i\tilde{g}_{\text{om}}\bar{a}\, \partial X(\tau). \tag{5.13}$$

$$\partial \ddot{X}(\tau) + \partial X(\tau) = -\tilde{g}_{\text{om}} \left[\bar{a}^* \partial a(\tau) + \bar{a} \partial a^*(\tau) \right] = \partial \mathrm{F}_{\text{opt}}^{g_{\text{om}}}(\tau). \tag{5.14}$$

Transforming eq. 5.13 into frequency space ($\tau \mapsto \omega$) and using Fourier transform identities for $\partial \ddot{X}$, $\partial \dot{X}$, expressions for $\partial a(\omega)$ and $\partial a^*(\omega)$ can be written as:

$$\partial a(\omega) = \frac{-i\tilde{g}_{\text{om}}\bar{a}}{-i\tilde{\Delta} + i\tilde{g}_{\text{om}}\bar{X} + \frac{\tilde{\gamma}_i}{2} + \frac{\tilde{\gamma}_e}{2} - i\omega} \partial X(\omega), \tag{5.15}$$

$$\partial a^*(\omega) = \frac{i\tilde{g}_{\text{om}}\bar{a}^*}{+i\tilde{\Delta} - i\tilde{g}_{\text{om}}\bar{X} + \frac{\tilde{\gamma}_i}{2} + \frac{\tilde{\gamma}_e}{2} - i\omega} \partial X(\omega), \tag{5.16}$$

which can be used to derive the backaction force:

$$\begin{aligned} &\partial \tilde{\mathrm{F}}_{\text{opt}}^{g_{\text{om}}}(\omega) = \\ &- \tilde{g}_{\text{om}}^2 \left| \bar{a} \right|^2 \left(\frac{\tilde{\Delta} - \tilde{g}_{\text{om}}\bar{X} + \omega}{(\tilde{\Delta} - \tilde{g}_{\text{om}}\bar{X} + \omega)^2 + \left(\frac{\tilde{\gamma}_i + \tilde{\gamma}_e}{2} \right)^2} + \frac{\tilde{\Delta} - \tilde{g}_{\text{om}}\bar{X} - \omega}{(\tilde{\Delta} - \tilde{g}_{\text{om}}\bar{X} + \omega)^2 + \left(\frac{\tilde{\gamma}_i + \tilde{\gamma}_e}{2} \right)^2} \right) \partial X(\omega) + \\ &+ i\tilde{g}_{\text{om}}^2 \left| \bar{a} \right|^2 \left(\frac{(\tilde{\gamma}_i + \tilde{\gamma}_e)/2}{(\tilde{\Delta} - \tilde{g}_{\text{om}}\bar{X} + \omega)^2 + \left(\frac{\tilde{\gamma}_i + \tilde{\gamma}_e}{2} \right)^2} - \frac{(\tilde{\gamma}_i + \tilde{\gamma}_e)/2}{(\tilde{\Delta} - \tilde{g}_{\text{om}}\bar{X} - \omega)^2 + \left(\frac{\tilde{\gamma}_i + \tilde{\gamma}_e}{2} \right)^2} \right) \partial X(\omega). \end{aligned} \tag{5.17}$$

The real and imaginary part of eq. 5.17 correspond to the in-phase and quadrature modulation of the circulating power with respect to the mechanical motion, which gives rise to the backaction induced optical spring effect, and backaction damping/amplification, respectively[10]. This equation can be evaluated at $\omega = \Omega_{\text{m}}$, noting that in dimensionless units $\Omega_{\text{m}} = 1$.

---

[10] This is analogous to the mechanical frequency shift and damping for active feedback cooling in chapter 4.

The dimensionless dispersive backaction damping rate is therefore given by:

$$\tilde{\Gamma}_{\mathrm{opt}}^{g_{\mathrm{om}}} \approx \tilde{g}_{\mathrm{om}}^{2}\bar{a}^{2}\left(\frac{(\tilde{\gamma}_i+\tilde{\gamma}_e)/2}{(\tilde{\Delta}-\tilde{g}_{\mathrm{om}}\bar{X}+1)^2+\left(\frac{\tilde{\gamma}_i+\tilde{\gamma}_e}{2}\right)^2}-\frac{(\tilde{\gamma}_i+\tilde{\gamma}_e)/2}{(\tilde{\Delta}-\tilde{g}_{\mathrm{om}}\bar{X}-1)^2+\left(\frac{\tilde{\gamma}_i+\tilde{\gamma}_e}{2}\right)^2}\right). \quad (5.18)$$

To use this equation, the steady state intracavity photon number $|\bar{a}|^2$ (eq. 5.10) and steady state position $\bar{X}$ (eq. 5.11) are inserted. The dispersive backaction damping rate is modelled in fig. 5.6 for varying detuning $\Delta/\Omega_{\mathrm{m}}$ and both a), laser power (represented by the pumping term $\mathrm{P_i} = S^2\hbar\omega\Omega_{\mathrm{m}}$, (note that $S^2 \equiv S_{\mathrm{in}}^2$) and b), the ratio of the extrinsic to intrinsic coupling rates, $\frac{\gamma_e}{\gamma_i}$, that defines the taper to microsphere coupling regime (this is dependent on d, investigated in chapter 2 section 1.4.). The parameters chosen are $g_{\mathrm{om}} = 2\pi \times 20\,\mathrm{MHz\ nm^{-1}}$, $\gamma_i = 2\pi \times 5\,\mathrm{MHz}$, a taper mode with frequency $\Omega_{\mathrm{m}} = 2\pi \times 8\,\mathrm{MHz}$, and effective mass 2×10^{-12} kg. A high Ω_{m} is chosen since the kilohertz taper modes are too low for passive cooling using the narrowest WGM excited within this thesis $\approx 5\,\mathrm{MHz}$.

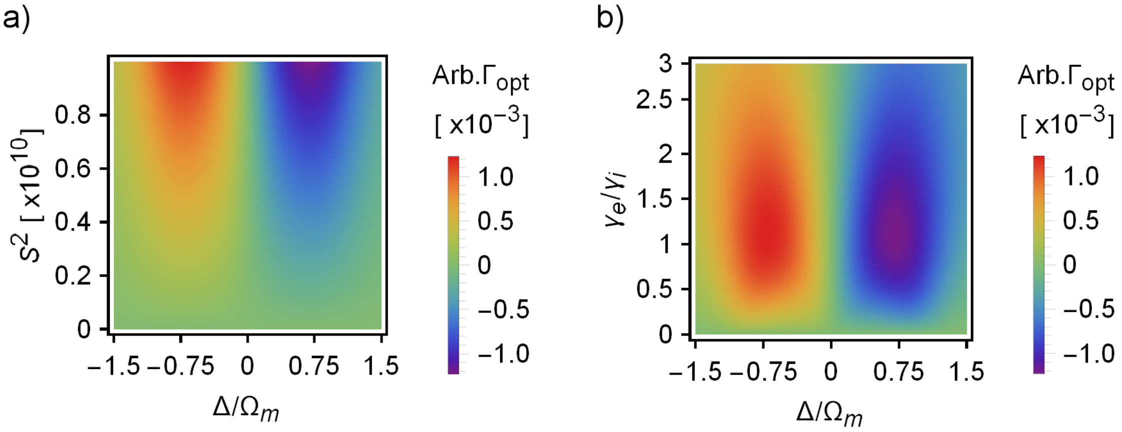

Figure 5.6: a) Density plot of the effective dispersive damping rate Γ_{opt} for varying detuning Δ (normalised to mechanical frequency Ω_{m}) whilst increasing the incident pumping photons (represented by $\mathrm{P_i} = S^2\hbar\omega\Omega_{\mathrm{m}}$). The laser power $\mathrm{P_i}$ is varied from 0 to 94 mW using 1064 nm light, and the WGM is undercoupled ($\gamma_e = \gamma_i/2$). b) Density plot of Γ_{opt} for varying detuning whilst changing the WGM coupling regime usig $\frac{\gamma_e}{\gamma_i}$, for $\mathrm{P_i} = 94\,\mathrm{mW}$.

From fig. 5.6 a) & b), red-detuning results in cooling of the taper motion whilst blue detuning leads to heating. The magnitude of $\Gamma_{\mathrm{opt}}^{g_{\mathrm{om}}}$ scales with the pump power. The maximum $\Gamma_{\mathrm{opt}}^{g_{\mathrm{om}}}$ occurs at the optimum detuning of $\Delta = -0.75\,\Omega_{\mathrm{m}} \approx 1.125 \times \kappa$, since the system is on the boundary of being sideband resolved. Using fig. 5.6 b) sets the optimum WGM coupling regime (and therefore the taper to microsphere coupling distance) to critical coupling when $\gamma_e/\gamma_i = 1$. Pushing the system further into the sideband resolved regime, as shown in fig. 5.7, shifts the optimum detuning to $\Delta = -\Omega_\mathrm{m}$, as expected from the Raman scattering picture[11].

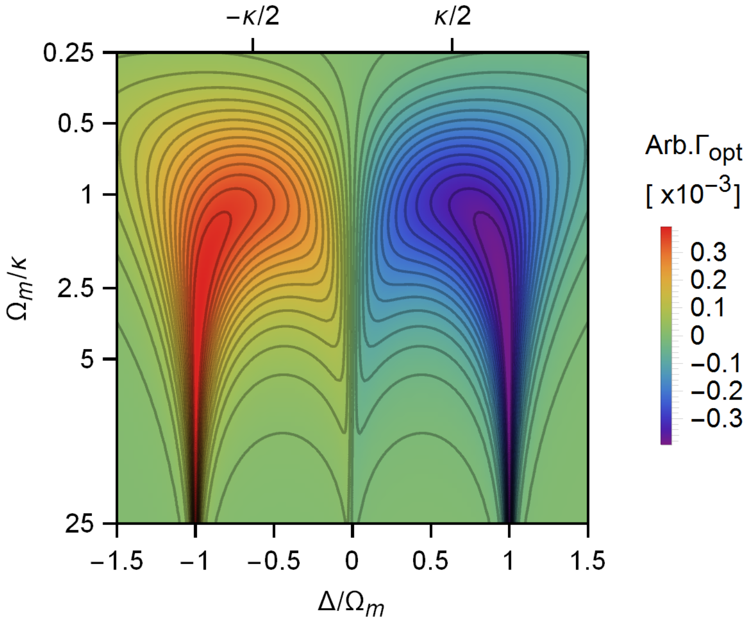

Figure 5.7: The effective dispersive damping rate Γ_opt on a mechanical oscillator near-field coupled to the WGM of a microsphere, plotted as a function of the detuning Δ of the pump light (with power $\mathrm{P_i} = 23\,\mathrm{mW}$) with respect to the WGM resonance, in the undercoupled regime given by $\gamma_e = 0.5\,\gamma_i$. In the sideband resolved regime ($\Omega_\mathrm{m}/\kappa \gg 1$, where $\kappa = \gamma_i + \gamma_e$), the largest Γ_opt is reached when $\Delta = -\Omega_\mathrm{m}$, whereas in the non-resolved sideband scheme $\Delta = -\kappa/2$.

5.3.4 Dissipative Backaction Damping

In order to directly compare with the dispersive cooling simulation in fig. 5.6, the same rate as dispersive coupling is used for dissipative coupling: $\gamma_\mathrm{om} = 2\pi \times 20\,\mathrm{MHz\ nm^{-1}}$, which is valid at a set DC distance between the moving tapered fibre and microsphere. The same values for $\mathrm{P_i}$, γ_i, Ω_m, and m_eff are inserted into the coupled dimensionless equations eq. 5.7 & eq. 5.8, with zero dispersive coupling ($g_\mathrm{om} = 0$).

The steady state solutions are then found by looking for the first real root of:

$$\frac{\tilde{\gamma}_\mathrm{om}^2}{4}\bar{X}^3 - \tilde{\gamma}_\mathrm{om}\left(\frac{\tilde{\gamma}_i}{2} + \frac{\tilde{\gamma}_e}{2}\right)\bar{X}^2 + \left(\tilde{\Delta}^2 + \left(\frac{\tilde{\gamma}_i + \tilde{\gamma}_e}{2}\right)^2\right)\bar{X} - \tilde{\gamma}_\mathrm{om}\tilde{\Delta}\tilde{S}_\mathrm{in}^2 = 0. \tag{5.19}$$

Following the procedure used to derive the effective damping from dispersive coupling, the imaginary part of the dissipative force $\partial\tilde{\mathrm{F}}_\mathrm{opt}^{\gamma_\mathrm{om}}(\omega) = \frac{\tilde{\gamma}_\mathrm{om}\tilde{\Delta}}{\tilde{\gamma}_e}(\bar{a}^*\partial a(\omega) + \bar{a}\partial a^*(\omega))$[12] gives

---

[11] The limit to cooling is still dependent on imprecision noise related to the light field itself which acts as detector, as well as radiation pressure backaction noise since the light also acts as an actuator, discussed in section 3.8 in chapter 3.

[12] Note that the negative sign of γ_om has been taken into account.

a new expression proportional to the dissipative damping rate, Γ_{opt}. When evaluated at $\omega = \Omega_{\text{m}}$, the dimensionless effective damping from dissipative cooling is:

$$\tilde{\Gamma}_{\text{opt}}^{\gamma_{\text{om}}} \approx \frac{\tilde{\gamma}_{\text{om}}\tilde{\Delta}}{\gamma_e}\bar{a}^2 \left(\frac{(\tilde{\gamma}_{\text{om}}/2)(\tilde{\Delta}+1)}{(\tilde{\Delta}+1)^2 + \left(\frac{\tilde{\gamma}_i}{2} + \frac{\tilde{\gamma}_e}{2} - \frac{\tilde{\gamma}_{\text{om}}}{2}X\right)^2} - \frac{(\tilde{\gamma}_{\text{om}}/2)(\tilde{\Delta}-1)}{(\tilde{\Delta}-1)^2 + \left(\frac{\tilde{\gamma}_i}{2} + \frac{\tilde{\gamma}_e}{2} - \frac{\tilde{\gamma}_{\text{om}}}{2}X\right)^2} \right). \tag{5.20}$$

This dissipative backaction damping rate is plotted as a function of detuning and pump power in fig. 5.8 a), whereas in b) the WGM coupling regime γ_e/γ_i is varied alongside the detuning. The same variables are used as in the dispersive case allowing direct comparison to fig. 5.6. Note that the ratio of γ_e/γ_i in fig. 5.8 b) is calculated from 0 to 1 whereas the dispersive case was calculated from 0 to 3.

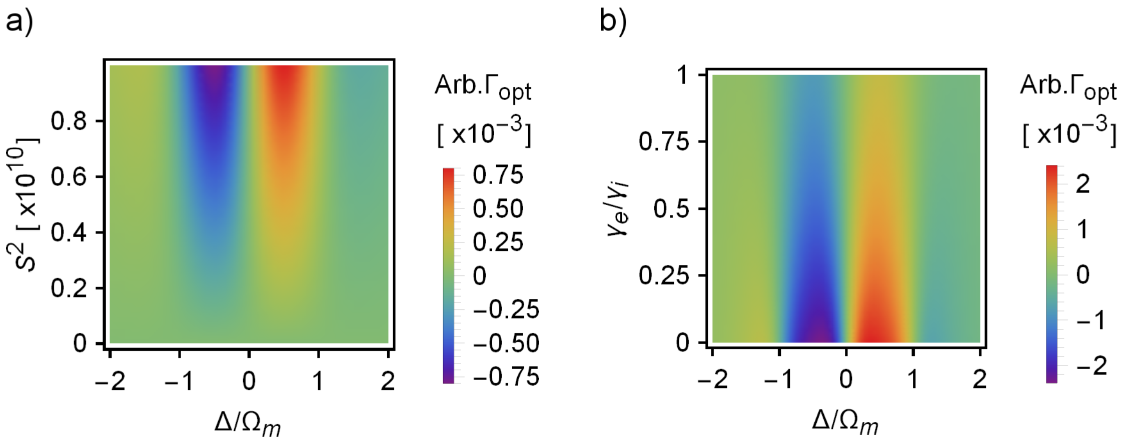

Figure 5.8: a) Density plot of the effective dissipative damping, Γ_{opt} for varying detuning Δ (normalised to the mechanical frequency Ω_{m}) and pump power defined as $\text{P}_{\text{i}} = S^2\hbar\omega\Omega_{\text{m}}$, where P_{i} is the incident power. P_{i} is varied from 0 to 94 mW using 1064 nm light, and the WGM is undercoupled $\gamma_e = \gamma_i/2$. b) Density plot of Γ_{opt} for varying detuning whilst changing the WGM coupling regime, i.e. $\frac{\tilde{\gamma}_e}{\tilde{\gamma}_i}$ for P_{i} =94 mW.

In contrast to dispersive cooling, the largest dissipative damping rate occurs for blue detuning, as predicted from the quantum noise analysis of dissipative systems [210, 212]. The effective dissipative damping is comparable to dispersive cooling, with the dispersive cooling rate larger by a factor of 1.3.

In order to validate the claim that non-resolved sideband cooling can be achieved, the dependence of $\Gamma_{\text{opt}}^{\gamma_{\text{om}}}$ on the ratio $\frac{\Omega_{\text{m}}}{\kappa}$ is modelled, as shown in fig. 5.9 a) & b) using the same P_{i} of 24 mW as the dispersive case of fig. 5.7. From fig. 5.9 a) it can be seen that cooling when blue detuned with respect to the WGM can be achieved for mechanical frequencies up to 20× lower than the total linewidth of the WGM. The narrowest WGM excited using our experiment is $2\pi \times 5\,\text{MHz}$, suggesting a 250 kHz mechanical frequency could be dissipatively cooled. This could correspond to the higher order modes of the tapered fibre [136]. As the sideband resolved parameter is further increased to 0.25, fig. 5.9 b), the characteristic appearance of two cooling regimes and two heating regimes become more pronounced.

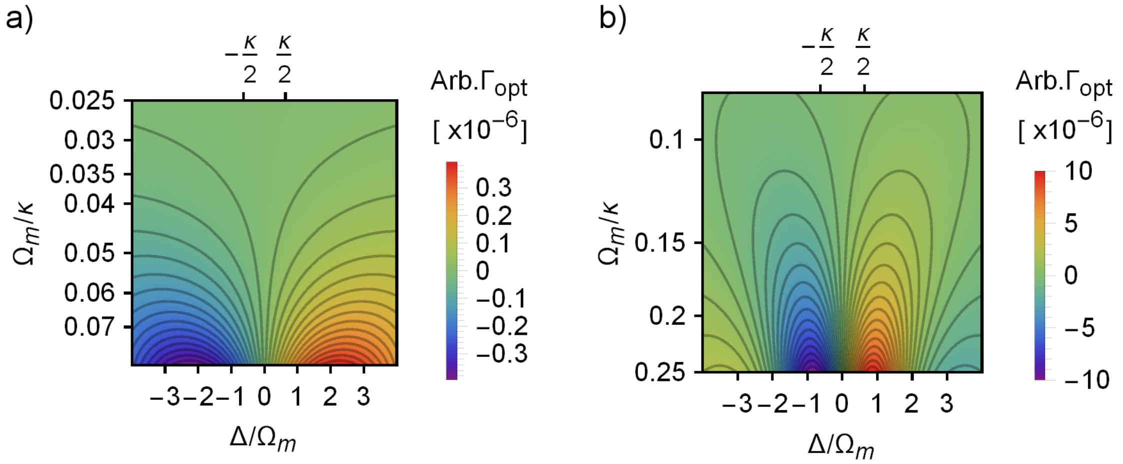

Figure 5.9: Density plot of the effective dissipative backaction damping Γ_{opt} with varying resolved sideband parameter from a) $\frac{\Omega_{\text{m}}}{\kappa}$ =0.025 to 0.14, and b) $\frac{\Omega_{\text{m}}}{\kappa}$ =0.14 to 0.25. The input laser power is P_{i} = 23 mW, and the WGM coupling regime is undercoupled $\gamma_e = \gamma_i/2$.

Increasing the sideband resolved parameter from 0.25 to 2.5, modelled in fig. 5.10a), obtains damping rates comparable to the dispersive scheme in fig. 5.7.

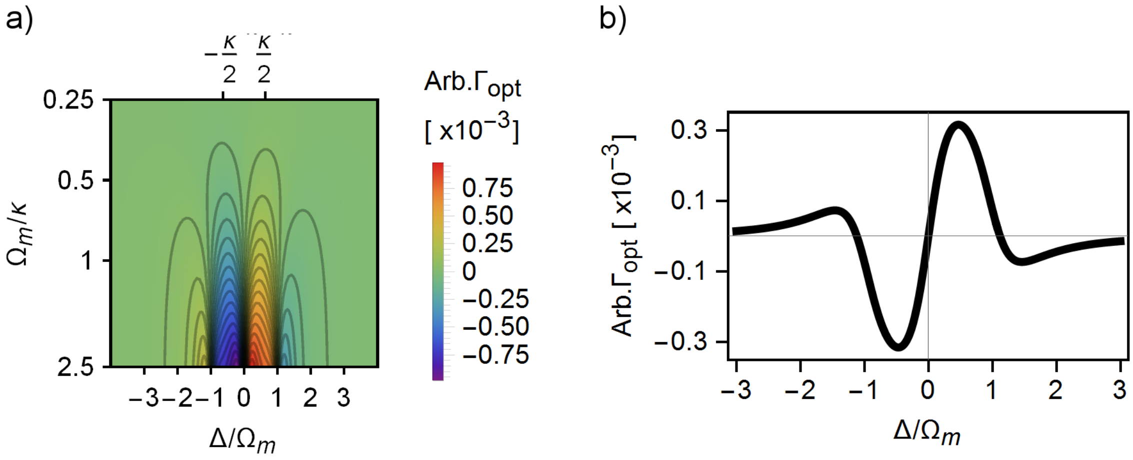

Figure 5.10: a) Effective dissipative backaction damping Γ_{opt} as a function of detuning (Δ) and the resolved sideband parameter $\frac{\Omega_{\text{m}}}{\kappa}$ for the WGM undercoupled regime $\gamma_e = \gamma_i/2$, with a laser power of 23 mW. In b) is shown a 2D slide of a) when $\frac{\Omega_{\text{m}}}{\kappa}$ = 1, showing 2 cooling and 2 heating regimes as a function of detuning.

In the figure next to it (fig. 5.10 b)), is displayed a 2D slice of the dissipative damping rate shown in a), but at a fixed $\frac{\Omega_{\text{m}}}{\kappa}$ = 1, which shows two cooling $\Gamma_{\text{opt}} > 0$, and two heating $\Gamma_{\text{opt}} < 0$ regimes.

5.3.5 Combined Passive Cooling in the Evanescent Field

If there is a combination of dissipative and dispersive backaction in the evanescent field, as is the case for the coupling between the microsphere-cantilever and taper (measured in chapter 3), the damping rate is:

$$\tilde{\Gamma}_{\text{opt}}^{g_{\text{om}},\gamma_{\text{om}}} \approx \left(-\tilde{g}_{\text{om}} + \frac{\gamma_{\text{om}}\tilde{\Delta}}{\gamma_e}\right)\bar{a}^2 \left[\frac{(\tilde{\gamma}_{\text{om}}/2)(\tilde{\Delta} - \tilde{g}_{\text{om}}\bar{X} + 1) - (\tilde{g}_{\text{om}}/2)\,(\tilde{\gamma}_e + \tilde{\gamma}_i)}{(\tilde{\Delta} - \tilde{g}_{\text{om}}\bar{X} + 1)^2 + \left(\frac{\tilde{\gamma}_i + \tilde{\gamma}_e - \tilde{\gamma}_{\text{om}}\bar{X}}{2}\right)^2}\right] + \\ + \left(-\tilde{g}_{\text{om}} + \frac{\gamma_{\text{om}}\tilde{\Delta}}{\gamma_e}\right)\bar{a}^2 \left[\frac{-(\tilde{\gamma}_{\text{om}}/2)(\tilde{\Delta} - \tilde{g}_{\text{om}}\bar{X} - 1) + (\tilde{g}_{\text{om}}/2)\,(\tilde{\gamma}_e + \tilde{\gamma}_i)}{(\tilde{\Delta} - \tilde{g}_{\text{om}}\bar{X} - 1)^2 + \left(\frac{\tilde{\gamma}_i + \tilde{\gamma}_e - \tilde{\gamma}_{\text{om}}\bar{X}}{2}\right)^2}\right]. \tag{5.21}$$

In order to understand how the ratio between the dissipative and dispersive coupling changes the backaction damping rate, fig. 5.11 a) & b) is simulated by changing $\frac{\tilde{\gamma}_{\text{om}}}{\tilde{g}_{\text{om}}}$ from $0 \rightarrow 0.5$ in a), and from $0.5 \rightarrow 4$ in b).

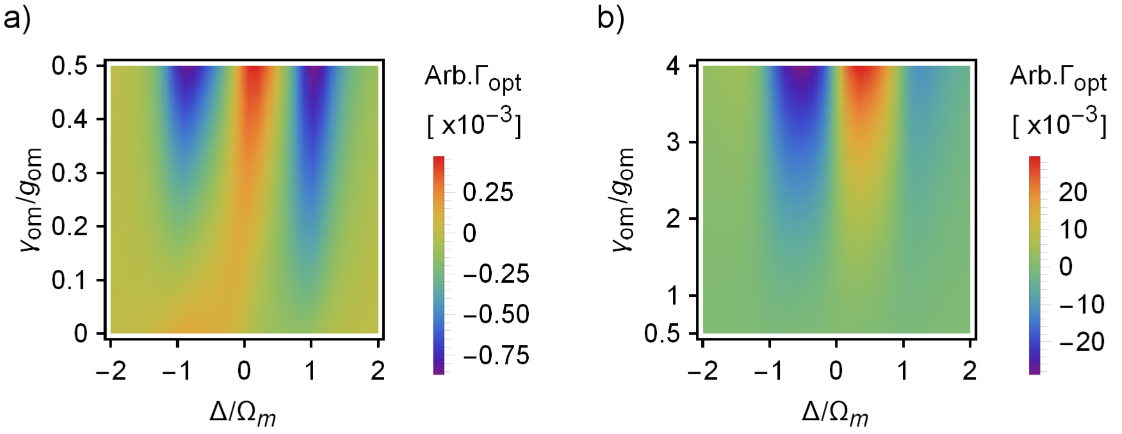

Figure 5.11: The effective damping rate Γ_{opt} from passive cooling using both dispersive and dissipative coupling. The ratio between the dissipative and dispersive coupling rates is varied from a) $\frac{\gamma_{\text{om}}}{g_{\text{om}}} = 0 \rightarrow 0.5$, and b) $\frac{\gamma_{\text{om}}}{g_{\text{om}}} = 0.5 \rightarrow 4$, for $\text{P}_\text{i} = 94\,\text{mW}$, $\gamma_e = 0.25\,\gamma_i$, $g_{\text{om}} = 20\,\text{MHz nm}^{-1}$, and a WGM linewidth of 5 MHz, and $\Omega_\text{m} = 8\,\text{MHz}$

The laser power in fig. 5.11 is set to 94 mW, and $g_{\text{om}} = 20\,\text{MHz nm}^{-1}$ is fixed whilst γ_{om} is varied. The system is in the undercoupled regime $\gamma_e = \gamma_i/4$, with a mechanical frequency of $\Omega_\text{m} = 8\,\text{MHz}$. Intuitively the dependence on detuning transitions from the dispersive cooling case where red-detuned light causes damping, to a regime where cooling can occur on-resonance ($\frac{\gamma_{\text{om}}}{g_{\text{om}}} \approx 0.5$), and then cooling for blue-detuning fig. 5.11 b) as the dissipative coupling is increased.

5.4 Measurement of the Optomechanical Coupling Rates

From the simulations, it is clear that the optomechanical coupling betwen the microsphere-cantilever WGM and the mechanical modes of the tapered fibre offer an unique test-bed for applying dissipative and dispersive cooling. In light of this, the dissipative and dispersive coupling rates are measured again using the experimental set-up in fig. 3.3 (pg. 64) of chapter 3, alongside an alternative method for determining the coupling rates than in section 3.3. The laser is scanned across the WGM whilst decreasing d (the coupling distance) so that the WGM resonance frequency, decay rate κ, and the power coupled to the WGM, $\mathrm{P_c}$ can be measured from the WGM transmission.

The dispersive coupling rate g_{om} is deduced by plotting the shift in WGM frequency against d. An exponential fit of $Ae^{-\eta d}$ is applied, where A is a constant, and η is the decay constant (equivalent to $2\alpha_s$ where α_s is the evanescent decay rate). The derivative of this fit, $A\eta e^{-\eta d}$, is equal to the linearised form of $g_{\mathrm{om}}(d)$, valid for small modulations around d. The linearised form of the dissipative coupling rate, $\gamma_{\mathrm{om}}(d)$, is equal to the derivative of the extrinsic coupling rate $\gamma_e = \gamma_{e,0}e^{-\eta d}$, which describes the rate that photons are transferred between the taper waveguide and the microsphere-cantilever which can be measured as in section 2.4.1 of chapter 2. However, the derivative of the *measured* change in linewidth with d is found to be larger than γ_{om} calculated from the measured $\gamma_e(d)$. The difference is attributed to scattering losses, denoted as γ_{s}, where photons are not coupled back into the taper. All three measured rates are plotted in fig. 5.12.

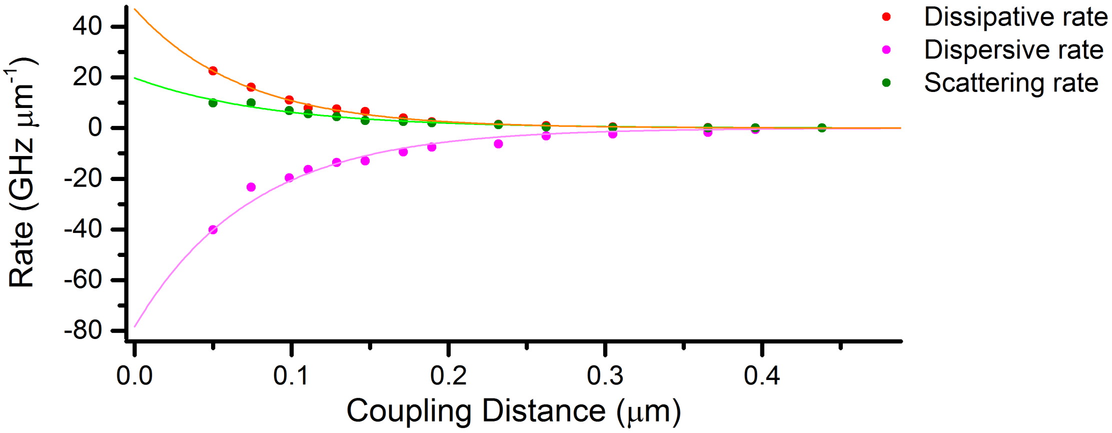

Figure 5.12: The measured dissipative, dispersive, and scattering rates for a microsphere-cantilever coupled to a tapered fibre A WGM of ≈ 470 MHz FWHM is used with ≈ 1 μW of input laser light. The rates are valid for small modulations about a DC coupling distance d.

In fig. 5.12 is displayed the measured dispersive, dissipative, and scattering rates for the taper coupled, microsphere-cantilever system studied in this thesis. At a DC coupling distance d, the coupling rates have been linearised such that they are valid for small displacements from d. The exponential fit to these curves can be used to approximate these rates as:

- Dispersive coupling rate $g_{\text{om}} \approx -78 \times e^{(-13.4\times10^{-3})d}\,\text{MHz nm}^{-1}$.
- Dissipative coupling rate $\gamma_{\text{om}} \approx 47 \times e^{(-14.7\times10^{-3})d}\,\text{MHz nm}^{-1}$
- Scattering rate $\gamma_{\text{s}} \approx 20 \times e^{(-11.5\times10^{-3})d}\,\text{MHz nm}^{-1}$

These values agree within an order of magnitude compared with the microsphere-taper system of [45] where the ratio between dispersive to dissipative coupling is 20, and the ratio between dispersive to scattering is 5. The ratios obtained here are 2 and 3.5 respectively, where differences will be related to geometric and surface differences between the two systems. The scattering rate γ_{s}, measured experimentally, but not included in the modelling of section 5.3, entails an additional loss to the system not associated with the cavity driving field. In the quantum noise picture this leads to a non-perfect destructive interference [212], which limits cooling to the ground state but is not expected to influence the classical dynamics.

In table 5.1 lists optomechanical structures where γ_{om} and g_{om} have been measured or predicted, including that of our own system (as in fig. 5.12), and those in similar systems [45, 225] . The lower panel of the table shows WGM resonator systems where near-field coupling is used to control the motion of an external mechanical oscillator (i.e. not the tapered fibre within the coupling junction), which have negligible dissipative coupling, but can achieve large g_{om}. The majority of systems with dissipative coupling have a larger dispersive coupling, and to date, increasing this dissipative component, whilst decreasing the dispersive contribution has proven unsuccessful.

In comparison to the systems with both dispersive and dissipative coupling, the taper coupled, microsphere-cantilever system ranks mid-level, with g_{om}=16 MHz nm^{-1} and $\gamma_{\text{om}} = 8\,\text{MHz}\,\text{nm}^{-1}$ at a DC coupling distance of 120 nm. Such large values are attributed to the taper, which is not simply a dielectric in the near-field of the WGM resonator, but also functions as a photon loss and pumping channel. The Michelson interferometer is currently the only system to demonstrate combined dispersive and dissipative cooling of a 80 ng membrane to 126 mK [211]. Purely dissipative cooling has not been obtained.

Ref.	Cavity Structure	Mechanical Oscillator	max.γ_{om} (MHz nm^{-1})	max.g_{om} (MHz nm^{-1})
[213]2013	Michelson interferometer	SiN membrane	0.114^{*}	0.448^{*}
[146]2014	Photonic crystal	Split-beam nanocavity	500	2000
[222]2013	Toroid with WGM	Carbon nanotube	$0.4^{\dagger}$	N.A.
[226]2015	Photonic crystal	Split-bean nanocavity	3	10
[227]2015	Microsphere	Graphene	0.1	0.21
[225]2009	Toroid with WGM	SiN waveguide	26.6	2
[32, 68]2007	SiN disk	Taper	35^{+}	10
[45]2015	SiO_2 Microsphere	Taper	0.845^{+}	14^{+}
UCL	SiO_2 Microsphere	Taper	8^{+}	16^{+}
[69]2005	Double sphere	Seperation gap	-	200^{*}
[70]2009	Stacked Double ring	Coupled motion	-	31,000
[1]2015	Toroid evansecent field	Nanostring	-	700

*Estimated from data within reference. † Predicted. + Deduced at a coupling distance of 120 nm.

Table 5.1: A table of systems with dispersive γ_{om}, and dissipative γ_{om} coupling rates, including the system studied in this thesis (ref: UCL).

5.5 Proposal for a Dissipative Cooling Scheme

The results of the simple model in section 5.3, and the measured optomechanical coupling rates of the taper coupled, microsphere-cantilever WGM system in section 5.4 indicate a worthwhile pursuit of dissipative cooling in a future experiment. However, three improvements are required:

1. A suitably high frequency mechanical mode ($\Omega_{\mathrm{m}} > 100\,\mathrm{kHz}$) must be used, which could belong to a torsional mode of the tapered fibre [136], or the microsphere-cantilever itself if the cantilever is tailored to obtain a high Ω_{m} (described in chapter 7).

2. The measured g_{om} is too large and must be suppressed with the aid of active feedback stabilisation of the laser frequency, similar to the PDH stabilisation implemented in chapter 2. However, if a high Ω_{m} is used, further optimisation of the feedback is required such that it is fast enough to counteract the dispersive shift of the WGM mode.

3. The predicted laser powers required to demonstrate dissipative cooling are less than 1 W. However, the current fabrication and storage methodology for the tapered fibres in this thesis (chapter 2) results in tapers that typically melt at input laser powers over 5 mW at atmospheric pressure, and less than 1 mW at 0.5 mBar. Switching to a hydrogen flame reduces surface contaminates, and working within a clean room can help reduce dust adhering onto the taper during installation into the vacuum chamber. This will allow for more light to be coupled into the taper, and thus the WGM.

It should be noted, that if successful dissipative cooling of the c.o.m. motion of the microsphere-cantilever is achieved, the system can be further optimised for reaching the quantum ground state and testing quantum phenomena, described in chapter 7. The microsphere can be untethered from the cantilever, and levitated using an optical and/or ion trap, whilst a tapered fibre optically couples light to the WGM circulating within it[13].

5.6 Conclusion

In conclusion, this chapter broadly introduces passive cooling methods utilising optomechanical coupling between mechanical motion and optical fields. Both dispersive and dissipative coupling exists between the tapered fibre and the microsphere-cantilever, whereby the motion of either oscillator shifts the WGM resonance (dispersive coupling rate g_{om}), and alters the WGM decay rate (dissipative coupling rate γ_{om}). The experimentally measured values of γ_{om} and g_{om} for the taper coupled microsphere-cantilever system, in the range of $10\,\mathrm{MHz\,nm^{-1}}$, are sufficient to obtain dispersive cooling, dissipative cooling or a combination of both. The latter two cooling schemes would herald new results, currently only achieved by one set-up [211].

A simple classical model using the coupled equations of motion to describe dispersive and/or dissipative cooling has been implemented. The classical and quantum model of dispersive cooling has been actively studied for many years, and as such, no new information is presented here. However, dissipative cooling is relatively new, with fewer experimental demonstrations. Although the original quantum analysis of dissipative cooling predicts cooling to the quantum ground state without requiring the sideband resolved regime, classical modelling is useful for investigating the validity of this claim when the oscillator contains many phonons. It is shown in section 5.3 that dissipatively cooling a high frequency ($\Omega_{\mathrm{m}} > 100\,\mathrm{kHz}$) mechanical mode of either the microsphere-cantilever or the tapered fibre could be demonstrated with relatively achievable laser powers. Signature behaviours predicted by the quantum theory of dissipative cooling is validated through the classical model, such as the existence of 2 heating and 2 cooling regimes dependent on the laser detuning with respect to the cavity resonance. Unlike dispersive cooling, where cooling is obtained with red-detuned light, dissipative cooling allows for cooling when blue-detuned. Of course, to obtain more accurate predictions of the damping rate, and the final cooled mode temperature, the simple model presented here should be modified to include the stochastic force responsible for Brownian motion.

---

[13] A $10\,\mu$m diameter silica sphere levitated in a Paul trap is demonstrated in chapter 1, fig. 1.7 (pg. 20).

Chapter 6

A Whispering Gallery Mode Accelerometer

6.1 Introduction

The cumulative work of chapters 2 & 3 can be combined into an optical whispering gallery mode (WGM) accelerometer, unlike any commercially available device.

Accelerometers are sensors that can measure the acceleration of a moving or vibrating body. Such devices play an integral role in precise navigation [228, 229], gravity gradiometry [135, 230], and structural health monitoring. There are two types of accelerometer; those using a test-mass on a spring, or free-fall accelerometers. The most common use a test-mass on a spring (i.e. cantilevers or electrodes), and measure the extension of the spring as the 'g-force' (also referred to as proper acceleration) is applied. The spring elongates until the restoring forces within the spring pull the test-mass back. This measurement of acceleration is relative to the Earth's reference frame, such that a constant reading of $-g$ ($g=9.81\,\mathrm{m\,s^{-2}}$) is obtained in the y-axis. Free-fall accelerometers such as atom interferometers [231] measure the time it takes for the test-mass to fall a set distance. This cancels out the measurement of the Earth's gravitational field, and are considered more accurate but are larger in size.

It will come as no surprise that within the last twenty years many optical systems have revolutionized the field of inertial sensing. Optical accelerometers operate by measuring the interaction of a moving test-mass with an optical field, for example, the change in light coupling efficiency into an optical fibre [23, 232], the optical mode coupling between two photonic-crystal zipper beams [12][1], or the dispersive coupling of a movable mirror in a Fabry-Perot cavity [21]. Optical sensors offer significant improvements over their electrical counterparts[2], as they are non-conductive, immune to electromagnetic interference and can reach sensitivities limited only by the quantum fluctuations of light [2, 71, 179] (and the mechanics of the test-mass).

The microsphere-cantilever fabricated and studied in chapter 2 offers both a test-mass and an optical resonance in the form of the WGM. Similar devices use WGMs to detect a moving test-mass placed in the WGM evanescent field [19, 24]. However, in this thesis, the test-mass is the WGM resonator itself, which has been studied previously by Haus et al. [20] using a WGM resonator coupled to a MEMS waveguide. Here, the coupling is provided by a tapered fibre (the fabrication and coupling of WGMs using the tapered fibre is shown in chapter 2). The circulating WGM within the microsphere can transduce its own motion on the cantilever, which is optimised and described in chapter 3. In that chapter, the thermal motion of the microsphere-cantilever could be detected, which demonstrates the feasibility of transducing a resultant deflection of the cantilever in response to acceleration[3]. An internal force known as stress (force per unit area) causes the cantilever to bend such that the deflection (related to strain) is proportional to acceleration. The theory that describes the relationship between stress, strain, and deflection will be presented in this chapter, in order to compare experimental measurements with prediction.

The limit to sensing, i.e. the minimum resolvable acceleration, is set by the noise floor in the displacement power spectral density (PSD). Typical displacement PSD's obtained in chapter 3 using the WGM transduction show a displacement sensitivity $\approx 10^{-12}\,\mathrm{m\,Hz^{-1}}$. For the purposes of measuring acceleration, this displacement sensitivity corresponds to an acceleration sensitivity, called the noise equivalent acceleration a_{NEA}, such that an $a_{\mathrm{NEA}} \approx 1\,\mu\mathrm{g\,Hz^{-1/2}}$ implies a measurement of $1\,\mu$g within a sample time of 1 s. It will be shown that the WGM sensor studied in this chapter offers the lowest reported a_{NEA} from a WGM device.

---

[1] A photonic zipper beam comprises of a clamped-clamped beam whose cross section is patterned for strong optical localisation into a small mode volume at the centre of the beam. Two nanobeams placed within the near-field of the other results in strong optomechanical coupling to the relative motion between the beams.

[2] Capacitive accelerometers measure the capacitance change between a fixed electrode and a movable electrode. They are prone to electromagnetic disturbance and jamming, often requiring significant investment and engineering to measure accelerations $\leq \mu$g.

[3] The taper can also function as an accelerometer but it is 20 times lighter therefore will have an acceleration sensitivity which is a factor of $\sqrt{20}$ smaller compared with a microsphere-cantilever with similar mechanical frequency and mechanical quality factor, see section 6.4.4 on the noise equivalent acceleration.

The sensing range is entirely determined by the material and geometry of the microsphere-cantilever, as well as the physical separation distance to the taper. This DC coupling distance between the taper and the microsphere is referred to as the 'null position d_0' in accordance with accelerometer terminology, and large displacements away from d_0 can eventually cause the microsphere to touch the taper, setting a maximum acceleration limit. The maximum sensing range for this type of system has not been previously reported, and no indication of the stability using the microsphere-cantilever has been studied. Stability in particular refers to drifts that may offset the measurement, providing a false signal. The so-called vibration rectification error (VRE) affects all test-mass sensors due to non-linearity caused by asymmetric clamping or geometry (i.e. the time averaged deflection is biased in one direction), and to a lesser extent, asymmetric damping. The VRE is troublesome in high vibration environments as it causes a false bias in the output.

The lack of experimental data characterising the WGM sensor in terms of drift, VRE, and the sensing range (i.e. linear range vs. non-linear range) motivates the majority of the experimental investigations presented here.

This chapter will:

- Discuss the theory behind the WGM microsphere-cantilever accelerometer.
- Present measurements of the WGM acceleration sensing range, compared with a commercial accelerometer.
- Present measurements of the noise equivalent acceleration, and measure the minimum resolvable acceleration over a range of driving frequencies.
- Investigate drift, including vibration rectification errors.

6.2 Accelerometer Theory

Accelerometers are classical mechanical systems whose principle of operation can be represented by a test-mass attached to a spring, shown in fig. 6.1 a). The test-mass (with mass m) is connected a flexible spring with spring constant k fixed to the base via the housing. The surrounding gas within the housing introduces damping defined by a damping coefficient, b.

When a force F is applied to the system, the casing and the base will be accelerated immediately, changing the base position by Y. Newton's first law of motion states that the test-mass tries to stay at rest and lags behind, requiring an internal force to elongate the

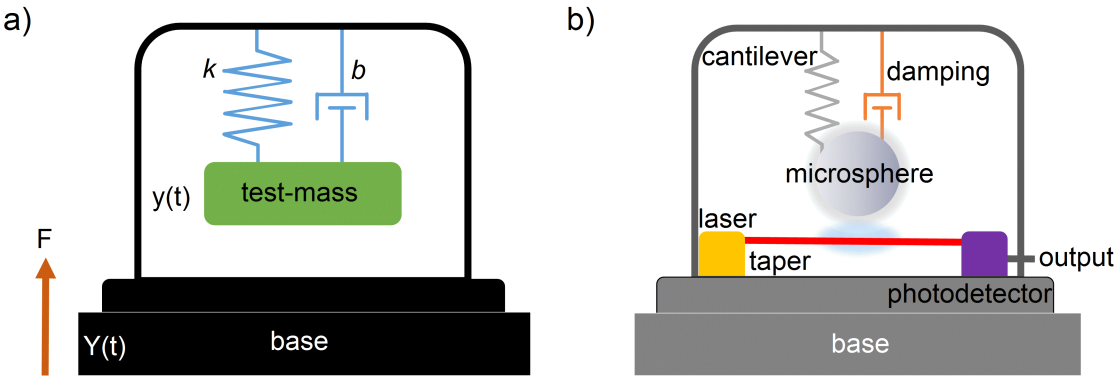

Figure 6.1: a) A simple test-mass accelerometer; the test-mass is attached to a spring with spring constant k and is damped by the surrounding gas with damping coefficient b. The spring is fixed to the housing that sits upon the base. When a force F is applied to the base, the base accelerates such that its position changes by a distance Y. The test-mass lags behind such that the spring is stretched by a distance y. The magnitude of y is linearly proportional to F $= ma$ and is therefore a measure of the acceleration. b) The corresponding picture for the WGM accelerometer is shown; the test-mass is a microsphere, attached to a cantilever which acts as the spring. The deflection of the microsphere-cantilever in response to acceleration is measured using the tapered fibre, which couples light in/out of the WGM. The evanescent field overlap of the taper and the WGM is sensitive to the relative distance between the two objects, and can transduce the displacement due to acceleration.

spring by y such that the test-mass experiences the same acceleration as the base. Hooke's law describes the linear relationship between the spring elongation and the applied force[4], which is proportional to acceleration (Newton's second law F $= ma$, where m is the mass of the test-mass assuming the spring has negligible mass).

The equation of motion that describes the change in test-mass position relative to the base (i.e. the distance $y - Y$), with effective mass m_{eff} and spring constant k is:

$$k(y - Y) + b\,\frac{\mathrm{d}(y - Y)}{\mathrm{d}t} = m_{\text{eff}}\,\frac{\mathrm{d}^2 Y}{\mathrm{d}t^2}, \tag{6.1}$$

where the acceleration of the test-mass $\frac{\mathrm{d}^2 y}{\mathrm{d}t^2}$ is equal to the acceleration of the base $\frac{\mathrm{d}^2 Y}{\mathrm{d}t^2}$ at driving frequencies lower than the test-mass resonant frequency. A new parameter is introduced to represent the relative displacement $y - Y = D$, which simplifies eq. 6.1:

$$m_{\text{eff}}\frac{\mathrm{d}^2 Y}{\mathrm{d}t^2} + k\,D + b\frac{\mathrm{d}D}{\mathrm{d}t} = 0. \tag{6.2}$$

---

[4] This is an approximation known as the elastic regime, as large forces can cause the cantilever to bend irreversibly, described later in this chapter.

At rest, or at a constant acceleration a, eq. 6.2 reduces to:

$$a = \frac{\mathrm{d}^2 Y}{\mathrm{d}t^2} = \frac{k\,D}{m_{\mathrm{eff}}}, \tag{6.3}$$

which connects $\mathrm{F} = m_{\mathrm{eff}}a$, and $\mathrm{F} = kD$, such that the relative displacement of the test-mass is proportional to the base acceleration. Re-arranging eq. 6.3 into $D = a\frac{m_{\mathrm{eff}}}{k}$, the amplitude of D for a given acceleration is inversely proportional to k, and proportional to m_{eff}, meaning heavier or floppier test masses will increase the displacement amplitude.

The dynamic response of the sensor can also be derived by considering a sinusoidal driving motion that causes the base to move by $Y(t) = A\cos(\Omega_{\mathrm{d}}t)$, where A is the peak amplitude, and Ω_{d} is the driving frequency. The equation of motion becomes:

$$\frac{\mathrm{d}^2 D}{\mathrm{d}t^2} + 2\zeta\Omega_{\mathrm{m}}\frac{\mathrm{d}D}{\mathrm{d}t} + \Omega_{\mathrm{m}}^2 D = -A\Omega_{\mathrm{d}}^2\cos(\Omega_{\mathrm{d}}t), \tag{6.4}$$

where Ω_{m} is the test-mass resonance frequency, defined by $\Omega_{\mathrm{m}} = \sqrt{\frac{k}{m_{\mathrm{eff}}}}$, and $\zeta = \frac{b}{2m_{\mathrm{eff}}\Omega_{\mathrm{m}}}$ is the damping ratio that expresses the level of damping relative to critical damping, introduced in chapter 3. It is expected that after an initial transient phase, the test-mass will start to copy the harmonic motion of the base, therefore a trial solution for D is chosen:

$$D(t) = D_0\cos(\Omega_{\mathrm{d}}t + \varphi), \tag{6.5}$$

where D_0 is the peak relative displacement, and φ is the phase lag with respect to the driving signal. This is substituted into eq. 6.4:

$$\left[\Omega_{\mathrm{m}}^2 - \Omega_{\mathrm{d}}^2\right] D_0\cos(\Omega_{\mathrm{d}}t - \varphi) - 2\zeta\Omega_{\mathrm{m}}\Omega_{\mathrm{d}}\sin(\Omega_{\mathrm{d}}t - \varphi) = \Omega_{\mathrm{d}}^2\, A\cos(\Omega_{\mathrm{d}}t). \tag{6.6}$$

The identities $\cos(\Omega_{\mathrm{d}}t - \varphi) \equiv \cos(\Omega_{\mathrm{d}}t)\cos(\varphi) + i\sin(\Omega_{\mathrm{d}}t)\sin(\varphi)$, and $\sin(\Omega_{\mathrm{d}}t - \varphi) \equiv \sin(\Omega_{\mathrm{d}}t)\cos(\varphi) - \cos(\Omega_{\mathrm{d}}t)\sin(\varphi)$, can be used in eq. 6.6 to form:

$$\begin{aligned} &\left[D_0\left(\Omega_{\mathrm{m}}^2 - \Omega_{\mathrm{d}}^2\right)\cos(\varphi) + 2D_0\zeta\Omega_{\mathrm{m}}\Omega_{\mathrm{d}}\sin(\varphi) - \Omega_{\mathrm{d}}^2 A\right]\cos(\Omega_{\mathrm{d}}t) \\ &+ D_0\left[\left(\Omega_{\mathrm{m}}^2 - \Omega_{\mathrm{d}}^2\right)\sin(\varphi) - 2\zeta\Omega_{\mathrm{m}}\Omega_{\mathrm{d}}\cos(\varphi)\right]\sin(\Omega_{\mathrm{d}}t) = 0. \end{aligned} \tag{6.7}$$

The solution to eq. 6.7, valid at all times, is when the terms in square brackets equal 0:

$$D_0\left[\Omega_{\mathrm{m}}^2 - \Omega_{\mathrm{d}}^2\right]\cos(\varphi) + 2D_0\zeta\Omega_{\mathrm{m}}\Omega_{\mathrm{d}}\sin(\varphi) - \Omega_{\mathrm{d}}^2 A = 0, \tag{6.8}$$

$$\left[\Omega_{\mathrm{m}}^2 - \Omega_{\mathrm{d}}^2\right] \sin(\varphi) - 2\zeta\Omega_{\mathrm{m}}\Omega_{\mathrm{d}} \cos(\varphi) = 0. \tag{6.9}$$

The phase lag can be derived from eq. 6.9 using the identity $\tan(\theta) = \frac{\sin(\theta)}{\cos(\theta)}$:

$$\tan(\varphi) = \frac{2\zeta\Omega_{\mathrm{m}}\Omega_{\mathrm{d}}}{\Omega_{\mathrm{m}}^2 - \Omega_{\mathrm{d}}^2}. \tag{6.10}$$

The peak amplitude of the test-mass response D_0 can be found using eqs. 6.8 & 6.10, alongside the substitutions $\cos(\varphi) = \frac{1}{\sqrt{1+\tan^2(\varphi)}}$, and $\sin(\varphi) = \frac{\tan(\varphi)}{\sqrt{1+\tan^2(\varphi)}}$:

$$D_0 = \frac{A\left(\frac{\Omega_{\mathrm{d}}}{\Omega_{\mathrm{m}}}\right)^2}{\sqrt{\left(1 - \left(\frac{\Omega_{\mathrm{d}}}{\Omega_{\mathrm{m}}}\right)^2\right)^2 + \left(2\zeta\frac{\Omega_{\mathrm{d}}}{\Omega_{\mathrm{m}}}\right)^2}}. \tag{6.11}$$

This equation reveals 3 characteristics of accelerometers;

- If $\zeta = 0$ (no damping), an uncontrollable resonance effect will occur when $\Omega_{\mathrm{d}} = \Omega_{\mathrm{m}}$ which can lead to damage. The majority of accelerometer designs impose finite damping to avoid this effect.

- If $\Omega_{\mathrm{d}} \ll \Omega_{\mathrm{m}}$, eq. 6.11 simplifies to:

  $$D_0 = \frac{\Omega_{\mathrm{d}}^2 A}{\Omega_{\mathrm{m}}^2}, \tag{6.12}$$

  such that the ratio D_0/A is linearly proportional to $(\Omega_{\mathrm{d}}/\Omega_{\mathrm{m}})^2$. The peak angular acceleration of the base $a = \Omega_{\mathrm{d}}^2 A$ equals the peak angular acceleration of the test-mass $a = \Omega_{\mathrm{m}}^2 D_0$, analogous to the DC response given in eq. 6.3.

- If $\Omega_{\mathrm{d}} > \Omega_{\mathrm{m}}$, eq. 6.11 implies that the ratio D_0/A tends to 1, such that the mass remains stationary as the base shakes around it. The displacement between the test-mass and frame is the same size as the motion of the base itself. This is known as the seismometer mode of operation.

A model of eq. 6.11 is shown in fig. 6.2, where the ratio $\frac{D_0}{A}$ is plotted as function of driving frequency Ω_{d}, normalised to Ω_{m}. Note that D_0 is the relative peak displacement of the accelerometer, and A is the peak amplitude of the sinusoidal modulation of the base. The damping ratio ζ is the ratio of damping with respect to critical damping, and is varied from underdamped to critically damped (critical damping is $\zeta = 1$). The accelerometer and seismometer modes of operation are highlighted.

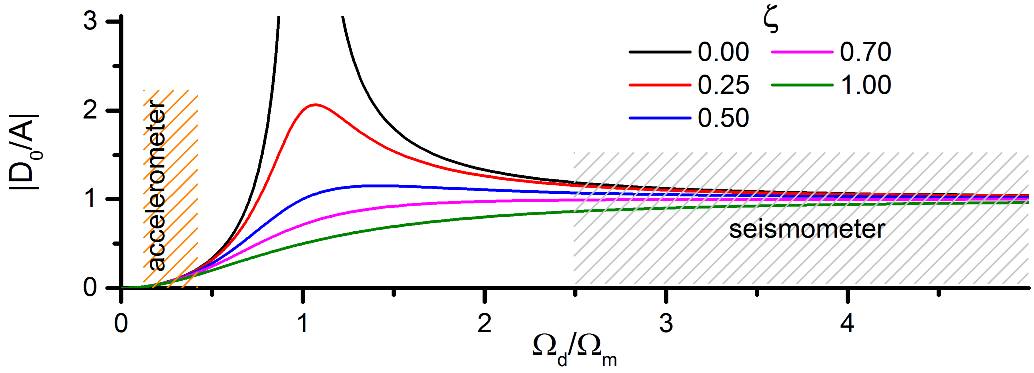

Figure 6.2: Predicted amplitude response D_0 of an accelerometer, normalised to the peak driving amplitude of the base A. This is plotted using eq. 6.11 as a function of sinusoidal driving frequency Ω_d, normalised to the accelerometer resonance Ω_m, for a range of damping ratios ζ. Shaded regions show the system operating as an accelerometer, with a linear response to acceleration, as well operating as a seismometer, which only detects the base displacement.

It can be seen from fig. 6.2 that damping plays an important role in defining the response of accelerometers, as it flattens the peak around the resonance Ω_m. A high damping ratio ζ therefore increases the linear bandwidth of the sensor and the damped test-mass responds linearly over a wider range of Ω_d. The increase in bandwidth can be theoretically shown by plotting the ratio of the actual response of the test-mass (D_0) governed by eq. 6.11, relative to the required linear response assuming the test-mass behaves as $D_\mathrm{lin} = \frac{\Omega_\mathrm{d}^2 A}{\Omega_\mathrm{m}^2}$ across all Ω_d. This leads to:

$$\frac{D_0}{D_\mathrm{lin}} = \frac{1}{\sqrt{\left(1 - \left(\frac{\Omega_\mathrm{d}}{\Omega_\mathrm{m}}\right)^2\right)^2 + \left(2\zeta \frac{\Omega_\mathrm{d}}{\Omega_\mathrm{m}}\right)^2}}, \tag{6.13}$$

which is plotted in fig. 6.3 with varying ζ. The bandwidth is defined as the range of driving frequencies where $\frac{D_0}{D_\mathrm{lin}} \approx 1$. The error between the expected linear measurement and the actual measurement is given by $(\frac{D_0}{D_\mathrm{lin}} - 1) \times 100\%$. The y-axis range of fig. 6.3 spans $\frac{D_0}{D_\mathrm{lin}} = \pm 5\%$. Increasing ζ towards critical damping results in a larger bandwidth where $\frac{D_0}{D_\mathrm{lin}} \approx 1$.

There are two main types of damping; structural and viscous air damping. At atmospheric pressure, viscous air damping is dominant for micron-sized objects, and structural damping related to the energy loss within the material can be neglected. This was confirmed in chapter 3 by experimentally reducing the pressure surrounding the microsphere-cantilever (and tapered fibre) whilst measuring the mechanical quality factor $\mathrm{Q_m} = \frac{1}{2\zeta}$,

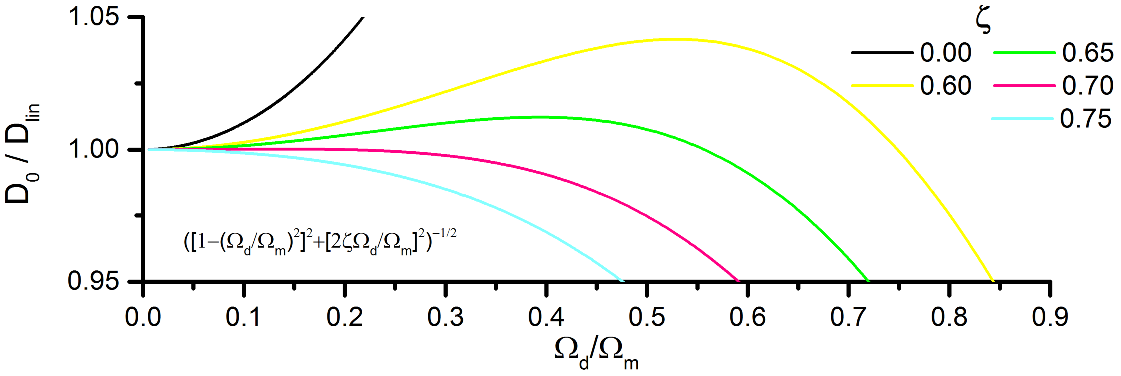

Figure 6.3: The ratio of the test-mass response D_0, relative to the expected response D_{lin} if the test-mass responds linearly across all frequencies. The damping ratio ζ is varied. The range of frequencies where $D_0/D_{\text{lin}} \approx 1$ sets the linear bandwidth, for example, with a damping ratio of $\zeta = 0.7$, the bandwidth between $0 \leq \frac{\Omega_d}{\Omega_m} \leq 0.2$ results in a measurement error less than 0.01%.

see fig. 3.12 (pg. 90. It was found that Q_m increases as the pressure is reduced from atmospheric pressure to 0.5 mbar, but did not reach the intrinsic Q_m, and is still dominated by air damping. A novel future experiment that has not been conducted with WGM inertial sensors is to apply cold damping or stabilisation using active feedback, which is commonly employed in with MEMS sensors [233, 234].

The above analysis only offers an insight into the expected response of a point-mass on a spring. In fact, the schematic shown in fig. 6.1 b) only represents an equivalent model for the microsphere-cantilever, where the total mass is lumped into an effective mass m_{eff} (i.e. a point mass), and body loads (e.g. forces that act over the distributed mass) such as gravity can be modelled as an equivalent single force applied at the c.o.m. position. A more realistic picture requires modelling the microsphere-cantilever as an elastic body which can flex and bend under transverse body loads (i.e. the acceleration acts perpendicular to the cantilever length). The uniformly distributed mass of the cantilever means that the deflection at each point along the length will vary. The following section describes how stress within the cantilever material causes strain, resulting in a measurable deflection that can be predicted using theory. This allows comparison with experimental data, presented later.

6.3 The Microsphere-cantilever as a Test-mass

In a similar fashion to the eigenfrequency analysis of chapter 3, the microsphere-cantilever is split into a beam with uniformly distributed mass and length L (fixed on one end), and the microsphere is modelled as a point-mass attached to a massless beam with length L. The total deflection at the free-end of the combined microsphere-cantilever is the sum of the calculated deflection from each model.

First the cantilever stem is analysed, which consists of a cylindrical rod with uniformly distributed mass, such that forces from acceleration are also distributed per unit length. A cantilever with no external loads is shown in fig. 6.4 a), whereas when a force per unit length (denoted as 'w') is applied in fig. 6.4 b), the cantilever bends. The deflection varies along the length and the largest deflection , $y(L)$, occurs at the tip.

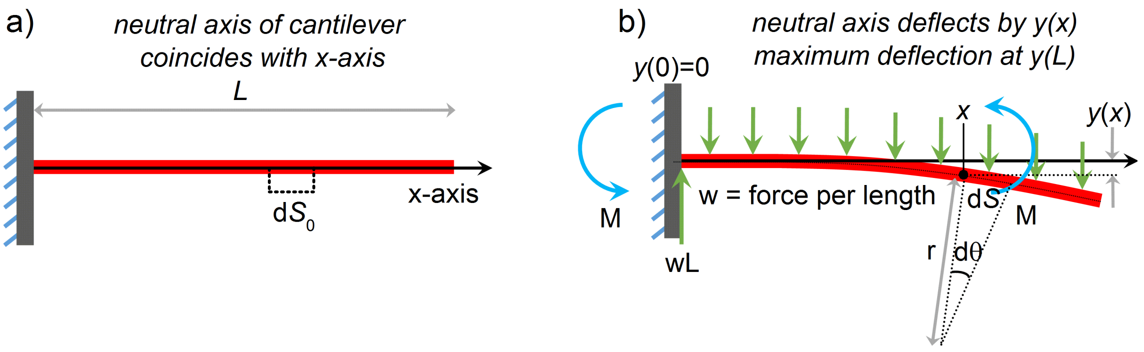

Figure 6.4: a) The cantilever portion of the microsphere-cantilever is modelled as a beam with length L, clamped on the left-hand side, with no external forces applied. b) When a force per unit length w is applied, the cantilever is deflected due to a bending moment M(x). The maximum deflection, $y(x)$, occurs when $x = L$, i.e. the cantilever tip.

The aim of the following analysis is to derive the relationship between the external and internal forces acting on the cantilever that cause deflection. The cantilever is analysed as segments with length $\mathrm{d}S_0$, which undergo bending (fig. 6.4 b)), such that $\mathrm{d}S$ is defined as an arc length.

With no external loads, fig. 6.4 a) shows the cantilever with its neutral axis (i.e. the axis that runs parallel to the length, through the origin of the cylinder cross-section) coinciding with the x-axis. When a downward body load w (force per unit length) is applied, the cantilever bends such that the neutral-axis deflects away from the x-axis, fig. 6.4 b), and a radius of curvature r exists at x, forming an arc length $\mathrm{d}S$. At each point along x, the deflection $y(x)$ represents the change in distance from the x-axis, and varies along the length such that at $x = L$, the maximum deflection occurs $y(L)$ and is the measured output of the accelerometer.

The deflection is caused by a bending moment, which is the reaction induced in the structure from the applied body load. The internal force that gives rise to the bending moment is known as stress, which governs the deflection ($\frac{\mathrm{d}y}{\mathrm{d}x}$) as layers of the cantilever are compressed and stretched. In order to derive $y(x)$, the moment arising from the applied force can be equated to the bending moment caused by the internal stress of the cantilever. First, a simple analysis of the moments (i.e. turning effect) from the *external* forces in fig. 6.4 b) are considered. The equation for the moment of a force F acting at a perpendicular distance l is $\mathrm{M} = \mathrm{F}l$, such that the sum of the external moments at position x is:

$$\mathrm{M} = -\mathrm{w}L\,\frac{L}{2} + \mathrm{w}L\,x - \mathrm{w}x\,\frac{x}{2} = -\frac{\mathrm{w}(x-L)^2}{2}, \tag{6.14}$$

Also present at x is an *internal* bending moment equal to eq. 6.14. A schematic of the bending mechanism is shown in fig. 6.5. The bending moment relates the internal stress force σ, acting perpendicular to the cross-section of the cantilever (fig. 6.5 a), such that:

$$\mathrm{M} = \int_A -h\sigma\,\mathrm{d}A, \tag{6.15}$$

where σ is the internal stress force that resists the force w, h is the vertical distance in the cross-section from the neutral axis, and A denotes that eq. 6.15 is an area integral.

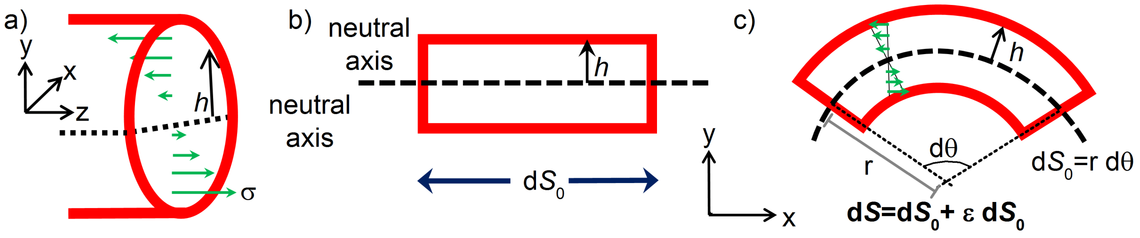

Figure 6.5: a) The cross-section of the cantilever experiences a varying stress force σ (green arrows) dependent on h, that resists the applied force, where h denotes the distance from the neutral axis. b) With no applied transverse force, a segment of the cantilever of length $\mathrm{d}S_0$, does not vary in length with h. c) When a force is applied, a stress field develops that varies with h, such that the cantilever deforms with an arc length $\mathrm{d}S$ dependent on h. The change in arc length from $\mathrm{d}S_0$ is related to the strain ϵ.

If the cross-section is considered as a thin layer i.e. a circular sheet, in the presence of an unequally distributed stress field, the upper portion ($h > 0$) will be pushed in the negative x-direction, whereas the lower portion $h < 0$ is pushed forwards in the x-direction. A segment of the cantilever contains many cross-sectional layers such that the total stress applied results in a deflection. A segment of the un-deflected beam with length $\mathrm{d}S_0$ is shown in fig. 6.5 b). Imagining now that the cantilever is made up of horizontal stacked layers, the layer at any point h has a constant length $\mathrm{d}S_0$. When the beam is subjected to an applied force, fig. 6.5 c), the varying stress field causes each horizontal layer to bend unequally. The neutral-axis maintains the original length $\mathrm{d}S_0$, since r is defined relative to $h = 0$ ($\mathrm{d}S_0(0) = r\,\mathrm{d}\theta$), whereas horizontal layers at positive h undergo a length elongation, and those at negative h are compressed (reduction in length). The length $\mathrm{d}S$ at each h is therefore defined by $\mathrm{d}S(h) = (r - h)\,\mathrm{d}\theta$.

Strain (ϵ) is the resultant change in length due to stress, and is defined as the ratio of the change in length compared with the unstressed length:

$$\epsilon = \frac{\mathrm{d}S(h) - \mathrm{d}S_0}{\mathrm{d}S_0} = \frac{(r-h)\,\mathrm{d}\theta - r\,\mathrm{d}\theta}{r\,\mathrm{d}\theta} = -\frac{h}{r}, \tag{6.16}$$

which describes a zero strain at $h = 0$ (neutral axis) that increases linearly with h. Young's modulus[5] is known as the elastic modulus as it governs the linear relationship between stress and strain through $\mathrm{E} = \frac{\sigma}{\epsilon}$, therefore using eq. 6.16, the stress can be defined by:

$$\sigma = -\frac{\mathrm{E}h}{r}, \tag{6.17}$$

which can be used in eq. 6.15 to define the bending moment that resists the moment due to the applied force:

$$M = -\int_A h\left[\frac{-\mathrm{E}h}{r}\right]\mathrm{d}A = \frac{\mathrm{E}}{r}\int_A h^2\,\mathrm{dA}. \tag{6.18}$$

The remaining integral in eq. 6.18 is known as the second moment of area denoted by I, which for a circular cross-section is equal to:

$$\mathrm{I} = \int_0^{2\pi}\int_0^{r_c} (r_c \sin(\theta))^2\, r_c\,\mathrm{d}r_c\,\mathrm{d}\theta = \frac{\pi r_c^4}{4}, \tag{6.19}$$

where r_c is the cantilever radius, and θ is the polar angle.

The radius of curvature can be approximated as $\frac{1}{r} \approx \frac{\mathrm{d}^2 y}{\mathrm{d}x^2}$ using lengthly geometric algebra. Therefore the rate of change of the deflection can be written as:

$$\mathrm{M} = \mathrm{EI}\,\frac{\mathrm{d}^2 y}{\mathrm{d}x^2}. \tag{6.20}$$

By equating eq. 6.14 with eq. 6.20, and integrating twice, a direct derivation of the deflection $y(x)$ at any point x can be formed:

$$\int\!\!\int \mathrm{EI}\,\mathrm{d}^2 y = -\int\!\!\int \frac{\mathrm{w}(x-L)^2}{2}\,\mathrm{d}x^2, \tag{6.21}$$

---

[5] Young's modulus for silica is 70 GPa

$$\mathrm{EI}\,y = \frac{\mathrm{w}}{2}\left[\frac{x^4}{12} - \frac{Lx^3}{3} + \frac{L^2x^3}{2} + Bx + C\right], \tag{6.22}$$

where B, C are constants of integration, found by applying the following boundary conditions:

- No deflection at the clamping point: $x = 0, y = 0$.
- Gradient is flat at the clamping point: $x = 0, \frac{dy}{dx} = 0$.

This leads to $B = C = 0$ which sets the deflection as:

$$y(x) = \frac{\mathrm{w}L}{24\,\mathrm{EI}}\left[\frac{x^4}{L} - 4x^3 + 6x^2L\right]. \tag{6.23}$$

At the free-end of the cantilever $x = L$, the maximum deflection is:

$$y(L) = \frac{\mathrm{wL}^4}{8\mathrm{EI}}. \tag{6.24}$$

The force acting on the cantilever per unit length is $\mathrm{w} = m_c\,a = a\rho\pi r_c^2$ where ρ is the density of silica ($2200\,\mathrm{kg\,m^{-3}}$), and m_c is the bulk mass of the cantilever. Substituting these values, and the equation for I (eq. 6.19) into eq. 6.24:

$$y(L) = \frac{a\rho L^4}{2\mathrm{E}\,r_c^2}, \tag{6.25}$$

which predicts the deflection of the cantilever stem at the tip, which contributes to the overall deflection of the microsphere-cantilever.

Next, the deflection due to the microsphere point-mass is considered, which gives rise to a bending moment at a point x along the cantilever length, equal to $\mathrm{M} = -\mathrm{F}L(1 - \frac{x}{L})$, where $\mathrm{F} = m_s a$ is the force experienced by the sphere with total mass $m_s = (4/3)\rho\pi r_s^3$, and r_s is the sphere radius. Equating this with the right hand side of eq. 6.20 and double integrating with respect to x gives:

$$\mathrm{EI}\,y = \frac{Fx^3}{6} - \frac{FLx^2}{2} + Bx + C \tag{6.26}$$

where B, C are constants of integration found using the same boundary conditions as the cantilever analysis. The boundary conditions set $B = C = 0$, and the deflection due to the microsphere is:

$$y(x) = \frac{\mathrm{F}L}{\mathrm{EI}}\left(-\frac{x^2}{2} + \frac{x^3}{6L}\right). \tag{6.27}$$

The point of interest is the deflection due to the microsphere at the free-end of the cantilever where $x = L$:

$$y(L) = \frac{\mathrm{F}L^3}{3\mathrm{EI}} = \frac{16\rho r_s^3 L^3 a}{9\mathrm{E}r_c^4}. \tag{6.28}$$

The combined effect of the force acting on both the microsphere, and the distributed cantilever mass, results in the total deflection at the free-end of the microsphere-cantilever $y_t(L)$ in response to acceleration, which is the sum of eq. 6.28 & eq. 6.25:

$$y_t(L) = \frac{a\rho L^3}{\mathrm{E}r_c^2}\left[\frac{16r_s^3}{9r_c^2} + \frac{L}{2}\right]. \tag{6.29}$$

This equation, which only requires knowledge about the geometry and material of the microsphere-cantilever will be useful to predict the sensing range, and compare with experimental data.

6.3.1 Whispering Gallery Mode Transduction of Acceleration

As proven in chapter 3, a change in the coupling distance d between the microsphere-cantilever and the taper perturbs the WGM such that the motion is imprinted onto the taper fibre transmission. The so-called transduction beam introduced in chapter 3, is created by continuously exciting the WGM with a laser red-detuned to the resonance. In this chapter, the transduction beam is used to detect an experimentally applied acceleration by measuring the deflection of the microsphere-cantilever.

When operating as an accelerometer, the microsphere-cantilever is placed at a DC coupling distance d relative to the taper. With no deflection, the corresponding position of the free-end (i.e. the microsphere) is referred to as the 'null-position' (d_0) using sensor terminology. Acceleration causes a deflection of the microsphere away or towards d_0 by $y(L)$ derived above, which is transduced by the WGM, and recorded in the output transmission of the taper. When applied forces are removed, the microsphere returns to d_0.

The transmission is a measure of the change in power coupled to the WGM ($\mathrm{P_c}$), which is shown to vary non-linearly with d in chapter 2. Since the null-position is chosen to be at a fixed d, it is expected that there is a limited range of accelerations which result in a deflection Δd around d_0[6] that causes a linear change of $\mathrm{P_c}$. Another unknown is the absolute sensing limit since Δd cannot exceed d_0, otherwise the microsphere will touch the taper. A previous study was conducted on a similar WGM accelerometer over 15 years ago [20], but did not experimentally measure either of these parameters. Therefore the results presented here are the first to characterise multiple parameters of a WGM accelerometer, where the test-mass is the WGM resonator itself.

6.4 Experimental Results

Two different microsphere-cantilevers are used in the following sets of data, labelled as microsphere-cantilever[$\mathcal{E}$], and microsphere-cantilever[$\mathcal{F}$], fabricated using the method in chapter 2. Note that microsphere-cantilever[$\mathcal{F}$] is only used in section 6.4.4 to measure the sensing bandwidth and the acceleration sensitivity, owing to its higher c.o.m. mechanical frequency. Using the experimental set-up of fig. 2.23 (pg. 53), also in chapter 2, a WGM is excited with counter-propagating beams, such that one beam forms the transduction signal (red-detuned with respect to the WGM), and the other is used as the strong beam in a passive thermal locking set-up[7]. The transduction signal is the output of the WGM sensor, and is measured with a photodetector.

In order to experimentally verify the performance of the WGM sensor, a commercial sensor by Analog Devices (ADXL327) is mounted close to the microsphere-cantilever. The ADXL327 is a 3-axis accelerometer with a sensing range of $\pm 2\,\mathrm{g}$, a maximum bandwidth of 1600 Hz, and a noise density of $250\,\mu\mathrm{g\,Hz^{-1/2}}$, where acceleration is measured with the unit g (defined relative to gravity $\mathrm{g}= 9.81\,\mathrm{ms^{-2}}$) as standard within the inertial sensing community. It operates by measuring a capacitance change due to a movable electrode test-mass.

A piezo-stack[8] is used to accelerate the combined system (i.e. by moving the 'base'). Due to the limited displacement range of $9.2\,\mu\mathrm{m}$, it is easier to apply large angular accelerations instead of a large DC acceleration. This is achieved by applying a sinusoidal driving signal to modulate the piezo-stack displacement. The peak amplitude of the angular acceleration is $a_{\max} = \Delta l\, \Omega_{\mathrm{d}}^2$, where Δl is the change in piezo-stack length from the null-position. The peak-to-peak angular acceleration is $2 \times a_{\max}$. As shown in eq. 6.12,

---

[6] Note that $y(L) \equiv \Delta d$.

[7] A passive thermal lock is employed instead of the Pound-Drever-Hall lock (chapter 2 section 2.5.1) because the high vibrational tests performed in this chapter destabilise the active lock.

[8] Thorlabs PK4DMP1.

the microsphere-cantilever responds linearly to the sinusoidal acceleration, and the WGM transduction signal will show a corresponding sinusoidal modulation, with a peak amplitude proportional to a_{max}. It is often more convenient to use measure peak-to-peak amplitudes (i.e. the sum of the deflection away and towards the null-position) since the null-position may shift. The term 'angular acceleration', which is used to highlight the use of a sinusoidal shaker test, will be dropped from this point onwards for clarity.

6.4.1 Sensing Range

The first measurement is of the sensing range, using microsphere-cantilever[$\mathcal{E}$] with dimensions $r_c = 60\,\mu$m, $r_s = 76\,\mu$m, and $L = 7\,$mm, placed at $d_0 = 0.35\,\mu$m from the taper. The piezo-stack is driven with driving frequency $\Omega_{\text{d}} = 2\pi \times 1400\,$Hz, and an increasing peak displacement amplitude A such that the WGM sensor and the ADXL327 experience a peak-to-peak acceleration of $2 \times A\Omega_{\text{m}}^2$. The peak-to-peak response from the ADXL327, and the WGM sensor is plotted in fig. 6.6 a) & b) respectively.

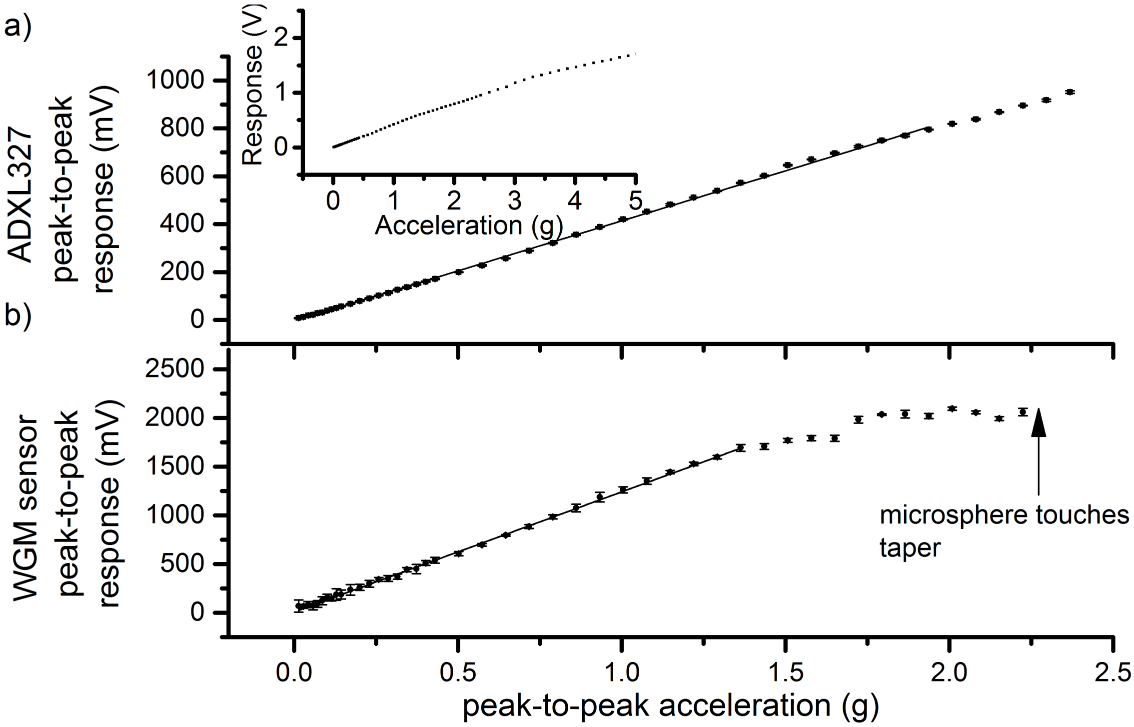

Figure 6.6: The ADXL327 and the WGM accelerometer are driven by a sinusoidal acceleration at $\Omega_{\text{d}} = 2\pi \times 1.4\,$kHz, with a increasing peak-to-peak acceleration. The peak-to-peak response of the ADXL327 is shown in a), where a linear fit is applied to deduce the scale factor. The inset graph shows the non-linearity of the ADXL327 output with increased acceleration. In b), the response of the WGM sensor using microsphere-cantilever[$\mathcal{E}$] is plotted, which displays a similar non-linearity. For both a) & b), fits are applied only within the linear response range where the scale factor error is $< 0.6\,\%$.

The ADXL327 provides a response with scale factor $418 \pm 2\,\mathrm{mV/g}$, found by measuring the gradient in fig. 6.6 , and in good agreement with the specified value of $420 \pm 42\,\mathrm{mV/g}$ in the specifications. The WGM sensor has a linear scale factor of $1233 \pm 7\,\mathrm{mV/g}$ but it should be noted that due to the use of a variable gain photodetector, this value can be amplified arbitrarily, at the cost of increasing photodetector noise. The experimental linear sensing range (i.e. ± peak acceleration) is found to be $\pm 1\,\mathrm{g}$ for the ADXL327, and $\pm 0.7\,\mathrm{g}$ for the WGM sensor using microsphere-cantilever[$\mathcal{E}$][9].

Using eq. 6.29, and the dimensions of microsphere-cantilever[$\mathcal{E}$], the predicted absolute peak-to-peak sensing range[10] due to a maximum $\Delta d = 0.35\,\mu\mathrm{m}$ is:

$$2 \times a_{\max} = 2 \times 0.35\,\mu\mathrm{m} \times \frac{\mathrm{E}\, r_c^2}{L^3 \rho \left[\frac{16 r_s^3}{9 r_c^2} + \frac{L}{2}\right]} \approx 6.4\, g. \tag{6.30}$$

The absolute peak-to-peak sensing range of the WGM sensor is marked in fig. 6.6 b), where a peak-to-peak acceleration of 2.3 g caused the microsphere to touch the taper. This is nearly 3 times smaller than prediction. It is anticipated that the null-position is shifted during vibration testing, which can be caused by vibration rectification errors, and is thoroughly investigated later. First, the influence of a shifted d_0 is analysed with experimental data to calculate the required $0\,g$ bias shift that would result in a reduction of the sensing range.

Sensing Range Dependence on Null-position

It has been verified in chapter 2 section 2.13 that the power coupled to the WGM ($\mathrm{P_c}$) is dependent on the coupling distance d. This is measured for the same microsphere-cantilever used in fig. 6.6 b) (microsphere-cantilever[$\mathcal{E}$]), by actuating d away and towards the null position d_0 using the piezo-stack that supports it. This mimics the deflection Δd that would occur in the presence of acceleration. The normalised P_c is plotted as a function of Δd, in fig. 6.7 (blue crosses). The predicted peak acceleration ($a_{\max}$) required to cause Δd is plotted in black, using eq. 6.29.

A large deflection of the microsphere-cantilever due to acceleration will modulate the transduction signal output according to the non-linear relationship between P_c and Δd in

---

[9] Here, ‘linear’ is strictly defined as the range of acceleration where the fitted scale factor has an error less than 0.6%. The ADXL327 spec sheet quotes a linear range of ±2 g, but with a scale factor error of 10 %.

[10] This is also referred to as the ‘dynamic range’ in the inertial sensor community.

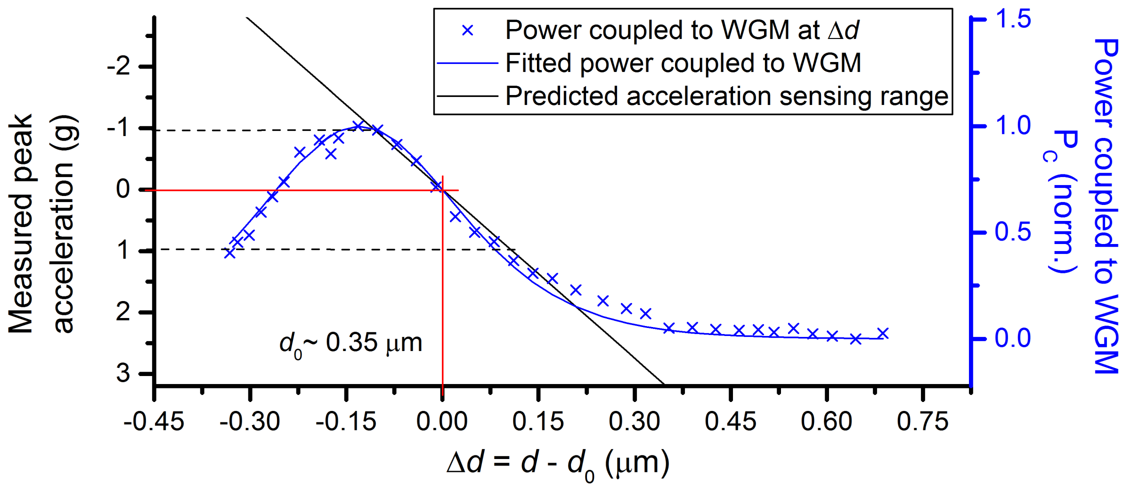

Figure 6.7: The power coupled to the WGM in microsphere-cantilever[$\mathcal{E}$] is measured as the coupling distance d is varied away from the null position d_0 by Δd, (blue crosses). This mimics the output response of the WGM if the microsphere-cantilever deflects by Δd due to a peak acceleration. The predicted peak acceleration required to cause a deflection equal to Δd is plotted in black using eq. 6.29. The linear sensing range is approximately the region where $\mathrm{P_c}$ changes linearly with $\pm\Delta d$ around d_0, corresponding to a predicted range of $\pm 1\,\mathrm{g}$, equal to a peak-to-peak max. acceleration of $2\,\mathrm{g}$.

fig. 6.7 (blue data). Note that the output of the transduction signal is the transmission, which is defined in chapter 2 as $\mathcal{T} = 1 - \mathrm{P_c}$. At a null-position of $d_0 = 0.35\,\mu\mathrm{m}$, the maximum linear relationship with $\mathrm{P_c}$ is limited by the value of Δd that reaches the turning point, $\Delta d_{\mathrm{lin}} \approx -0.13\,\mu\mathrm{m}$ (marked in dashed lines). This turning point sets a maximum $\mathrm{P_c}$, such that after the turning point, P_c decreases with further acceleration, and the transduction signal will show a double-well shape. Since P_c varies exponentially with large $+\Delta d$, i.e. in response to a high acceleration with peak-to-peak amplitude $> 2\times\Delta d_{\mathrm{lin}}$ results in very little change in $\mathrm{P_c}$ at $\Delta d > 0.3$, and will show a smaller reading that deviates from the linear scale factor.

The predicted linear sensing range from fig. 6.7 is marked out by the black dashed lines, representing a region where $\mathrm{P_c}$ is approximately linear with $\pm\Delta d$, that corresponds to a sensing range of $\pm 1\,\mathrm{g}$, not too dissimilar to the experimentally measured range $\pm 0.7\,\mathrm{g}$ in fig. 6.6 b). However, the discrepancy between the absolute sensing range is unaccounted for.

A possible explanation is that a DC drift in the null-position occurred part way through testing. Using the results in fig. 6.7, a shift in the null position by $-0.1\,\mu\mathrm{m}$ (i.e. if d_0 changes to $0.25\,\mu\mathrm{m}$) is predicted to limit the absolute sensing range to $\pm 1\,\mathrm{g}$, and could account for the peak-to-peak range of $2.3\,\mathrm{g}$ in fig. 6.6 b). There are three possible causes for a null-position drift:

- A random misalignment of the supporting mounts, posts or the flexure stage.
- The cavity enhanced optical dipole force (CEODF) due the WGM[11] may attract the taper towards the microsphere at small d (i.e. when the sphere is deflected closer to the taper), which can lead to a DC offset.
- Vibration rectification errors, which shifts d_0 in vibrational environments.

To see if the CEODF is a possible source of drift, the long term stability in the presence of no vibration is measured.

6.4.2 Long Term Stability

An indication of a continuous systematic drift of the null-position, unrelated to shocks or changes in mounting stability, is to measure the long term stability of the WGM transmission, $\mathcal{T}$. Microsphere-cantilever[$\mathcal{E}$] is once again coupled to the tapered fibre at $d_0 = 0.35\,\mu$m, and the WGM $\mathcal{T}$ is recorded for 10 mins, with zero applied acceleration (i.e. the measured $\mathcal{T}$ from the photodetector corresponds to the 0 g bias level). The plot is displayed in fig. 6.8, and the drift of d_0 corresponds to the gradient of the linear fit in red, converted into g units using the scale factor from fig. 6.6 b). This drift is not related to a change in coupling power (which is monitored), or dust adhering to the surface of the taper or microsphere (which causes staggered jumps that decrease $\mathcal{T}$).

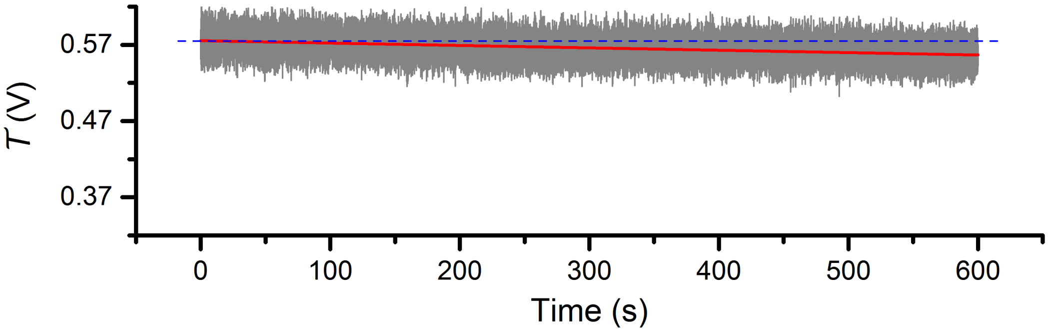

Figure 6.8: The long term stability of the WGM sensor output is measured by fitting the transmission, $\mathcal{T}$ over time (data in gray, fit in red). This corresponds to the 0 g bias level (no acceleration is applied). The gradient corresponds to the rate of decrease in $\mathcal{T}$ (the dashed blue line represents a constant $\mathcal{T}$), which is converted using the scale factor of fig. 6.6 b) to convert into the equivalent false acceleration measurement of $-25 \pm 0.1\,\mu$g/s.

It is found that over 10 mins, due to the drift of the 0 g bias level, the WGM sensor outputs a false acceleration reading that drifts by $-25 \pm 0.1\,\mu$g/s. A decrease in trans-

---

[11] This force was used in chapter 4 to feedback cool the mechanical modes of the taper.

mission equals an increase in P_c, which would correspond to the taper and sphere moving closer together, perhaps an indication of the CEODF attracting the taper towards the microsphere, and should be studied more closely in future experiments. This means that over time, unless the null-position is returned to d_0, a false reading of an acceleration in the negative y-axis will be reported. In order to fully account for the limited sensing range of fig. 6.6 b), the taper needs to be actuated towards the microsphere by 100 nm, corresponding to a decrease in $\mathcal{T}$ of approximately 28 %, and would require the experiment to be functional over 1.5 hours. For this reason, the long term drift can be eliminated as a major contribution to the lower than expected sensing range, since the data in fig. 6.6 b) is taken within 20 min. The CEODF may not be responsible for the slow drift, but should be tested in future experiments by increasing the input laser power which will linearly increase the magnitude of the force. This leaves two remaining sources of null-position drift; a random misalignment from the supporting stages due to the high vibrational conditions, or, vibration rectification errors, which are characterised next.

6.4.3 Vibration Rectification Errors

The vibration rectification error (VRE) is a measure of the DC offset in null-position when a test-mass is exposed to vibration, measured in units of g/g^2. The DC output of the sensor changes as a function of the peak acceleration, even though the total time-averaged acceleration is zero. There are two main causes of vibration rectification; asymmetric damping, and DC scaling non-linearity [235].

Asymmetric damping occurs if the motion of the test-mass is more strongly damped in one direction, i.e. +g direction, than the opposite, i.e. -g. The deflection of the test-mass as it responds to vibration will therefore be biased towards the negative direction. If the signal is time-averaged it will give a net DC output that is shifted to the negative g direction compared to when no vibration is present.

The other mechanism that leads to vibration rectification is a non-linearity in the sensing range due to the test-mass, where the time averaged response in one direction is not equal to that in the other direction. This is often related to a geometric asymmetry, or cross-coupling to another axis direction. This tends to be the more dominant effect over asymmetric damping.

The theoretical description of the VRE requires an additional quadratic term in the test-mass deflection equation in response to an acceleration a, such that the deflection $D(t)$ is written as [235]:

$$D(t) = Ca + \beta_c a^2, \tag{6.31}$$

where C, β_c are constants. The constant C is the linear scale factor, measured in fig. 6.6, and β_c is referred to as the co-efficient of the second order non-linearity. If the test-mass is now subjected to a sinusoidal acceleration of $A \cos \Omega_\mathrm{d} t$, eq. 6.31 becomes:

$$D(t) = CD_0 \cos(\Omega_\mathrm{d} t) + \beta_c D_0^2 \cos^2(\Omega_\mathrm{d} t), \tag{6.32}$$

where D_0 is the scale factor. The time average of the first term in eq. 6.32 is zero, whereas the time average of the squared term is proportional to $\int_t \cos^2(\Omega_\mathrm{d} t)\,\mathrm{d}t = \frac{1}{2}$, therefore the time averaged deflection is:

$$\bar{D}_0 = \frac{\beta_c D_0^2}{2}. \tag{6.33}$$

The measurement of $\bar{D}_0$ (the 0 g bias level) reports a false acceleration that is proportional to acceleration squared, and is governed by the constant $\beta_2/2$, more commonly referred to as the VRE:

$$\mathrm{VRE} = \frac{\beta_c}{2} = \frac{\bar{D}_0}{D_0^2}. \tag{6.34}$$

Therefore, the deflection can be written as:

$$D_0 = C\,\mathrm{g} + 2\mathrm{g}^2 \times \mathrm{VRE}. \tag{6.35}$$

The VRE is measured for the ADXL327 and the WGM sensor (using microsphere-cantilever[$\mathcal{E}$]) in two ways and then compared to investigate if the non-linearity of the WGM sensor response can account for the reduced sensing range found in fig. 6.6 b).

First, the 0 g bias level is measured by averaging the modulated WGM transduction signal/ADXL327 signal when the system is driven by a sinusoidal acceleration with increasing amplitude g, and plotted as a function of g^2. The results for the ADXL327and the WGM sensor are shown in fig. 6.9 and fig. 6.10 respectively. Since the data presented here corresponds to the same data used to deduce the sensing range in figs. 6.6 a)& b), a direct comparison can be made using a second method to find the VRE by fitting the previously measured sensing range with eq. 6.31.

The results of the first method are as follows; the gradient of the fits in figs. 6.9 & 6.10

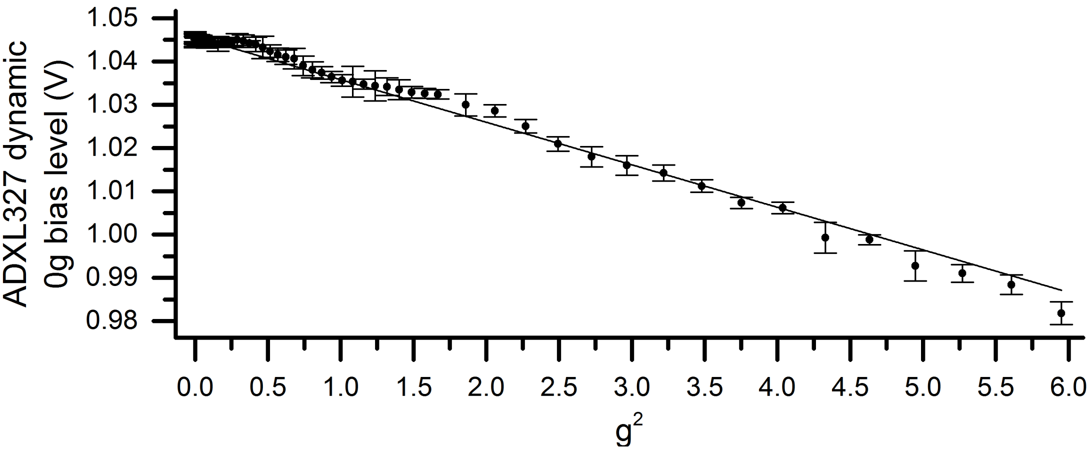

Figure 6.9: The VRE for the ADXL327 is calculated by measuring the DC bias shift of the output signal, at increasing acceleration, plotted as a function of g^2. The gradient gives a VRE of $-23.5 \pm 0.3\,\mathrm{mg/g^2}$, found by using the scale factor in fig. 6.6 a). This data is the same as that used in fig. 6.6 a).

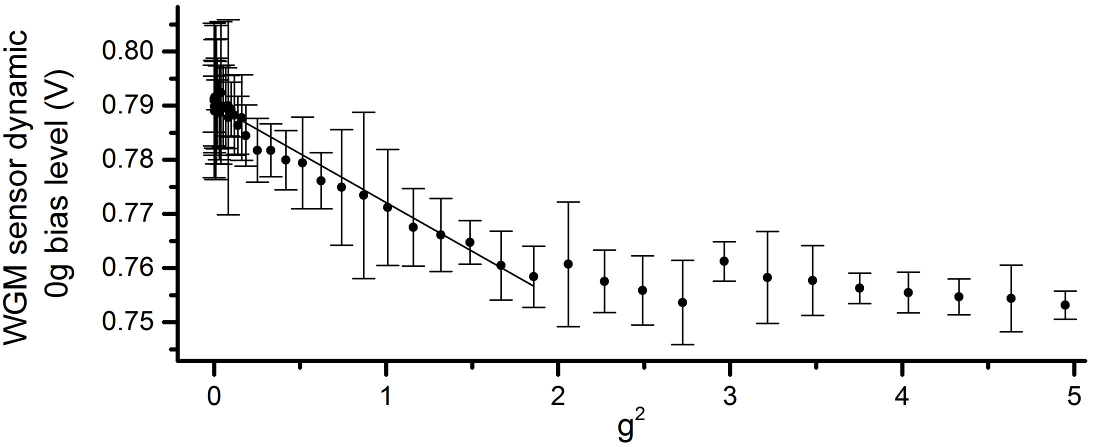

Figure 6.10: The VRE for the WGM sensor using microsphere-cantilever[$\mathcal{E}$] is calculated by measuring the DC bias shift of the output signal, at increasing acceleration, plotted as a function of g^2. This data is the same as that used in fig. 6.6 b). A linear fit is applied, but only up to the linear sensing limit found in fig. 6.6 b) (i.e. $g < 1.7$). The gradient of the fit gives a VRE of $-14.6 \pm 0.5\,\mathrm{mg/g^2}$, using the scale factor in fig. 6.6 b). At $g^2 > 2^2$, the WGM transmission is non-linear with respect to larger acceleration (see fig. 6.7), such that the transduced signal is no longer equal to the actual motion of the microsphere-cantilever. The VRE will cause d_0 to further decrease, but the time averaged WGM measures d_0 non-linearly.

are converted into acceleration units using the scale factors obtained for the ADXL327 (fig. 6.6 a)) and the WGM sensor (fig. 6.6 b)) respectively, such that figs. 6.9 & 6.10 represent $\frac{\bar{D_0}}{D_0^2}$. Therefore, using eq. 6.34 the VRE for the ADXL327 is $-23.5 \pm 0.3\,\mathrm{mg/g^2}$ and for the WGM sensor, $-14.6 \pm 0.5\,\mathrm{mg/g^2}$. Note that the plot of the 0 g bias level for the WGM sensor is only fitted up to $2\,\mathrm{g}^2$. This is because the WGM does not transduce large Δd around d_0 linearly, as described by fig. 6.7, and the sinusoidal modulation of the WGM $\mathcal{T}$

with respect to the sinusoidal acceleration becomes distorted such that the 0 g level is not equal to half the peak-to-peak amplitude.

To verify *if* the source of the vibration rectification is due to the non-linearity of the sensor, the second method to find the VRE is applied. Here, eq. 6.35 is fitted to each sensor's full measured range (i.e. including the non-linearity in figs. 6.6 a) & b)), to obtain the second order non-linearity co-efficient $\beta_c = 2 \times \text{VRE}$. Using this method, a VRE of $-104 \pm 4\,\text{mg/g}^2$ and $-25.0 \pm 0.9\,\text{mg/g}^2$ is obtained for the WGM sensor and the ADXL327 respectively. The value for the ADXL327 VRE from fitting β_c is in good agreement with the value obtained directly from measurement. However, the VRE of the WGM sensor from measurement of β_c is significantly higher. If eq. 6.35 is now fitted over the linear sensing range of the WGM sensor in fig. 6.6 b), a value of $\beta_c = -2 \times (21 \pm 7)\,\text{mg/g}^2$ is obtained, which is closer to the measured VRE in fig. 6.10.

Therefore, a possible explanation for the lower than expected absolute WGM sensing range (i.e. until the microsphere touches the taper) is as follows; at a peak acceleration of $\sqrt{3}\,$g, a mechanical misalignment of the supporting mounts or stages occurred, pushing the null position towards the taper (in fig. 6.10, at $\text{g}^2 = 3$, the WGM DC transmission increases, signifying a jump over the turning point in the WGM power coupling of fig. 6.7). A misalignment of 100 nm is feasible, especially as the system is exposed to continuously high vibrations. Currently the tapered fibre and the microsphere-cantilever are held by mounts on separate supports, which are then fixed to a common base. If the mechanical shift in d_0 is related to these supporting mounts, the relative stability can be improved by mounting both the microsphere-cantilever and a tensioned taper onto the same frame.

The sensing range is ultimately limited by the microsphere-cantilever material properties. The proportionality limit defines when stress is equal to strain, governed by a material specific constant (Young's modulus). This is the basis of Hooke's law, and relates applied stress to the linear deflection of the cantilever. The elastic limit of silica determines when the cantilever becomes permanently deformed, and does not return to its original state once the applied force is removed. The stress required for silica fibre to break is approximately 6 GPa [236]. A cylindrical cantilever with $r_c = 60\,\mu\text{m}$, $m = 20 \times 10^{-9}\,\text{kg}$, and $L = 5\,\text{mm}$, can therefore withstand a load of $\text{F}_{\text{max}} = 0.2\,\text{N}$ acting on the free-end before rupture[12]. This is equivalent to an applied acceleration of over $1 \times 10^6\,$g, and implies the cantilever

---

[12] Here eqs. 6.18 & 6.17 are used to form the relationship $\sigma = \text{M}h/\text{I}$, where h is the distance from the neutral axis, M is the moment, and I is the second moment of area. The maximum stress occurs at $h = r_c$.

could withstand a car crashing into a wall whilst travelling at a velocity of 100 km/hr (approx 100 g deceleration) [237]. However, the deflection of the cantilever in response to $a = 100\,\mathrm{g}$ is $10\,\mu$m, over 100 times larger than the coupling distance between the sphere and the taper. In comparison, the ADXL327 is specified to survive a shock of 10,000 g, and would be more suitable for high g environments unless the microsphere-cantilever is actively prevented from touching the tapered fibre i.e. in a closed-loop scheme.

Clearly, the WGM sensor studied here requires further work to survive 10,000 g, including the need for re-calibration if the microsphere-cantilever must be seperated from the taper after touching. This may not be an issue if one considers the other end of the sensing scale; the minimum resolvable acceleration. The exquisite transduction sensitivity obtained in chapter 3 has already proven that the WGM is able to detect the thermal motion of the microsphere-cantilever, enabling feedback cooling in chapter 4. The next section derives the minimum noise equivalent acceleration, limited by the thermal motion of the test-mass, and sets the absolute sensitivity for detecting acceleration. The sensitivity is then experimentally deduced and tested.

6.4.4 Sensitivity & Bandwidth

The sensitivity of the WGM accelerometer can be quantified by its noise equivalent acceleration a_{NEA}, which converts the total noise floor of the displacement PSD into an equivalent minimum resolvable acceleration. It is defined as:

$$a_{\mathrm{NEA}} = \sqrt{a_{\mathrm{th}}^2 + a_{\mathrm{det}}^2 + a_{\mathrm{add}}^2 + ...}, \tag{6.36}$$

which is a sum of all noise sources present in the WGM sensor; a_{th} is the equivalent acceleration from the microsphere-cantilever thermal motion, a_{det} is related to readout noise, and a_{add} is a lumped parameter of other noise sources. For example, miniaturised capacitive sensors require consideration of the Johnson noise. The fundamental limit to a_{NEA} is the thermal noise equivalent acceleration a_{th}, as electronic noise and detector noise can be minimised.

The value of a_{th} can be derived by considering the average force power density $\bar{\mathrm{F}}(\omega)$ required to drive a deflection equivalent to the thermal motion. The derivation of $\bar{\mathrm{F}}(\omega)$ can be obtained by finding the total kinetic energy $\mathrm{E_k} = \frac{1}{2}m_{\mathrm{eff}}\bar{v}^2$ gained by the test-mass from $\bar{\mathrm{F}}(\omega)$ where $\bar{v}$ is the mean velocity, and equating it to the thermal energy $\frac{1}{2}\mathrm{k_B T_0}$

[52][13]. Starting with the test-mass equation of motion in frequency space, written as a function of velocity:

$$i\omega m_{\mathrm{eff}}\, v(\omega) + b\, v(\omega) + \frac{k}{i\omega}\, v(\omega) = \mathrm{F}(\omega), \tag{6.37}$$

where $v(\omega) = \mathrm{FFT}\left[\frac{\mathrm{d}x(t)}{\mathrm{d}t}\right] = i\omega x(\omega)$. The mean square velocity is therefore:

$$\bar{v}^2(\omega) = \frac{\bar{\mathrm{F}}^2(\omega)}{b^2 + (m_{\mathrm{eff}}\omega - k/\omega)^2}. \tag{6.38}$$

The kinetic energy within a frequency interval dω can be written using eq. 6.38:

$$\mathrm{dE_k} = \frac{m_{\mathrm{eff}}}{2b^2} \frac{\bar{\mathrm{F}}^2(\omega)}{1 + \mathrm{Q_m}^2 \left(\frac{\omega}{\Omega_{\mathrm{m}}} - \frac{\Omega_{\mathrm{m}}}{\omega}\right)^2}, \tag{6.39}$$

where the mechanical quality factor is used ($\mathrm{Q_m} = \frac{\Omega_{\mathrm{m}} m_{\mathrm{eff}}}{b}$). Writing eq. 6.39 in terms of frequency f, i.e. $\omega = 2\pi f$, the total kinetic energy is:

$$\mathrm{E_k} = \frac{1}{4\pi b} \int_0^\infty \frac{\bar{\mathrm{F}}^2(f)\, \mathrm{Q_m}}{1 + \mathrm{Q_m}^2 \left(\frac{f}{f_{\mathrm{m}}} - \frac{f_{\mathrm{m}}}{f}\right)^2} \mathrm{d}(f/f_{\mathrm{m}}) = \frac{\bar{\mathrm{F}}^2(f)}{8b}, \tag{6.40}$$

which is equal to the thermal energy $\frac{1}{2}\mathrm{k_B T_0}$, such that:

$$\bar{\mathrm{F}}^2(f) = 4\mathrm{k_B T_0} b. \tag{6.41}$$

The square root of eq. 6.41 is the root mean square (r.m.s.) amplitude of the force, measured in units of N Hz$^{1/2}$. The resultant deflection of the cantilever in response to this force can be derived using eq. 6.11, which for this case, relates the r.m.s. deflection of the microsphere-cantilever ($\sqrt{\bar{D}_0^2}$), to the r.m.s. driving amplitude of the base ($\sqrt{\bar{A}^2}$), such that $\bar{\mathrm{F}}(f) = m_{\mathrm{eff}}\sqrt{\bar{A}^2}\Omega_{\mathrm{d}}^2$. Writing eq. 6.11 in terms of f and $\bar{F}(f)$:

$$\sqrt{\bar{D}_0^2} = \frac{\sqrt{4\mathrm{k_B T_0} b}}{k\sqrt{\left(1 - \left(\frac{f_{\mathrm{d}}}{f_{\mathrm{m}}}\right)^2\right)^2 + \mathrm{Q_m}^2 \left(\frac{f_{\mathrm{d}}}{f_{\mathrm{m}}}\right)^2}}, \tag{6.42}$$

Assuming the microsphere-cantilever is operated in the accelerometer regime ($f_{\mathrm{d}} << f_{\mathrm{m}}$),

---

[13] A thermal equilibrium between the microsphere-cantilever and its surroundings at $\mathrm{T_0}$ is assumed.

eq. 6.42 is approximated as $\sqrt{\bar{D}_0^2} = \sqrt{4k_B T_0 b/k}$, which can be expressed in terms of :

$$\sqrt{\bar{D}_0^2} = \sqrt{\frac{4k_B T_0}{\Omega_m^3 m_{\text{eff}} Q_m}}. \tag{6.43}$$

Since $f_d << f_m$, the applied RMS acceleration $\left(\sqrt{\bar{A}^2}\Omega_d^2\right)$ is equal to the RMS acceleration experienced by the cantilever $\left(\sqrt{\bar{D}_0^2}\Omega_m^2\right)$, (as governed by eq. 6.12). Therefore:

$$a_{\text{th}} = \sqrt{\bar{D}_0^2}\Omega_m^2, \tag{6.44}$$

where a_{th} is the RMS noise equivalent acceleration. Inserting eq. 6.43 into eq. 6.44 obtains:

$$a_{\text{th}} = \sqrt{\frac{4k_B T_0 \Omega_m}{m_{\text{eff}} Q_m}}. \tag{6.45}$$

The *total* (RMS) noise equivalent acceleration, a_{NEA}, that is measured in experiments will be larger than a_{th} unless shot-noise limited lasers and low noise electronics are used. In order to measure a_{NEA}, and compare with the predicted thermally limited value of a_{th}, the experiment methodology of [12] is used in this thesis. Firstly the PSD of the WGM transduction signal is recorded from the photodetector, in units of $\text{V Hz}^{-1/2}$. A sinusoidal acceleration is applied across a range of driving frequencies Ω_d, and the peak-to-peak WGM response measured, such that the frequency dependent scale-factor is deduced, in units of V/g. Lastly, a_{NEA} is found by dividing the displacement PSD with this scale factor, which results in a frequency dependent a_{NEA}, in units of $\text{g Hz}^{1/2}$.

Microsphere-cantilever[$\mathcal{F}$] is used to conduct the above described experiment. It has dimensions of $r_c = 60\,\mu\text{m}$, $r_s = 90\,\mu\text{m}$, and $L = 5.2\,\text{mm}$ and is chosen because of its high fundamental mechanical frequency of $\Omega_m = 2\pi \times 3400\,\text{Hz}$, allowing a large range of driving frequencies to be applied. The mechanical quality factor is $Q_m = 350$, and $m_{\text{eff}} = 3.1 \times 10^{-8}\,\text{kg}$, such that $a_{\text{th}} = 5.8 \times 10^{-7}\,\text{g Hz}^{-1/2}$. The experimental results are shown in fig. 6.11, where the displacement PSD is displayed in the middle panel, the frequency dependant scale-factor is displayed in the lower panel, and a_{NEA} is shown on the top panel.

The usable bandwidth is defined by the frequency range where a_{NEA} is flat, corresponding to $\approx 2.5\,\text{kHz}$, where $a_{\text{NEA}} = (2.3 \pm 1.5)\,\mu\text{g Hz}^{1/2}$, which is 4 times larger than the predicted thermal noise equivalent acceleration, $a_{\text{th}} = 5.8 \times 10^{-7}\,\text{g Hz}^{-1/2}$. This will be

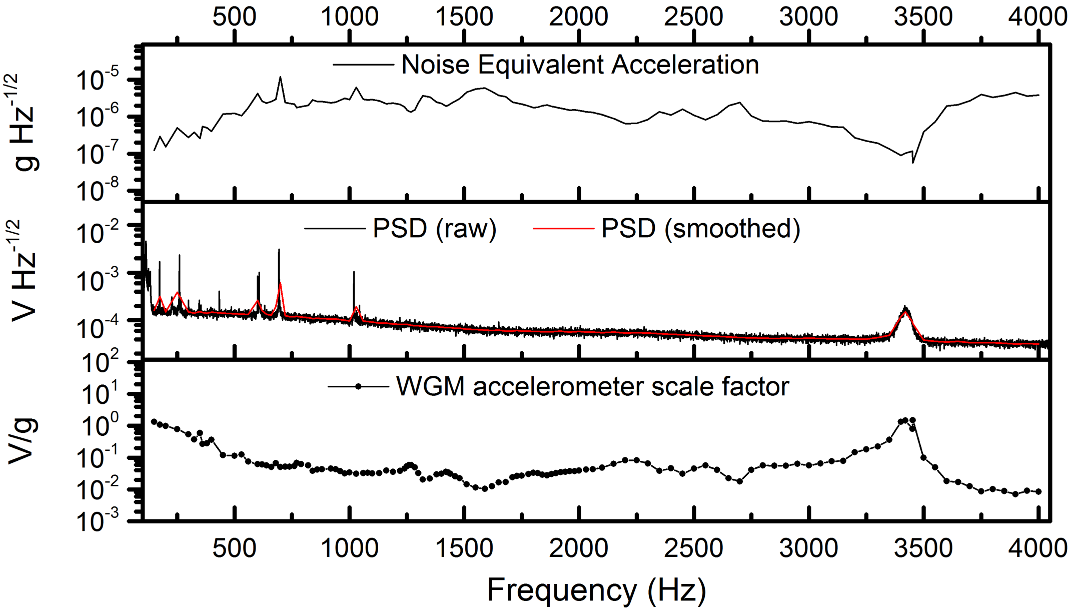

Figure 6.11: (top panel) The measured noise equivalent acceleration, found by dividing the displacement PSD of the WGM transduction signal (middle panel) with the scale factor (bottom panel), following the method of [12].

related to noise from the photodetector, resonant vibration from supports, and noise from the piezo-stack. The large error in a_{NEA} requires further investigation, but is likely to arise from mechanical resonances of the supporting mounts or the tapered fibre, causing resonant enhancement of the scale factor (fig. 6.11 (lower panel)). A resonant enhancement naturally occurs when the driving frequency approaches Ω_{m}, leading to an improvement of a_{NEA}. A similar but unexpected effect appears at low frequency (<500 Hz), and may be related to a low frequency mechanical mode of a supporting post or mount.

The deduced value of a_{NEA} is over 100 times better than the specified noise density of the ADXL327 sensor ($250\,\mu\mathrm{g}\,\mathrm{Hz}^{1/2}$), which is due to the larger mass of the microsphere-cantilever (electrodes tend to be a few micron in length), and the lower noise density of the optical field. In order to experimentally verify that the WGM sensor is more sensitive than the ADXL327, a sinusoidal acceleration is applied at various frequencies, with increasing peak acceleration, until either sensor detects the acceleration in the FFT of their respective outputs. The results are shown in fig. 6.12, where the driving frequency Ω_{d} ranges from 80 Hz to 1.4 kHz (the bandwidth of the ADXL327 is 1.6 kHz).

From fig. 6.12, the WGM sensor is conclusively more sensitive than the ADXL327 at every tested Ω_{d}, and is able to detect accelerations in the tens of μg range, limited by the minimum peak amplitude displacement that can be applied. The ADXL327 is only able to resolve the highest peak acceleration of ±650 μm (applied at $\Omega_{\mathrm{d}} = 800\,\mathrm{Hz}$), but with

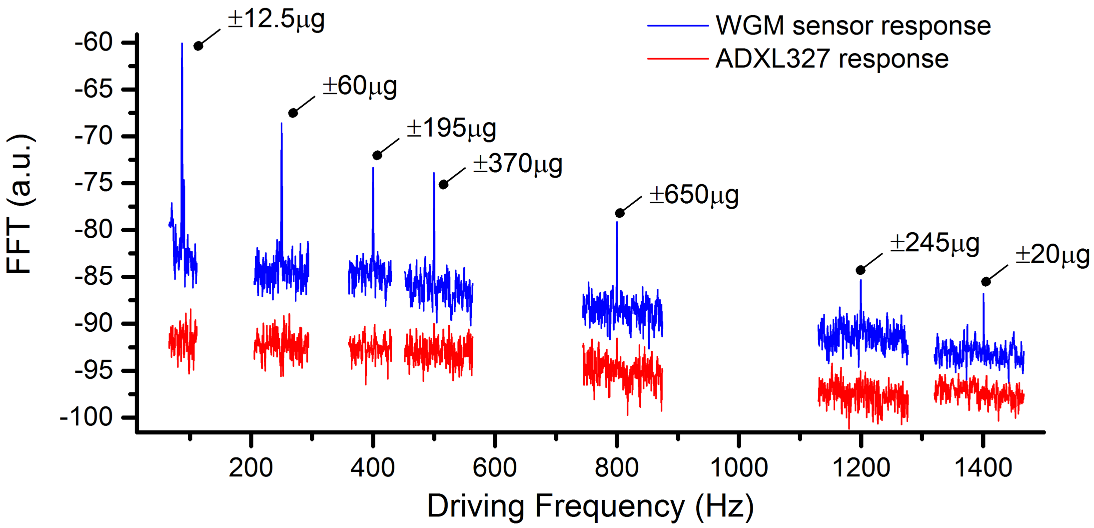

Figure 6.12: A sinusoidal acceleration is applied to the WGM accelerometer (microsphere-cantilever[$\mathcal{F}$]) and the ADXL327 at varying driving frequency. The minimum peak acceleration that is detected in the FFT of the WGM at each frequency is labelled. The WGM sensor outperforms the ADXL327 at every tested driving frequency, and is able to detect μg accelerations.

poor signal-to-noise.

The only other WGM sensor where the test-mass is the WGM resonator itself, studied by [20] over 15 years ago, is quoted to have $a_{\text{NEA}} = 20.8\,\mu\text{g}\,\text{Hz}^{-1/2}$, but the authors state a minimum measured acceleration of 'less than 1 mg'. Therefore the WGM accelerometer studied in this thesis is the most sensitive yet when tested with sinusoidal excitement.

6.5 Discussion of Results

The summary of the most important parameters measured in this chapter is presented in table 6.1& 6.2, where the first table summarises the type of device, and the second table lists the linear sensing range, the bandwidth, the noise equivalent acceleration a_{NEA}, the minimum measured peak acceleration a_{min}, and the vibration rectification error (VRE).

In the overall landscape of available accelerometers, the sensing range and bandwidth of the WGM sensor is not exceptional. The bandwidth of the WGM sensor can be increased by using thicker diameter cantilevers or a smaller cantilever length. The linear sensing range can also be tailored by modifying the mechanical dimensions, for example other microsphere-cantilevers with shorter lengths used in this Ph.D. (but not displayed here), have obtained linear sensing ranges above ±2 g, but their thermal motion could not be detected in the PSD. The measurement sensitivity of the WGM sensor in this thesis is

Ref.	Test-mass	Detection
UCL	WGM cavity on cantilever	optical WGM
[20]	WGM cavity on cantilever	optical WGM
[12]	photonic crystal	evanescent field from tapered fibre
[21]	movable fibre	Fabry-Perot formed by movable fibre & fixed fibre
ADXL327	electrode	capacitance change w.r.t. fixed electrode
[238]	electrode	capacitance change w.r.t. fixed electrode, closed-loop

Table 6.1: The top panel shows four novel optical accelerometers developed by research groups, including that of our own. The bottom panel shows the electrical commercial sensor characterised in this chapter (ADXL327), and a state-of-the art MEMS sensor by Colibrys [238] employing a closed-loop feedback scheme.

Ref.	Linear Range g	Bandwidth kHz	a_{NEA} $\mu\mathrm{g\,Hz}^{1/2}$	a_{min} measured μg	VRE mg/g^2
UCL	$\pm0.7^*$	2.5^*	2.3^*	12.5^*	14.6^*
[20]	$\pm0.01^{\nabla\nabla}$	0.25	20.8	1000^{∇}	-
[12]	±8	2	2	10	-
[21]	-	10	0.1	8500	-
ADXL327	$\pm1^*$	1.6^+	250^+	650^*	23.5^*
[238]	±11.7	0.4	1.7	-	0.01

Table 6.2: The parameters of each device in table 6.1. * Measured in this thesis. $^+$ Quoted from specification. $^{\nabla\nabla}$ From data presented in [20], but not stated as the absolute linear range. $^{\nabla}$ Presented in text of [20] as ‘below 1 mg’.

only a factor of 4 from obtaining $a_{\mathrm{th}} = 5.8 \times 10^{-7}\,\mathrm{g\,Hz}^{-1/2}$, which is the ultimate limit for sensing, and is extremely competitive against commercial accelerometers shown in table 6.2. Reduction of background noise is the optimum solution for obtaining a_{th}, and it should be noted that the noise floor of [12, 21] is over 3 orders of magnitude lower ($\approx 10^{-15}\,\mathrm{m\,Hz}^{-1/2}$) than that for the WGM system presented here. Combined with a heavier test-mass in the range of 10^{-6} kg, and/or a microsphere attached to a cantilever with a higher Young’s modulus such as silicon carbide[14], such a noise floor would allow for $a_{\mathrm{NEA}} \approx \mathrm{ng\,Hz}^{-1/2}$, which could be used for ultrasensitive gravity gradiometry, discussed in the chapter 7.

The WGM microsphere-cantilever accelerometer of [20] is coupled to a MEMS fabricated waveguide instead of a tapered fibre. Their sensor is quoted with $a_{\mathrm{NEA}} = 20.8\,\mu\mathrm{g\,Hz}^{1/2}$, around 10 times larger than obtained here, but the authors only state the minimum measured acceleration as ‘less than 1 mg’ [20]. Since their displacement PSD is not shown, it is not possible to determine the mechanical quality factor to compare a_{th}, and deduce if noise is preventing detection of micro-g accelerations.

---

[14] Silicon carbide has E = 410 GPa (ceramic), approximately 6 times higher than for silica.

6.6 Conclusion

This chapter has explored the interaction between the optical WGM and the motion of the microsphere-cantilever in response to acceleration. This WGM accelerometer is entirely fabricated following the methods in chapter 2; the microsphere-cantilever forms the test-mass, and the tapered fibre supplies light to the WGM. The level of displacement sensitivity (comparable to picometers) found in chapter 3, allows for detection of micro-g accelerations as the microsphere-cantilever deflects proportionally to g-forces. Although one group experimentally studied a WGM microsphere-cantilever accelerometer 15 years ago [20], in this thesis, a wider range of experimental tests have been performed that characterise the bandwidth, a_{NEA}, and the null-position dependence. This directly contributes original work to the WGM sensing field that has not been achieved until now.

The WGM accelerometer requires three improvements in order to create a viable prototype. The first is a robust feedback system employing the WGM transduction to counteract slow DC drifts, vibrations, and shock. Such a system can be created using multiple feedback loops, and controlled with a field-programmable gate array (FPGA). The results of chapter 4 show successful feedback cooling of the microsphere-cantilever thermal motion using a *derivative* feedback loop that drives the piezo-stack supporting it, optimised for frequencies around Ω_{m}. Active feedback cooling can only extend the sensor bandwidth (see fig. 6.3), such that the thermal limit is not surpassed. Quiescence feedback cooling where the feedback is switched off, and measurements are obtained within the time it takes for the cooled test-mass to re-thermalise, can circumvent this limit [17]. Alternatively, a proportional-integral-derivative (PID) feedback loop, optimised for a wide range of frequencies and DC accelerations, can continuously counter the deflection of the microsphere-cantilever, returning it to the null-position, such that the microsphere is actively prevented from touching the taper. Such a feedback scheme has been shown to lower the VRE of a MEMS accelerometer to $10\,\mu\mathrm{g/g}^2$ [238]. This would improve the current WGM VRE by a factor of 1000, and fulfil military grade requirements of VRE$\approx \mu\mathrm{g}^2$ for precision navigation.

The second improvement relies on manufacturing a suitable frame which both the tapered fibre and the microsphere-cantilever can be mounted, with minimal supporting beams, and no additional flexure stages or translation stages. Reducing the number of mechanical elements minimises noise due to resonant mechanical modes of supporting rods. A common frame removes mismatched vibrations (i.e. two separate mounts will move with different phases and amplitudes relative to one another).

The third improvement is to further study the non-linear read out from the WGM in fig. 6.6 & fig. 6.7, the slow drift of fig. 6.8, and the VRE in fig. 6.10. By mapping all these sources of drift, an algorithm which corrects for each can be used to process the WGM transduction signal, such that non-linearity is removed from the final measurement.

Chapter 7

Future Work & Conclusions

7.1 Introduction

This thesis has experimentally studied the optomechanical coupling between optical whispering gallery modes (WGMs) and mechanical motion. The system comprises of a microsphere -cantilever evanescently coupled to a tapered fibre which excites the WGM of the microsphere, fabricated in-house (chapter 2). The transduction properties of the WGM is investigated, showing successful detection of the thermal motion of the microsphere-cantilever (and tapered fibre) (chapter 3), which is exploited for the purposes of active feedback cooling (chapter 4), and sensing acceleration (chapter 6). This chapter outlines potential experiments that can further extend the reach of these achievements, including plans to realise the dissipative passive cooling modelled in chapter 5.

Cooling towards the mechanical ground state opens up a plethora of experiments, and can be achieved using active feedback cooling (chapter 4), and passive cooling methods (chapter 5). Both methods require shot-noise limited light, which is not the case for the laser used in this thesis, and passive cooling methods ideally require a mechanical frequency 100× larger than those of the microsphere-cantilever. For conducting quantum experiments, the microsphere-cantilever is not suitable for obtaining a c.o.m. quantum ground state due to the environmental coupling through the clamp, the low mechanical frequency, and the low mechanical quality factor. This chapter will discuss methods to improve these three parameters, for example, through the use of levitation, or cryogenic operation. Possible experiments to study the behaviour of a quantum macroscopic object are proposed.

Future work to extend the inertial sensing capability of the WGM microsphere-cantilever is presented. The results of chapter 6 demonstrated the WGM microsphere-cantilever as an excellent sensor of acceleration. Tailoring the geometry and mechanical properties of this test-mass opens up a variety of applications such as gravity gradiometry. A full inertial navigational unit can be formed using the Sagnac effect to sense the rate of rotation, such that the WGM microsphere functions as a gyroscope. A short introduction towards achieving these measurements is presented.

The concluding section of this chapter outlines the work presented in this thesis, with a summary that highlights the main achievements contributed to the WGM field.

In this chapter:

- The importance of a high frequency mechanical oscillator is highlighted with regards to cooling toward its quantum state.
- Methods of tailoring the mechanical frequencies of the taper-coupled microsphere-cantilever system are discussed.
- Further work on the inertial sensing capabilities of the WGM resonator are outlined, including use of the microsphere-cantilever accelerometer for gravity gradiometry. By combining the WGM Sagnac effect with the accelerometer functionality, one can form a complete navigational device.
- A final conclusion summarises the work undertaken during the Ph.D.

7.2 Reaching the Micromechanical Quantum Ground State

For all types of backaction cooling discussed in chapter 5, a high mechanical frequency sets a longer delay between the light field and the mechanical oscillator and increases the cooling rate. Similar to atomic laser cooling, where κ is equivalent to the spontaneous emission of the atom, the lowest temperature that can be attained in the non-resolved sideband regime for dispersive cooling is given by:

$$\mathrm{T}_{\mathrm{min}} = \frac{\hbar\kappa}{2\mathrm{k_B}}, \tag{7.1}$$

which is known as the Doppler temperature [239]. This limit prevents cooling to the ground state $\bar{n} < 1$, where $\bar{n}$ is the average phonon occupancy, as a direct relation to the Heisenberg uncertainty principle: the spontaneous emission of a photon that occurs over the timescale $\frac{1}{\kappa}$ implies an energy uncertainty of $\Delta\mathrm{E} \approx \hbar\kappa$. Since the average energy of the oscillator, $\bar{\mathrm{E}} = \hbar\Omega_{\mathrm{m}}\left(\bar{n} + \frac{1}{2}\right)$, cannot be lower than this uncertainty, it implies ground state cooling cannot be reached if $\kappa \gg \Omega_{\mathrm{m}}$.

The minimum $\bar{n}$ that can be obtained through sideband resolved cooling using dispersive coupling is expressed by:

$$\bar{n}_{\mathrm{min}} = \frac{\kappa^2}{16\Omega_{\mathrm{m}}^2}, \tag{7.2}$$

obtained at a detuning of $\Delta = -\Omega_{\mathrm{m}}$ [219], implying that ground state cooling is feasible when $\kappa \leq \frac{4}{\sqrt{2}}\Omega_{\mathrm{m}}$. However, one issue with passive cooling methods is Heisenberg's uncertainty principle which leads to the existence of radiation pressure backaction, discussed in chapter 3. This noise acts to heat the mechanical oscillator such that the minimum added noise for displacement measurements is equivalent to the power spectral density (PSD) of the zero point fluctuations (ZPF), known as the standard quantum limit (SQL). The smallest displacement that can be measured is therefore $2 \times x_{\mathrm{ZPF}}$.

It should be noted that dissipative only passive cooling, modelled in chapter 5, does not require the sideband resolved scheme to cool to the ground state [210], although a mechanical frequency of 100's of kHz will relax the laser power required for cooling. In chapters 3 & 5, both dissipative and dispersive coupling is measured between the microsphere-cantilever and taper, therefore further work should be conducted to minimise the dispersive component. This could be achieved using a fast laser stabilisation feedback loop which counteracts the dispersive shifting of the WGM resonance with respect to the mechanical motion.

Conversely, active feedback cooling can theoretically cool the motion of the oscillator to its zero point motion by counteracting backaction noise to cool the oscillator to its ZPF [164]. However, stringent demands are placed on the feedback loop used for active cooling due to the larger number of electronics required for processing the transduction signal compared with passive cooling. This would require that classical noise from electronics, photodetectors and the laser is suppressed, all of which currently limit the active feedback cooling conducted in chapter 4. A higher c.o.m. frequency of the microsphere-cantilever would aid feedback cooling, since it is currently amongst many mechanical modes of the taper in the PSD, shown in chapter 3.

7.2.1 Tailored Mechanical Properties

The importance of a high mechanical frequency, Ω_m, is apparent for meeting the resolved sideband condition, since making cavities with low κ is challenging. The most successful demonstrations of optomechanical cooling employ mechanical oscillators of thin slab dimensions [196], or large heavy mirrors [172, 180] that naturally have higher Ω_m and mechanical quality factors, $\mathrm{Q_m}$. A downside of having a high Ω_m, is that it sets a smaller zero point motion, $x_\mathrm{zpf} = \sqrt{\frac{\hbar}{2m_\mathrm{eff}\Omega_\mathrm{m}}}$, that requires an improved measurement sensitivity (i.e. low imprecision noise). It also defines the starting phonon occupancy $\bar{n}_\mathrm{th} \approx \frac{\mathrm{k_B T_0}}{\hbar\Omega_\mathrm{m}}$, thermalised with the environment temperature $\mathrm{T_0}$.

In order to increase the mechanical taper frequencies above the kilohertz range, one could use the taper dimensions specified in [136] (notably the use of tensioning), where the authors measure torsional mechanical modes with $\frac{\Omega_\mathrm{m}}{2\pi} > 100\,\mathrm{kHz}$, or, the use of a MEMS fabricated waveguide such as in [225] with 23 MHz frequency. If cooling to the ground state of the microsphere-cantilever is required, the microsphere can be attached to a stiffer cantilever made of higher Young's Modulus material such as silicon nitride or silicon carbide [240] to increase Ω_m. Often it is easier to place an external oscillator into the near-field of the WGM resonator (as in fig. 5.5 b in chapter 5), such as a clamped-clamped nanostring [241], but often these have reduced $\mathrm{Q_m}$ [157]. The increase of surface-to-volume ratio is one factor which is attributed to the lowering of $\mathrm{Q_m}$ [157, 242], as well as defects on the surface due to fabrication processes.

Large quality factors are preferred as it sets the cooling ratio $\frac{\mathrm{T_0}}{\mathrm{T_{eff}}} < \mathrm{Q_m}$. Using ultrahigh vacuum, and lowering the environmental temperature using a cryostat are both ways to increase $\mathrm{Q_m}$ towards its intrinsic value. When the sideband resolved condition is met, and imprecision noise is minimised, cryogenic conditions have helped achieve an occupancy of less than 1 [25, 26][1]. Especially important for clamped systems is the value $\Omega_\mathrm{m} \times \mathrm{Q_m}$, which quantifies the degree of decoupling from the environmental thermal reservoir [160]. In general, cantilever type resonators will have low $\Omega_\mathrm{m} \times \mathrm{Q_m}$, due to mechanical clamping losses. Investigating the dissipation through clamping losses (from radiation of elastic waves into the substrate), and changing to a low dissipation material like silicon or sapphire [180], one can increase the intrinsic $\mathrm{Q_m}$. For a typical microsphere-

---

[1] One consideration for a WGM system is the reversal of the thermally induced optical frequency shift due to the change in the temperature induced refractive index change [243]. This aids dispersive cooling as it renders the red-detuned side of the WGM resonance thermally stable [128]

cantilever used in this thesis, $\Omega_\mathrm{m} \times \mathrm{Q}_\mathrm{m} \approx 2\pi \times 1\,\mathrm{MHz}$, whereas a radial breathing mode of a silicon carbide toroid can reach $2\pi \times 10\,\mathrm{GHz}$ [240] (the largest reported product amongst WGM resonators).

7.2.2 Levitated Optomechanics

Conducting experiments to probe quantum behaviour, such as the iconic Young's double-slit experiment or matter interferometry, requires cooling to the c.o.m. quantum ground state in an environmentally decoupled system. For this reason, levitated nanosphere experiments using an optical and/or ion trap have garnered interest recently. Such optical traps can obtain trapping frequencies of 10-500 kHz, and extremely high mechanical quality factors up to 1×10^{12} [158] in ultrahigh vacuum. A levitated microsphere version of the active feedback experiment conducted in chapter 4, or the passive cooling setup in fig. 5.5 b) (chapter 5) could be considered in future experiments. Such an experiment, where the levitated WGM resonator is cooled to the c.o.m. ground state by utilising the coupling of the WGM to a stationary tapered fibre, has never been conducted. Obtaining high optical quality factor, Q_opt WGMs on an untethered sphere cannot be achieved with colloidally produced spheres (as shown in chapter 1 fig. 1.7) due to the low surface quality. Re-flowing the surface using a focussed CO_2 laser improves Q_opt. Other methods such as dropping glass powder through a microwave plasma torch, or an electric arc, have been reported to produce 10 μm diameter spheres [244], and up to 24 μm diameter spheres [245] respectively.

7.2.3 Probing Quantum Phenomena

An area of focus and significant achievement within optomechanics is cooling close to, or at a micromechanical quantum ground state [25–27, 246]. Cooling large bulk objects is appealing for conducting fundamental tests on collapse models [33, 34], creating a superposition of states [86, 202, 247, 248], quantum squeezing of the mechanical motion [36], as well as quantum limited sensing applications [2, 40, 71, 249].

In particular, if the mechanical oscillator is cooled to a low phonon occupancy, tests for continuous spontaneous localisation (CSL) could be achieved without requiring the mechanical ground state [33, 250]. Within the CSL model, the Schrödinger equation is modified by inclusion of a non-linear stochastic term that accounts for genuine collapses of superposition states. Mass is included in this model such that 'localisation' events occur at a frequency scaled with the mass, implying that macroscopic objects undergo collapse more readily. In order to conduct an experimental test of CSL, environmental decoherence, which is an entirely different mechanism, must be minimised to distinguish the noise signatures of CSL. Due to the stringent requirement for minimal environmental coupling, the microsphere-cantilever would not be a suitable test-case due to the mechanical coupling from the clamping point. Since the decoherence rate (and localisation rate) increases with mass, smaller objects on the order of a 400 nm diameter silica nanosphere are predicted to be ideal candidates with an appreciable localisation rate without being masked by decoherence [250]. A variation of the CEODF active feedback cooling in chapter 4, or the modelled passive cooling in chapter 5 can be used to cool the motion of a near-field coupled levitated nanosphere, where the WGM of an anchored microsphere (i.e. a microsphere-cantilever with a short cantilever) provides the CEODF and optomechanical coupling. If the nanosphere is levitated using a hybrid trap comprised of an optical tweezer and a Paul trap [7, 250], the optical field can be switched off after cooling, allowing the c.o.m. mechanical state to evolve. If sources of environmental noise are characterised such as the blackbody radiation and gas collisions, the comparison between the initial phonon number and the final phonon number after the period of free evolution can reveal the effect of extra heating unrelated to these conventional noise. Such heating is predicted by the CSL model, although care must be taken to ensure optical scattering, a dominant source of heating, is included in the analysis [250].

7.3 Inertial Sensing

The sensing ability of the WGM microsphere-cantilever coupled to a tapered fibre is shown to resolve micro-g accelerations in chapter 6. Here, two potential applications of this optical accelerometer are considered; gravity gradiometry and the sensing of rotation.

7.3.1 Gravity Gradiometry

The use of an ultrasensitive accelerometer to measure variations in the local gravitational field opens up a range of applications, such as the detection of underground hydrocarbon reserves, volcanic magma build up [251], and measurement of the Earths tides [135]. The Earth's land tides are elastic deformations of the Earth's crust caused by the residual force from the Moon's gravitation field and the Earth's centrifugal force, fig. 7.1. These land deformations vary in amplitude and frequency but typically have a peak signal strength of 0.4 μg and frequencies of 10^{-5} Hz. Since the time period spans a day, the long-term stability and drift characteristics of the accelerometer could be tested.

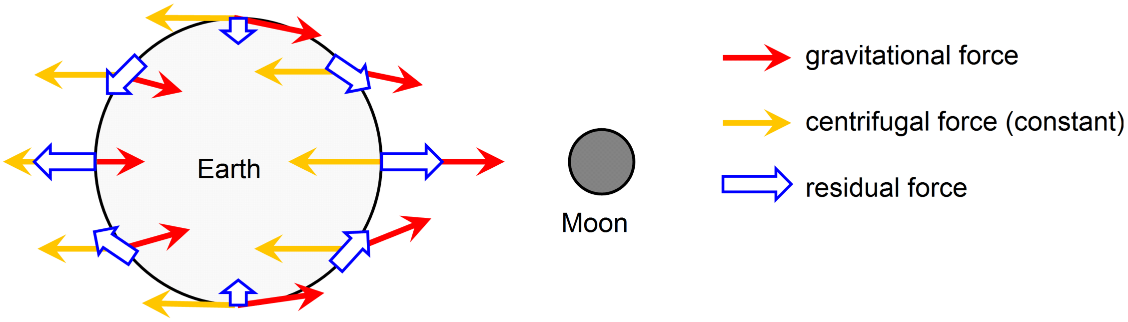

Figure 7.1: A schematic to show the influence of the moon's gravitational field on the Earth. The residual force when the centrifugal force is subtracted from the gravitational field causes a localised modulation of the Earth's crust due to the change in the gravity gradient.

It was found in chapter 6 that the microsphere-cantilever WGM sensor has a noise equivalent acceleration of 2.3 μg $\mathrm{Hz}^{-1/2}$, which can be further improved to its thermal noise equivalent sensitivity of 0.6 μg $\mathrm{Hz}^{-1/2}$ by lowering electronic noise and using a shot-noise limited laser. This would be sensitive enough to detect a tunnel with cross-sectional area of 2 m^2, length 4 m, at a depth of 2 m, in 1 s [135], and is comparable to the sensitivity of the MEMS device in [135], which was used to measure the Earth's land tides, specifically designed with a low mechanical frequency $\Omega_\mathrm{m} = 2\pi \times 4\,\mathrm{Hz}$. However, unlike the MEMS device in [135] the WGM accelerometer bandwidth is over 1000 times larger, does not require ultralow pressures, and is fabricated without clean room facilities. As with any vibration monitoring device tested on the Earth's surface, the authors is [135] state that seismic noise limits the sensitivity.

Gravitational Waves

A special case of gravity gradiometry is the detection of ripples in space-time called gravitational waves. Such waves can be thought of as the 'sounds' of the Universe, and are created by matter in its most extreme form, for example, when neutron stars and black holes form and collide, as well as gravitational waves propagating from the Big Bang itself [230]. A non-spherical acceleration of mass-energy distributions is required to create gravitational waves[2]. By late 2015 LIGO confirmed the detection of gravitational waves from two colliding black holes [37]. A rich spectrum of gravitational waves are expected to span across a frequency range between nanohertz to tens of kilohertz. Detection of waves in the audio frequency band can be conducted using Earth-based detectors (i.e. LIGO), whereas those in the microhertz to millihertz range require space-based detectors such as LISA to avoid seismic noise.

Gravitational waves can be considered classical but measurement systems must be treated quantum mechanically since the expected signals create relative test-mass displacements on the order of 10^{-18}m, approaching or below the SQL. This required sensitivity is one reason why Earth based detectors are typically kilometre long interferometers such as LIGO. The microsphere-cantilever test-mass system in chapter 6 is not sensitive enough to detect gravitational waves, as the SQL is 1000 times noisier than the required PSD of $10^{-18}\,\mathrm{m\,Hz^{-1/2}}$. However, reaching this level could be achieved with a high frequency, heavier microsphere-cantilever with a lower ZPF (i.e. $m_{\mathrm{eff}} \approx 10^{-6}\,\mathrm{kg}$, $\Omega_{\mathrm{m}} \approx 100\,\mathrm{kHz}$).

7.3.2 Sagnac Effect

The Sagnac effect is related to a difference in path length experienced by counterpropagating optical beams in an interferometer or cavity that undergo rotation. When the beams are recombined, the resultant interference fringes are shifted according to the angular velocity of the system, denoted as $\Omega_R = \frac{\mathrm{d}\theta}{\mathrm{d}t}$. Counterpropagating WGMs shown in fig. 7.2, undergo this effect, whereby rotation changes the respective path lengths of the clockwise (CW) and counter-clockwise (CCW) WGMs, breaking the degeneracy of these $\pm m$ modes. This creates a WGM doublet. The path length of light travelling in the same direction as the rotation is increased by ΔL, and the counterpropagating light experiences a path length decrease of equal amplitude.

The time it takes for $\mathrm{WGM_{CW}}$ to propagate around the sphere in the same direction as the rotation is $t_1 = \frac{2\pi a + \Delta L}{c}$, where a is the microsphere radius, and $\mathrm{WGM_{CCW}}$ takes $t_2 = \frac{2\pi a - \Delta L}{c}$. The increase/decrease in path length ΔL is equivalent to the motion of the sphere itself such that $\Delta L = a\,\Omega_{\mathrm{R}}\,t_1$. Therefore the time difference between the counterpropagating beams is $\Delta t = t_1 - t_2 = \frac{4\pi a^2 \Omega_{\mathrm{R}}}{c^2 - a^2\Omega_{\mathrm{R}}^2}$. For $\Omega_{\mathrm{R}} \gg \frac{c}{a}$, the time difference is $\Delta t \approx \frac{4A\Omega_R}{c^2}$, where A is the cross-sectional area of the microsphere. This causes a WGM

---

[2] No gravitational waves are produced for a symmetrical array or distribution of masses gravitationally collapsing towards a point, as from afar, this is equivalent to the gravitational field of a point mass.

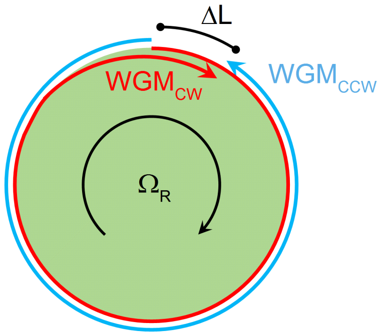

Figure 7.2: A microsphere can be used as a gyroscope to measure rotation. Two counterpropagating WGMs, labelled as the clockwise beam WGM$_{\mathrm{CW}}$, and counterclockwise beam WGM$_{\mathrm{CCW}}$, travel different path lengths due to the Sagnac effect when the sphere rotates at a rate Ω_{R} in the clockwise direction. The WGM$_{\mathrm{CW}}$ beam travels an extra path length of ΔL, and WGM$_{\mathrm{CCW}}$ travels ΔL less.

doublet with peak separation of:

$$\Delta f_{[\mathrm{CW-CCW}]} = 2\frac{a}{\lambda_0}\Omega_{\mathrm{R}}, \tag{7.3}$$

where λ_0 is the WGM wavelength. Such a device capable of measuring the rate of change of rotation is known as a gyroscope and is used for determining orientation. The dynamic range of the gyroscope is limited by the FWHM of the mode such that a frequency split of 1.25 MHz can be resolved using a FWHM WGM linewidth of 5 MHz. This would enable detection of $\Omega_{\mathrm{R}} \approx 7400\,\mathrm{rad\,s^{-1}}$, which is approximately $42 \times 10^4\,\mathrm{deg\,s^{-1}}$, using a $180\,\mu$m diameter sphere. This value can be improved to $3000\,\mathrm{deg\,s^{-1}}$ by using a narrower WGM of FWHM 1 MHz with a 5 mm diameter microsphere, but is still not sensitive enough to measure the $0.004\,\mathrm{deg\,s^{-1}}$ angular velocity of Earth. Errors associated with WGM gyroscopes are related to changes of the bulk material, such as modulations in the WGM path lengths caused by bulk heating. Stable operation therefore requires thermal control of the surrounding temperature such that changes are less than a milli-Kelvin [57]. Bulk heating can also arise from fluctuations in the intracavity intensity, therefore the power coupled to the WGMs should be stabilised to pico-Watt fluctuations using feedback electronics. Maleki et al. have experimentally created a CaF$_2$ WGM toroid gyroscope, 1 cm in diameter, with a WGM linewidth of 200 kHz, excited using 1550 nm light. A bias drift of $2\,\mathrm{deg\,hr^{-1}}$ was measured [57], which is considered poor for the next generation of high precision navigational gyroscopes aimed at a maximum bias drift $< 0.0001\,\mathrm{deg\,hr^{-1}}$. The limiting aspects in [57] were identified as dynamic misalignment of measurement optics, and WGM power fluctuations due to humidity. Fibre optic gyroscopes are currently the best performing gyroscopes using the Sagnac effect, with sensitivities on the order of $16\,\mu\mathrm{deg}/\sqrt{\mathrm{hr}}$ and bias stability of less than $0.00003\,\mathrm{deg/hr}$[252]. It should be noted that the WGM resonator does not have an large enhanced sensitivity compared to an optimised fibre optic gyroscope as shown in eq. 7.3, which also describes a fibre optic gyro that forms a single ring enclosing an area defined by radius a. This is because resonant gyroscopes utilising the Sagnac effect e.g. a resonant fibre optic gyroscope with multiple coils, or the WGM resonator studied here, although employing multiple round trips, will also have an associated increase in loss [253].

Navigation

An inertial measurement unit (IMU) can comprise of 3 gyroscopes and 3 accelerometers to measure rotation and acceleration in all 3 axes[3], used in a strapdown configuration where the sensors are mounted directly onto the moving body frame. A more complex method positions the sensors on a free-to-move platform, surrounded by gimbals and torque motors that are used in a feedback loop to keep alignment with the global frame [229].

Although the output of the WGM accelerometer can be double integrated to give position, each integral step compounds the influence of drift. Unless the orientation of each accelerometer axis is guaranteed not to drift, which is only valid if the x-axis or z-axis do not measure components of the y-axis[4], the calculation of position will have an error rising quadratically in time. Similarly, the use of a gyroscope to measure rotation around each axis cannot be used to accurately define position because the gyroscope alone has no absolute reference and is prone drifts and errors once the signal is integrated to determine the relative angles. In order to navigate using accelerometers and gyroscopes, both devices require inputs from each other to reduce drift error.

An IMU comprising of both sensors is often used in a Kalman filter [228] to determine position with reduced uncertainty. The Kalman filter is an algorithm that uses a series of noisy measurements over time to produce an optimised estimate of future measurements. It works as follows; step by step, starting at t_0; the Kalman filter is provided with an initial estimate of location, including its uncertainty. Using a user defined mathematical

---

[3] Often magnetometers are also used which can measure the Earth's magnetic field to assign the north and south directions. The extra redundancy in information can correct for long term drift errors.

[4] A perfectly aligned y-axis measures a constant acceleration due to gravity, equal to -g, which can cause a DC bias if another axis can also detect this acceleration. Cross coupling is unavoidable because of imperfect alignment of the sensors in each axis.

model, a new estimate valid at t_1 is predicted based on t_0, taking into account the initial uncertainty and the accuracy of the model. Then, the measurement at t_1 and the predicted value at t_1 are weighted by considering the measurement noise and the total prediction uncertainty. The output is a new updated estimate of position, valid at t_1, which is used for subsequent analysis at t_2.

Although the construction of an IMU using WGM resonators has not been achieved yet, this is an emerging technology that would open up a new class of optical inertial sensors for commercial applications. A WGM accelerometer employing the Sagnac effect requires substantial technical improvements, with little gain in sensitivity compared to fibre optic gyroscopes [253]. Alternatively, the Coriolis force acting on the microsphere-cantilever could be used instead to perform a measurement of the rotation. This is can be achieved by sinusoidally driving the fundamental mechanical mode in the x-axis whilst measuring the resultant oscillation in the y-axis due to the Coriolis force induced by a rotation Ω_z around the z-axis. In this case, the amplitude of the oscillation in the sensing mode (Δy) is dependent on the driven amplitude of the cantilever in the x-axis (Δx) such that $\Delta y = \frac{2\Omega_z \Delta x \mathrm{Q_m}}{\omega_x}$, where ω_x is the fundamental mechanical frequency of the cantilever. A sinusoidal modulation with peak amplitude of $\Delta x = 50\,\mathrm{nm}$ allows detection of $\Omega_z \approx 0.07\,\mathrm{deg/s}$ using typical parameters for $\omega_x = 2\pi \times 2800\,\mathrm{rad/s}$, $\mathrm{Q_m} = 400$, and minimum detectable displacement of $\Delta y = 3\,\mathrm{pm}$. Two waveguides are required to transduce the motion in the y and z-axis. Such a device requires further work on determining drift and cross-coupling, which are considered more important than sensitivity for long term navigation. Due to fabrication imperfections when melting microspheres, each sensor will have a different WGM resonant frequency and $\mathrm{Q_{opt}}$, thus requiring a self-calibration procedure using a reference F-P interferometer, or a transition line in an atomic gas sample.

7.4 Conclusion

In conclusion, this thesis has explored the ability of optical WGM resonances to transduce mechanical motion, and enhance optical forces for actuation and cooling. A test system comprising of a microsphere-cantilever and a tapered fibre, allows for evanescent coupling of light from the taper to a WGM in the microsphere. A CO_2 laser and a tapering rig were set-up to fabricate high optical Q microspheres ($\mathrm{Q_{opt}} \approx 10^{-7}$), and micron-waist tapered fibres respectively. The thermal motion of both objects is imprinted as fluctuations of the WGM, and can be analysed in the PSD of the transmission through the taper (transduction signal). Differentiation of the transmission creates a feedback signal, proportional to velocity.

Active feedback cooling was implemented by driving a piezo-stack with the feedback signal to damp the c.o.m. and second eigenfrequency of the microsphere-cantilever supported by the piezo-stack, which demonstrates cooling of the WGM resonator itself, rather than an object placed within a cavity. It should be noted that a high Q_{opt} silica microsphere tethered to a stem (i.e. microsphere-pendulum or microsphere-cantilever) was first studied by Braginsky et al. in 1989. Only within the last five years have groups characterised the transduction mechanism for the taper coupled, microsphere-pendulum version [45, 129]. The CEODF is driven by active feedback to cool two higher order mechanical modes of the clamped-clamped taper. Although tapered fibres are highly popular for coupling to WGMs [12, 45, 46], and for near-field coupling [254–256], cooling of the mechanical modes has not been achieved until now. Combining these two feedback schemes together allows for simultaneous cooling of coupled (and separate) oscillators, conducted for the first time using WGMs. Cooling of the c.o.m. mode of the WGM resonator, or modes of the tapered fibre has only been achieved within this Ph.D [55].

Alternative to active feedback cooling is passive cooling; where the optomechanical coupling between the light field and mechanical motion is dispersively coupled (motion causes a shift in the cavity resonance), and/or dissipatively coupled (motion causes a change in the cavity decay rate). Both types of passive cooling are classically modelled for 3 scenarios; a mechanical oscillator placed in the evanescent field of the microsphere-cantilever, the motion of the microsphere-cantilever itself[5], or a near-field coupled tapered fibre with high mechanical frequency. The results of this modelling indicate possible future investigations owing to the large optomechanical coupling rates measured from the microsphere-cantilever taper system. Such an experiment, where mechanical motion is dissipatively cooled to the ground state with light blue-detuned with respect to the WGM resonance would signify a world first, and validate the theory of [210], who use quantum noise analysis rather than classical equations of motion.

Lastly, the exquisite transduction and active control of the motion of the microsphere-cantilever can be used for sensing micro-g accelerations, and has a sensitivity unmatched

---

[5] This requires a tailored microsphere-cantilever with > 100 kHz mechanical frequency, coupled to a fixed planar waveguide. A levitated microsphere could also be considered.

by any accelerometer employing a WGM resonator test-mass. An open loop WGM accelerometer has been demonstrated, capable of resolving micro-g acceleration. Further work to utilise the active feedback cooling of the microsphere-cantilever in chapter 4 could extend the sensing range and bandwidth to create a robust closed-loop device for real-world applications such as gravity gradiometry, or navigation.

The main outcomes of each chapter are summarised below:

- Chapter 1 outlined the motivation behind conducting the experiments, which focus on studying the transduction and cooling properties of WGM resonators. An introduction providing the theoretical description of morphology dependent optical WGMs is presented.
- Chapter 2 detailed the fabrication of the WGM resonator used in this thesis, the microsphere-cantilever. Since an evanescent field exists around the WGM that extends beyond the geometric boundary, coupling of light to the WGM is achieved using a tapered optical fibre (also fabricated in-house). Pound-Drever-Hall locking is used to stabilise the laser frequency onto the WGM resonance, used in chapter 4. Due to the extremely small mode volume and high optical quality factor of the WGMs, a large intracavity power can build up, and bulk heating of the WGM resonator is measured. This resulting thermal bi-stability offers an alternative method to thermally lock the WGM to the laser source, which is implemented in chapters3 , 4 & 6. Many aspects of this chapter are reported in our conference proceedings [114].
- Chapter 3 explored the mechanism behind WGM enhanced transduction of the relative motion between the optical cavity and the tapered fibre. Experimental data is presented revealing the role of dissipative and dispersive coupling in this detection process. Optimisation of the signal-to-noise ratio of the transduction signal is achieved using red-detuned light with respect to the WGM, and a DC coupling distance close to critical coupling. The thermal motion of the oscillators was analysed using the PSD, and the mechanical properties such as the spring constant, effective mass, and mechanical quality factor were extracted from the PSD. An attractive optical dipole force (CEODF) from the WGM, which is actively controlled by modulating the laser intensity, is shown to preferentially actuate the tapered fibre, since the microsphere-cantilever is stiffer and heavier.
- Chapter 4 described the main results of the publication obtained during this Ph.D.

[55], where multiple mechanical modes of the microsphere-cantilever and tapered fibre are actively cooled using a piezo-stack and the CEODF respectively. The thermal motion of both oscillators is reduced to picometer fluctuations, comparable to the size of a single atom. However, the average phonon occupancy is only reduced to tens of millions of phonons, and classical noise fluctuations prevent further feedback cooling. Simultaneous cooling is achieved, allowing stabilisation of the coupling junction and could be explored for timing applications. As well as probing the noise characteristics of the entire feedback loop, the role of time delay is experientially verified against theory. Instantaneous differentiation of the transduction signal requires further work. The influence of noise is seen through squashing, implying that a lower noise photodetector and piezo-driver (or a piezo with a smaller tuning range), is required in future experiments.

- Chapter 5 presented classical modelling of passive cooling schemes, which utilise dynamical backaction to damp motion, and do not require electronic processing as is the case for active feedback cooling. Dispersive and/or dissipative cooling of a high frequency mechanical mode of a tailored microsphere-cantilever (or tapered fibre) is predicted, with dissipative cooling especially attractive as it remains an elusive goal. The classical model validates outcomes specific to the original quantum noise analysis of dissipative cooling, such as cooling when blue-detuned with respect to the cavity resonance. The experimentally measured dissipative coupling rate between the tapered fibre and the WGM of the microsphere-cantilever is over $10\,\mathrm{MHz\,nm^{-1}}$, and compares well against other optomechanical devices, validating the system as a promising candidate for novel dissipative cooling.
- Chapter 6 described the use of the taper coupled, microsphere-cantilever system as an accelerometer, measured against a commercial device. The acceleration sensitivity of the WGM sensor was found to be consistently better than the commercial capacitive accelerometer across its entire sensing bandwidth, allowing detection of micro-g accelerations. The non-linear response when sensing large amplitude displacements (i.e. due to a large acceleration) is calibrated by considering the change in power coupled to the WGM with coupling distance.
- Chapter 7 presented a list of applications and future work to extend the achievements of this Ph.D. Increased mechanical frequencies and cryogenic temperatures could be

used in future to allow for ground state cooling of a WGM resonator, that can then be tested in a range of experiments to probe quantum behaviour such as the creation of exotic squeezed states, macroscopic superpositions, and tests of collapse theories. The acceleration sensing capability can be applied for gravity gradiometry with $\mu\mathrm{g}\,\mathrm{Hz}^{-1/2}$ sensitivity, for example, to measure the Earth's slowly oscillating land tides. The use of the WGM Sagnac effect to measure rotation can form a WGM gyroscope. When used in combination with the WGM accelerometer studied in chapter 6, forms an optical navigational positioning system. Finally, a summary of the conclusions is presented.

Chapter 8

Appendix

8.1 Quadrupole Ion Trap Set-up

The trap consists of electrodes oriented to produce a quadrupole trap with a 3D quadratic potential. This saddle potential cannot produce 2D confinement due to Earnshaw's theorem that states 3D confinement is not possible with purely static fields. Therefore a rotating field is also applied, the frequency of which is optimised to maintain a stable orbit near the trap centre [257]. This RF modulation moves the saddle field in axial and radial directions so that the time variance will subject the particle to a pondermotive force. The ion trap employed consists of two facing cylindrical electrodes (spacing of 1 mm) of outer diameter 5 mm and inner diameter 3 mm, which house rod electrodes 1 mm in diameter. RF voltage is applied to the rods and the cylindrical electrodes are grounded.

The typical trapping voltage (peak to peak) is 1.2 kV with a driving frequency of 750 Hz. Spheres are loaded into the trap from below using a piezo speaker modulated at 1 kHz, which springs beads into the trapping region. Spheres are only loaded at a pressure of approximately 10^{-3} mbar, avoiding the breakdown voltage of air at a few mbar (related to the Paschen curve) as the live electrodes shorts with the ground electronics. Under vacuum it was possible to find the trapping frequency (the centre-of-mass motion) of the microspheres as their motion, at approximately 19.3 Hz. A green laser is used for illumination and a photomultiplier tube collects the scattered light in order to Fourier transform the signal, as shown in fig. 8.2.

In an attempt to excite whispering gallery modes, two light sources were added; a broadband white light source, and a 635 nm wavelength external cavity diode laser (ECDL), as shown in fig. 8.1 b), where the red laser illuminates from above, and the white

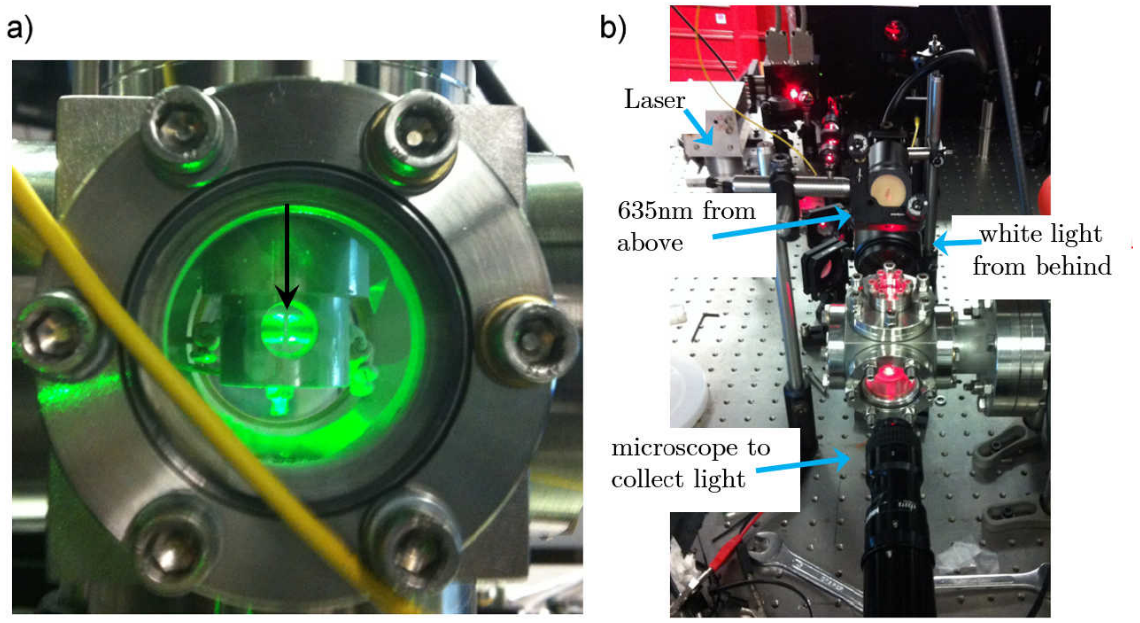

Figure 8.1: a) An illuminated 10 μm diamater silica sphere is visibly seen trapped in between the cylindrical electrodes of the ion trap, marked with an arrow. b) The set-up for illuminating the trapped microsphere with laser light from above, and white light from behind. Scattered light is collected using a microscope facing the chamber.

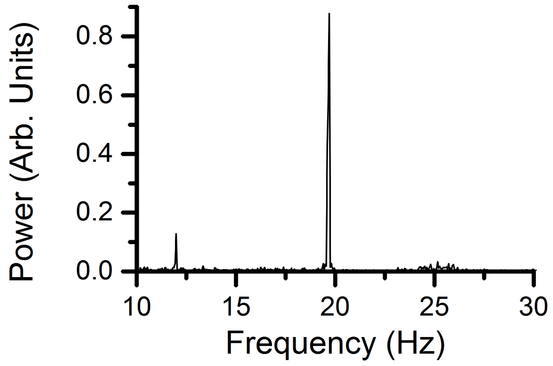

Figure 8.2: a) The power spectrum shows a primary secular frequency of 20 Hz belonging to the centre of mass motion of an ion trapped silica microsphere.

light source illuminates from behind with respect to the microscope position. The ECDL was used to try monochromatic free-space coupling of WGMs belonging to the levitated sphere, but was not successful, as explained in chapter 1. However, the white light source was able to excite broad WGMs over the visible spectrum, shown in fig. 1.7 of chapter 1.

8.2 Quantum Noise Spectral Density

8.2.1 Quantum Power Spectral Density of Mechanical Motion

To derive the quantum power spectral density (PSD) of a mechanical oscillator, it is first quantised, as detailed in [140]. Starting with the Hamiltonian for a 1D quantum harmonic oscillator:

$$\hat{\mathrm{H}} = \frac{\hat{p}^2}{2m_{\mathrm{eff}}} + \frac{1}{2}m_{\mathrm{eff}}\Omega_{\mathrm{m}}^2\hat{x}^2, \tag{8.1}$$

where $\hat{p} = -i\hbar\,\delta_x$ is the momentum operator, and $\hat{x}$ is the position operator. The eigenstates are found by looking for solutions of the linear second order differential equation corresponding to the time-independent Schrodinger equation $\mathrm{H}\varphi = \mathrm{E}\varphi$:

$$\hat{\mathrm{H}}\varphi = -\frac{\hbar^2}{2m_{\mathrm{eff}}}\frac{\delta^2\varphi}{\delta x^2} + \frac{1}{2}m_{\mathrm{eff}}\Omega_{\mathrm{m}}^2\hat{x}^2\varphi = \mathrm{E}\varphi. \tag{8.2}$$

The operator $\hat{a} = \sqrt{\frac{m_{\mathrm{eff}}\Omega_{\mathrm{m}}}{2\hbar}}\left(x + i\frac{p}{m_{\mathrm{eff}}\Omega_{\mathrm{m}}}\right)$, and its complex conjugate can be used to form the identity $\hat{a}^\dagger\hat{a} = \frac{m_{\mathrm{eff}}\Omega_{\mathrm{m}}x^2}{2\hbar} + \frac{p}{2\hbar m_{\mathrm{eff}}\Omega_{\mathrm{m}}} + \frac{i}{2\hbar}[x,p] = \frac{\mathrm{H}}{\hbar\Omega_{\mathrm{m}}} - \frac{1}{2}$, and $\hat{a}\hat{a}^\dagger = \frac{\mathrm{H}}{\hbar\Omega_{\mathrm{m}}} + 1/2$, so that the average phonon number is $\bar{n} = \hat{a}^\dagger\hat{a}$ [1], and the energy levels are $\mathrm{H} = \hbar\Omega_{\mathrm{m}}(\bar{n} + 1/2)$. This leads to the phonon eigenstates $|n\rangle$ that have eigen-energies of $\mathrm{E}_n = \hbar\Omega_{\mathrm{m}}(\bar{n} + 1/2)$. The zero point energy when $\bar{n} = 0$ is $\mathrm{E}_0 = \frac{\hbar\Omega_{\mathrm{m}}}{2}$.

However, even at the zero point energy there are zero point fluctuations (ZPF) which are quantum in nature. The origin of ZPF is found by decomposing the object's trajectory into two quadratures, $\widehat{x}(t) = \widehat{X}\cos(\Omega_{\mathrm{m}}t) + \widehat{Y}\sin(\Omega_{\mathrm{m}}t)$, where Y, X are constant during time intervals smaller than the damping time. If these represent position and momentum, $\widehat{X} = \widehat{x}(0)$, and $\widehat{Y} = \frac{\widehat{p}(0)}{m_{\mathrm{eff}}\Omega_m}$, respectively, the commutator $[\widehat{x}, \widehat{p}] = i\hbar$ leads to $[\widehat{X}, \widehat{Y}] = \frac{i\hbar}{m_{\mathrm{eff}}\Omega_m}$ so that Heisenbergs relation is [160][2]:

$$\Delta X.\Delta Y \geq \frac{\hbar}{2m_{\mathrm{eff}}\Omega_{\mathrm{m}}} = x_{\mathrm{zpf}}^2. \tag{8.3}$$

Any (non-perturbing) measurement that simultaneously measures both quadratures with equal precision is limited to the ZPF.

The double sided quantum noise PSD is analogous to the classical PSD except with

---

[1] Note that $\bar{n} = (e^{\frac{\hbar\Omega_{\mathrm{m}}\mathrm{m}}{\mathrm{k_B T}}} - 1)^{-1}$ is also known as the Bose occupation factor, where T is the mode temperature.

[2] The relation $\Delta X = \sqrt{\left\langle(\widehat{X} - \left\langle\widehat{X}\right\rangle)^2\right\rangle}$ is used.

quantum operators:

$$S^*_{xx}(\omega) = \int_{-\infty}^{\infty} \mathrm{d}t\, e^{i\omega t} \langle \hat{x}(t)\hat{x}(0)\rangle = \int_{-\infty}^{\infty} \mathrm{d}t\, e^{i\omega t} G_x(t), \tag{8.4}$$

where $\hat{x}$ is the quantum operator for position, and $G_x(t)$ is the autocorrelation function. To find $\hat{x}(t)$, it is assumed the oscillator is maintained in equilibrium with a large heat bath at $\mathrm{T_0}$, with some infinitesimal coupling, so that the Hamiltonian (total kinetic and potential energy) is given by:

$$\hat{\mathrm{H}}(\hat{x}, \hat{p}) = \frac{\hat{p}^2}{2m_{\mathrm{eff}}} + \frac{1}{2} m_{\mathrm{eff}} \Omega_{\mathrm{m}}^2 \hat{x}^2 = \hbar\Omega_{\mathrm{m}} \left(\hat{a}^\dagger \hat{a} + \frac{1}{2} \right). \tag{8.5}$$

The solution for $\hat{x}(t)$ and $\hat{p}(t)$ can be found by considering the classical relation $m_{\mathrm{eff}} \frac{\mathrm{d}^2 x}{\mathrm{d}t^2} = -\Omega_{\mathrm{m}}^2 m_{\mathrm{eff}} x$, whose solution, given initial conditions $x(0)$ and $p(0)$ is:

$$x(t) = x(0) \cos \Omega_{\mathrm{m}} t + \frac{p(0)}{m_{\mathrm{eff}} \Omega_{\mathrm{m}}} \sin{(\Omega_{\mathrm{m}} t)}. \tag{8.6}$$

When eq. 8.6 is differentiated and multiplied by m_{eff} this gives the equation for the momentum:

$$p(t) = p(0) \cos{(\Omega_{\mathrm{m}} t(- m_{\mathrm{eff}} \Omega_{\mathrm{m}} x(0) \sin{(\Omega_{\mathrm{m}} t)}. \tag{8.7}$$

The position autocorrelation function $G_x(t)$ is therefore:

$$G_x(t) = \langle \hat{x}(t)\hat{x}(0)\rangle = \langle \hat{x}(0)\hat{x}(0)\rangle \cos{(\Omega_{\mathrm{m}} t)} + \langle \hat{p}(0)\hat{x}(0)\rangle \frac{1}{m_{\mathrm{eff}} \Omega_{\mathrm{m}}} \sin(\Omega_{\mathrm{m}} t). \tag{8.8}$$

Classically, the second term disappears because there are no correlations between position and momentum, producing a single sided PSD. In the quantum case, the canonical commutation relation between position and momentum implies some correlations i.e. $\langle \hat{x}(0)\hat{p}(0)\rangle - \langle \hat{p}(0)\hat{x}(0)\rangle = i\hbar$, therefore $\langle \hat{p}(0)\hat{x}(0)\rangle = -i\frac{\hbar}{2}$. Since the correlator is imaginary it means that the autocorrelation function is complex. Using the relations $\hat{x} = \sqrt{\frac{\hbar}{2m_{\mathrm{eff}}\Omega_{\mathrm{m}}}}(\hat{a} + \hat{a}^\dagger)$, and $\hat{p} = -i\sqrt{\frac{m_{\mathrm{eff}}\hbar\Omega_{\mathrm{m}}}{2}}(\hat{a} - \hat{a}^\dagger)$, eq. 8.8 becomes:

$$G_x(t) = \frac{\hbar}{2m_{\mathrm{eff}}\Omega_{\mathrm{m}}} \left[\bar{n} \cos{(\Omega_{\mathrm{m}} t)} + (\bar{n}+1) \cos{(\Omega_{\mathrm{m}} t)} + i\bar{n} \sin{(\Omega_{\mathrm{m}} t)} - i(\bar{n}+1) \sin{(\Omega_{\mathrm{m}} t)} \right], \tag{8.9}$$

where the relations $\hat{a}^\dagger\hat{a} = \bar{n}$ and $\hat{a}\hat{a}^\dagger = \bar{n} + 1$ are used. This leads to:

$$G_x(t) = \frac{\hbar}{2m_{\mathrm{eff}}\Omega_{\mathrm{m}}} \left(\bar{n}e^{i\Omega_{\mathrm{m}}t} + (\bar{n}+1)e^{-i\Omega_{\mathrm{m}}t}\right), \tag{8.10}$$

where the trigonometric identities $\cos(A) = \frac{e^{iA}+e^{-iA}}{2}$, and $e^{-iA} = \cos(A) - i\sin(A)$, are inserted.

This autocorrelation function is used in chapter 3 to further derive the PSD of the ZPF, which is stated here as:

$$S^*_{xx}(\omega) = 2\pi x^2_{\mathrm{zpf}} \left\{\bar{n}\delta(\omega + \Omega_{\mathrm{m}}) + (\bar{n}+1)\delta(\omega - \Omega_{\mathrm{m}})\right\}, \tag{8.11}$$

where $\bar{n}$ is the average phonon occupancy of the mechanical oscillator, and δ is the Dirac delta function. This double sided PSD is clearly asymmetrical around $\omega = 0$.

For weak damping Γ_0, eq. 8.11 can be written with the delta function replaced by a Lorentzian (assuming the oscillator frequency is still sharply defined) [144]:

$$S^*_{xx}(\omega) = x^2_{\mathrm{zpf}} \left\{\bar{n}\frac{\Gamma_0}{(\omega+\Omega_m)^2 + (\Gamma_0/2)^2} + (\bar{n}+1)\frac{\Gamma_0}{(\omega-\Omega_m)^2 + (\Gamma_0/2)^2}\right\}. \tag{8.12}$$

In the classical regime, i.e. $\bar{n} \approx \frac{\mathrm{k_B T_0}}{\hbar\Omega_{\mathrm{m}}}$, such that eq. 8.12 becomes the classical single sided PSD derived in chapter 3.

8.2.2 Shot-noise Limited Light

If a shot-noise limited laser is used to measure motion, Poisson statistics define the random vacuum fluctuations of the light field which determine the measurement sensitivity. The phase noise (fluctuations in the phase quadrature), often referred to simply as 'shot-noise' increases the measurement imprecision, and increases the noise floor of the PSD. This scales with $1/\sqrt{n_p}$, where n_p is the number of photons. The random arrival of photons leads to radiation pressure backaction (amplitude quadrature fluctuations), which is referred to as backaction noise, that will heat the motion. This increases with $\sqrt{n_p}$ [143] The generic definition of the standard quantum limit (SQL) is when these two noise sources contribute equally to the total measurement noise, at the mechanical frequency. The number of photons with fluctuations of $(\Delta n_p)^2 = \bar{n}_p$, where $\bar{n}_p$ is the mean photon number. Since coherent states of different phase are not orthogonal to each other there is a uncertainty in any measurement of the phase θ, obeying Heisenberg's uncertainty principle of $\Delta n_p \Delta\theta = \frac{1}{2}$. The PSDs associated with these measurements, S_{n_p} and S_θ also obey this limit.

8.2.3 Using Shot-noise Limited Light for Displacement Measurements

A continuous beam carrying an average photon flux of $\dot{\bar{N}}$ has a variance of $(\Delta N)^2/t = S_n = \dot{\bar{N}}$. The phase of the beam will therefore have fluctuations of $S_\theta = \frac{1}{4\dot{\bar{N}}}$ [144]. The noise on a phase measurement that attempts to resolve the phase shift of $2\kappa x$ from a photon as it interacts with the observed object is $S_{\text{SN}} = S_\theta / 4\kappa^2$ and the radiation pressure that transfers a momentum of $2\hbar\kappa$ to the object is $S_{\text{RP}} = 4\hbar^2\kappa^2 S_n$. The expression $\sqrt{S_{\text{RP}} S_{\text{SN}}} = \frac{\hbar}{2}$ sets the ideal scenario which is the lower bound on the Heisenberg uncertainty principle [144].

The equivalent displacement PSD of S_{RP} and S_{SN} in units of $\text{m}^2\,\text{Hz}^{-1}$, i.e. when light is used to detect displacement, determines the sensitivity, and is derived in chapter 3.

8.2.4 Influence of Phonons and Detection Efficiency

A realistic detector, such as a photodetector will have a detection efficiency $\epsilon < 1$ (this also applies to the coupling efficiency of the light to the mechanical motion where scattering losses and absorption can limit ϵ). The imprecision noise introduced previously is therefore re-defined as $S_{\text{imp},xx}(\omega) = \frac{\hbar}{2}\frac{|\chi_{\text{m}}(\omega)|}{\epsilon^{1/2}}$. Excess phonons may also be present in a realistic system due to residual thermal motion that cannot be damped further, or backaction effects from the light. Including both these effects and approximating $x_{\text{zpf}}^2 |\chi(\Omega_{\text{m}})| = \hbar |\chi_{\text{m}}(\Omega_{\text{m}})|$ in eq. 3.60 of chapter 3, the total noise PSD of eq. 3.62 changes to:

$$S_{\text{det}',xx}(\Omega_{\text{m}}) = \hbar |\chi_{\text{m}}(\Omega_{\text{m}})| (2\bar{n} + 1) + \frac{\hbar}{2} |\chi_{\text{m}}(\Omega_{\text{m}})| + \frac{\hbar}{2} \frac{|\chi_{\text{m}}(\Omega_{\text{m}})|}{\epsilon^{1/2}}, \tag{8.13}$$

which reduces to $S_{\text{det},xx}(\Omega_{\text{m}}) = \frac{2\hbar}{m\Gamma_0\Omega_{\text{m}}}$ for an ideal detector and a ground state oscillator, in agreement with eq. 3.66. The total excess noise from residual phonons and inefficient detection on-resonance is:

$$S_{\text{add},xx}(\Omega_{\text{m}}) = 2\hbar\bar{n} |\chi_{\text{m}}(\Omega_{\text{m}})| + \frac{\hbar}{2} |\chi_{\text{m}}(\Omega_{\text{m}})| + \frac{\hbar}{2} \frac{|\chi_{\text{m}}(\Omega_{\text{m}})|}{\epsilon^{1/2}}, \tag{8.14}$$

which is plotted in fig. 8.3 a) for an ideal detector $\epsilon = 1$, but varying phonon occupancy $\bar{n}$, and fig. 8.3 b) for $\bar{n} = 10$ but varying ϵ. The x-axis is defined by the ratio of the input laser power to the optimum laser power, $\mathrm{P_{SQL}}$, which defines the balance between $S_{\mathrm{BA},xx}$ and $S_{\mathrm{imp},xx}$ by tuning the average photon number $\bar{n}_p$. The SQL is shown for $\bar{n} = 0$, whereas higher phonon occupancies result in noise levels far higher.

The role of the detection efficiency in fig. 8.3 b) where the phonon occupancy is $\bar{n} = 10$ and ϵ is varied from 1 to 0.001 shows that at a certain ϵ the total added noise is no longer minimised. Derived elsewhere is the minimum ϵ that does not add further noise, which is related to $\bar{n}$ through $\bar{n} + \frac{\eta^{-1/2}-1}{2} << 1$ [166]. In order to approach the SQL when $\bar{n} = 0$, the minimum detection efficiency must be $\epsilon = 1/9$. Using optical homodyne detection, the quantum efficiency can be as high as 0.9 [140].

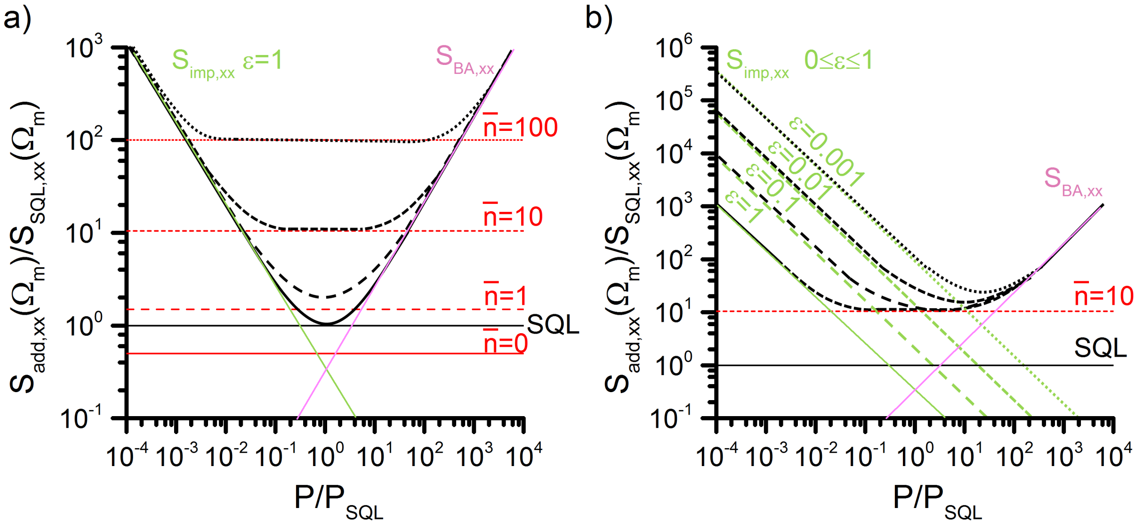

Figure 8.3: The additional noise introduced by continous weak measurement of position for a) perfect detection efficiency ($\epsilon = 1$) with varying phonon occupancy from the ideal case of $\bar{n} = 0$ to $\bar{n} = 100$. $S_{n=0\to100,xx}$ is shown as individually patterned red lines, with the corresponding total added noise (eq. 8.14) in matching patterned black lines. b) The added noise when the oscillator has $\bar{n} = 10$, but the detection efficiency is varied from $0 \leq \epsilon \leq 1$ which alters $S_{\mathrm{imp,xx}}$, shown as patterned green lines.

The optimum laser power $\mathrm{P_{SQL}}$ as seen in fig. 8.3, has consequences for passive cooling whereby the power required to cool to the ground state may be larger $\mathrm{P_{SQL}}$ and will result in unwanted backaction heating. For a WGM cavity (or F-P cavity) with total cavity decay rate κ, and dispersive coupling to the mechanical oscillator parametrised by g_{om}, there exists a balance between g_{om} and the required cooling power that sets the minimum added noise, which can potentially reach the SQL and cool to $\bar{n} = 0$.

8.3 Comparison of Fitting Methods to Infer Mode Temperature

In order to validate that the fit function employed in chapter 4 (described in section 4.3.3), is an accurate measure of the reduced mode temperature, all four methods for inferring the mode temperature as detailed on pg. 108 are compared.

Plotted in fig. 8.4 are the extracted mode temperatures and errors, found from analysing the PSDs of the feedback cooled c.o.m. mode of microsphere-cantilever[$\mathcal{A}$] (labelled c1), and eigenmode 8 of taper[$\mathcal{B}$] (labelled c2).

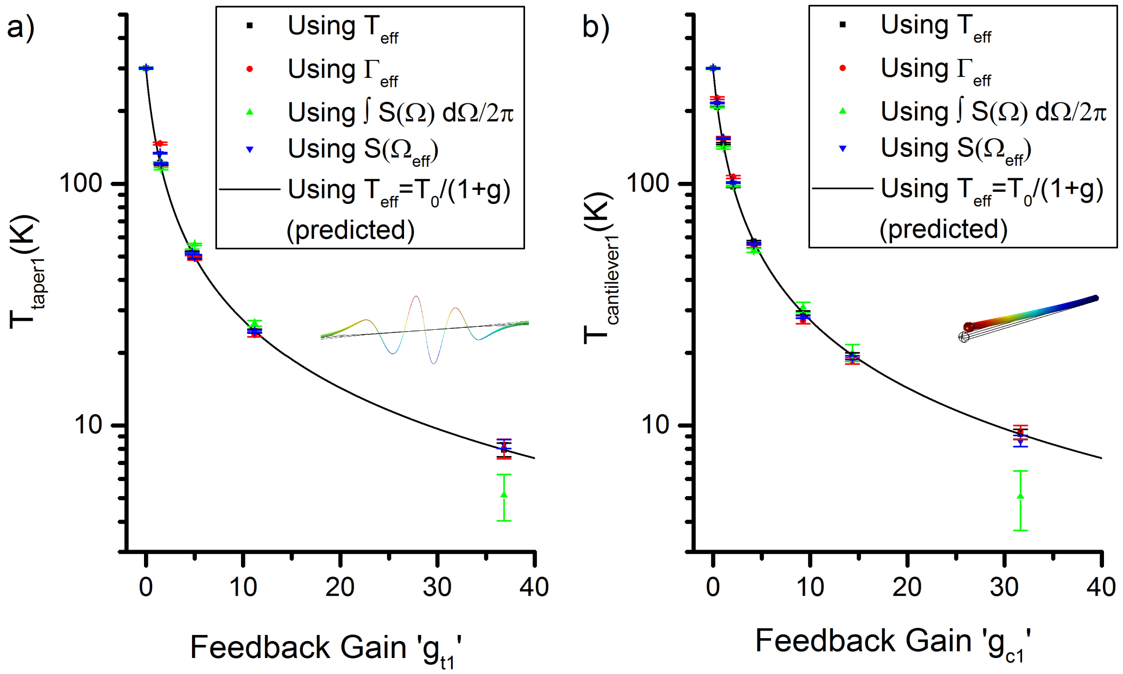

Figure 8.4: The mode temperatures reached for feedback gain g are plotted for a) the taper[$\mathcal{B}$] mode at 5.5 kHz, and b) the c.o.m. mode of microsphere-cantilever[$\mathcal{A}$] at 2.8 kHz, using the four methods described previously, where the temperature can be found by comparing i) $\mathrm{T_{eff}}$, ii) Γ_{eff}, iii) the area under the PSD, and iv) the peak height of the PSD. The predicted decrease in mode temperature using $\mathrm{T_0}(1+g)$ is plotted as a line. Errors are taken from the respective fitting functions.

The mode temperatures can be inferred by comparison to the calibration PSD, taken when no feedback is applied. The first two methods to find $\mathrm{T_{eff}}$ require fitting with eq. 4.19 to find fitting parameters.

- Firstly, $A_{\mathrm{fb}} = \frac{2\mathrm{k_B T_0}}{(1+g)m}$, which is similar to the amplitude of a Lorentzian-like lineshape, can be used such that $\mathrm{T_{eff}} = \frac{\mathrm{A_{fb}}}{\mathrm{A_0}/300}$, where A_0 is taken at zero gain.
- Secondly, the fitted parameter $\Gamma_{\mathrm{eff}} = (1+g)\Gamma_0$, that is proportional to the linewidth, can be used in $\mathrm{T_{eff}} = \frac{300}{\Gamma_{\mathrm{eff}}/\Gamma_0}$.

- A third method for determining the temperature is to integrate the area under the PSD: $\mathrm{Area_{fb}} = \int_{-\infty}^{+\infty} \mathrm{S_{xx}^{fb,imp}}(\Omega)\,\mathrm{d}\Omega \approx \frac{\mathrm{k_B T_{eff}}}{\mathrm{m_{eff}}\Omega_\mathrm{m}^2}$, such that $\mathrm{T_{eff}} = \frac{300\mathrm{Area_{fb}}}{\mathrm{Area_0}}$.
- Lastly, the peak height of the PSD at the mechanical frequency, $S_{xx}^{\mathrm{fb,imp}}(\Omega_\mathrm{m}) = \frac{2\mathrm{k_B T_0}}{m_{\mathrm{eff}}(1+g)^2\Omega_\mathrm{m}^2\Gamma_0}$ can be used to find $\mathrm{T_{eff}} = \frac{300}{\sqrt{S_{xx}^{\mathrm{fb=0,imp}}(\Omega_\mathrm{m})/S_{xx}^{\mathrm{fb,imp}}(\Omega_\mathrm{m})}}$.

The x-axis of fig. 8.4 is the gain 'g' that corresponds to the currently used fitting function employing $A_{\mathrm{fb}} = \frac{2\mathrm{k_B T_0}}{(1+g)m}$, described in the experimental methods (section 4.3.3).

All methods of extrapolating the mode temperature are in good agreement for the cooling of mode t1 of taper[$\mathcal{B}$] and mode c2 (c.o.m.) of microsphere-cantilever[$\mathcal{A}$], with only the lowest mode temperature derived from integrating the PSD area showing disagreement. These errors are due to integrating a noisy, low amplitude, highly damped peak in the PSD.

8.4 List of Dimensions

The dimensions of the microsphere-cantilevers tested in this thesis is presented in table 8.1, where the measurement errors are less than 10 %.

Name	Sphere Diameter μm	Stem Length mm	Stem Diameter μm
$\mathcal{A}$	177	5.6	120
$\mathcal{B}$	179	5.5	114
$\mathcal{C}$	142	4.4	103
$\mathcal{D}$	192	6.1	115
$\mathcal{E}$	152	7.0	120
$\mathcal{F}$	180	5.2	120

Table 8.1: The dimensions of the microsphere-cantilevers used in this thesis, with measurement errors of less thn 10%.

The dimensions of the taper shown in chapter 2, fig. 2.4 is representative of all the tapers used in this thesis since the same pulling speed is used alongside a similar number of pulling steps and consistent flame dimensions[3]. The same dimension of mount is used for each taper, such that the overhang length does not significantly vary between each fibre, and the mechanical mode frequencies shift by less than 500 Hz (see for example the two different tapers used in chapter 3, fig. 3.13.). Measuring the dimensions of each taper is not required for obtaining the mechanical properties, and is only conducted for a few cases i.e. taper[$\mathcal{B}$], to compare with FEM modelling.

---

[3] This was confirmed by comparing the waist diameter of two tapers made on different days using the exact same pulling parameters, showing agreement within the measurement error of ±0.6 μm.

Bibliography

[1] D. J. Wilson, V. Sudhir, N. Piro, R. Schilling, A. Ghadimi, and T. J. Kippenberg. Measurement-based control of a mechanical oscillator at its thermal decoherence rate. *Nature*, 524:325–329, Aug 2015.

[2] J. D. Teufel, T Donner, M. A. Castellanos-Beltran, J. W. Harlow, and K. W. Lehnert. Nanomechanical motion measured with an imprecision below that at the standard quantum limit. *Nature Nanotechnology*, 4(12):820–823, 2009.

[3] G. Anetsberger, O. Arcizet, Q. P. Unterreithmeier, R. Riviere, A. Schliesser, E. M. Weig, J. P Kotthaus, and T. J. Kippenberg. Near-field cavity optomechanics with nanomechanical oscillators. *Nature Physics*, 5:909–914, 2009.

[4] A. Schliesser, P. Del'Haye, N. Nooshi, K. J. Vahala, and T. J. Kippenberg. Radiation pressure cooling of a micromechanical oscillator using dynamical backaction. *Phys. Rev. Lett.*, 97:243905, Dec 2006.

[5] K. Usami, A. Naesby, T. Bagci, B. Melholt Nielsen, J. Liu, S. Stobbe, P. Lodahl, and E. S. Polzik. Optical cavity cooling of mechanical modes of a semiconductor nanomembrane. *Nature Physics*, 8:168–172, 2012.

[6] P. Asenbaum, S. Kuhn, U. Sezer, and M. Arndt. Cavity cooling of free silicon nanoparticles in high vacuum. *Nature Communications*, 4:2743, 2013.

[7] J. Millen, P. Z. G. Fonseca, T. Mavrogordatos, T. S. Monteiro, and P. F. Barker. Cavity cooling a single charged levitated nanosphere. *Phys. Rev. Lett.*, 114:123602, Mar 2015.

[8] N. Kiesel, F. Blaser, U. Delić, D. Grass, R. Kaltenbaek, and M. Aspelmeyer. Cavity cooling of an optically levitated submicron particle. *Proceedings of the National Academy of Sciences*, 110(35):14180–14185, 2013.

[9] M. Eichenfield, R. Camacho, J. Chan, K. J. Vahala, and O. Painter. A picogram- and nanometre-scale photonic-crystal optomechanical cavity. *Nature*, 459:550–555, 2009.

[10] W. H. P. Pernice, M. Li, and H. X. Tang. Optomechanical coupling in photonic crystal supported nanomechanical waveguides. *Opt. Express*, 17(15):12424–12432, Jul 2009.

[11] M. Eichenfield, J. Chan, R. M. Camacho, K. Vahala, and O. Painter. Optomechanical crystals. *Nature*, 462:78–82, 2009.

[12] A. G. Krause, M. Winger, T. D. Blasius, Q. Lin, and O. Painter. A high-resolution microchip optomechanical accelerometer. *Nature Photonics*, 6:768–772, Oct 2012.

[13] V.B. Braginsky, M.L. Gorodetsky, and V.S. Ilchenko. Quality-factor and nonlinear properties of optical whispering-gallery modes. *Physics Letters A*, 137(7):393 – 397, 1989.

[14] A. Schliesser and T. J. Kippenberg. Cavity optomechanics with whispering-gallery-mode microresonators. In M. Aspelmeyer, T. J. Kippenberg, and F. Marquardt, editors, *Cavity Optomechanics*. Springer, 2014.

[15] Q. Lin, J. Rosenberg, X. Jiang, K. J. Vahala, and O. Painter. Mechanical oscillation and cooling actuated by the optical gradient force. *Phys. Rev. Lett.*, 103:103601, Aug 2009.

[16] T. Ioppolo, M. Kozhevnikov, V. Stepaniuk, M. V. Ötügen, and V. Sheverev. Micro-optical force sensor concept based on whispering gallery mode resonators. *Appl. Opt.*, 47(16):3009–3014, Jun 2008.

[17] M. Hosseini, G. Guccione, H. J. Slatyer, B. C. Buchler, and P. Koy Lam. Multi-mode laser cooling and ultra-high sensitivity force sensing with nanowires. *Nature Communications*, 5:4663, Aug 2014.

[18] G. Ranjit, D. P. Atherton, J. H. Stutz, M. Cunningham, and A. A. Geraci. Attonewton force detection using microspheres in a dual-beam optical trap in high vacuum. *Phys. Rev. A*, 91:051805, May 2015.

[19] E. Gavartin, P. Verlot, and T. J. Kippenberg. A hybrid on-chip optomechanical transducer for ultrasensitive force measurements. *Nature Nanotechnology*, 7:509–514, 2012.

[20] J-P. Laine, C. Tapalian, B. Little, and H. Haus. Acceleration sensor based on high-q optical microsphere resonator and pedestal antiresonant reflecting waveguide coupler. *Sensors and Actuators A: Physical*, 93(1):1 – 7, 2001.

[21] F. Guzman Cervantes, L. Kumanchik, J. Pratt, and J. M. Taylor. High sensitivity optomechanical reference accelerometer over 10 khz. *Applied Physics Letters*, 104(22), 2014.

[22] B. Dong, H. Cai, J. M. Tsai, D. L. Kwong, and A. Q. Liu. An on-chip optomechanical accelerometer. In *Micro Electro Mechanical Systems (MEMS), 2013 IEEE 26th International Conference on*, pages 641–644, Jan 2013.

[23] A. Malki, P. Lecoy, J. Marty, C. Renouf, and P. Ferdinand. Optical fiber accelerometer based on a silicon micromachined cantilever. *Appl. Opt.*, 34(34):8014–8018, Dec 1995.

[24] H. Miao, K. Srinivasan, and V. Aksyuk. A microelectromechanically controlled cavity optomechanical sensing system. *New Journal of Physics*, 14(7):075015, 2012.

[25] J. Chan, T. P. M. Alegre, A. H. Safavi-Naeini, J. T. Hill, A. Krause, S. Gröblacher, M. Aspelmeyer, and O. Painter. Laser cooling of a nanomechanical oscillator into its quantum ground state. *Nature*, 478(7367):89–92, 2011.

[26] J. D. Teufel, T. Donner, D. Li, J. W. Harlow, M. S. Allman, K. Cicak, A. J. Sirois, J. D. Whittaker, K. W. Lehnert, and R. W. Simmonds. Sideband cooling of micromechanical motion to the quantum ground state. *Nature*, 475(7356):359–363, 2011.

[27] A. D. O'Connell, M. Hofheinz, M. Ansmann, R. C. Bialczak, M. Lenander, E. Lucero, M. Neeley, D. Sank, H. Wang, N. Weides, J. Wenner, J. M. Martinis, and A. N. Cleland. Quantum ground state and single-phonon control of a mechanical resonator. *Nature*, 464:697–703, 2010.

[28] M. Montinaro, A. Mehlin, H. S. Solanki, P. Peddibhotla, S. Mack, D. D. Awschalom, and M. Poggio. Feedback cooling of cantilever motion using a quantum point contact transducer. *Applied Physics Letters*, 101(13), 2012.

[29] G. Jourdan, G. Torricelli, J. Chevrier, and F. Comin. Tuning the effective coupling of an afm lever to a thermal bath. *Nanotechnology*, 18(47):475502, 2007.

[30] M. Poot, S. Etaki, H. Yamaguchi, and H. S. J. van der Zant. Discrete-time quadrature feedback cooling of a radio-frequency mechanical resonator. *Applied Physics Letters*, 99(1), 2011.

[31] M. Poggio, C. L. Degen, H. J. Mamin, and D. Rugar. Feedback cooling of a cantilever's fundamental mode below 5mK. *Phys. Rev. Lett.*, 99:017201, July 2007.

[32] M. Eichenfield, C. P. Michael, R. Perhaia, and O. Painter. Actuation of micro-optomechanical systems via cavity-enhanced optical dipole forces. *Nature Photonics*, 1:416–422, July 2007.

[33] S. Bera, B. Motwani, T. P. Singh, and H. Ulbricht. A proposal for the experimental detection of csl induced random walk. *Scientific Reports*, 5(7664), 2015.

[34] L. Diósi. Notes on certain newton gravity mechanisms of wavefunction localization and decoherence. *Journal of Physics A: Mathematical and Theoretical*, 40(12):2989, 2007.

[35] G. I. Harris, D. L. McAuslan, T. M. Stace, A. C. Doherty, and W. P. Bowen. Minimum requirements for feedback enhanced force sensing. *Phys. Rev. Lett.*, 111:103603, Sep 2013.

[36] E. E. Wollman, C. U. Lei, A. J. Weinstein, J. Suh, A. Kronwald, F. Marquardt, A. A. Clerk, and K. C. Schwab. Quantum squeezing of motion in a mechanical resonator. *Science*, 349(6251):952–955, 2015.

[37] B. P. Abbott et al. Observation of gravitational waves from a binary black hole merger. *Phys. Rev. Lett.*, 116:061102, Feb 2016.

[38] F. Y. Khalili, H. Miao, H. Yang, A. H. Safavi-Naeini, O. Painter, and Y. Chen. Quantum back-action in measurements of zero-point mechanical oscillations. *Phys. Rev. A*, 86:033840, Sep 2012.

[39] T. P. Purdy, R. W. Peterson, and C. A. Regal. Observation of radiation pressure shot noise on a macroscopic object. *Science*, 339(6121):801–804, 2013.

[40] A. H. Safavi-Naeini, J. Chan, J. T. Hill, T. P. Mayer Alegre, A. Krause, and O. Painter. Observation of quantum motion of a nanomechanical resonator. *Phys. Rev. Lett.*, 108:033602, Jan 2012.

[41] M. L. Gorodetsky, A. A. Savchenkov, and V. S. Ilchenko. Ultimate Q of optical microsphere resonators. *Opt. Lett.*, 21(7):453–455, Apr 1996.

[42] A. Serpengüzel, G. Griffel, and S. Arnold. Excitation of resonances of microspheres on an optical fiber. *Opt. Lett.*, 20(7):654–656, Apr 1995.

[43] M. Cai, O. Painter, and K. J. Vahala. Observation of critical coupling in a fiber taper to a silica-microsphere whispering-gallery mode system. *Phys. Rev. Lett.*, 85:74–77, Jul 2000.

[44] M. Pǿllinger, D. O'Shea, F. Warken, and A. Rauschenbeutel. Ultrahigh-q tunable whispering-gallery-mode microresonator. *Phys. Rev. Lett.*, 103:053901, Jul 2009.

[45] R. Madugani, Y. Yang, J. M. Ward, V. H. Le, and S. Nic Chormaic. Optomechanical transduction and characterization of a silica microsphere pendulum via evanescent light. *Appl. Phys. Lett.*, 106:251101, June 2015.

[46] A. Schliesser, R. Riviere, G. Anetsberger, O. Arcizet, and T.J. Kippenberg. Resolved sideband cooling of a micromechanical oscillator. *Nature Physics*, 4:415–419, 2008.

[47] G. Griffel, J. Connolly, N. Morris, S. Arnold, D. Taskent, and A. Serpengüzel. Morphology-dependent resonances of a microsphere–optical fiber system. *Opt. Lett.*, 21(10):695–697, May 1996.

[48] Y. Zhao, D. J. Wilson, K.-K. Ni, and H. J. Kimble. Suppression of extraneous thermal noise in cavity optomechanics. *Opt. Express*, 20(4):3586–3612, Feb 2012.

[49] A. Gillespie and F. Raab. Thermally excited vibrations of the mirrors of laser interferometer gravitational-wave detectors. *Phys. Rev. D*, 52:577–585, Jul 1995.

[50] F. Matichard et al. Seismic isolation of advanced ligo: Review of strategy, instrumentation and performance. *Classical and Quantum Gravity*, 32(18):185003, 2015.

[51] H. J. Butt and M. Jaschke. Calculation of thermal noise in atomic force microscopy. *Nanotechnology*, 6(1):1, 1995.

[52] T. B. Gabrielson. Mechanical-thermal noise in micromachined acoustic and vibration sensors. *IEEE Transactions on Electron Devices*, 40(5):903–909, May 1993.

[53] H. Kerdoncuff. *Squeezing-enhnaced feedback cooling of a microresonator*. PhD thesis, Technical University of Denmark, 2015.

[54] D. O'Shea, A. Rettenmaier, and A. Rauschenbeutel. Active frequency stabilization of an ultra-high q whispering-gallery-mode microresonator. *Applied Physics B*, 99(4):623–627, 2010.

[55] Y. L. Li, J. Millen, and P. F. Barker. Simultaneous cooling of coupled mechanical oscillators using whispering gallery mode resonances. *Opt. Express*, 24(2):1392–1401, Jan 2016.

[56] A. B. Matsko, A. A. Savchenkov, V. S. Ilchenko, and L. Maleki. Optical gyroscope with whispering gallery mode optical cavities. *Optics Communications*, 233(13):107 – 112, 2004.

[57] W. Liang, V. Ilchenko, D. Eliyahu, E. Dale, A. Savchenkov, A. Matsko, and L. Maleki. Whispering gallery mode optical gyroscope. In *2016 IEEE International Symposium on Inertial Sensors and Systems*, pages 89–92, Feb 2016.

[58] T. Ioppolo and M. Volkan Ötügen. Pressure tuning of whispering gallery mode resonators. *J. Opt. Soc. Am. B*, 24(10):2721–2726, Oct 2007.

[59] L. Labrador-Paez, K. Soler-Carracedo, M. Hernandez-Rodriguez, I. R. Martin, T. Carmon, and L. L. Martin. Optical humidity sensor based on a liquid whispering-gallery mode resonator. *ArXiv e-prints*, February 2016.

[60] S. Mehrabani, P. Kwong, M. Gupta, and A. M. Armani. Hybrid microcavity humidity sensor. *Applied Physics Letters*, 102(24), 2013.

[61] T. Ioppolo, U. Ayaz, and M. Volkan Ötügen. Tuning of whispering gallery modes of spherical resonators using an external electric field. *Opt. Express*, 17(19):16465–16479, Sep 2009.

[62] S. Arnold, D. Keng, S. I. Shopova, S. Holler, W. Zurawsky, and F. Vollmer. Whispering gallery mode carousel – a photonic mechanism for enhanced nanoparticle detection in biosensing. *Opt. Express*, 17(8):6230–6238, Apr 2009.

[63] M. R. Foreman, W.-L. Jin, and F. Vollmer. Optimizing detection limits in whispering gallery mode biosensing. *Opt. Express*, 22(5):5491–5511, Mar 2014.

[64] J. D. Swaim, J. Knittel, and W. P. Bowen. Detection of nanoparticles with a frequency locked whispering gallery mode microresonator. *Applied Physics Letters*, 102(18), 2013.

[65] D. Keng. *Whispering Gallery Mode Bioparticle Sensing and Transport.* PhD thesis, 2009.

[66] W. H. P. Pernice M. Li and H. X. Tang. Tunable bipolar optical interactions between guided lightwaves. *Nature Photonics*, 3:464–468, 2009.

[67] A. G. Krause, T. D. Blasius, and O. Painter. Optical read out and feedback cooling of a nanostring optomechanical cavity. June 2015. preprint, arxiv.org/abs/1506.01249.

[68] M. Eichenfield and O. Painter. Measurement of optical forces within a high-q microcavity-waveguide system. In *Conference on Lasers and Electro-Optics/Quantum Electronics and Laser Science Conference and Photonic Applications Systems Technologies*, page JMB3. Optical Society of America, 2007.

[69] M. L. Povinelli, S. G. Johnson, M. Lončar, M. Ibanescu, E. J. Smythe, F. Capasso, and J. D. Joannopoulos. High-q enhancement of attractive and repulsive optical forces between coupled whispering-gallery-mode resonators. *Opt. Express*, 13(20):8286–8295, Oct 2005.

[70] J. Rosenberg, Q. Lin, and O. Painter. Static and dynamic wavelength routing via the gradient optical force. *Nature Photonics*, 3:478–483, 2009.

[71] G. Anetsberger, E. Gavartin, O. Arcizet, Q. P. Unterreithmeier, E. M. Weig, M. L. Gorodetsky, J. P. Kotthaus, and T. J. Kippenberg. Measuring nanomechanical motion with an imprecision below the standard quantum limit. *Phys. Rev. A*, 82:061804, Dec 2010.

[72] A. Ashkin, J. M. Dziedzic, J. E. Bjorkholm, and S. Chu. Observation of a single-beam gradient force optical trap for dielectric particles. *Opt. Lett.*, 11(5):288–290, May 1986.

[73] J. M. Dziedzic A. Ashkin. Optical trapping and manipulation of single cells using infrared laser beams. *Nature*, 330:769–771, 1987.

[74] A. Ashkin and J. M. Dziedzic. Optical trapping and manipulation of viruses and bacteria. *Science*, 235(4795):1517–1520, 1987.

[75] C. T. Lim, M. Dao, S. Suresh, C. H. Sow, and K. T. Chew. Large deformation of living cells using laser traps. *Acta Materialia*, 52(7):1837 – 1845, 2004.

[76] J. Millen, T. Deesuwan, P Barker, and J. Anders. Nanoscale temperature measurements using non-equilibrium brownian dynamics of a levitated nanosphere. *Nature Nanotechnology*, 9:425–429, 2014.

[77] T. Li, S. Kheifets, and M. G. Raizen. Milikelvin cooling of an optically trapped microsphere in vaccuum. *Nature Physics*, 7, 2011.

[78] J. Gieseler, B. Deutsch, R. Quidant, and L. Novotny. Subkelvin parametric feedback cooling of a laser-trapped nanoparticle. *Phys. Rev. Lett.*, 109:103603, Sep 2012.

[79] A. A. Geraci, S. B. Papp, and J. Kitching. Short-range force detection using optically cooled levitated microspheres. *Phys. Rev. Lett.*, 105:101101, Aug 2010.

[80] M. Li, W. H. P. Pernice, C. Xiong, T. Baehr-Jones, M. Hockberg, and H. X. Tang. Harnessing optical forces in integrated photonic circuits. *Nature*, 456:480–484, 2008.

[81] V. B. Braginskiǐ and A. B. Manukin. Ponderomotive Effects of Electromagnetic Radiation. *Soviet Journal of Experimental and Theoretical Physics*, 25:653, October 1967.

[82] A. Ashkin and J. M. Dziedzic. Observation of resonances in the radiation pressure on dielectric spheres. *Phys. Rev. Lett.*, 38:1351–1354, Jun 1977.

[83] Y. Li, O. V. Svitelskiy, A. V. Maslov, D. Carnegie, E. Rafailov, and V. N. Astratov. Giant resonant light forces in microspherical photonics. *Light: Science & Applications*, 2, 2013.

[84] A. Heidmann, G. Anetsberger, E. M. Weig, J. P. Kotthaus, and T. J. Kippenberg. Cavity optomechanics and cooling nanomechanical oscillators using microresonator enhanced evanescent near-field coupling. *Comptes Rendus Physique*, 12(9):800 – 816, 2011.

[85] F. Marquardt. Quantum optomechanics. Les Houches Lecture Notes, School on Quantum Machines, 2001.

[86] M. Arndt and K. Hornberger. Testing the limits of quantum mechanical superpositions. *Nature Physics*, 10(4):271–277, 2014.

[87] E. Joos, H. D. Zeh, C. Kiefer, D. J. W. Giulini, J. Kupsch, and I.-O. Stamatescu. *Decoherence and the Appearance of a Classical World in Quantum Theory*. Springer, 2003.

[88] G. C. Ghirardi, A. Rimini, and T. Weber. Unified dynamics for microscopic and macroscopic systems. *Phys. Rev. D*, 34:470–491, Jul 1986.

[89] R. Penrose. Quantum computation, entanglement and state reduction. *Philosophical Transactions of the Royal Society of London A: Mathematical, Physical and Engineering Sciences*, 356(1743):1927–1939, 1998.

[90] S. Kolkowitz, A. C. Bleszynski Jayich, Q. P. Unterreithmeier, S. D. Bennett, P. Rabl, J. G. E. Harris, and M. D. Lukin. Coherent sensing of a mechanical resonator with a single-spin qubit. *Science*, 335(6076):1603–1606, 2012.

[91] T. A. Palomaki, J. W. Harlow, J. D. Teufel, R. W. Simmonds, and K. W. Lehnert. Coherent state transfer between itinerant microwave fields and a mechanical oscillator. *Nature*, 495:210–214, 2013.

[92] M. Montinaro, G. Wüst, M. Munsch, Y. Fontana, E. Russo-Averchi, M. Heiss, A. Fontcuberta i Morral, R. J. Warburton, and M. Poggio. Quantum dot optomechanics in a fully self-assembled nanowire. *Nano Letters*, 14(8):4454–4460, 2014. PMID: 25010118.

[93] Lord Rayleigh. The problem of the whispering gallery. *Scientific Papers*, 20(120):1001–1004, 1910.

[94] S. Maayani, L. L. Martin, and T. Carmon. Water-walled microfluidics for high-optical finesse cavities. *Nature Communications*, 7, 2016.

[95] A. D. Ward, M. Zhang, and O. Hunt. Broadband mie scattering from optically levitated aerosol droplets using a white led. *Opt. Express*, 16(21):16390–16403, Oct 2008.

[96] J. C. Knight, G. Cheung, F. Jacques, and T. A. Birks. Phase-matched excitation of whispering-gallery-mode resonances by a fiber taper. *Opt. Lett.*, 22(15):1129–1131, Aug 1997.

[97] L. Arques, A. Carrascosa, V. Zamora, A. Díez, J. L. Cruz, and M. V. Andrés. Excitation and interrogation of whispering-gallery modes in optical microresonators using a single fused-tapered fiber tip. *Opt. Lett.*, 36(17):3452–3454, Sep 2011.

[98] N. Dubreuil, J. C. Knight, D. K. Leventhal, V. Sandoghdar, J. Hare, and V. Lefèvre. Eroded monomode optical fiber for whispering-gallery mode excitation in fused-silica microspheres. *Opt. Lett.*, 20(8):813–815, Apr 1995.

[99] Y.-S Park and H. Wang. Resolved-sideband and cryogenic cooling of an optomechanical resonator. *Nature Physics*, 5:489–493, 2009.

[100] S. M. Lacey. *Ray and Wave Dynamics in Three Dimensional Asymmetric Optical Resonantors*. PhD thesis, University of Oregon, 2003.

[101] G. Mie. Beiträge zur optik trüber medien, speziell kolloidaler metallösungen. *Annalen der Physik*, 330:377–445, 1908.

[102] T. J. Kippenberg. *Nonlinear Optics in Ultra-high-Q Whispering Gallery Optical Microcavities*. PhD thesis, California Institute of Technology, 2004.

[103] C. Matzler. Matlab functions for mie scattering and absorption. Technical report, Institut fur Angewandte Physik, 2002.

[104] S. Balac and P. Féron. Whispering gallery modes volume computation in optical micro-spheres. Technical report, Mathematics Research Institute of Rennes, Fonctions Optiques pour les Technologies de Information, 263 avenue du Général Leclerc, 2015.

[105] C. F. Bohren and D. R. Huffman. *Absorption and Scattering of Light by Small Particles*. Wiley Science, 2010.

[106] M. Abramowitz and I. A. Stegun. *Handbook of Mathematical Functions: with Formulas, Graphs, and Mathematical Tables*. Dover Publications, 1965.

[107] F. Vollmer and S. Arnold. Whispering-gallery-mode biosensing: label-free detection down to single molecules. *Nature methods*, 5(7):591–596, 2008.

[108] C. C. Lam, P. T. Leung, and K. Young. Explicit asymptotic formulas for the positions, widths, and strengths of resonances in mie scattering. *J. Opt. Soc. Am. B*, 9(9):1585–1592, Sep 1992.

[109] S. Schiller. Asymptotic expansion of morphological resonance frequencies in mie scattering. *Appl. Opt.*, 32(12):2181–2185, Apr 1993.

[110] M. Fujiwara, K. Toubaru, and S. Takeuchi. Optical transmittance degradation in tapered fibers. *Opt. Express*, 19(9):8596–8601, Apr 2011.

[111] H. Rokhsari, S. M. Spillane, and K. J. Vahala. Loss characterization in microcavities using the thermal bistability effect. *Applied Physics Letters*, 85(15):3029–3031, 2004.

[112] B. E. Little, J. P. Laine, and H. A. Haus. Analytic theory of coupling from tapered fibers and half-blocks into microsphere resonators. *Journal of Lightwave Technology*, 17(4):704–715, Apr 1999.

[113] M. L. Gorodetsky, A. D. Pryamikov, and V. S. Ilchenko. Rayleigh scattering in high-q microspheres. *J. Opt. Soc. Am. B*, 17(6):1051–1057, Jun 2000.

[114] Y. L. Li, J. Millen, and P. F. Barker. Cooling the centre-of-mass motion of a silica microsphere. In *Proc. SPIE 9164, Optical Trapping and Optical Micromanipulation XI, 916404*, 2014.

[115] L. Ding, C. Belacel, S. Ducci, G. Leo, and I. Favero. Ultralow loss single-mode silica tapers manufactured by a microheater. *Appl. Opt.*, 49(13):2441–2445, May 2010.

[116] J. M. Ward, D. G. OShea, B. J. Shortt, M. J. Morrissey, K. Deasy, and S. G. Nic Chormaic. Heat-and-pull rig for fiber taper fabrication. *Review of Scientific Instruments*, 77(8), 2006.

[117] G. Keiser. *Optical Fiber Communications.* McGraw-Hill,, 1991.

[118] D. Gloge. Weakly guiding fibers. *Appl. Opt.*, 10(10):2252–2258, Oct 1971.

[119] H. A. Waves. *Waves and Fields in Optoelectronics.* Prentice-Hall, 1984.

[120] S. M. Spillane, T. J. Kippenberg, O. J. Painter, and K. J. Vahala. Ideality in a fiber-taper-coupled microresonator system for application to cavity quantum electrodynamics. *Phys. Rev. Lett.*, 91:043902, Jul 2003.

[121] C. Schmidt, A. Chipouline, T. Pertsch, A. Tünnermann, O. Egorov, F. Lederer, and L. Deych. Nonlinear thermal effects in optical microspheres at different wavelength sweeping speeds. *Opt. Express*, 16(9):6285–6301, Apr 2008.

[122] D. W. Vernooy, V. S. Ilchenko, H. Mabuchi, E. W. Streed, and H. J. Kimble. High-Q measurements of fused-silica microspheres in the near infrared. *Opt. Lett.*, 23(4):247–249, Feb 1998.

[123] T. A. Birks and Y. W. Li. The shape of fiber tapers. *J. Lightwave Technol.*, 10:432–438, 1992.

[124] J. D. Love, W. M. Henry, W. J. Stewart, R. J. Black, S. Lacroix, and F. Gonthier. Tapered single-mode fibres and devices, part 1: Adiabaticity criteria. *IEE Proceedings J (Optoelectronics)*, 138:343–354(11), October 1991.

[125] F. Xu and G. Brambilla. Preservation of micro-optical fibers by embedding. *Japanese Journal of Applied Physics*, 47(8S1):6675, 2008.

[126] A. Gerakis. *Controlling and probing molecular motion with optical lattices.* PhD thesis, University College London, 2014.

[127] K. S. Repasky, G. W. Switzer, and J. L. Carlsten. Design and performance of a frequency chirped external cavity diode laser. *Review of Scientific Instruments*, 73(9):3154–3159, 2002.

[128] T. Carmon, L. Yang, and K. J. Vahala. Dynamical thermal behaviour and thermal self-stability of microcavities. *Opt. Express*, 12:4742–4750, Sept 2004.

[129] Y. Wu, J. Ward, and S. Nic Chormaic. Observation of thermal feedback on the optical coupling noise of a microsphere attached to a low-spring-constant cantilever. *Phys. Rev. A*, 85:053820, May 2012.

[130] G. Guan, S. Arnold, and M. V. Otugen. Temperature measurements using a microoptical sensor based on whispering gallery modes. *AIAA Journal*, 44(10):2385–2389, 2006.

[131] E. D. Black. An introduction to pounddreverhall laser frequency stabilization. *American Journal of Physics*, 69(1):79–87, 2001.

[132] R. W. P. Drever, J. L. Hall, F. V. Kowalski, J. Hough, G. M. Ford, A. J. Munley, and H. Ward. Laser phase and frequency stabilization using an optical resonator. *Applied Physics B*, 31(2):97–105, 1983.

[133] L. Collot, V. Lefvre-Seguin, M. Brune, J. M. Raimond, and S. Haroche. Very high-Q whispering-gallery mode resonances observed on fused silica microspheres. *EPL (Europhysics Letters)*, 23(5):327, 1993.

[134] I. Teraoka. Analysis of thermal stabilization of whispering gallery mode resonance. *Optics Communications*, 310:212 – 216, 2014.

[135] R. P. Middlemiss, A. Samarelli, D. J. Paul, J. Hough, S. Rowan, and G. D. Hammond. Measurement of the Earth tides with a MEMS gravimeter. *Nature*, 531:614–617, Mar 2016.

[136] C. Wuttke, G. D. Cole, and A. Rauschenbeutel. Optically active mechanical modes of tapered optical fibers. *Phys. Rev. A*, 88:061801, Dec 2013.

[137] C. Hohberger Metzger and K. Karrai. Cavity cooling of a microlever. *Nature*, 432:1002–1005, 2004.

[138] T.J. Kippenberg and K.J. Vahala. Cavity optomechanics: Back action at the mesoscale. *Science*, 321, 2008.

[139] M. R. Vanner, J. Hofer, G. D. Cole, and M. Aspelmeyer. Cooling-by-measurement and mechanical state tomography via pulsed optomechanics. *Nature Communications*, 4:2295, 2013.

[140] M. Poot. *Mechanical Systems at the nanoscale.* PhD thesis, TU Delft, 2009.

[141] G. Heinzel, A. Rüdiger, and R. Schilling. Spectrum and spectral density estimation by the discrete Fourier transform (DFT), including a comprehensive list of window functions and some new at-top windows. Technical report, 2002.

[142] A. H. Safavi-Naeini, S. Groblacher, J. T. Hill, J. Chan, M. Aspelmeyer, and O. Painter. Squeezed light from a silicon micromechanical resonator. *Nature*, 500:185–189, 2013.

[143] U. B. Hoff, G. I. Harris, L. S. Madsen, H. Kerdoncuff, M. Lassen, B. M. Nielsen, W. P. Bowen, and U. L. Andersen. Quantum-enhanced micromechanical displacement sensitivity. *Opt. Lett.*, 38(9):1413–1415, May 2013.

[144] A. A. Clerk, M. H. Devoret, S. M. Girvin, F. Marquardt, and R. J. Schoelkopf. Introduction to quantum noise, measurement, and amplification. *Rev. Mod. Phys.*, 82:1155–1208, Apr 2010.

[145] P. F. Cohadon, A. Heidmann, and M. Pinard. Cooling of a mirror by radiation pressure. *Phys. Rev. Lett.*, 83:3174–3177, Oct 1999.

[146] M. Wu, A. C. Hryciw, C. Healey, D. P. Lake, H. Jayakumar, M. R. Freeman, J. P. Davis, and P. E. Barclay. Dissipative and dispersive optomechanics in a nanocavity torque sensor. *Phys. Rev. X*, 4:021052, Jun 2014.

[147] L. Chen, X. Yu, and D. Wang. Cantilever dynamics and quality factor control in AC mode AFM height measurements. *Ultramicroscopy*, 107(45):275 – 280, 2007.

[148] C. C. Fuller, S. Elliot, and P. A. Nelson. *Active Control of Vibration.* Academic Press, 1996.

[149] K. H. Lee, T. G. McRae, G. I. Harris, J. Knittel, and W. P. Bowen. Cooling and control of a cavity optoelectromechanical system. *Phys. Rev. Lett.*, 104:123604, Mar 2010.

[150] L. Novotny and B. Hecht. *Principles of nano-optics, ch 13.* Cambridge Univ Press, 2006.

[151] D. Damjanovic. Hysteresis in piezoelectric and ferroelectric materials. In G. Bertotti and I. D. Mayergoyz, editors, *The Science of Hysteresis: Hysteresis in materials.* Academic Press, 2006.

[152] S. Blundell. *Concepts in Thermal Physics.* Oxford Univeristy Press, 2009.

[153] Application Note 255 National Semiconductor SNOA719. Power spectra estimation. Technical report, 1980.

[154] M. R. Nelis, L. Yu, W. Zhang, Y. Zhao, C. Yang, A. Raman, S. Mohammadi, and J. F. Rhoads. Sources and implications of resonant mode splitting in silicon nanowire devices. *Nanotechnology*, 22(45):455502, 2011.

[155] O. Basarir, S. Bramhavar, and K. L. Ekinci. Near-field optical transducer for nanomechanical resonators. *Applied Physics Letters*, 97(25), 2010.

[156] W. F. Stokey. Vibration of systems having distributed mass and elasticity. In C. M. Harris and A. G. Piersol, editors, *Harris' Shock and Vibration Handbook, 5th edition*, chapter 7. McGraw-Hil, Oxford, 2002.

[157] K. L. Ekinci and M. L. Roukes. Nanoelectromechanical systems. *Review of Scientific Instruments*, 76(6), 2005.

[158] D. E. Chang, C. A. Regal, S. B. Papp, D. J. Wilson, J. Ye, O. Painter, H. J. Kimble, and P. Zoller. Cavity opto-mechanics using an optically levitated nanosphere. *Proceedings of the National Academy of Sciences*, 107(3):1005–1010, 2010.

[159] J. D. Thompson, B. M. Zwickl, A. M. Jayich, F. Marquardt, S. M. Girvin, and J. Harris. Strong dispersive coupling of a high finesse cavity to a micromechanical membrane. *Nature*, 452:72–75, 2008.

[160] M. Aspelmeyer, T. J. Kippenberg, and F. Marquardt. Cavity optomechanics. *Rev. Mod. Phys.*, 86:1391–1452, Dec 2014.

[161] X. Liu, J. F. Vignola, H. J. Simpson, B. R. Lemon, B. H. Houston, and D. M. Photiadis. A loss mechanism study of a very high q silicon micromechanical oscillator. *Journal of Applied Physics*, 97(2), 2005.

[162] F. R. Blom, S. Bouwstra, M. Elwenspoek, and J. H. J. Fluitman. Dependence of the quality factor of micromachined silicon beam resonators on pressure and geometry. *Journal of Vacuum Science Technology B*, 10(1):19–26, 1992.

[163] O. Svitelskiy, V. Sauer, N. Liu, K-M. Cheng, E. Finley, M. R. Freeman, and W. K. Hiebert. Pressurized fluid damping of nanoelectromechanical systems. *Phys. Rev. Lett.*, 103:244501, Dec 2009.

[164] J.-M. Courty, A. Heidmann, and M. Pinard. Quantum limits of cold damping with

optomechanical coupling. *The European Physical Journal D - Atomic, Molecular, Optical and Plasma Physics*, 17(3):399–408, 2001.

[165] P. C. D. Hobbs. Reaching the shot noise limit for $10. *Opt. Photon. News*, 2(4):17–23, Apr 1991.

[166] W. P. Bowen and G. J. Milburn. *Quantum Optomechanics.* CRC Press, Taylor & Francis Group, 2016.

[167] G. Milburn and M. Woolley. An Introduction to Quantum Optomechanics. *Acta Physica Slovaca*, 61:483–601, October 2011.

[168] J. Suh, A. J. Weinstein, C. U. Lei, E. E. Wollman, S. K. Steinke, P. Meystre, A. A. Clerk, and K. C. Schwab. Mechanically detecting and avoiding the quantum fluctuations of a microwave field. *Science*, 344(6189):1262–1265, 2014.

[169] K. W. Murch, K. L. Moore, S. Gupta, and D. M. Stamper-Kurn. Observation of quantum-measurement backaction with an ultracold atomic gas. *Nature Physics*, 4:561–564, 2008.

[170] C. M. Caves. Quantum-mechanical radiation-pressure fluctuations in an interferometer. *Phys. Rev. Lett.*, 45:75–79, Jul 1980.

[171] D. J. Wilson, V. Sudhir, N. Piro, R. Schilling, A. Ghadimi, and T. J. Kippenberg. Feedback cooling of a nanomechanical oscillator to near its quantum ground state. In *2015 Conference on Lasers and Electro-Optics (CLEO)*, pages 1–2, May 2015.

[172] B. Abbott and LIGO Scientific Collaboration. Observation of a kilogram-scale oscillator near its quantum ground state. *New Journal of Physics*, 11(7):073032, 2009.

[173] G. Schulz. Active multivariable vibration isolation for a helicopter. *Automatica*, 15(4):461 – 466, 1979.

[174] M. J. Balas. Direct velocity feedback control of large space structures. *Journal of Guidance and Control*, 2(3):252–253, 1979.

[175] T. Sulchek, R. Hsieh, J. D. Adams, G. G. Yaralioglu, S. C. Minne, C. F. Quate, J. P. Cleveland, A. Atalar, and D. M. Adderton. High-speed tapping mode imaging with active Q control for atomic force microscopy. *Applied Physics Letters*, 76(11):1473–1475, 2000.

[176] K. J. Bruland, J. L. Garbini, W. M. Dougherty, and J. A. Sidles. Optimal control of force microscope cantilevers. ii. magnetic coupling implementation. *Journal of Applied Physics*, 80(4):1959–1964, 1996.

[177] J. Mertz, O. Marti, and J. Mlynek. Regulation of a microcantilever response by force feedback. *Applied Physics Letters*, 62(19):2344–2346, 1993.

[178] J. M. Nichol, E. R. Hemesath, L. J. Lauhon, and R. Budakian. Controlling the nonlinearity of silicon nanowire resonators using active feedback. *Applied Physics Letters*, 95(12), 2009.

[179] O. Arcizet, P.-F. Cohadon, T. Briant, M. Pinard, A. Heidmann, J.-M. Mackowski, C. Michel, L. Pinard, O. Français, and L. Rousseau. High-sensitivity optical monitoring of a micromechanical resonator with a quantum-limited optomechanical sensor. *Phys. Rev. Lett.*, 97:133601, Sep 2006.

[180] A. Vinante, M. Bignotto, M. Bonaldi, M. Cerdonio, L. Conti, P. Falferi, N. Liguori, S. Longo, R. Mezzena, A. Ortolan, G. A. Prodi, F. Salemi, L. Taffarello, G. Vedovato, S. Vitale, and J.-P. Zendri. Feedback cooling of the normal modes of a massive electromechanical system to submillikelvin temperature. *Phys. Rev. Lett.*, 101:033601, Jul 2008.

[181] D. Kleckner and D. Bouwmeester. Sub-kelvin optical cooling of a micromechanical resonator. *Nature*, 44:75–78, Aug 2006.

[182] O. Arcizet, P. F. Cohadon, T. Briant, M. Pinard, and A. Heidmann. Radiation-pressure cooling and optomechanical instability of a micromirror. *Nature*, 444:71–74, 2006.

[183] J. H. Chow, M. A. Taylor, T. T-Y. Lam, J. Knittel, J. D. Sawtell-Rickson, D. A. Shaddock, M. B. Gray, D. E. McClelland, and W. P. Bowen. Critical coupling control of a microresonator by laser amplitude modulation. *Opt. Express*, 20(11):12622–12630, May 2012.

[184] S. Mancini, D. Vitali, and P. Tombesi. Optomechanical cooling of a macroscopic oscillator by homodyne feedback. *Phys. Rev. Lett.*, 80:688–691, Jan 1998.

[185] C. Genes, D. Vitali, P. Tombesi, S. Gigan, and M. Aspelmeyer. Ground-state cooling of a micromechanical oscillator: Comparing cold damping and cavity-assisted cooling schemes. *Phys. Rev. A*, 77:033804, Mar 2008.

[186] A. Dantan, C. Genes, D. Vitali, and M. Pinard. Self-cooling of a movable mirror to the ground state using radiation pressure. *Phys. Rev. A*, 77:011804, Jan 2008.

[187] B. S. Sheard, M. B. Gray, C. M. Mow-Lowry, D. E. McClelland, and S. E. Whitcomb. Observation and characterization of an optical spring. *Phys. Rev. A*, 69:051801, May 2004.

[188] C. M. Mow-Lowry, A. J. Mullavey, S. Goßler, M. B. Gray, and D. E. McClelland. Cooling of a gram-scale cantilever flexure to 70 mk with a servo-modified optical spring. *Phys. Rev. Lett.*, 100:010801, Jan 2008.

[189] T. Corbitt, C. Wipf, T. Bodiya, D. Ottaway, D. Sigg, N. Smith, S. Whitcomb, and N. Mavalvala. Optical dilution and feedback cooling of a gram-scale oscillator to 6.9 mk. *Phys. Rev. Lett.*, 99:160801, Oct 2007.

[190] S. W. Schediwy, C. Zhao, L. Ju, D. G. Blair, and P. Willems. Observation of enhanced optical spring damping in a macroscopic mechanical resonator and application for parametric instability control in advanced gravitational-wave detectors. *Phys. Rev. A*, 77:013813, Jan 2008.

[191] P. Phohomsiri, F. E. Udwadia, and H. F. von Bremen. Time-delayed positive velocity feedback control design for active control of structures. *Journal of Engineering Mechanics*, 132(6):690–703, 2006.

[192] G. Sagué, E. Vetsch, W. Alt, D. Meschede, and A. Rauschenbeutel. Cold-atom physics using ultrathin optical fibers: Light-induced dipole forces and surface interactions. *Phys. Rev. Lett.*, 99:163602, Oct 2007.

[193] M. Zhang, G. S. Wiederhecker, S. Manipatruni, A. Barnard, P. McEuen, and M. Lipson. Synchronization of micromechanical oscillators using light. *Phys. Rev. Lett.*, 109:233906, Dec 2012.

[194] R. W. Peterson, T. P. Purdy, N. S. Kampel, R. W. Andrews, P.-L. Yu, K. W. Lehnert, and C. A. Regal. Laser cooling of a micromechanical membrane to the quantum backaction limit. *Phys. Rev. Lett.*, 116:063601, Feb 2016.

[195] A. Schliesser, G. Anetsberger, R. Riviére, O. Arcizet, and T. J. Kippenberg. High-sensitivity monitoring of micromechanical vibration using optical whispering gallery mode resonators. *New Journal of Physics*, 10(9):095015, 2008.

[196] A. Schliesser, O. Arcizet, R. Riviére, G. Anetsberger, and T. J. Kippenberg. Resolved-sideband cooling and position measurement of a micromechanical oscillator close to the Heisenberg uncertainty limit. *Nature Physics*, 5:509–514, 2009.

[197] G. Van der Sande, M. C. Soriano, M. Yousefi, M. Peeters, J. Danckaert, G. Verschaffelt, and D. Lenstra. Influence of current noise on the relaxation oscillation dynamics of semiconductor lasers. *Applied Physics Letters*, 88(7), 2006.

[198] K. Petermann. *Laser Diode Modulation and Noise.* Klümer Academic, Dordrecht, 1988.

[199] T. J. Kane. Intensity noise in diode-pumped single-frequency nd:yag lasers and its control by electronic feedback. *IEEE Photonics Technology Letters*, 2(4):244–245, April 1990.

[200] M. L. Gorodetsky and I. S. Grudinin. Fundamental thermal fluctuations in microspheres. *J. Opt. Soc. Am. B*, 21(4):697–705, Apr 2004.

[201] B. Dahlgren. Noise in fiber optic communication links. online.

[202] I. Pikovski, M. R. Vanner, M. Aspelmeyer, M. S. Kim, and Č. Brukner. Probing planck-scale physics with quantum optics. *Nature Physics*, 8, 2012.

[203] T. J. Kane and E. A. P. Cheng. Fast frequency tuning and phase locking of diode-pumped nd:yag ring lasers. *Opt. Lett.*, 13(11):970–972, Nov 1988.

[204] I. S. Grudinin, V. S. Ilchenko, and L. Maleki. Ultrahigh optical Q factors of crystalline resonators in the linear regime. *Phys. Rev. A*, 74:063806, Dec 2006.

[205] M. Poggio, M. P. Jura, C. L. Degen, M. A. Topinka, H. J. Mamin, D. Goldhaber-Gordon, and D. Rugar. An off-board quantum point contact as a sensitive detector of cantilever motion. *Nature Physics*, 4:635–638, 2008.

[206] R. Thijssen, E. Verhagen, T. J. Kippenberg, and A. Polman. Plasmon nanomechanical coupling for nanoscale transduction. *Nano Letters*, 13(7):3293–3297, 2013. PMID: 23746212.

[207] M. D. Baaske, M. R. Foreman, and F. Vollmer. Single-molecule nucleic acid interactions monitored on a label-free microcavity biosensor platform. *Nature Nanotechnology*, 9:933–939, 2014.

[208] A. Hopkins, K. Jacobs, S. Habib, and K. Schwab. Feedback cooling of a nanomechanical resonator. *Phys. Rev. B*, 68:235328, Dec 2003.

[209] M. D. LaHaye, O. Buu, B. Camarota, and K. C. Schwab. Approaching the quantum limit of a nanomechanical resonator. *Science*, 304(5667):74–77, 2004.

[210] F. Elste, S. M. Girvin, and A. A. Clerk. Quantum noise interference and backaction cooling in cavity nanomechanics. *Phys. Rev. Lett.*, 102:207209, May 2009.

[211] A. Sawadsky, H. Kaufer, R. M. Nia, S. P. Tarabrin, F. Y. Khalili, K. Hammerer, and R. Schnabel. Observation of generalized optomechanical coupling and cooling on cavity resonance. *Phys. Rev. Lett.*, 114:043601, Jan 2015.

[212] T. Weiss and A. Nunnenkamp. Quantum limit of laser cooling in dispersively and dissipatively coupled optomechanical systems. *Phys. Rev. A*, 88:023850, Aug 2013.

[213] T. Weiss, C. Bruder, and A. Nunnenkamp. Strong-coupling effects in dissipatively coupled optomechanical systems. *New Journal of Physics*, 15(4):045017, 2013.

[214] Y-C. Liu, Y-F. Xiao, X. Luan, and C. W. Wong. Dynamic dissipative cooling of a mechanical resonator in strong coupling optomechanics. *Phys. Rev. Lett.*, 110:153606, Apr 2013.

[215] T. Chen and X-B. Wang. Fast cooling in dispersively and dissipatively coupled optomechanics. *Scientific Reports*, 5(7745), 2015.

[216] J. Fan, C. Huang, and L. Zhu. Optomechanical nonlinearity enhanced optical sensors. *Opt. Express*, 23(3):2973–2981, Feb 2015.

[217] S. Gigan, H.R. Bohm, G. Langer, M. Aspelmeyer, and A. Zeillinger. Self cooling of a micromirror by radiation pressure. *Nature*, 444:7115, 2006.

[218] A. Dorsel, J. D. McCullen, P. Meystre, E. Vignes, and H. Walther. Optical bistability and mirror confinement induced by radiation pressure. *Phys. Rev. Lett.*, 51:1550–1553, Oct 1983.

[219] T.J. Kippenberg and K.J. Vahala. Cavity opto-mechanics. *Opt. Express*, 15(25):17172–17205, Dec 2007.

[220] C. Monroe, D. M. Meekhof, B. E. King, S. R. Jefferts, W. M. Itano, D. J. Wineland, and P. Gould. Resolved-sideband raman cooling of a bound atom to the 3D zero-point energy. *Phys. Rev. Lett.*, 75:4011–4014, Nov 1995.

[221] S. P. Tarabrin, H. Kaufer, F. Y. Khalili, R. Schnabel, and K. Hammerer. Anomalous dynamic backaction in interferometers. *Phys. Rev. A*, 88:023809, Aug 2013.

[222] M-Y. Yan, H-K. Li, Y-C. Liu, W-L. Jin, and Y-F. Xiao. Dissipative optomechanical coupling between a single-wall carbon nanotube and a high-Q microcavity. *Phys. Rev. A*, 88:023802, Aug 2013.

[223] I. Hassani nia and H. Mohseni. Surface-plasmon-polariton˘assisted dissipative back-action cooling and amplification. *Phys. Rev. A*, 92:053852, Nov 2015.

[224] P. Maystre and M. Sargent. *Elements of Quantum Optics.* Springer, 2007.

[225] M. Li, W. H. P. Pernice, and H. X. Tang. Reactive cavity optical force on microdisk-coupled nanomechanical beam waveguides. *Phys. Rev. Lett.*, 103:223901, Nov 2009.

[226] A. C. Hryciw, M. Wu, B. Khanaliloo, and P. E. Barclay. Tuning of nanocavity optomechanical coupling using a near-field fiber probe. *Optica*, 2(5):491–496, May 2015.

[227] R. M. Cole, G. A. Brawley, V. P. Adiga, R. De Alba, J. M. Parpia, B. Ilic, H. G. Craighead, and W. P. Bowen. Evanescent-field optical readout of graphene mechanical motion at room temperature. *Phys. Rev. Applied*, 3:024004, Feb 2015.

[228] W. Wieczorek, S. G. Hofer, J. Hoelscher-Obermaier, R. Riedinger, K. Hammerer, and M. Aspelmeyer. Optimal state estimation for cavity optomechanical systems. *Phys. Rev. Lett.*, 114:223601, Jun 2015.

[229] O. Woodman. An introduction to inertial navigation: Technical report 696. Technical report, University of Cambridge, 2007.

[230] D. G. Blair, E. J. Howell, Ju. L., and C. Zhao. *Advanced Gravitational Wave Detectors.* Cambridge University Press, 2012.

[231] S. M. Dickerson, J. M. Hogan, A. Sugarbaker, D. M. S. Johnson, and M. A. Kasevich. Multiaxis inertial sensing with long-time point source atom interferometry. *Phys. Rev. Lett.*, 111:083001, Aug 2013.

[232] J. Kalenik and R. Pajk. Eurosensors XI: A cantilever optical-fiber accelerometer. *Sensors and Actuators A: Physical*, 68(1):350 – 355, 1998.

[233] M. Kraft, C. P. Lewis, and T. G. Hesketh. Closed-loop silicon accelerometers. *IEE Proceedings - Circuits, Devices and Systems*, 145(5):325–331, Oct 1998.

[234] J. Soen, A. Voda, and C. Condemine. Controller design for a closed-loop micromachined accelerometer. *Control Engineering Practice*, 15(1):57 – 68, 2007.

[235] L. A. Christel, M. Bernstein, R. Craddock, and K. Petersen. Vibration rectification in silicon micromachined accelerometers. In *Solid-State Sensors and Actuators, 1991. Digest of Technical Papers, TRANSDUCERS '91., 1991 International Conference on*, pages 89–92, June 1991.

[236] S. Holleis, T. Hoinkes, C. Wuttke, P. Schneeweiss, and A. Rauschenbeutel. Experimental stressstrain analysis of tapered silica optical fibers with nanofiber waist. *Applied Physics Letters*, 104(16), 2014.

[237] A. B. Chidester, J. Hinch, and T. A. Roston. Real world experiences with event data recorders. In *Proc., 17th International Technical Conference on the Enhanced Safety of Vehicles*, page 247, 2001.

[238] Y. Dong, P. Zwahlen, A. M. Nguyen, F. Rudolf, and J. M. Stauffer. High performance inertial navigation grade sigma-delta mems accelerometer. In *Position Location and Navigation Symposium (PLANS), 2010 IEEE/ION*, pages 32–36, May 2010.

[239] D. J. Wineland and W. M. Itano. Laser cooling of atoms. *Phys. Rev. A*, 20:1521–1540, Oct 1979.

[240] X. Lu, J. Y. Lee, and Q. Lin. High-frequency and high-quality silicon carbide optomechanical microresonators. *Scientific Reports*, 5:17005, 2015.

[241] S. S. Verbridge, D. Finkelstein Shapiro, H. G. Craighead, and J. M. Parpia. Macroscopic tuning of nanomechanics: substrate bending for reversible control of frequency

and quality factor of nanostring resonators. *Nano Letters*, 7(6):1728–1735, 2007. PMID: 17497822.

[242] Q. P. Unterreithmeier, T. Faust, and J. P. Kotthaus. Damping of nanomechanical resonators. *Phys. Rev. Lett.*, 105:027205, Jul 2010.

[243] O. Arcizet, R. Rivière, A. Schliesser, G. Anetsberger, and T. J. Kippenberg. Cryogenic properties of optomechanical silica microcavities. *Phys. Rev. A*, 80:021803, Aug 2009.

[244] F. Lissillour, K. Ait Ameur, N. Dubreuil, G. Stephan, and M. Poulain. Whispering-gallery-mode nd-zblan microlasers at 1.05 μm. volume 3416, pages 150–156, 1998.

[245] J. M. Ward, Y. Wu, K. Khalfi, and S. Nic Chormaic. Short vertical tube furnace for the fabrication of doped glass microsphere lasers. *Review of Scientific Instruments*, 81(7), 2010.

[246] J. B. Hertzberg, T. Rocheleau, T. Ndukum, M. Savva, A. A. Clerk, and K. C. Schwab. Back-action-evading measurements of nanomechanical motion. *Nature Physics*, 6:213–217, 2010.

[247] O. Romero-Isart, A. C. Pflanzer, F. Blaser, R. Kaltenbaek, N. Kiesel, M. Aspelmeyer, and J. I. Cirac. Large quantum superpositions and interference of massive nanometer-sized objects. *Phys. Rev. Lett.*, 107:020405, Jul 2011.

[248] S. Nimmrichter and K. Hornberger. Macroscopicity of mechanical quantum superposition states. *Phys. Rev. Lett.*, 110:160403, Apr 2013.

[249] M. A. Taylor, J. Janousek, V. Daria, J. Knittel, B. Hage, H.-A. Bachor, and W. P. Bowen. Biological measurement beyond the quantum limit. *Nature Photonics*, 7:229–233, 2013.

[250] D. Goldwater, M. Paternostro, and P. F. Barker. Testing wave-function-collapse models using parametric heating of a trapped nanosphere. *Phys. Rev. A*, 94:010104, Jul 2016.

[251] M. Battaglia, J. Gottsmann, D. Carbone, and J. Fernández. 4D volcano gravimetry. *Geophysics*, 73(6):WA3–WA18, 2008.

[252] G. A. Sanders, S. J. Sanders, L. K. Strandjord, T. Qiu, J. Wu, M. Smiciklas, D. Mead, S. Mosor, A. Arrizon, W. Ho, and M. Salit. Fiber optic gyro development at honeywell, 2016.

[253] M. Terrel, M. J. F. Digonnet, and S. Fan. Performance comparison of slow-light coupled-resonator optical gyroscopes. *Laser Photonics Reviews*, 3(5):452–465, 2009.

[254] E. Vetsch, D. Reitz, G. Sagué, R. Schmidt, S. T. Dawkins, and A. Rauschenbeutel. Optical interface created by laser-cooled atoms trapped in the evanescent field surrounding an optical nanofiber. *Phys. Rev. Lett.*, 104:203603, May 2010.

[255] K. Wada, K. Sasaki, and H. Masuhara. Optical measurement of interaction potentials between a single microparticle and an evanescent field. *Applied Physics Letters*, 76(20):2815–2817, 2000.

[256] G. Brambilla, G. Senthil Murugan, J. S. Wilkinson, and D. J. Richardson. Optical manipulation of microspheres along a subwavelength optical wire. *Opt. Lett.*, 32(20):3041–3043, Oct 2007.

[257] J. D. Prestage, A. Williams, L. Maleki, M. J. Djomehri, and E. Harabetian. Dynamics of charged particles in a paul radio-frequency quadrupole trap. *Phys. Rev. Lett.*, 66:2964–2967, Jun 1991.